Ultraviolet Radiation of Hypervelocity Stagnation Flows and Shock/Boundary-Layer Interactions

Thesis by
Nelson Javier Yanes

In Partial Fulfillment of the Requirements for the
Degree of
Doctor of Philosophy

CALIFORNIA INSTITUTE OF TECHNOLOGY
Pasadena, California

2020
Defended January 27, 2020

Nelson Javier Yanes
ORCID: 0000-0001-8423-6958

ACKNOWLEDGEMENTS

I would like to thank Professor Austin for allowing me to join the hypersonics group and the years of interesting conversations on ultraviolet radiation. She always knew how to bring excitement in my research and was a great advisor. I thank Professor McKeon for always being open to discuss my research and to chat about future goals. Dr. James Polk has been a great mentor during my time at Caltech and I thank him for his years of help. I always enjoyed our pupusa lunches for catching up and sharing ideas. Professor Shepherd has been the foundation of my growth as a researcher. I thank him for his tremendous help at a time when I needed the most guidance. Finally, I would like to thank Professor Hornung for his all-knowing advice in research and in life. Some of the best ideas were formed whenever Professor Hornung dropped by to see what was new.

There are countless names in the Caltech community I would like to acknowledge. First, I thank my former and current group members Matt Leibowitz (who I will be joining at APL), Galina Shpuntova, Joel Lawson, Mallory Neet, Ilan Grossman, and Wesley Yu for being awesome people. Bahram Valiferdowsi, Christine Ramirez, and Denise Ruiz made my time very enjoyable from the many conversations we had together during my time in GALCIT. Many of my projects would not be possible without the tireless work of Ali Kiani, who was always willing to share his advice for machine work. My first year class have all been wonderful people and I always enjoyed our fun trips and conversations, even after first year was completed. I thank my former Catalina apartment roommates Paul Mazur, Juba Ziani, and Akshay Sridhar for the years of laughs, trips, and support during my time in Southern California. Finally, I thank the members of the Caltech Concert Band and the Slide Rule Trombone Choir for years of awesome music and performances.

I am fortunate to have so much support from folks in my home state of Maryland. I express my gratitude to Dr. Christopher Cadou for his years of advice from my time as an undergraduate student through my studies in graduate school. My path into the sciences would not have been possible without my former chemistry teacher Joseph Magdelinskas (“Mr. Mag”), who once told me, “Instead of flipping burgers over the summer, I want you to experience scientific research.” In my final conversation with him, I was proud to share that I was attending Caltech for graduate school. My Maryland friends have always been there to support me, often traveling across the country to spend time and catch up. This type of friendship lasts a lifetime and I am

grateful to have so much of it.

Finally, I have my family to give my gratitude. Thank you, mom and dad, for listening to me and helping me with every step of my journey in life. You often say I "made it" all by myself. In reality, I would not be in this position without your constant support. I give thanks to my fantastic brother Alexis, who has been a source of emotional support and friendship. Alexis has managed to keep me sane throughout this journey, and I am lucky to have a brother like him.

Partial support of the author was provided by the National Science Foundation Graduate Research Fellowship Program. The research performed at the California Institute of Technology was supported by the Air Force Office of Scientific Research (FA-9550-15-1-0288, FA-9550-19-1-0219) with Dr. Ivett Leyva.

ABSTRACT

Shock/boundary-layer interactions can induce flow distortion, create flow separation with loss of control authority, and result in high thermal loads. Correct prediction of the flow structure and heating loads is vital for vehicle survival. However, a recent NATO workshop revealed severe underprediction of thermal loads and discrepancies in the location of separation by simulations of high enthalpy air flows. Due to the coupling between thermochemistry and fluid mechanics, a substantial effort has been placed on the development and validation of thermochemical models. As a result, there is a need for experimental data that are more than mean flow surface measurements.

Spatially resolved emission spectra are collected in the post-shock regime of hypervelocity flow over a circular cylinder and a 30-55 degree double wedge. The Hypervelocity Expansion Tube (HET) is used to generate high Mach number, high enthalpy flow (Mach numbers $5-7$, $h_0 = 4-8$ MJ/kg) with minimal freestream dissociation. The NO γ band ($A^2\Sigma^+ - X^2\Pi$) emission is measured in the ultraviolet range of 210-250 nm at downstream locations behind shock waves. Excitation temperatures are extracted from the NO γ emission from spectrum fitting. The result is a temperature relaxation profile that quantifies the state thermal non-equilibrium. Profiles of vibrational band intensity as a function of streamwise distance are used as direct measurements of chemical non-equilibrium in the flow.

Cylinder experiments are performed with varying freestream total enthalpy, Mach number, and test gas O_2 mole fraction to examine changes in relaxation profile. Schlieren images are used to accurately measure standoff distance. Temperature measurements are compared against a zero-dimensional state-to-state model. Strategies for spectrum fitting are presented for cases where the gas is not optically thin and for radiation containing multiple electronic states. For freestream mixtures with reduced oxygen mole fraction, an electronic excitation temperature is required to describe the radiation of the NO γ, β ($B^2\Pi - X^2\Pi$), and δ ($C^2\Pi - X^2\Pi$) transitions. The creation of electronically excited NO is discussed in the context of measured vibrational band intensities and computed NO(A) number density profiles using a two-temperature reactive Landau-Teller model.

Emission spectra are collected in the post bow shock and reattachment shock region of hypervelocity flow over a double wedge. High speed schlieren imaging

is performed to investigate facility startup effects and for tracking features in a shock/boundary-layer interaction. Detector exposures occur at select times throughout the flow development process to study temporal changes in thermal and chemical non-equilibrium. Time evolution of temperatures at strategic locations of the flow is obtained from spectrum fitting. Two-temperature calculations of the oblique shock system are compared against the emission results. Radiation data are discussed in the context of recent simulation efforts.

PUBLISHED CONTENT AND CONTRIBUTIONS

[1] N. J. Yanes and J. M. Austin. Nitric oxide spectroscopic measurements in a hypervelocity stagnation flow. In *AIAA Scitech 2019 Forum*, 2019. doi: 10.2514/6.2019-0794.

N.J.Y. performed all experiments, performed data analysis, generated figures, and participated in the writing of the manuscript.

TABLE OF CONTENTS

LIST OF ILLUSTRATIONS

LIST OF TABLES

Chapter 1

INTRODUCTION

At hypervelocity conditions relevant for earth re-entry and single stage-to-orbit flight, real gas effects play an important role in the behavior of the flow field. These real gas effects include dissociation/recombination, vibrational excitation, and radiation absent in the description of perfect gases. The terms hypersonic and hypervelocity flow both describe a regime of supersonic conditions where Mach number is greater than 5 [7], with hypervelocity flow corresponding to a total enthalpy on the order of the gas dissociation energy [34]. An open question in hypervelocity flows is the impact of real gas effects on shock/boundary-layer interactions. The interaction of a shock wave with a boundary layer can induce flow distortion and impair vehicle performance, where flow separation leads to loss of control authority and severe localized heating on surfaces [71]. Vehicles such as the North American X-15 [11] and the Boeing X-51 Waverider [32] are vulnerable to such interactions at the locations of control surfaces and engine inlets. The coupling between the molecular processes of the gas and the macroscopic fluid mechanics makes the problem extremely challenging, where a broad range of length and time scales are exhibited. However, correct prediction of the flow structure and heating loads is vital for vehicle survival.

Hypervelocity flow over a double wedge geometry is a canonical example of a shock/boundary-layer interaction. Figure 1.1 shows an example schlieren image of a shock/boundary-layer interaction over a double wedge geometry for a Mach 7.2 condition. During flow development, a laminar boundary layer interacts with an oblique shock wave at the location of the hinge. Due to the adverse pressure gradient from the presence of the shock, separation of the boundary layer occurs, generating an additional oblique shock at the upstream location of separation. The separation region propagates upstream with time, allowing the separation shock to interact with other flow features, such as the bow shock and the lead oblique shock. The result is a complex system of waves formed downstream of the separation region. Oscillations occur in the bow shock location and in the shear layer, making the flow field highly time-dependent.

In a recent NATO workshop, experimental measurements of hypervelocity double

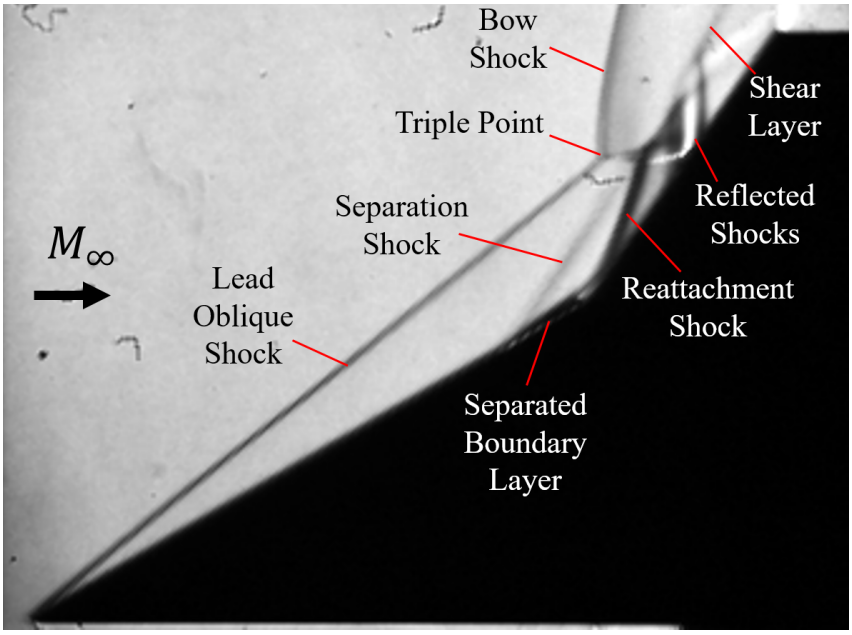

Figure 1.1: Major features in a hypervelocity shock/boundary-layer interaction over a double wedge geometry.

wedge flow were compared against simulations from around the world in an effort to test predictive capabilities and determine future areas of research [47]. The study revealed severe underprediction of thermal loads and discrepancies in the location of separation in high enthalpy air flows. Significant differences were observed between the simulations as well, where a variety of computational methods and thermochemical models were implemented.

State-of-the-art simulations of high enthalpy flows heavily rely on accurate models for thermal and chemical non-equilibrium. As a result, substantial effort has been placed on the development of thermochemical models [8, 13–15, 26, 59, 61, 74]. Validation of these models in fight tests is limited to a few examples [24, 25, 41]. Impulse facilities, such as reflected shock tunnels and expansion tunnels, can achieve high enthalpy conditions relevant for flight. High resolution diagnostics can be implemented in ground testing to address the demand for experimental data that are more than mean flow surface measurements.

A feasible solution to resolving discrepancies in thermochemical modeling is the use of spectroscopic techniques. Spectroscopic emission and absorption measurements can provide direct insight into the molecular processes in hypervelocity flow, while remaining non-intrusive to the gas. At hypersonic flight conditions up to about 9 km/s in the Earth's atmosphere, NO electronically excited states are significant

molecular radiators in the shock layer [96], and emission measurements at the relevant ultraviolet (UV) wavelengths can readily be made using only collection optics. As such, NO emission measurements can feasibly assess non-equilibrium effects in flight. In ground tests, NO shock layer emission measurements can be used to test thermochemical models and develop theory on radiative processes for interpretation of flight data. Very good spatial resolution can be achieved in emission measurements, critical in relaxation regions with steep gradients. NO γ ($A^2\Sigma^+ - X^2\Pi$) emission from the first electronically excited state to the ground state is one of the dominant bands in the 210-250 nm wavelength range. Other electronically excited NO states also emit in this wavelength range, such as NO β ($B^2\Pi - X^2\Pi$) and NO δ ($C^2\Pi - X^2\Pi$) systems.

The objective of the current study is to use emission spectroscopy as a tool for linking measured molecular processes, such as non-equilibrium relaxation profiles, to macroscopic variations in shock configuration of double wedge flows. This spectroscopic method will aid in understanding how real gas effects play a role in the development of features in a shock/boundary-layer interaction. As radiative processes are not fully understood, a steady cylinder experiment will serve as a benchmark for testing an emission diagnostic and to develop models for NO γ radiation. The bow shock of a cylinder flow will also serve as an analog to the bow shock in double wedge flows. Afterwards, emission measurements will be performed at strategic regions in a shock/boundary-layer interaction to understand the thermochemical non-equilibrium processes in the flow. The outcome of the work will include strategies for extracting quantitative properties from an unsteady radiating gas. Emission measurements from the cylinder and double wedge flows will serve as valuable validation data for thermochemical and radiation modeling of high enthalpy flows. With these validation data, it is possible to aid in resolving discrepancies between ground tests and simulations of hypervelocity flows.

1.1 Overview of Previous Work

Radiative Processes

The Bow Shock UV sounding rocket flight experiments [24, 25] obtained integrated shock layer emission measurements at 3.5 km/s and 5.1 km/s over a range of altitudes, and significant progress in radiative modeling for NO was made in analyzing the data [56, 58]. A key step is predicting NO formation and number densities in the electronically excited states. It was found that the altitude dependence of the data could be better captured by characterizing the NO excited state populations with the

translational, rather than vibrational, temperature [57]. In the work of Kossi and Boyd, the inclusion of vibration-dissociation coupling in direct simulation Monte Carlo (DSMC) models significantly improved agreement with the data [49]. It is found that the typical assumption for rotational and vibrational temperature of electronic states to be equivalent to the ground state bulk gas does not hold in the investigated flow regime. Discrepancies remained for the 0.28 μm and 0.31 μm peaks in the flight data, which Kossi and Boyd believed may be related to inaccurate quenching and collision modeling of OH. Further improved agreement was achieved through quasiclassical trajectory (QCT) calculations for NO ground state formation reaction rates [15]. Bose and Candler noted discrepancies in the NO vibrational temperature and attributed these to inaccurate modeling of de-excitation processes of NO(A).

The sensitivity of NO formation in the electronically excited NO(A) state to vibrational/translational relaxation models was examined using forced harmonic oscillator and Schwartz-Slawsky-Herzfeld (SSH) models in DSMC calculations by Li et al. [59]. Using quenching rate data from Settersten et al. [84], the excitation rate coefficients in quasi-steady state (QSS) were calculated to obtain number densities of NO(A) along a shock layer stagnation streamline, together with NEQAIR predicted spectra. Calculations were carried out at 5 and 7 km/s and comparisons between models were made, but experimental data were not available. The predicted number density profiles and spectra were reported to be noticeably and systematically different when NO internal temperatures were used rather than bulk flow temperatures. The authors suggest that comparisons of such predictions with experimental emission data would provide insight into energy transfer models.

In expanding flows, emission measurements of species, including NO, were used to investigate non-equilibrium at the exit of an arc-heat jet facility nozzle [2, 10, 40, 78, 79]. Three experimental campaigns were carried out in a series of studies in the NASA Ames Aerodynamic Heating Facility. Experimental spectra for γ and δ ($C^2\Pi - X^2\Pi$) bands, with unexpectedly weak signal from the ϵ band, were observed, while β ($B^2\Pi - X^2\Pi$) emission was not detected. Rotational, species-specific vibrational, and electronic temperatures were extracted from the spectra using NEQAIR [78, 79]. The electronic excitation temperature greatly exceeded the calculated electron temperature. A subsequent work by Hyun et al. examined this discrepancy and concluded that in these expanding flows, the population of NO(A) was largely due to radiative decay from NO(C), which is populated by inverse

dissociation during recombination of N and O atoms. The electronic excitation temperature could not be assumed to be the same as the electron temperature for all excited states [40].

Numerous works have been performed on radiation measurements in shock tube facilities. A piston-driven shock tube was used to generate two post-shock flow conditions with shock velocities of approximately 8 km/s with NO post-shock measurements of the emission spectrum by Abe et al. [1]. Both rotational and vibrational temperatures were obtained by fitting the NO γ (0,1) band using SPRADIAN. NO rotational temperatures were found to be significantly higher than the vibrational temperatures, as also predicted by the the thermochemical model.

Shock layer NO and N_2^+ radiation measurements at 5 to 10 km/s were carried out in an arc-driven shock tube facility at TsAGI by Gorelov et al. and used to develop a radiation model [29]. The electron temperature T_e is found to be close to the translational temperature T directly after the shock. However, for the remainder of the relaxation region, Gorelov et al. predict that T_e closely follows the vibrational temperature T_v due to the inelastic excitation of nitrogen vibrations by electron impact.

Experiments targeting velocities up to 9 km/s were carried out at the NASA Electric Arc Shock Tunnel (EAST) to investigate molecular radiative heating for portions of lunar return or low earth orbit entry [18]. Post-shock UV and IR emission spectra were obtained for initial mixtures of O_2 and N_2. Analysis by Cruden and Brandis revealed that initial DPLR stagnation line simulations combined with NEQAIR spectral calculations resulted in poor matches with experimental data, leading to an update to the kinetics model in DPLR and non-Boltzmann calculations in NEQAIR. The authors note that the two-temperature model typically used in DPLR assumes that the energy is described by a translational-rotational-electronic temperature and a separate vibrational temperature. The use of $T_{ex} = T$, however, resulted in excessive population of excited states and poor agreement between NEQAIR calculations and experiments. Spectra were analyzed assuming $T_{ex} = T_v$ in spite of the inconsistency with the flow simulations.

Gimelshein and Wysong compared the EAST data through a direct simulation Monte Carlo calculation [26]. At velocities of 6.81 km/s, the agreement was found to be sensitive to the model refinement for nitrogen vibration-dissociation coupling, the equilibrium constant, and energy distribution after the N_2+O exchange reaction. The authors point out that conclusions about the level of model refinement based

on comparisons with the spectra were subject to the unverified assumption of equal translational and electronic excitation temperatures. This was a concern, as the UV emission spectra of NO are extremely sensitive to the electronic excitation temperature. The authors note the current lack of time dependant shock layer data for NO UV bands for verification of computations.

Implementation of NO and its electronic states in the framework of a state-to-state model has recently been made by Kadochnikov and Arsentiev [45]. Comparisons were made with the NO γ emission measurements in shock tube experiments in the range of 5 to 10 km/s mentioned above [29]. Although the Kadochnikov and Arsentiev's kinetic model provided a correct qualitative description of these experimental data, the authors noted that peak NO gamma intensities from the state-to-state model were 1.5 to 3 times higher than those from the experiments summarized in Gorelov et al. [30] for velocities below 7.5 km/s. The post-shock NO(A) profile was reported to depend primarily on the formation of O atoms, and discrepancies between simulations and experiments in NO γ emission are suggested to come from inaccuracies in the rate constants of the associated chemical reactions.

Shock/Boundary-layer Interactions

Decades of experimental and theoretical work have examined shock-laminar boundary layer interactions in hypersonic flows. The experimental work of Holden [36, 37] provided one of the earliest examples of ground testing for measurements of hypervelocity separated flows, where measurements of pressure and heat flux were performed on the surface of flat plate-wedge models for M>14. In a joint experimental/computational study, Nompelis et al. [68] used a 25-55 degree double cone for studying shock wave boundary layer interactions. Modeling of the nozzle flow for the Large Energy National Shock (LENS) facility was performed to take into account vibrational freezing. Initial predictions show overestimates in the peak heating loads on the surface, with simulation resolution heavily determining the location of separation. In 2010, an updated set of experiments and computations were performed by Nompelis et al. [67] with new numerics for the CFD model [21]. Good agreement was obtained for lower enthalpy conditions with nitrogen, but poor agreement in the location of separation and magnitude of peak heating remained for high enthalpy cases. The authors noted that characterization of freestream conditions is required for high enthalpy experiments, since the calculated nozzle conditions with finite-rate vibrational relaxation and chemical reactions may only be realistic for low enthalpies and moderate enthalpies with nitrogen.

In the work of Olejniczak et al. [70–72], a considerable effort was made to assess the predictive capabilities of simulations for double wedge and double cone geometries. Comparisons of heat flux and flow structure were made, where a three-dimensional Navier-Stokes solver DPLR was used to design and simulate experiments performed at the T5 Hypervelocity Shock Tunnel. Underpredictions of separation length and disagreement in peak heating location were reported. Uncertainties in the non-equilibrium nitrogen dissociation rates and vibrational non-equilibrium in the freestream were cited as probable causes of the discrepancy [72].

Theoretical and experimental work on separation length in hypervelocity flows was performed by Davis and Sturtevant [20] for double wedge experiments in the T5 Hypervelocity Shock Tunnel. Scaling laws for the separation length were derived from a momentum balance proposed by Roshko [82] for flow over a step and the triple-deck theory developed by Stewartson and Williams [88] for laminar boundary layers. An increase in the scaled separation length of high enthalpy cases compared to low enthalpy cases was attributed to possible recombination in the free shear layer downstream of separation. In addition, Davis and Sturtevant showed that in the case of dissociation occurring downstream of the reattachment shock and not the leading shock, the reattachment pressure decreases relative to the chemically frozen case and causes a decrease in separation length. In a recent experimental campaign, Knisely performed experiments in the Hypervelocity Expansion Tube (HET) and T5 reflected shock tunnel using a 30-55 degree double wedge, a 25-55 degree double cone, and a 25-48 degree double cone geometry [48]. Heat flux measurements and schlieren videos were presented for T5 experiments at conditions that overlap the two facilities. Using new high speed schlieren imaging, oscillations were observed to occur in the bow shock and separation shock locations throughout test time. An updated analysis was performed using the scaling proposed by Davis and Sturtevant for double cones, where scaling of the mean separation length was consistent with the historical results for double wedges.

Experiments in the Hypervelocity Expansion Tube were performed by Swantek and Austin for double wedge and double cone geometries [91]. Diagnostics included surface heat flux measurements and high speed schlieren for stagnation enthalpies ranging from 2 to 8 MJ/kg and Mach numbers from 4 to 7. At higher enthalpies, nitrogen is observed to exhibit a larger standoff distance. The propagation distance of the triple-point structure was found to be larger in N_2 than in the air case, with larger oscillations present in the bow shock for high enthalpy nitrogen freestreams.

The measured establishment time of the triple point was also observed to be longer for nitrogen than in air. Preliminary emission work was performed in the post-bow shock region. However, results were heavily time averaged and only performed at a few point locations [90].

As mentioned previously, the predictive capabilities of several computational groups were compared against the data of Swantek and Austin, with the conclusion that three-dimensional time resolved calculations are required for accurate predictions of the flow field [47]. Direct Simulation Monte Carlo (DSMC) calculations were performed by Patil et al. [80] and Tumuklu et al. [93] to simulate the HET experiments. Initial two-dimensional simulations reveal the flow is unsteady throughout the experimental test time for the highest enthalpy case [80]. Improvement in the time evolution of shock features was obtained using a three-dimensional calculation, with better agreement in the peak heating loads on the second wedge [93]. In a followup study, a modal analysis of a DSMC calculation was implemented by Tumuklu, Levin and Theofilis [94] for low density freestreams. The windowed proper orthogonal decomposition (WPOD) method highlights that the bow, separation and transmitted shocks are strongly coupled. The authors commented that thermochemical effects are extremely sensitive to changes in shock structure, with computed nitrogen and air cases exhibiting differences in time behavior.

Three dimensional simulations of the Swantek and Austin nitrogen data were performed by Reinert et al. using the CFD package US3D [81]. Results show flow unsteadiness for both low and high enthalpy conditions within the experimental test times. Three-dimensionality of the separation region was observed, with separation occurring further downstream at the ends of the span. Khraibut and Gai performed a separate calculation using the US3D package with emphasis on investigating the effects of trailing edge expansion on flow steadiness [46]. For the highest enthalpy condition, a steady state was achieved 500 μs for an air freestream, beyond the experimental test time duration. Modifying the trailing edge of the double wedge geometry revealed marginal differences in flow steadiness. Numerical predictions of Hao, Wen, and Wang used the CFD code PHAROS for simulations of the double wedge flow [34]. Similar to previous studies, the computation shows that the flow has not reached steady state within the allotted experimental test time, with discrepancies in heat flux profile observed for high enthalpy air flows. Modeling of the startup processes of the HET was suggested for future computational studies of the double wedge flow.

1.2 Contributions of Present Work and Outline

A diagnostic to obtain spatially-resolved emission spectra for the NO ultraviolet emission is applied to post-shock gas for 3.95 and 3.30 km/s freestream velocities. Configuration of the collection optics is based on the work of Hornung and Sandeman [39], where emission is collected along a line downstream of a shock by projecting the image of the spectrometer slits at a location of interest. The result is an image on an intensified detector where one axis represents wavelength space and the other axis is in streamwise position. Binning data along the position axis allows for spectra to be extracted at locations downstream of the shock wave. Through a fitting procedure, the experimental spectra are compared with synthetic spectra calculated using a NO γ code based on the work of Sharma et al. [87] and the commercial code SpecAir [53]. From spectrum fitting, temperatures are extracted to generate a relaxation profile of the gas. When optical depth is not thin, temperature extraction can be achieved by fitting vibrational bands that exhibit the same change in intensity from the optically thin limit.

For stagnation flows, integrated radiance is extracted for varying freestream oxygen mole fraction. At the optically thin limit, measured vibrational band profiles provide insight in the production of NO(A) number density. As oxygen is reduced from the value in air, measured standoff distance increases and electronically excited states experience a reduction in quenching. The result is additional radiance of NO γ and other electronic transitions, such as the NO δ system. Spectra containing multiple electronic states of NO are modeled to investigate the role of oxygen quenching in mixture experiments. Profiles of NO(A) number density are also computed and compared with experimental data.

A new set of optical measurements is performed for high enthalpy air flows over a double wedge geometry. High speed schlieren videos with improved spatial resolution are recorded to investigate the effects of facility startup and for tracking of features in a shock/boundary-layer interaction. Emission measurements are performed in the post-bow shock region of the flow and downstream of the reattachment shock. Exposure times are set at multiple time intervals to track temporal variations in ultraviolet radiation. Time evolution of temperature profiles are obtained from spectrum fitting of double wedge radiation. Two-temperature reactive Landau-Teller calculations of the system of oblique shock waves are performed and compared with the reattachment shock data. Results of the time resolved radiation data are discussed in the context of recent simulation efforts.

The organization of this document begins with a review of the expansion tube facility and diagnostics used for studying radiating flow in Chapter 2. This is followed by a discussion on the relevant radiative processes found in hypervelocity flows in Chapter 3. The theory and models developed in this chapter will be applied to experimental measurements of ultraviolet radiation. Chapter 4 presents the experimental and computational results of ultraviolet radiation of stagnating flow. From the knowledge gained in cylinder flows, double wedge emission measurements are presented and interpreted in Chapter 5. The document concludes in Chapter 6 with a summary of the findings and future work.

Chapter 2

EXPERIMENTAL FACILITY AND DIAGNOSTICS

Ground testing facilities allow the ability for the experimenter to perform repeat tests at conditions relevant for hypervelocity flight. New diagnostics can be developed for non-intrusive measurements of hypervelocity flows without the logistics and heavy costs of flight experiments. In order to effectively study these high speed flows in a lab setting, an understanding of the facilities and diagnostics are required. In this chapter, a detailed look at the expansion tube facility will be presented. In addition, the design and methodology for spatially resolved emission spectroscopy will be covered.

2.1 The Hypervelocity Expansion Tube Facility

The hypervelocity expansion tube (HET) is used to produce high Mach number, high total enthalpy flows. The facility consists of a driver, driven, and accelerator section, all with an inner diameter of 150 mm. The HET is capable of Mach numbers in the range of 3.0-7.2 and total enthalpies in the range of 2.0-8.3 MJ/kg. The novelty of the facility is the minimal dissociation of the freestream, as only one shock processes the test gas without stagnating the flow. As there is no nozzle used in the facility, flow conditions can be selected by varying the initial pressures of the driven and acceleration sections of the facility, as well as the gas composition in the acceleration section. Details regarding the operation of the facility and its capabilities can be found in Dufrene et al. [22]. However, a brief summary of the physical processes of the flow will be presented here.

The unsteady gas dynamics of the facility can be described using a standard x-t diagram. Figure 2.1 shows an example x-t diagram of a high Mach number condition. When the primary diaphragm ruptures, the driven gas in state 1 is processed by a primary shock with speed U_p. Once the primary shock processes the entire driven section, the driven gas is at a state 2 defined by the shock jump conditions. A left facing expansion fan is also formed and processes the driver helium gas in state 4 until it reflects off the end wall. When the secondary diaphragm ruptures, a right facing transmitted shock and left facing expansion fan are generated. This unsteady expansion fan processes the post-shock driven gas and accelerates it to the final state 7. At the test section, test time is defined by the arrival of the contact surface

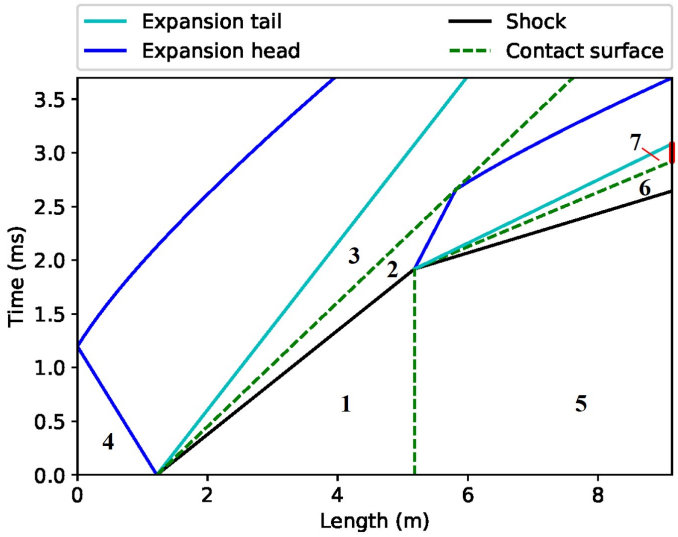

Figure 2.1: Labeled x-t diagram of the unsteady gas dynamic processes in an expansion tube operation. Calculation of waves is performed using LETS [54] with the M7-H8-He fill pressures.

between states 6 and 7 and the arrival of expansion waves. In the example shown in Fig. 2.1, the test time is indicated in red and is terminated by the arrival of the expansion tail.

One of the most important parameters in the HET is the velocity of the transmitted shock $U_{s,\text{accel}}$ and state 6 of the post-shock acceleration gas. Since a contact surface is formed between the final test gas and the post-shock acceleration gas, mass and momentum conservation requires that velocity and pressure must be identical between the two gases in states 6 and 7. As a result, the acceleration gas state is ultimately constrained to the final velocity and pressure of the test gas in state 7. A physical process of concern is deceleration of the transmitted shock due to viscous effects. Deceleration of the transmitted shock directly changes the final enthalpy of the test gas. Viscous effects also determine the core flow size of the final test gas. The time duration of the post-shock acceleration gas is highly relevant in the study of boundary layer separation of double wedge flow. Depending on the initial fill pressures, the flow is started with post-shock acceleration gas for a finite amount of time before the arrival of test gas. It is this defining feature that motivated the creation of a new nomenclature for HET conditions, where the first two letter and number pairs represent the nominal Mach number and enthalpy, respectively, while the third letter is the acceleration gas used in the experiment.

Data acquisition in the HET is preformed by two PXI-6133 data acquisition cards

Condition	Driver	Driven	Acceleration
M5-H4-A	3.3 MPa	6.0 kPa (Air)	600 mTorr (Air)
M5-H6-A	3.1 MPa	1.2 kPa (O_2/N_2)	173 mTorr (Air)
M7-H8-He	3.3 MPa	1.2 kPa (Air)	173 mTorr (He)
M7-H8-A	3.1 MPa	1.2 kPa (O_2/N_2)	28 mTorr (Room Air)

Table 2.1: Target fill pressures used for HET conditions

with a PXI-1031 chassis. Each card is connected to a BNC-2110 module that is used for measuring voltages of pressure transducers and delivering trigger signals. The National Instruments Labview VI software is used with the hardware, where data are recorded at 1 MHz for 30 ms with a pretrigger duration of 12 ms. Burst pressures are recorded using a Setra Model 206 (SN: 5099927). A Setra Datum 2000 display is used for monitoring the driver section pressure. The driven section fill pressure is measured using a Type 626 Baratron (SN: 01727048) with a range of 1000 Torr. The expansion section fill pressure is measured using a Type 626 Baratron (SN: 016476555) with a 2 Torr range. A YOKOGAWA DL850E oscilloscope is used exclusively for double wedge emission measurements for triggering purposes.

Calculated Freestream Conditions

To compute the freestream conditions, 1-D unsteady gas dynamic calculations solving the expansion tube processes are performed assuming either perfect gas or thermal and chemical equilibrium, for which the Shock and Detonation Toolbox [51] using Cantera [28] was implemented. Calculations of freestream conditions are performed using the software LETS developed by Lawson and Austin [54]. Table 2.1 lists the target fill pressures and gas compositions of the three sections of the HET. Predicted freestream conditions are shown in Table 2.2 and Table 2.3 using the target fill pressures. Calculations are performed assuming a perfect gas or equilibrium processes. In addition, air and nitrogen are used as test gases for the computations. The freestream conditions span stagnation enthalpies from 4.33 MJ/kg to 8.25 MJ/kg.

In Table 2.3, the M7-H8-A and M7-H8-He conditions share similar perfect gas solutions. However, M7-H8-A uses an air acceleration gas as opposed to helium in the M7-H8-He condition. The development of these two conditions allows for studies of facility effects on the generation of test gas. Comparisons of these two conditions will be made in terms of measured transmitted shock speed and double

	M5-H4-A			M5-H6-A		
Test Gas	Air	Air	N_2	Air	Air	N_2
Method	Perfect	Equi.	Equi.	Perfect	Equi.	Equi.
M_∞	5.15	5.30	5.24	4.87	5.13	5.07
h_0, MJ/kg	4.33	4.40	4.43	6.23	6.30	6.33
U_∞, m/s	2791	2814	2824	3283	3303	3309
T_∞, K	731	720	714	1129	1085	1075
p_∞, Pa	8848	8314	8367	3513	3238	3249
ρ_∞, g/m^3	42.14	40.20	39.48	10.84	10.39	10.18
t_{Test}, µs	342	327	331	311	290	294
Re, 1/m	-	3.27×10^6	3.35×10^6	-	7.56×10^5	7.73×10^5
$U_{s,\text{accel}}$, m/s	3382	3149	3159	3968	3633	3639

Table 2.2: Calculated freestream conditions for low enthalpy experiments assuming a perfect or equilibrium process.

	M7-H8-A			M7-H8-He		
Test Gas	Air	Air	N_2	Air	Air	N_2
Method	Perfect	Equi.	Equi.	Perfect	Equi.	Equi.
M_∞	7.18	7.32	7.26	7.18	7.20	7.13
h_0, MJ/kg	8.14	8.26	8.30	8.25	8.27	8.31
U_∞, m/s	3922	3949	3959	3948	3943	3954
T_∞, K	743	745	734	752	770	760
p_∞, Pa	807	744	748	821	818	822
ρ_∞, g/m^3	3.79	3.48	3.43	3.80	3.70	3.65
t_{Test}, µs	163	158	160	162	162	163
Re, 1/m	-	3.88×10^5	4.01×10^5	-	4.03×10^5	4.16×10^5
$U_{s,\text{accel}}$, m/s	4728	4325	4336	5456	5449	5462

Table 2.3: Calculated freestream conditions for high enthalpy experiments assuming a perfect or equilibrium process.

wedge flow startup.

Facility Upgrades and Updates to Operation

Substantial modifications to the facility were made to replace wear damage of components and to improve facility performance. In August 2018, the facility was upgraded with a new primary diaphragm cutter for use with 1.575 mm thick 5052 aluminum. The design of the flange allowed the diagram petals to open to the inner diameter of the tube and strike a flat surface. This minimizes the potential choking of helium from the driver section. The knife blades were based on the design of Sharma [86], with A2 tool steel as the material. Heat treatment was performed to a

hardness of 58-60 HRC before cutting. The heat treatment starts with preheating at 816 °C for 90 minutes. Heating is then set at 968 °C for an additional 90 minutes. Afterwards, the part is cooled in nitrogen for 10 minutes. Finally, the material is tempered at 204 °C for 2 hours. Electrical discharge machining was performed by Advanced Engineering and EDM to cut the material. Weld material used is silicon bronze, where the assembly is allowed to heat to 121 °C uniformly before two welding passes are made at the junctions. The assembly was finally tempered to 121 °C for 2 hours before the blades are ready for experiments. All heat treatment was performed by Supreme Steel Treating Inc. On the initial design, weld material was only applied at the 90 degree junctions of the steel pieces. A crack on weld material in one corner appeared in February 20, 2019. A second set of blades were created after the incident, with additional support material and welding material applied to the intersection of the three pieces at the backside of the assembly. No damage was observed on the second set of blades for the remainder of the campaign.

(a) Driver Flange and Knife Blades (b) Wire Cutters

Figure 2.2: Facility upgrades to the primary and secondary diaphragm.

It was found that torque applied to the bolts of the driver section heavily determines the burst pressure of the facility. This is reflected in Table 2.1, where some experiments used a higher burst pressure before the link between torque and burst pressure was made. As a result, a standard procedure of lubricating the bolts and sealing the driver flange was developed for consistency. The settings of the torque wrench and final burst pressure is recorded for every experiment.

A new set of wire cutters were also machined in August 2018. Wire cutters are used in the second flange to aid in the rupture of the secondary diaphragm. Without the wire cutters, the plastic material will not fully break apart and cause unwanted damage to test articles. In the former Illinois design, four protruding blocks held the

wire material and likely caused unwanted disturbances to the flow. The new design features an aluminum body with a groove on the outer diameter to allow for wire material to be wound and secured. The entire assembly fits flushed with the inner diameter of the tube, where a 0.660 mm (0.026 inch) diameter Malin music wire is used as the cutters. To improve the rupturing process of the secondary diaphragm, thinner material is used for the present experiments. Previous work by Swantek [90] used 12.7 μm mylar sheets. Birkelbach PTPLAIN material with a thickness of 8.5 μm is used as the new secondary diaphragm. An improvement in the pitot traces was observed when operating the facility with the new wire cutters and thinner diaphragm material.

In order to extend the number of operating conditions possible, an Agilent TwisTorr 304 FS turbo molecular pump is used for evacuating the acceleration section. The pump features a base pressure of 1E-7 mTorr and a gas throughput of 170 sccm. The turbo molecular pump is only used with the preparation of the M7-H8-A, which requires a target fill pressure of 28 mTorr. Leak tests are preformed by pumping down to 5 mTorr and recording pressures at 10 minute increments for 30 minutes. Afterwards, the acceleration section is pumped down a second time, where a second leak test is performed at 20 mTorr for 2 minutes. The operator uses a stop watch during the final firing preparations to record the time between isolation of the static pressure gauge and the rupture of the primary diaphragm. This allows for an accurate measurement of the leak rate from the recorded fill pressure. Due to the high rate of leaking, room air is only used in the acceleration section for M7-H8-A.

Transmitted Shock Speed Measurements

In a 2009 computational and experimental study, McGilvray et al. [65] characterized the AIR-1 condition for the HET using wall mounted pressure probes and pitot gauges. The experimental results were then compared with both a 1-D Lagrangian code and an axisymmetric CFD simulation that takes into account diaphragm effects and viscous effects. The gases used for the driver, driven, and acceleration sections were 4.23 MPa of He, 1.5 kPa of air, and 200 mTorr of He, respectively. Wall mounted PCB 113A26 probes were used to record shock speeds and static pressures for the driven and acceleration sections. It was found that the primary shock speed matches well with the 1-D computation and CFD simulation. However, the measured transmitted shock speed in the acceleration section was nearly 1 km/s slower than the inviscid computation. The viscous CFD simulation closely matched the experimental transmitted shock speed. The CFD solution predicts a

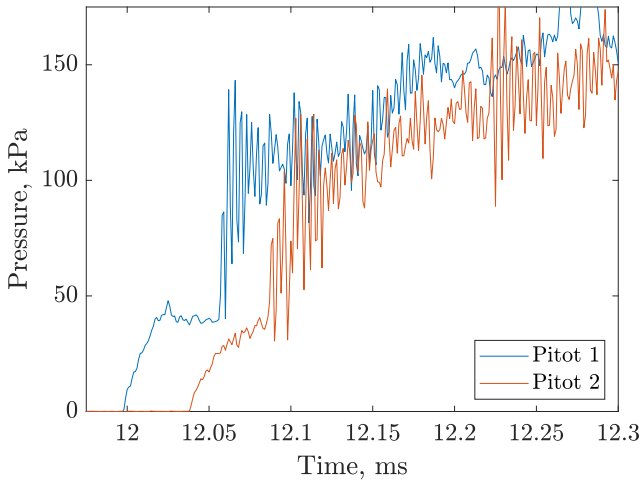

Figure 2.3: Example pitot traces of a staggered pitot rake for the M5-H6-A condition.

significant increase in test gas Mach number, while the freestream static pressure, temperature, density, and pitot pressure decrease in value when compared to the 1-D computation. It was found that experimental values of the expansion gas pitot pressure were significantly larger than the computed values. Air contamination in the acceleration section was investigated as a possible cause for the discrepancy. It was found that assuming 8% - 10% contamination of air by volume would best agree with experimental data. CFD computations assuming air contamination show that a decrease in freestream Mach number would occur, while static pressure, temperature, density, and pitot pressure of the test gas would increase. McGilvray et al. concluded that air contamination in the expansion section of the tube can significantly alter the test freestream.

In the present work, wall mounted pressure probes are unable to measure shock speed and static pressure in all sections of the facility. The capability was presumed to be lost when the facility moved to the California Institute of Technology with new mounting and infrastructure in 2015. Increased mechanical vibrations and recoil is observed, which generates high levels of noise in the pressure traces. Attempts to extract shock speed from the noise resulted in large uncertainties. As a result, staggered pitot probes are the only means to measure transmitted shock speed until a diagnostic is developed to measure shock arrival in situ.

Tests are performed at the four conditions using a staggered pitot rake. To avoid interference of other pitot probes, the most upstream pitot probe (denoted as pitot 1) is placed at the centerline of the tube and used to measure pitot pressure. The second

pitot probe is positioned 37 ± 1 mm radially away from the centerline of the tube. In an effort to carefully characterize the facility, all tests use identically mounted PCB112A22 probes that were previously verified to be calibrated for pressure. Transmitted shock speed can be inferred from the time of arrival of the transmitted shock and the measured distance between the probes. The streamwise position of the pitot probes are carefully measured using calipers before every test and are typically 147 ± 3 mm apart. Figure 2.3 shows an example trace of the M5-H6-A condition with the staggered pitot rake. At a time t = 12 ms, the first pitot encounters the arrival of the transmitted shock, where a steady pitot pressure of 39.6 ±1.2 kPa is measured. After t = 12.05 ms, the arrival of the contact surface is indicated by another rise in pressure. A time shift in the trace between the two probes is observed in this example.

Table 2.4 lists all measured transmitted shock speeds and pitot pressures of the acceleration gas for the four conditions. Excellent repeatability in measured transmitted shock speed is observed in the M5-H4-A and M5-H6-A conditions. For the two lowest enthalpy conditions, the measured shock speeds fall in between the perfect gas and equilibrium calculated shock speeds in Table 2.2. To aid in determining which process is best for comparisons, the frozen pitot pressure of the acceleration gas is computed using the perfect and equilibrium solutions of state 6 in the x-t diagram. It is observed that the equilibrium LETS solution better represents the measured pitot pressure of the post-shock acceleration gas. The calculated equilibrium shock speed agrees with the low enthalpy experiments and is within the uncertainty of the measurement.

Condition	Shot #	Exp. $U_{s,\text{accel}}$ km/s	Exp. $P_{0,\text{accel.}}$ kPa	Perf. $P_{0,\text{accel.}}$ kPa	Equ. $P_{0,\text{accel.}}$ kPa
M5-H4-A	1567	3.15 ± 0.14	71.6 ± 3.0	42.1	71.9
M5-H4-A	1570	3.15 ± 0.14	70.8 ± 3.1	42.1	71.9
M5-H6-A	1564	3.77 ± 0.19	39.6 ± 1.2	17.5	36.2
M5-H6-A	1568	3.76 ± 0.19	34.7 ± 1.3	17.5	36.2
M7-H8-A	1565	4.41 ± 0.26	-	4.2	9.5
M7-H8-A	1569	4.40 ± 0.26	-	4.2	9.5
M7-H8-A	1571	4.54 ± 0.27	-	4.2	9.5
M7-H8-He	1566	4.53 ± 0.27	3.8 ± 0.3	2.2	2.2
M7-H8-He	1575	4.42 ± 0.26	3.8 ± 0.4	2.2	2.2

Table 2.4: Measured transmitted shock speeds using a staggered pitot rake. The right two columns are the computed frozen pitot pressure using the expansion tube solution of a perfect gas or equilibrium process.

Experiments with M7-H8-A also show that the experimental shock speed is bounded by the perfect gas and equilibrium solutions for $U_{s,\text{accel}}$. The duration of the post-shock acceleration gas is approximately 19 µs with no steady plateau in pressure observed. The PCB112A22 transducer has a rise time of 2 µs, contributing to the slow response of the low pressure gas. As a result, pitot pressure of the acceleration gas cannot be reported for M7-H8-A. The M7-H8-He experiment is the only condition where measured shock speeds disagree with the unsteady calculations. Measured shock speeds of M7-H8-He are approximately 17% lower than inviscid calculations using 1-D gas dynamics, comparable to the decrease observed in McGilvray et al. [65]. The arrival of the post-shock helium provides a steady pitot pressure of 3.8 ± 0.4 kPa in M7-H8-He. When comparing with the calculated pitot pressure, it is found that the computation underpredicts the experiment. The underprediction of the acceleration gas pitot pressure was also observed in the work of McGilvray et al. [65], verifying the conclusions made in the previous study.

This slowdown in shock speed and increase in pitot pressure are likely to be caused by a combination of viscous effects and contamination of air in the acceleration section. The extent of contamination can vary from shot to shot, making the freestream conditions difficult to predict for experiments using helium acceleration gas. For experiments where the acceleration section fill pressure is greater than 100 mTorr, the expansion section is pumped down to 50 mTorr and the leak rate is recorded for 10 minute increments before the expansion gas is used. Depending on facility preparations, leak rates range between 4 mTorr/min to 7 mTorr/min. Filling the expansion section with a gas requires the facility to be first pumped down to 50 mTorr and then filled with expansion gas to 2 kPa (15 Torr). The procedure is done twice in order to flush the expansion section. When timing an experienced HET user with a stopwatch, a duration of 50 s to 90 s occurs between recording the fill pressure and the rupture of the primary diaphragm. It is possible to estimate the amount of leaking between isolation and diaphragm rupture with these parameters, but an additional source of uncertainty comes from the flushing procedure. During flushing, 200 s to 360 s is required to evacuate the expansion section from 2 kPa to 50 mTorr, depending on how well the facility is sealed. It is possible for additional air to leak in the test section during evacuation, making it extremely difficult to estimate the amount of leaking in the expansion section. Due to the amount of previous work done on this condition, the M7-H8-He condition will continue to be used for some schlieren experiments. For emission measurements of high enthalpy conditions, the alternative M7-H8-A will be used instead.

2.2 Model Geometries

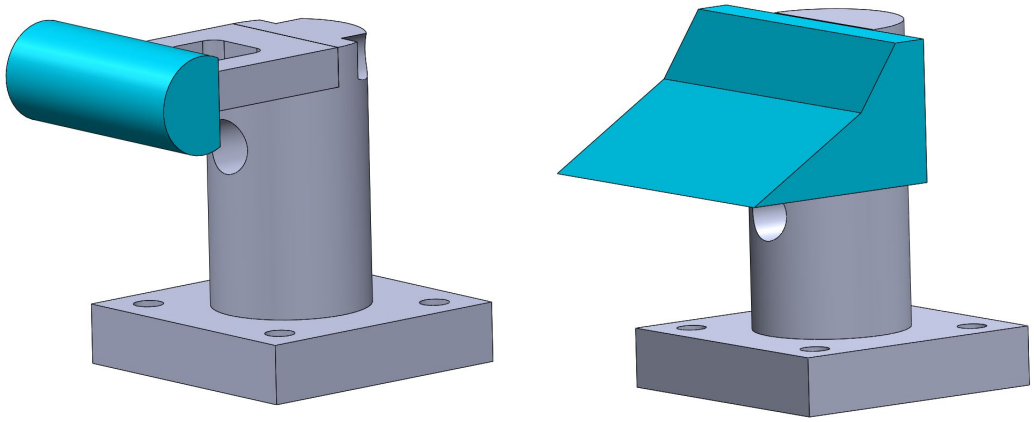

(a) Cylinder

(b) Double Wedge

Figure 2.4: Test articles used in present work. Cylinder diameter is 31.75 mm and a 30-55 degree double wedge is used. Mounting sting is shown in grey.

Two geometries are used for emission measurements. Figure 2.4 shows two assembly drawings of the test articles. A cylinder with diameter of 31.75 mm (1.25 inches) and a span of 76.20 mm (3 inches) is used for studying stagnation flow. The geometry is cut from A2 tool steel cylinder stock, where a vertical cut is made 22.86 mm from the cylinder surface. This allows for the cylinder to be mounted from behind using a steel spacer. The spacer is fastened to a 50.8 mm diameter sting using two 1/4"-20 screws. If desired, shims can be added in between the spacer and sting for streamwise movement relative to the optics. The height of the stagnation line is located at the centerline of the exit of the tube.

The double wedge geometry is taken from the work of Swantek [90] and Knisely [48]. The lead wedge is set at an inclination of 30° with a surface length of 50.80 mm (2 inches). A second wedge at 55° forms a hinge with the first wedge and has a surface length of 25.40 mm (1 inch). The test article is cut from A2 tool steel without surface instrumentation. A span of 101.60 mm (4 inches) is used for the model. The double wedge is mounted on a sting that features the capability of streamwise movement through the use of shims. All stings feature a pitot mount underneath the test articles with a feed-through for cables.

2.3 Schlieren Imaging

A z-type configuration consisting of two Edmund Optics aluminum coated spherical mirrors is used for imaging shock waves. The mirrors have a diameter of 108 mm (4.25 inches) and a focal length of 1143 mm (45 inches). The lens used for focusing

and magnification is a Nikon AF Nikkor 70-300 mm camera lens. Arrangement of the schlieren optics in the HET is identical to the one used by Knisely [48]. For single shot imaging, a pco.1660 charge-couple device camera is used with a Xenon nanopulser (10 ns duration) white light source. The cutoff is performed using a DSC Laboratories gradient filter. Triggering for single shot images is achieved using the pitot probe mounted underneath all test articles and using the rise in pressure of the contact surface as the trigger voltage. For recording schlieren videos, a Shimadzu Hyper Vision HPV-X2 is used to record images at 200,000 and 400,000 fps with an exposure of 200 ns. A Photogenic PowerLight 2500 DR flash lamp is used as the primary light source. As the discharge time is long, the lamp must be triggered 200 μs before the arrival of test gas. Triggering for schlieren videos is accomplished through wall mounted PCB113B26 at the driven section of the HET. A delay of 1.305 ms is set using a Berkeley Nucleonics Model 577 pulse generator, with an additional delay of 200 μs set between the camera and the lamp.

2.4 Emission Spectroscopy of Hypervelocity Flow

Ultraviolet emission is one of the most accessible physical processes that occur in high enthalpy flows. Emitted photons from atomic and molecular transitions can be collected through the use of optics and dispersed into wavelengths to measure the population distribution among energy levels. The intensity of signals also indicates the level of excitation present in a high temperature gas. Through the use of careful optical design, dispersion of light can be performed at multiple spatial locations, allowing for radiation to be resolved spectrally and spatially. In this section, a description of the spectroscopic technique is presented.

Operation of Spectrograph and Intensified Camera

The spectrometer is an optical device used for imaging dispersed light. Multiple types of spectrometers exist depending on the application. The spectrometer used in this study is a SPEX 270M spectrograph, classified as a Czerny-Turner configuration. The components of this spectrometer type include an imaging slit, collimating mirror, grating, and focusing element. The grating is the primary component in a spectrometer, which serves to disperse incoming light into wavelength components. The groove spacing of a grating determines the extent of dispersion of the incoming light. The spectrograph is equipped with a 1200 g/mm diffraction grating blazed at 200 nm and used for fine measurements of emission in the 210 nm - 250 nm wavelength range.

Operation of the SPEX 270M begins with focusing light on the plane of the slits, which can be achieved through the use of collection optics. The length of the slit is 15 mm and can be opened or closed through the use of a micrometer mounted at the top. Slit spacing determines the resolution of the spectra features and will be discussed further in Section 3.1. After the slits, a collimating mirror turns the incoming light and allows it to impinge on the grating surface. Dispersion occurs, where the angle of reflection is dependent on the wavelength of the light. The dispersed light is focused for imaging through the use of a spherical mirror, where a detector is set at the focal plane to image the spectrum. Because the slit and grating have a finite length, it is possible to image multiple point sources along the slit length and disperse them into wavelengths. The internal magnification of the spectrometer is 1.23, limiting the imaging length to be approximately 9 mm along the slit length. Fortunately, most of the radiating flows that will be studied have length scales less than 1 cm. No additional magnification is required from the collection optics external to the spectrometer. Changing the wavelength range is achieved through manually rotating the turret housing the grating. Wavelengths are typically selected depending on the species of interest.

To image the spatially resolved radiation, a Princeton Instruments PM4-1024i intensified CCD is used for recording the spectrum. The camera features a 1024×1024 pixel array with a variable gain from 1 to 100 set by the software LightField. For all tests, the intensifier was run with air cooling to a temperature of -27 °C. It is possible to liquid cool the detector to achieve lower temperatures for a reduction in signal-to-noise ratio, but this was found unnecessary for the emission measurements.

Considerations for Imaging UV Radiation

As the spectrometer optics and detector are self-contained, the optics used for focusing light into the spectrometer slits require rigorous design in order to correctly image a radiating gas with ultraviolet content. Four requirements must be satisfied for spectroscopy of hypersonic radiating flow: a small acceptance angle, a magnification of 1, minimal or no chromatic aberration, and minimal geometric aberration. The requirement of magnification is governed by the internal optics of the spectrometer and the length scales of the experiment. The remaining three criteria reduces the uncertainty of imaging a gas with finite span.

Reducing the acceptance angle of the optics minimizes the effective imaging volume of the gas of interest. As it is desired to collect radiation along a line, it is beneficial

to not image other parts of the radiating gas onto the spectrometer slits. To reduce the effective collection volume, long focal lengths are desired for collection optics. In cases where imaging is performed close to the surface of the test article, effects of UV surface scatter is worsened with a large collection volume. Surface scatter of UV was studied using a deuterium lamp shining over the surface of a 25.4 mm cylinder machined out of A2 tool steel. Two $f = 200$ mm fused silica lenses based on the work by Sharma [86] and a periscope were tested. Radiation from the deuterium lamp was shined over the surface of the steel model, where an image of the radiation was taken. A second image was taken without the model present. Subtracting the two images reveals a non-negligible contribution of ultraviolet radiation to the intensifier detector from the surface scatter. Figure 2.5 shows that a significant portion of the detector measures additional light due to scattering and short focal length lenses. Therefore, reducing the collection volume has the added benefit of reducing the effects of surface scatter.

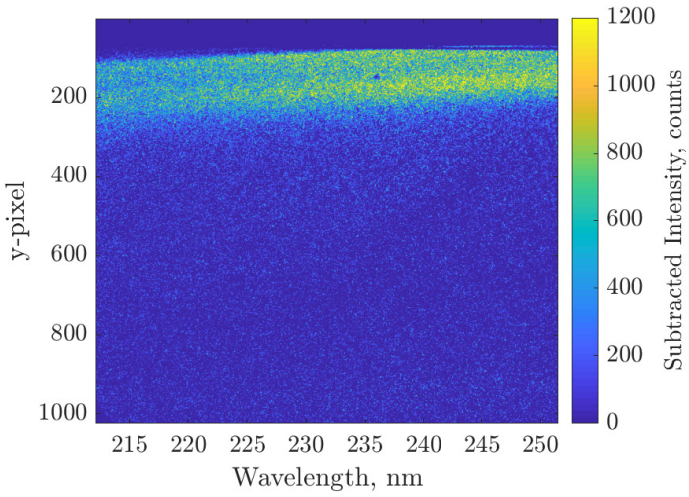

Figure 2.5: Measured surface scatter of ultraviolet light using 200 mm focal length lenses. Measurements of deuterium radiation are taken with and without a cylinder model present, where subtraction is performed to highlight contributions of scattered light. Imaging is performed along the cylinder centerline. Cylinder surface is located at a y-pixel coordinate of 100 on the detector.

Chromatic aberration is an optical artifact that arises from differences in index of refraction with varying wavelength. For materials such as fused silica, the index of refraction is higher for shorter wavelengths. Therefore, it is possible for dispersion to occur from light traveling through lenses and windows before entering the spectrometer slits. In the work of Sharma [86], two $f = 200$ mm fused silica lenses served as the primary collection optics for ultraviolet spectroscopy. To estimate the

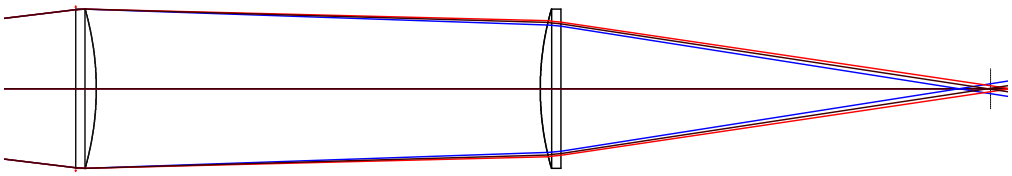

Figure 2.6: WinLens3D simulation of the Sharma [86] arrangement of fused silica lenses to demonstrate chromatic aberration. Blue and red rays are 210 nm and 250 nm light respectively. Diameter of the lenses is 50.8 mm and a point source is located 200 mm away from the first lens along the optical axis.

longitudinal chromatic aberration present from a lens system, the WinLens3D software is used to perform ray tracing studies. Figure 2.6 is a simulation of Sharma's collection optics for NO γ emission measurements. It is important to note that focal lengths listed for the Throlabs lenses correspond to a wavelength of 587 nm. As the index of refraction is higher for the ultraviolet wavelengths, the true focal length is computed to be $f = 177$ mm for 230 nm light, substantially shorter than the listed value of $f = 200$ mm. Chromatic aberration is present at the location of the slits, where a difference of $\Delta d = 17.5$ mm is computed between the focus of 210 nm light and 250 nm light. An additional WinLens3D simulation was performed with $f = 750$ mm fused silica lenses to satisfy the requirement of long focal length collection optics. Due to the longer path length of the rays, the difference in foci was computed to be $\Delta d = 77.6$ mm, approximately the same length as the span of the cylinder model. From this analysis, it was concluded that fused silica lenses with long focal lengths could not be used for emission spectroscopy measurements for ultraviolet wavelengths.

One method of circumventing the issue of chromatic aberrations is to implement achromatic triplets as the focusing element. The basic principle involves using three different media for the light to travel through to bring all wavelengths to the same focus. Designs either consist of a CaF_2/fused-silica/CaF_2 combination or a fused-silica/air/CaF_2 combination. This has the advantage of easy alignment and mounting to other components such as cameras. However, long focal length achromatic triplets are typically not commercially available and require custom manufacturing. In addition, radiation is collected along the span of the gas, and therefore not all rays emanate from the centerline of the test article. Therefore, corrections must be done for sources outside the focus of the system. As a result, lenses were not selected for imaging UV radiation to the spectrometer.

Mirrors are selected as the primary imaging optic for its lack of chromatic aberration and commercial availability at long focal lengths. Another advantage of mirrors is that they allow for the system to be folded on an optical table, while long focal length lenses must be oriented along the imaging axis. Other groups have used mirror setups for emission spectroscopy, such as Grinstead et al. [31], Cruden [16], and Jacobs [42]. However, the disadvantage of using off-axis mirrors is the formation of geometric aberrations in the final image. Not all geometric aberrations can be removed completely, but they can be minimized through careful optical design. Mirror systems exhibit two off-axis aberrations: coma and astigmatism. Coma occurs when the direction of light reflected from a surface depends on the location of the point of reflection. Typically, this appears as an oval shape at the focal point. From Settles [85], coma grows proportionally to the offset angle θ and the inverse square of mirror f-number. For a non-symmetric system, coma can be reduced by keeping θ small and using long focal length mirrors. In a z-type configuration, two mirrors have the same focal length and offset angle. If a z-type configuration is perfectly aligned, the effects of coma can be removed completely. Astigmatism arises from differences along the path length along the optical centerline. It cannot be removed like coma, but it is reduced with small θ and large f-number mirrors. Fortunately, the design criterion requires a long focal length mirrors, which has the added benefit of reducing astigmatism. For light imaged along the span of a radiating gas, astigmatism becomes more pronounced for point sources at the extreme ends of the slab. Therefore, it is beneficial to also consider the span length of the test article when designing a z-type configuration. The double wedge model contains the largest span of 101.6 mm, which will determine the location for producing spot diagrams.

Depending on the choice of mirror, spherical aberrations can also distort the final image. When incoming parallel light reflects off different locations of a large diameter spherical mirror, the rays no longer coalesce into a defined focus as the angle of reflection are not corrected. Parabolic mirrors correct this artifact through changes in surface curvature along the radius of the mirror. The disadvantage of parabolic mirrors are the difficulty in manufacturing and high cost of the optics. Spherical aberration can be reduced by using small diameter mirrors and long focal lengths. As the design requires a long focal length, this will benefit the reduction of spherical aberration.

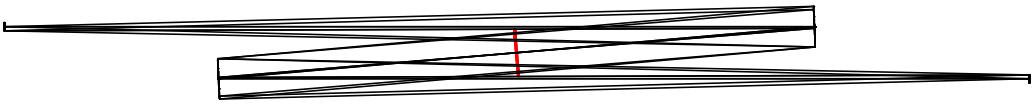

Figure 2.7: WinLens3D simulation of two 50.8 mm spherical mirrors in a z-type configuration. A system stop is marked in red and object/image length is 10 mm. Rays emanating from two point sources are shown in this calculation.

Selected Configuration of Collection Optics

With the knowledge of the possible geometric aberrations that can exist in mirror imaging, it is now possible to design the optimal configuration for a spectroscopy experiment. The selected optics include two Edmund Optics 50.8 mm UV Enhanced Aluminum Spherical mirrors in a z-type configuration with a focal length of 1016 mm. This mirror is selected for its long focal length and favorable size for a compact z-type configuration within the allowable space on the optical table. The long focal length is favorable for reducing the effective collection volume, minimizing geometric aberrations, and removing chromatic aberrations. WinLens3D was used to simulate the rays for a system of mirrors. Figure 2.7 shows an example simulation of the rays from an image 10 mm long for mirrors in a z-type configuration. The dimensions of the mirrors were taken from Edmund Optics and specified in WinLens3D, where a radius of curvature of 2032 mm is used. A mirror tilt of 2.5 degrees is specified (angle between incoming and reflected ray is 5 degrees) with a separation of 750 mm between the two spherical mirrors. This angle is selected to allow for two Thorlabs KM200CP kinematic mirror mounts to fit in the z-type configuration without clipping rays.

To study the extent of geometric aberrations of a point source along the span and off-axis of the imaging system, spot diagrams are generated to visualize distortion of images. A spot diagram displays the distribution of rays on the imaging plane from a point source imaged by the optics. It is useful in identifying aberrations such as astigmatism, which is identified by asymmetry in the distribution of rays. Figure 2.8 is a WinLens3D spot diagram calculation of the configuration shown in Fig. 2.7. Each column represents movement of the imaging plane along the optical axis. Since the z-type configuration is symmetric, this can also be interpreted as the image of a point source with varying spanwise location. Each row represents a different off-axis location of the imaged point source. In this example, the full field is 5 mm long, equivalent to an image length of 10 mm. The middle column of Fig.

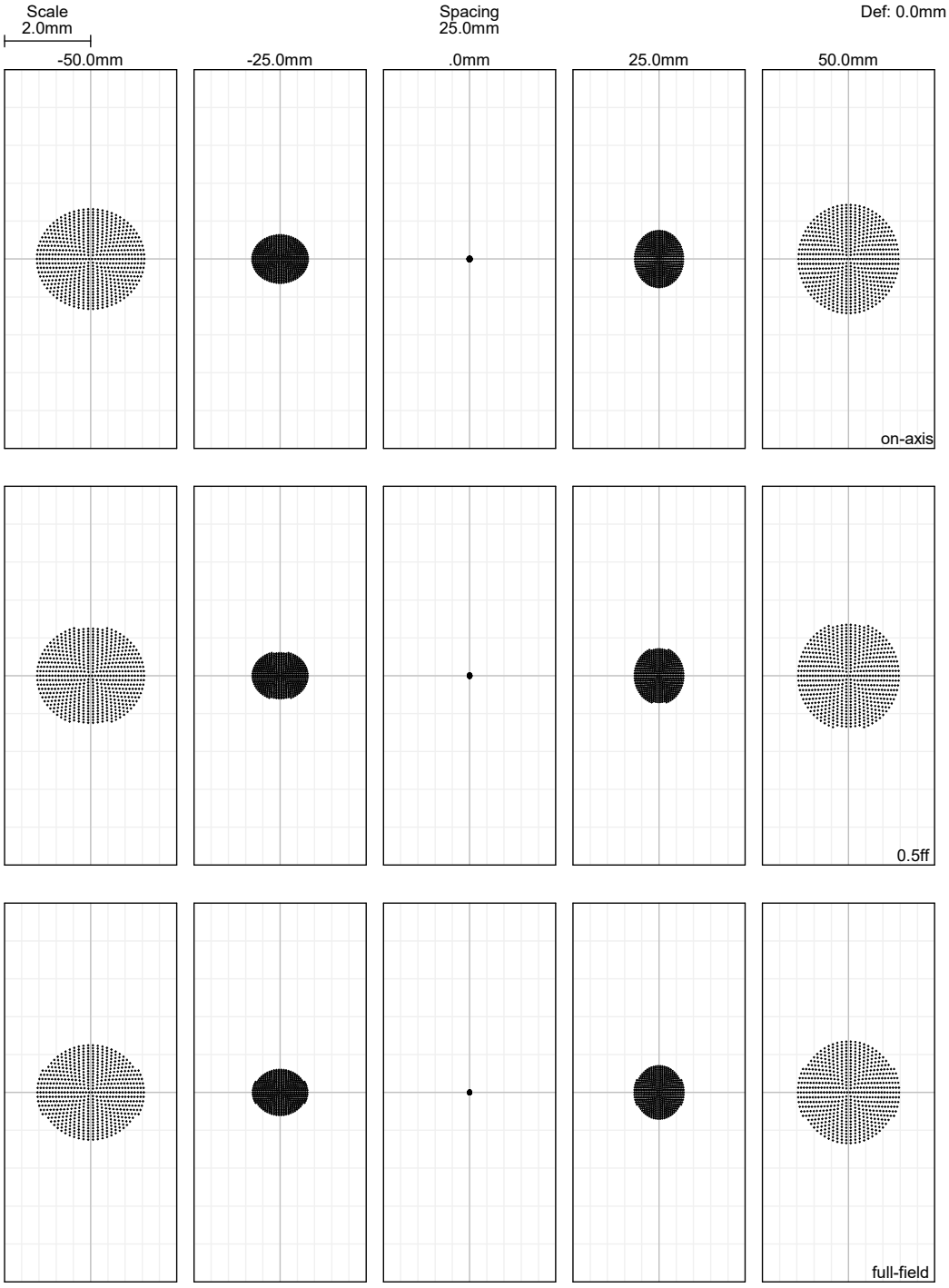

Figure 2.8: WinLens3D spot diagrams of final optical design. Columns are spanwise variations of image, while rows are off axis variations of image. Full field size is 5 mm. Scale shown is only valid for horizontal axis.

2.8 is the focus of the system, where all rays coalesce to a single point. As the point source moves away from the axis of the system, the rays remain in focus with no observable change in shape. As a point source is moved along the spanwise direction (representing the columns), the effects of astigmatism is identified by the elliptical distribution of rays. Depending on which side of the span the point source originates, either the sagittal or meridional plane will be closer to focus than the other plane. Therefore, radiation collected from different spanwise locations can be imaged with or without ray stretching along the slit length. Consider the extreme case of a point source located 966 mm away from the first spherical mirror (representing the span edge of the double wedge geometry) and 5 mm away from the optical axis. Using WinLens3D, a maximum radius of 1.27 mm is calculated along the sagittal plane while 1.12 mm is calculated along the meridional plane. Not only is there some astigmatism left in the image, radiation from the extreme ends of a double wedge will transform into a spot approximately 1 mm in radius along the slit length. As a result, radiation measurements of a shock wave with finite span will result in signal upstream of the true shock location. Radiation can only be used as an approximate measurement of the location of the shock and schlieren must be used to precisely measure the flow features. Despite the presence of astigmatism in this configuration, it was concluded that the aberrations were minor in comparison to the added benefit of removing chromatic aberration and the compactness of the system. Therefore, the optical arrangement was determined to satisfy the imaging requirements.

As the slits of the spectrometer are oriented vertically, a horizontal image must be transformed to focus along the slit length. A Thorlabs RS99 periscope assembly with two 25 mm Edmund optics Deep UV mirrors serves as an image rotator. To rotate the image 90 deg, the flat mirrors are tilted at a 45 degree with respect to the horizontal plane of the table surface. Mirrors are arranged such that the top mirror reflects incoming rays downward and the second mirror is rotated 45 degrees in the counter clockwise direction about the post, where the rays are now traveling perpendicular to the incoming light. It is possible to position a periscope after or before the z-type configuration. However, positioning a periscope before the z-type configuration requires larger flat mirrors to turn all of the diverging rays. For this study, the periscope was located after the z-type mirrors, where the WinLens3D software was used to verify that the position of the first turning mirror will not clip any of the focusing rays.

A sketch of the final configuration of optics is shown in Fig. 2.9 with the cylinder

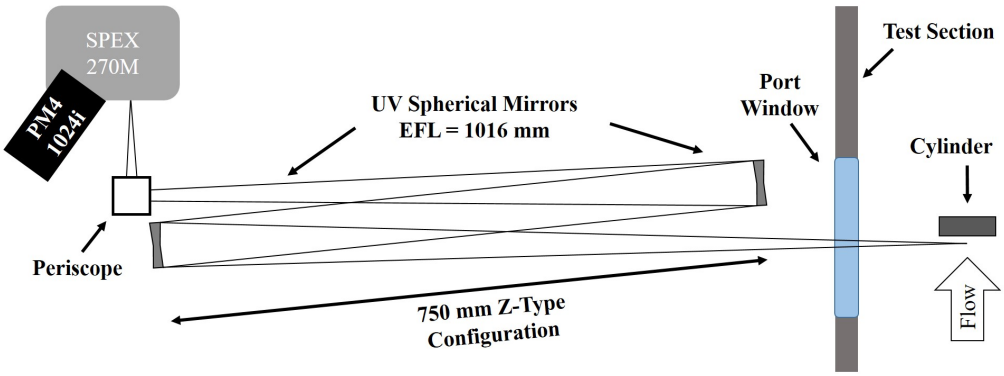

Figure 2.9: Two-dimensional schematic of collection optics for spectroscopy.

as the test article. The material used for the test section window is Corning 7980 UV grade glass with a diameter of 125 mm and a thickness of 20 mm. For precision alignment, each mirror post was mounted atop two Newport 423 linear stages with SM-25 micrometers. A Melles Griot 05-LHR-151-91 helium neon laser was used for alignment of all optics, including the calibration lamps mounted on the opposite table. For fine alignment of the spectrometer slits to the centerline of a test article, a Hamamatsu L10290 light source with a halogen lamp is used. To limit imaging possible scatter of light from reflective surfaces inside the test section, the entire assembly is enclosed in a casing and baffles are mounted along the path length of rays. Figure 2.10 contain labeled images of the final configuration of the experiment.

2.5 Calibration of Spectroscopic Measurements

A detector image contains valuable spatial and spectral information used for understanding the production and population of an electronically excited molecule. As a result, attention must be placed in converting the image axes into wavelength and space coordinates. Every test campaign was calibrated for wavelength, space, relative intensity, and instrument line shape. When using ultraviolet sources for calibration, each lamp is mounted on rails outside the test section on the opposing side of the spectrometer. Radiation enters the test section unobstructed and is captured by the collection optics on the spectrograph side.

Wavelength

A Hamamatsu L233-26NU iron lamp is used for wavelength calibration in the ultraviolet region. Light from the lamp window is typically dim and difficult to align due to its large size. An Ocean Optics QP600-2-SR fiber optic cable with a

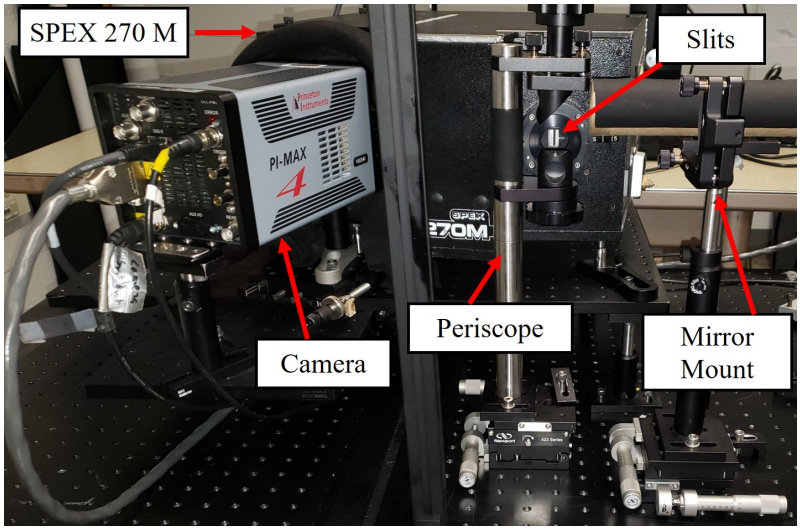

(a) View of Spectrometer

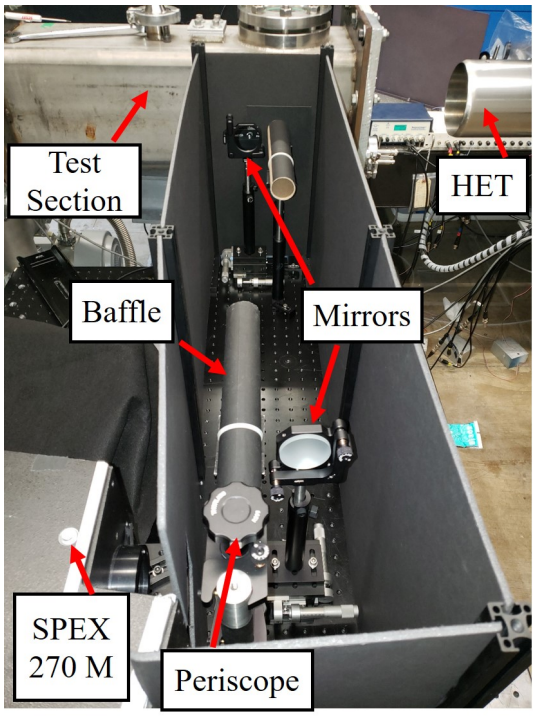

(b) View of Collection Optics

Figure 2.10: Images of the final experimental configuration for ultraviolet emission spectroscopy.

600 µm core and two Ocean Optics 74-UV fiber optic collimating lenses are used to both collect light from the iron lamp and to deliver it to a post mounted collimating lens. The delivered light from the fiber optic is focused using a f = 100 mm fused silica lens at the location of the model centerline. This delivers as much light as possible into the the spectrometer slits. Despite the large amount of focusing, the

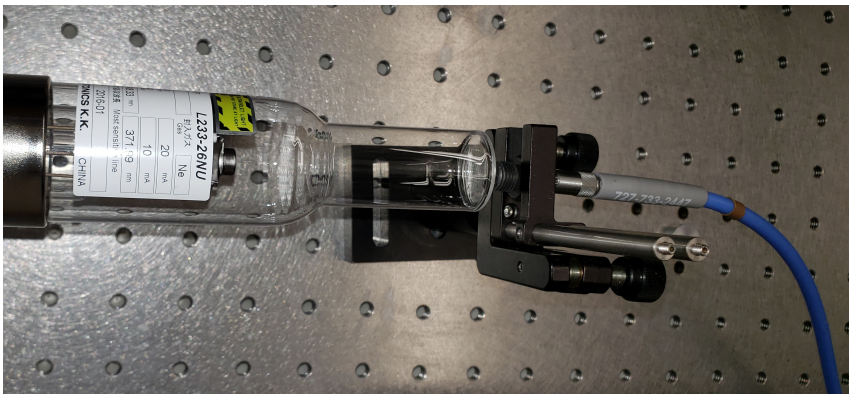

Figure 2.11: Iron hollow cathode lamp (left) configured to shine UV radiation into a fiber optic cable.

camera must be run with an exposure of 650 ms and a gain of 91, the longest exposure time used for the camera. The grating turret is adjusted until the user can identify the Fe I 248.33 nm peak. Typically, camera settings must be selected to clearly observe lines below 230 nm. To post-process the iron lamp image, subtraction is

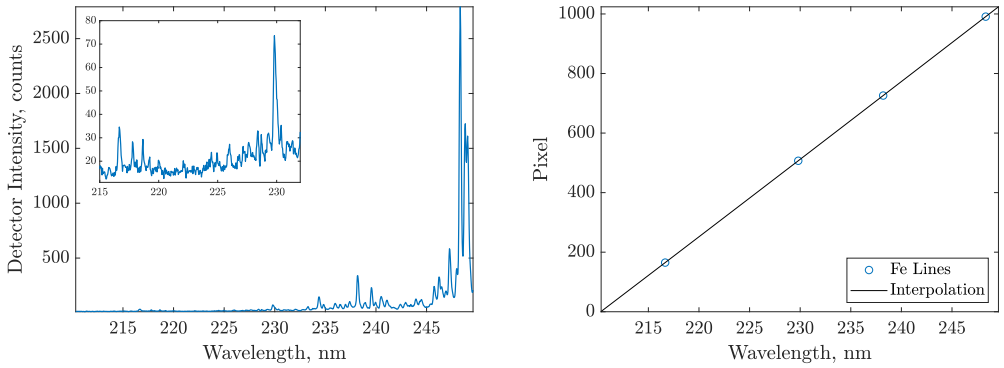

(a) Iron lamp radiation

(b) Pixel to wavelength conversion

Figure 2.12: Example wavelength calibration for a spectroscopy experiment.

done using a background image taken at the same camera settings without the lamp on. After subtraction, the detector is binned 500 pixels along the position axis to obtain enough signal for the shorter wavelength lines. A plot of counts versus pixels is generated, where lines can be identified. Typically, four lines are enough to correct for wavelength. The lines used for wavelength calibrations include Fe I 252.28 nm (used for Hg-Ar lamp measurements), Fe I 248.33 nm, Fe II 238.20 nm, Fe I 229.81 nm, and Fe II 216.67 nm. Interpolation is performed using a piecewise cubic Hermite spline to obtain a smooth and continuous function for wavelength conversion. The uncertainty in wavelength calibration is ±0.08 nm.

Position

(a) Cylinder (b) Double wedge

Figure 2.13: SolidWorks drawings of alignment plates used for position calibration.

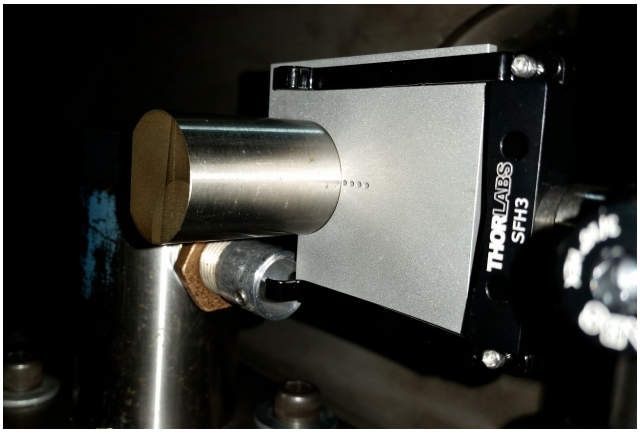

Figure 2.14: Alignment of spatial calibration plate over the surface of a cylinder model inside the HET test section.

To calibrate for streamwise position, aluminum plates 2.54 mm thick are machined to fit over the surface of a test article. Holes are drilled to 1.2 mm in diameter and spaced at 2 mm increments to serve as targets. The alignment plate is positioned at the centerline of the test article and held in place with a mount inside the test section. A Hamamatsu L10290 deuterium light source, combined with a fiber optic cable and a f = 200 mm fused silica lens, is used to shine collimated UV radiation through the alignment holes. The result is illuminated regions on the detector that correspond to the hole locations. Detector signals are typically 3000 counts or greater to obtain the sharpest image of the radiation. The four corners of the rectangle are identified by the user, which identifies the center of the hole location with accuracy. Following the discussion of spherical aberrations, no change in rectangle width is observed for holes off-axis to the first mirror, suggesting that the effects of off-axis aberration are negligible. Linear interpolation is performed between the target locations to

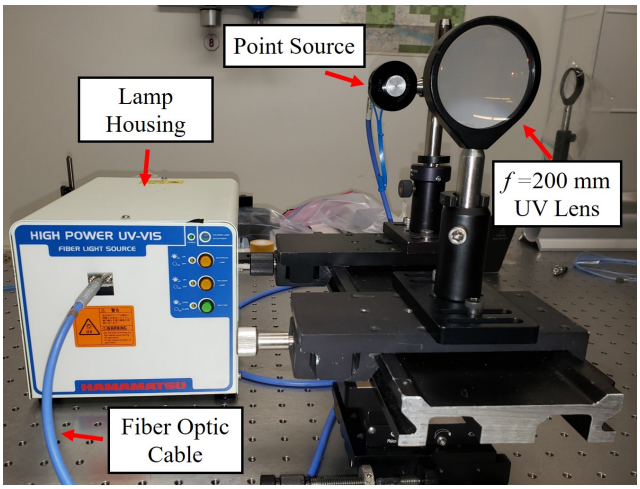

Figure 2.15: Configuration of optics for collimating deuterium radiation. The optical rail is capable of streamwise and vertical movement.

correct the position axis of the detector. The conversion to length is typically 103 pixels/mm and the error in streamwise position is ± 0.06 mm using the calibration images. Uncertainty in vertical position from the stagnation streamline is ± 0.6 mm.

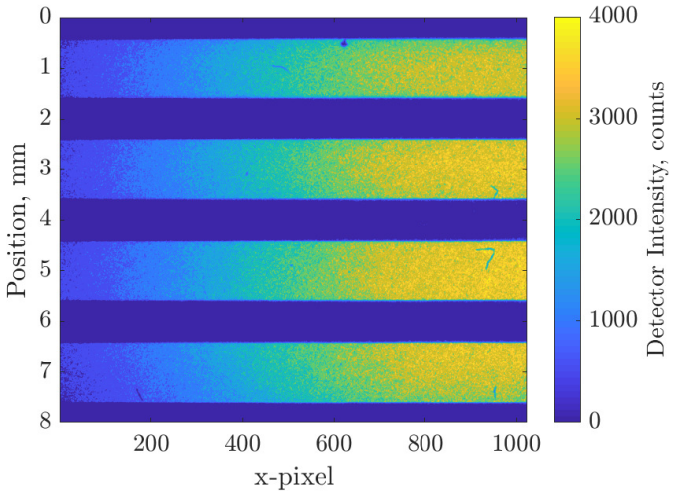

Figure 2.16: Collimated deuterium radiation through alignment holes of a cylinder alignment plate. Position axis is measured relative to the surface of the test article.

Relative Intensity

When ultraviolet light travels through materials and reflects off mirrors, the efficiency of transmission and reflection is a function of wavelength. Detector efficiencies typically drop for shorter wavelengths. Wavelengths below 200 nm are

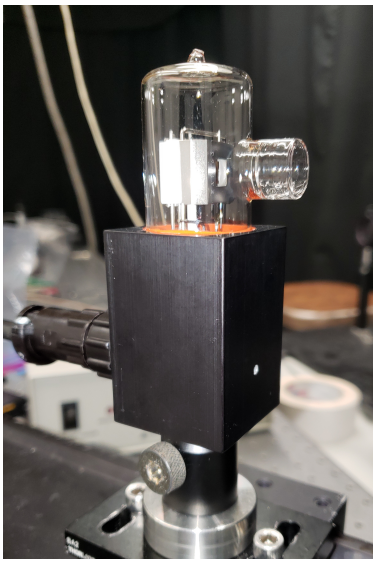

Figure 2.17: Deuterium lamp used for relative intensity calibration.

categorized as vacuum ultraviolet, where absorption in air along the path length is also possible. To correct for these losses, a Gooch & Housego OL UV-40 Spectral Irradiance Standard deuterium lamp is used for broadband emission in the ultraviolet. An explanation of the NIST traceable calibration is provided by Yoon, Proctor, and Gibson [97]. The NIST procedure involves a moving spectrometer platform that contains an integrating sphere, collection optics, and a spectrometer with a photo multiplier tube. The integrating sphere, which serves to remove spatial variations of the incoming light, is positioned 30 cm away from the sources used at the NIST facility. The calibration of the lamp was performed at the Gooch and Housego facility before shipping. In order to calibrate for relative intensity, the UV-40 deuterium lamp must also be positioned 30 cm away from the object that is to be irradiated. Since the image of the slits is projected at the centerline of the test article, the window of the deuterium lamp is positioned 30 cm from the centerline with the window plane parallel to the slit orientation.

The deuterium lamp is operated by turning on the light source and allowing it to stabilize for 20-30 minutes before each calibration. The deuterium radiation is recorded after performing the wavelength and position calibrations. The lamp radiation is spatially non-uniform, with peak intensities corresponding to the width of the plasma discharge. As a result, the lamp is translated at 1 mm increments to correct every portion of the detector surface. The camera settings are configured to a gain of 3 and an exposure of 300 ms in order to obtain enough counts for reducing the signal to noise ratio. A background image is also captured to remove

charge accumulation and hot pixels. The calibration is only valid for relative intensity along the wavelength range. Configuring the camera at the experimental settings will result in no signal on the detector, because the lamp has extremely low radiance compared to experiment. If a calibration source has radiance bright enough to match the experiment, then the camera can be simply configured at the experimental settings and the correction curve will directly correspond to absolute radiance from the factory calibration. Cruden [16] uses an alternative method, where two light sources calibrated at different wavelength ranges are used to anchor the measurement of the deuterium lamp at a longer wavelength and extrapolated to the wavelengths of interest. Temperature fits do not require absolute intensities and spatial variation of radiation downstream of a shock wave are still valuable in understanding the thermochemical non-equilibrium. For the purposes of this work, relative intensity is sufficient for all measurements. To process the intensity im-

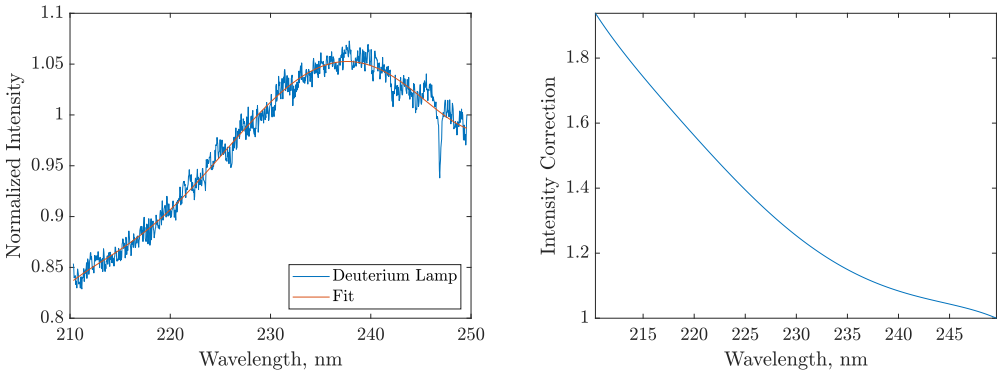

(a) Normalized deuterium radiation (b) Relative intensity correction curve

Figure 2.18: Relative intensity calibration using a deuterium lamp.

ages, background subtraction is performed for each spatial increment of the lamp. Binning is performed around the region of peak intensity of the detector images, which corresponds to 100 pixels in the streamwise axis. Each rectangular region provides one curve of counts versus wavelength. To have a smooth representative correction curve for all wavelengths, fifth order polynomial fits are performed on the binned radiation of the deuterium lamp and the factory calibration data. All fits are normalized to the longest wavelength. The relative intensity correction is given by the ratio of the normalized expected intensity to the normalized measured intensity. Figure 2.18b is an example calibration correction curve. It is found that the relative intensity correction does not vary with lamp position, meaning the detector response is uniform in the spatial axis for a translating light source. Nevertheless,

multiple correction curves are generated for each lamp location. Since the binned regions overlap for every lamp position, the boundary of each curve is defined by the median of the two overlapping regions. It is often the case where a portion of the peak intensity is cutoff by the surface of the test article. In these situations, the last position of the lamp where cutoff is avoided will be used for calibration of the remainder of the near surface region.

Uncertainties in the irradiance data are reported from the factory. A combined uncertainty of 2.24% is reported for spectral radiance at 250 nm. In order to quantify the uncertainties in detector signal for experiments, an expression for the uncertainty of the relative calibration is required. Define C to be the intensity correction shown in Fig. 2.18b and S to be the measured signal of the lamp in units of counts. Since normalization is performed at the longest wavelength, propagation of errors must be performed taking into account the normalization. The uncertainty in relative intensity calibration is given as

$$\sigma_C^2 = 2C^2\left(\frac{P}{100}\right)^2 + \left[\frac{1}{S^2} + \frac{1}{S_{\max\lambda}^2}\right]C^2\sigma_S^2, \tag{2.1}$$

where P is the percent error from the factory data. The uncertainty in the signal of the calibration lamp is approximated with the variance between the measured signal and the polynomial fit

$$\sigma_S^2 = \frac{1}{N-1}\sum_{i=1}^{N}\left(S_i - S_{\text{fit}}\right)^2, \tag{2.2}$$

where N is typically the length of the 1024×1024 detector array. Equation 2.1 shows that for every wavelength, the uncertainty of the intensity correction increases for increasing lamp uncertainty from the factory calibration and low signals during the calibration procedure.

Instrument Line Shape

For a measurement of the instrument line shape, a Hg-Ar UVP Pen-Ray lamp is used. The lamp is positioned 26 cm away from the image of the slits and the radiating element is oriented horizontally along the slit length. Intensities of the lamp are bright enough to create ozone in the lab, so ventilation and proper safety equipment are required. The lamp is only operated 60-120 s at a time to minimize health risks. The grating turret is adjusted to observe the dominant Hg I 253.65 nm transition.

Figure 2.19: Mercury-argon lamp mounted for instrument line shape measurement.

The Hg-Ar Pen-Ray is the only lamp bright enough to be imaged at camera settings relevant for the experiment, allowing it to be useful for selecting intensifier gain between tests. Typical camera settings are a gain of 14 and an exposure time of 90 µs. Note that a separate wavelength calibration is required, as the transition is only visible at a longer wavelength. Similar to the other lamps, a background image is also taken and subtracted from the lamp image. Calibration using the Hg-Ar Pen-Ray is only done once for every experimental campaign, as the instrument line shape is assumed to be constant for every configuration of the collection optics. Whenever realignment of the optics is performed or the slit width is changed, a new Hg-Ar measurement is performed. Further details on the post-processing of the Hg-Ar lamp will be found in Section 3.1.

Chapter 3

RADIATIVE PROCESSES OF NITRIC OXIDE ELECTRONIC TRANSITIONS

In the shock layer of a hypervelocity flow, the most common molecular radiators in the ultraviolet regime include N_2^+, OH (A-X), CO 4+, CN violet, and the O_2 Schumann-Runge bands [18, 29, 78, 87]. In the 210-250 nm range of wavelengths, NO γ ($A^2\Sigma^+ - X^2\Pi$) is one of the dominant radiators in hypervelocity flow. It is also naturally produced in dissociating flow, allowing for the species to serve as a marker of chemical and thermal non-equilibrium. In this chapter, the radiative processes of NO electronic transitions will be discussed and modeled. The content developed in this section will be used in interpreting spectroscopic measurements of post-shock flow and extracting quantitative properties of the gas.

3.1 Computing the NO A-X Spectrum

As the NO γ system is one of the most important transitions observed in hypervelocity flow, it is critical to have the capability of computing synthetic spectra with a high level of fidelity. Two useful references in studying molecular electronic emission are "Molecular Spectra and Molecular Structure" by Herzberg [35] and "Spectroscopy and Optical Diagnostics for Gases" by Hanson, Spearrin, and Goldenstein [33].

Review of Molecular Structure

For diatomic molecules, the potential energy for a given electronic state can be described by the Lennard-Jones potential. Figure 3.1 shows the energy levels of two electronic states, where r is the inter-molecular separation of the two nuclei. Within each potential curve, vibrational and rotational levels describe the internal energy of a molecule. The spectroscopic notation of vibrational quantum number is v, while rotational quantum number is denoted as J. The numbering of vibrational and rotational quantum numbers begins with zero and increases in integer values. The order of electronic states in spectroscopy is given by letters, where the ground state is denoted as X while each successive electronic state is assigned the letter A, B, C. An electronic state is represented by a separate potential energy curve, with differing dissociation energy and potential minimum. When describing transitions between two states, the convention is to use a single prime for the upper state (v', J')

and double prime for the lower state (v'', J''). The photon emitted for a particular transition is given by the energy difference between the two levels:

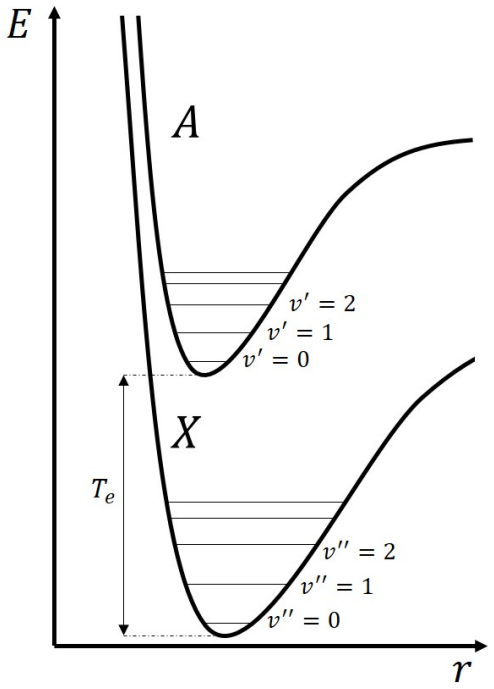

Figure 3.1: Intermolecular potential of the ground X and first electronic state A.

$$\Delta E = E' - E'' = h\nu = \frac{hc}{\lambda}, \tag{3.1}$$

where E is the energy, ν is the frequency, and h is the Planck constant. Energy is in units of J and the frequency is in units of s^{-1}. When used with the speed of light c, the wavelength λ also describes energy of a photon. For ultraviolet emission, the most common units are nanometers (nm) or Angstroms (Å). When computing the energy of a specific level for a molecule, the wavenumber $\bar{\nu}$ is commonly used in spectroscopy. Wavenumber is given as $\bar{\nu} = \frac{1}{\lambda}$ and contains units of inverse centimeters (cm^{-1}). As a result, wavelength, frequency, and wavenumber can sometimes be used interchangeably. Transitions between vibration and rotational levels fall in the regime of infrared spectroscopy, while rovibronic transitions are typically in the visible and ultraviolet regime.

The simplest model of describing the rovibrational states of a molecule is the rigid rotator and harmonic oscillator model (RRHO). Although it is useful for hand computations, the RRHO model requires corrections to obtain realistic results, since molecules stretch with increasing rotation and higher modes of vibration. To model

non-rigid rotations, the addition of centrifugal distortion is required in the expression for rotational energy:

$$F(J, v) = B_v J(J+1) - D_v J^2 (J+1)^2, \tag{3.2}$$

where B_v is the coefficient for rotational distortion and D_v is the centrifugal distortion term. The inclusion of vibrational coupling to the rotation is made through the two coefficients:

$$B_v = \beta_e - \alpha_e\left(v + \frac{1}{2}\right) + \gamma_e\left(v + \frac{1}{2}\right)^2 + \delta_e\left(v + \frac{1}{2}\right)^3 + \ldots \tag{3.3}$$

$$D_v = D_e + \beta_e\left(v + \frac{1}{2}\right) + \ldots \tag{3.4}$$

The above model for non-rigid rotation describes the non-uniform spacing of rotational states in a realistic problem. Rotational energy levels become closer in spacing with increasing J and v, a phenomenon modeled by the above expressions. Spectroscopic constants are typically tabulated and can be looked up for various molecules from a variety of sources.

The anharmonic oscillator model for vibrational energy is given by the following:

$$G(v) = \omega_e\left(v + \frac{1}{2}\right) - \omega_e x_e\left(v + \frac{1}{2}\right)^2 + \omega_e y_e\left(v + \frac{1}{2}\right)^3 + \ldots \tag{3.5}$$

For small v, the anharmonic oscillator behaves identically to the simple harmonic oscillator, given by $G(v) = \omega_e\left(v + \frac{1}{2}\right)$. However, as v becomes large, the spacing between vibrational levels becomes closer up to the dissociation limit. As a result, the higher order terms describe the close spacing for large vibrational quantum numbers. Similar to the rotational coefficients, coefficients for the higher order terms are tabulated from various sources. Coefficients for rotation and vibration used in this work are obtained from Amoit [6] for the X state and from Danielak et al. [19] for the A state. Accurate computation of Equ. 3.1 for the NO γ emission requires a good model for rotational and vibrational energies for the X and A states of the molecule.

Population Fraction

When calculating the contribution of a specific transition, one must consider the number of molecules in the initial level. In thermal equilibrium, the fraction of

all N_a molecules which are in a specific energy level N_i can be described by the Boltzmann fraction:

$$\frac{N_i}{N_a} = \frac{g_i e^{\frac{-hcE_i}{kT}}}{Q}, \tag{3.6}$$

where g_i is the degeneracy of the energy level and k is the Boltzmann constant. The energy of a specific level is the sum of the electronic, vibrational, and rotational energies. For the upper electronic level, the energy is given by

$$E_i = T_e + G(v) + F(J, v). \tag{3.7}$$

The electronic term T_e is the energy of the A state with respect to the ground state and is defined by the difference between the potential well minimums. For the ground state, the energy is the sum of the rotational and vibrational energies alone. The partition function Q is given as:

$$Q = \sum_i g_i e^{\frac{-hcE_i}{kT}} = Q_{\text{elec.}} Q_{\text{vib.}} Q_{\text{rot.}}. \tag{3.8}$$

Computers can compute the sums very easily. However, it is often convenient to write the fraction into separable expressions:

$$\frac{N(v, J)}{N_a} = \frac{e^{\frac{-hcT_e}{kT}}}{Q_{elec.}} \cdot \frac{e^{\frac{-hcG(v)}{kT}}}{Q_{vib.}} \cdot \frac{(2J+1)e^{\frac{-hcF(J,v)}{kT}}}{Q_{rot.}} = f_{elec.} f_{vib.} f_{rot.}, \tag{3.9}$$

where the rotational degeneracy $(2J + 1)$ is used. For absorption computations, the population of the ground state (or absorbing state) must be considered (v'', J''). Likewise, emission requires the upper state (v', J') population, because the intensity of a specific transition is dependent on the number of molecules in the initial state N_i'. Boltzmann fractions for all the possible energy levels are computed for synthetic spectrum calculations of NO γ in this work.

Multi-Temperature Model of Population Fraction

As high enthalpy hypersonic flows are inherently in thermal non-equilibrium, the assumption of thermal equilibrium for computing the Boltzmann fraction appears to be out of place. In addition, the assumption of a Boltzmann distribution may not hold for strong shock waves. Molecules like NO are well-known to exhibit non-Boltzmann behavior behind strong shocks and steep temperature gradients [8, 13, 14]. Non-Boltzmann statistics requires a detailed model of the potential energy surface for interactions with the NO(A) molecule and still remains an active area of research [45]. Although the concept of temperature is limited in describing

the Boltzmann distribution of molecular states, it is nevertheless a useful tool for interpreting the state of the gas.

A common model for thermal non-equilibrium uses the assumption that the energy distribution of the molecules can be described by separate temperatures: electronic excitation temperature, T_{ex}, vibrational temperature, T_v, and rotational temperature, T_r. A translational temperature T_{tr} finally describes the kinetic motion of molecules and influence other aspects of radiation, such as Doppler broadening. Each Boltzmann fraction is described by a separate temperature and the expression for the population fraction can be modified as:

$$\frac{N(v,J)}{N_a} = \frac{e^{\frac{-hcT_e}{kT_{ex}}}}{Q_e(T_{ex})} \cdot \frac{e^{\frac{-hcG(v)}{kT_v}}}{Q_v(T_v)} \cdot \frac{(2J+1)e^{\frac{-hcF(J,v)}{kT_r}}}{Q_r(T_r)}, \tag{3.10}$$

where the partition functions are calculated using the corresponding temperature. In thermal equilibrium, all temperatures share the same value, returning to the expression in Equ.3.9. For certain transitions, the spectrum shape is heavily determined by the extent of non-equilibrium between T_r and T_v. Depending on the wavelength range of interest, it is theoretically possible to extract two temperatures from an experimental spectrum. The electronic excitation temperature T_{ex} describes the population distribution between the X and A states and is used to compute absolute radiance. If other electronic states are considered in radiation calculations, such as NO β ($B^2\Pi - X^2\Pi$) and NO δ ($C^2\Pi - X^2\Pi$) transitions, the electronic temperature also describes the distribution of energies amongst the various electronic states.

Special Considerations for Electronic Configuration

Up to this point, the expressions used for computing energies and Boltzmann fractions can be readily applied to any diatomic molecule when tabulations exist. However, the electronic configuration of a species must be taken into account for detailed calculation of spectral features. For the remainder of the section, the $A^2\Sigma^+$ and $X^2\Pi$ electronic configurations only will be considered. Treatment of other electronic configurations is covered in Herzberg [35]. For details on calculating spectra of other electronic configurations, the NEQAIR96 manual written by Whiting et al. is another good source [95].

The notation used for electronic states is of the form ${}^{(2S+1)}\Lambda$, where S is the total electronic spin angular momentum and Λ is the term symbol for projection of orbital angular momentum on the internuclear axis. The notation for molecules is

analogous to the one used in describing the electronic configuration of an atom, where $\vec{\ell}$ is the orbital angular momentum for an atom and is a strong function of the electron distance to the nucleus described by the Bohr model. Atoms have an intrinsic spin angular momentum notated as $\vec{s}$. For molecules, $\vec{\Lambda}$ is the projection of $\vec{\ell}$ on the internuclear axis. The magnitude is defined as $|\vec{\Lambda}| = \Lambda\hbar$, where $\hbar$ is the reduced Planck constant and Λ is in integer values. For $\Lambda = 0, 1, 2$ integers, the term symbols are assigned Σ, Π, Δ, respectively. Similarly, $\vec{S}$ is the net sum of electronic spin in unfilled shells. Magnitude is defined as $|\vec{S}| = S\hbar$, where S has $\frac{1}{2}$ values. Finally, the addition of plus or minus terms in ${}^{(2S+1)}\Lambda^{+}$ or ${}^{(2S+1)}\Lambda^{-}$ is related to whether or not wave functions are odd or even.

Spin Splitting

In the case of NO $A^2\Sigma^+$ and $X^2\Pi$, we observe that both levels have $S = \frac{1}{2}$ in the total electronic spin term. This results from the configurations having an unpaired electron in a suborbital. The consequence of having an unpaired electron is that each electronic configuration now consists of two spin sub levels: one spin "up" level and one spin "down" level. This phenomena is commonly known as spin splitting. For detailed calculation of absorption or emission spectra, the inclusion of spin splitting requires additional corrections.

Instead of writing a different electronic term energy T_e for each of the two sublevels, it is more convenient to denote two spin-split levels with the same rotational quantum number J, but with different energies F_1, F_2. Following convention, we define a new quantum number N as

$$N = \begin{cases} J - \frac{1}{2} \text{ for } F_1 \\ J + \frac{1}{2} \text{ for } F_2. \end{cases} \tag{3.11}$$

When computing rotational energy, $F(N)$ is used in the place of $F(J)$. From the above expression, the difference in energies between the spin-split states is equivalent to the spacing between two adjacent quantum numbers. For high resolution absorption experiments, this change in spacing is critical for measuring rotational lines. The computation of Hönl-London factors also requires knowledge of the spin-split states. The treatment of Hönl-London factors will be reviewed in a later section in the context of line strength calculation.

Energy Correction for Spin Multiplets

In addition to modeling non-rigid rotation, corrections to the rotational energy term are needed to describe the interaction of spin on the structure of the electronic state. When $S \neq 0$, Hund's case a and Hund's case b are common models used for computing diatomic electronic spectra. The detailed theory of multiplet structure can be found in "Rotational Structure in The Spectra of Diatomic Molecules" by Kovacs [50] and is beyond the scope of the current discussion. Kovacs derives a general expression of the rotational energy term that is an intermediate between the two Hund's cases.

For NO $A^2\Sigma^+$, the term symbol corresponds to $\Lambda = 0$, where spin is not coupled to internuclear axis. For this electronic configuration, Kovacs simplifies Hund's intermediate case to the following expressions for rotation:

$$F_1(N, v) = B_v N(N+1) - D_v N^2(N+1)^2 + \frac{1}{2}\gamma N. \tag{3.12}$$

$$F_2(N, v) = B_v N(N+1) - D_v N^2(N+1)^2 - \frac{1}{2}\gamma(N+1). \tag{3.13}$$

The above is typically referred to as Hund's case b. The spin splitting constant γ is introduced in this updated expression for rotational energy. This is not to be confused with the γ_e constant in the correction for rotational distortion. The coefficients B_v and D_v are unchanged, but now the rotational energy is computed using the quantum number N. Substituting $F(N, v)$ into the summation in Equ. 3.7 describes the energy of the (N,v) level of the A state of NO.

For $X^2\Pi$, the situation of $\Lambda \neq 0$ requires an estimate of the spin-orbit coupling to the internuclear axis. The expression of the spin-orbit coupling constant A_v is obtained from Amoit [6] for NO(X) and is reproduced here:

$$\begin{aligned} A_v = {} & 123.252407 - 0.235702v - 4.0762 \times 10^{-}3v^2 \\ & - 1.8629 \times 10^{-4}v^3 - 2.5207 \times 10^{-7}v^5 \\ & - 2.386 \times 10^{-9}v^6. \end{aligned} \tag{3.14}$$

It is common to normalize the spin-orbit coupling constant with the coefficient for rotational distortion, given by $Y = \frac{A_v}{B_v}$. Following Kovacs, the intermediate of Hund's cases can be simplified to the following expressions for rotational energy:

$$F_1(N,v) = B_v\Big((N+1)^2 - \Lambda^2 - \frac{1}{2}\sqrt{Y(Y-4)\Lambda^2 + 4(N+1)^2}\Big) \\ - D_v(N(N+1) - \Lambda^2)^2 + H_N^{sr}. \tag{3.15}$$

$$F_2(N,v) = B_v\Big(N^2 - \Lambda^2 + \frac{1}{2}\sqrt{Y(Y-4)\Lambda^2 + 4N^2}\Big) \\ - D_v(N(N+1) - \Lambda^2)^2 + H_N^{sr}. \tag{3.16}$$

In Kovacs' short discussion of $^2\Pi$ terms, Hund's case b for centrifugal distortion is appropriate and used in the above expressions. Recall that the $X^2\Pi$ case corresponds to $\Lambda = 1$. The term H_N^{sr} is the intermediate form of the spin-rotation correction defined by Kovacs.

Franck-Condon Factors

The probability for an electronic transition to occur is described by the Franck-Condon principle in spectroscopy. The concept is based on the idea that the time to move or excite electrons is much shorter than the time required to move/excite nuclei during vibrations or rotations. If we consider the time scales relevant to the problem, $\tau_{elec} \approx 10^{-16}$ s and $\tau_{vib} \approx 10^{-13}$ s for energy exchange within the molecule [33]. Note that these characteristic times are different for molecule-molecule energy exchanges. Therefore, $\tau_{elec} << \tau_{vib}$ in the majority of situations. An equivalent description is that a change from one vibrational energy level in the excited state to another vibrational level in the ground state will be more likely to occur if the two vibrational wave functions overlap.

Franck-Condon factors are often computed and tabulated for transitions between vibrational levels in the NO γ system. The constants computed by Ory et al. [73] are used in the present work, where a 12×20 matrix of Franck-Condon factors, $q_{v',v''}$, is tabulated. As an example, the vibrational band $\gamma(1,0)$ is a transition from the v'= 1 in the A state to v"=0 in the X state. The tabulated Franck-Condon factor for this vibrational band is $q_{1,0} = 0.3295$. In contrast, the transition $\gamma(0,0)$ has a Franck-Condon factor of $q_{0,0} = 0.1656$, nearly half that of the $\gamma(1,0)$ transition. Later on, it will be shown that the $\gamma(1,0)$ vibrational band contains higher intensity compared to the $\gamma(0,0)$ band in the emission spectrum.

Hönl-London Factors

When a NO molecule transitions from the A state to the X, the rotational quantum number can change to a new value. Typically, the change in rotational quantum number is governed by selection rules, which describe which rotational/vibrational transitions are physically allowed and which are forbidden. The selection rules for rotation are $\Delta J = J'' - J' = \pm 1, 0$. The three allowed transitions are each assigned a branch and the naming convention is as follows:

$$\text{P branch: } \Delta J = -1$$
$$\text{Q branch: } \Delta J = 0$$
$$\text{R branch: } \Delta J = +1$$

The Hönl-London factor describes the distribution of total intensity amongst the branches for an electronic transition. Expressions for branch intensities can be derived from wave mechanics for a given electronic transition and structure of a molecule. Details in the derivation of expressions can be found in "Rotational Structure in the Spectra of Diatomic Molecules" by Kovacs [50]. The reference also takes into account the spin splitting within the two electronic states. For NO γ emission, 12 Hönl-London factors are required to describe the rotational distribution of intensities: 3 rotational branches (P, Q, R) $\times$ 2 spin split states of Π $\times$ 2 spin split states of Σ.

Expressions for Hönl-London factors are taken from Kovacs and can be found in Appendix C. To provide an example, the Hönl-London calculation for the R_1 branch will be shown. Recall that R branches have $\Delta J = +1$ and $N = J - 1/2$ for the spin split state. The Hönl-London factor is given as:

$$S_{R_1} = \frac{(J - 1/2)(J + 1/2)}{8(J + 1)c'^{-}c''^{-}}\left(u'^{-}u''^{-} + 4(J + 3/2)^2\right)^2. \tag{3.17}$$

The prime and double prime notation is used here to denote the upper and lower states respectively. Kovacs defines two new terms for the Hönl-London factor:

$$c^{-} = \frac{1}{2}(u^{-})^2 + 4\left((J + \frac{1}{2})^2 - \Lambda^2\right), \tag{3.18}$$

$$u^{-} = \sqrt{\Lambda^2 Y(Y - 4) + 4\left(J + \frac{1}{2}\right)^2} - \Lambda(Y - 2). \tag{3.19}$$

Again, the expression $Y = A_v/B_v$ is used to describe the spin-orbit coupling.

Line Intensity

The strength of a transition is dependant on the number of molecules at the upper state, the probability of the vibrational transition to occur as described by the Franck-Condon principle, the distribution of the intensity amongst rotational transitions described by the Hönl-London factor, and the dipole moment of the molecule. The intensity of spectral radiance is taken from Arnold, Whiting, and Lyle [9]. As absolute radiance is not required for this work, the emission intensity is proportional to:

$$I_v \propto (\bar{\nu})^4 \cdot q_{v',v''} \cdot \frac{S_{J'',J'}}{2J'+1} \cdot \frac{N(v',J')}{N_a}, \tag{3.20}$$

where the energy of each transition $\bar{\nu}$ is given in units of wavenumber.

Procedure for computing NO A-X Spectrum

The method of computing the NO γ spectrum is as follows:

1. Locate spectroscopic coefficients for the molecule and electronic state of interest. Find tabulations of Franck-Condon factors for the electronic transition and expressions for Hönl-London factors.

2. Calculate the energies of the upper and lower electronic states. Depending on the fidelity of the calculation, models correcting for non-rigid rotation, anharmonic vibration, and electronic configuration are desired.

3. For emission, compute the Boltzmann fraction for all A state energies. This requires computation of the partition functions for a given set of temperatures (T_r, T_v). For absorption, the population of the ground state energy levels are calculated instead.

4. Compute the line strength of the transitions, given by the product of system oscillator strength, Franck-Condon factor, and the normalized Hönl-London factor, the fourth power of the energy of the transition, and the Boltzmann fraction. This will give the intensity of each transition.

5. All computed energies are in vacuum wave numbers. To convert from vacuum wavelengths to air wavelengths, the expression derived by Edlen is used [23]:

$$(n-1)_s = \left(8342.13 + \frac{2406030}{130-\sigma^2} + \frac{15997}{38.9-\sigma^2}\right)10^{-8}, \tag{3.21}$$

where $\sigma = 1/\lambda_{\text{vac}}$ with units of μm^{-1} and $(n-1)_s$ is the refractivity of the gas. The conversion is valid from 200 nm to visible wavelengths.

6. Perform a convolution of the final intensities using a selected instrument line shape.

Line Shape

An important aspect of the code is the inclusion of line shape options. Line broadening is primarily caused from the combination of Doppler broadening, collisional broadening, and instrument broadening. The contribution of Doppler broadening was calculated to be $\Delta\bar{\nu}_D = 0.499\ \text{cm}^{-1}$, while collisional broadening was estimated to be $\Delta\bar{\nu}_c = 0.029\ \text{cm}^{-1}$ for the highest enthalpy condition. Details on computing Doppler and collisional broadening will be discussed in Section 3.2 in the context of absorption calculations. Instrument broadening is the largest contributor, measured to be $\Delta\bar{\nu}_I = 34\ \text{cm}^{-1}$ from recording the full width at half maximum (FWHM) of the Hg-Ar UVP Pen-Ray lamp for work with cylinders. Instrument line shape is heavily dependent on the selected slit width, diffraction grating groove spacing, camera resolution, and broadening from lenses or mirrors. As a result, a Hg-Ar lamp is used for every experimental campaign to gauge extent of instrumental line broadening.

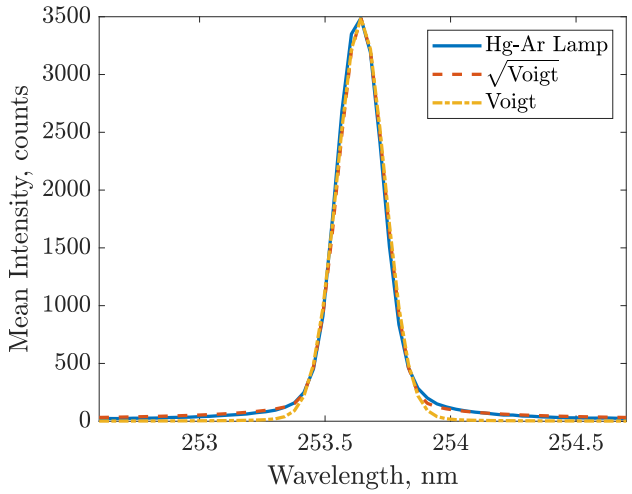

Figure 3.2: Mercury-Argon lamp radiation plotted alongside proposed instrument line shapes. This line shape is used for all cylinder experiments.

To provide the best fit possible between experimental spectra and simulations, several line shapes have been investigated to best represent the instrument line shape. Nubbemeyer and Wende proposed an instrument line shape in the form of a sine

squared function for their Czerny-Turner spectrometer [69]. Cruden finds that for UV/Vis cameras, the instrument line shape can be best described by the square root of a Voigt function [16]. Table 3.1 lists each method's R^2 coefficient when fitting the radiation of a Hg-Ar lamp. Figure 3.2 plots the Voigt and the square root of the Voigt function to approximate the measured instrument line shape. It is found that the square-root of the Voigt function provides the best possible fit without resorting to polynomial fitting.

Shape	R^2 Coefficient
$\sqrt{\text{Voigt}}$	0.998
Voigt	0.995
Gaussian	0.994
Sine-Squared	0.977
Lorentzian	0.966

Table 3.1: Coefficient of determination for each proposed instrument line shape for FWHM = 34 cm^{-1}.

Example Calculation of NO A-X Emission

The wavelength range of interest for the current methodology is between 210 nm and 255 nm. Figure 3.3 shows a comparison between the present model, Specair 3.0, and NEQAIRv14.0 of a computed NO γ spectrum at $T_v = T_r = 7000$ K with FWHM = 34 cm^{-1}. Specair is a commercially available software package used for computing emission and absorption spectra with applications for air plasmas [53]. The software has built-in routines for spectrum fitting and computing spectra with self-absorption. NEQAIR is a radiation transport solver developed by NASA Ames for aerothermal problems such as Earth or Mars re-entry [17, 95]. NEQAIR can be coupled with CFD codes to generate radiation profiles for a given simulated gas. Despite differences in calculations and spectroscopic constants, general agreement is observed for all three calculations, validating the current model to state-of-the-art computations. An important consideration is the lack of spin splitting correction in the NEQAIR calculation. From Cruden and Brandis [17], spin multiplicity is not treated explicitly in NEQAIRv14.0. This can be seen in Fig. 3.3, where the NEQAIR spectrum does not contain detailed features that arise from including spin effects.

Four major vibrational bands exist in this wavelength range: γ(1,0), γ(0,0), γ(0,1), and γ(0,2). Three of the major vibrational bands are electronic transitions originating from the v'=0 state. As a result, the shape of the spectrum is heavily determined

by the rotational temperature and the Franck-Condon factors. The rotational temperature determines the broadband structure within the vibrational band. It is found that the FWHM of γ(0,1) and γ(0,2) increases with increasing rotational temperature. This is a result of the peak population in the Boltzmann distribution pushed toward larger rotational quantum numbers. Because the Franck-Condon factors are constant, they only determine the difference in peak intensity between vibrational bands. On the other hand, γ(1,0) intensity is mainly determined by the population of NO in the v'=1 level. As the distribution of vibrational levels is governed by T_v, this transition can be used to determine vibrational temperature. The peak intensity of γ(1,0) is a strong function of T_v and the Franck-Condon factors, while the width of the band is described by T_r. Therefore, estimates for vibrational temperature can be achieved through the ratio of peak intensity between γ(1,0) and other vibrational bands.

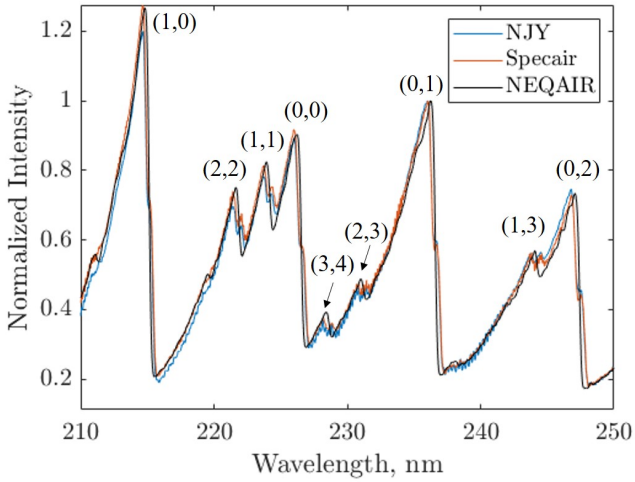

Figure 3.3: Calculation of NO γ spectrum using present model, Specair 3.0, and NEQAIRv14.0 for $T_v = T_r = 7000$ K. Vibrational band locations are marked following the convention (v',v").

Additional vibrational bands can still influence the overall shape of the spectrum, despite having lower intensities than the four major bands. For example, γ(2,2) and γ(1,1) are transitions from upper vibrational levels from NO(A) and are a strong function of vibrational temperature. Often, vibrational bands overlap with one another, causing overall intensities to increase after convolving the transitions into the line shape. Knowledge of the behavior of transitions can allow for a better understanding of the internal temperatures of the NO(A) molecule.

Effect of Background Signal to NO A-X Spectrum

In an ideal experiment, NO γ emission would be the only transition measured by the spectrometer. However, other species can radiate in the same range of wavelengths, increasing the final intensity of the measured spectrum. Transitions such as the O_2 Schumann-Runge and NO β exhibit broadband radiation in the 210-250 nm range of wavelengths. Other sources of background signal can include dark charge accumulation of an intensified detector if background subtraction is not performed. This ultimately affects the shape of the spectrum after normalization, as there is additional radiation to the troughs of the NO γ spectrum. As the NO γ signal decreases, the effect of background intensity becomes more apparent. When modeling radiation, it is desired to have some capability of taking into account background signals to the final radiation shape.

Consider the radiation of NO γ with a uniform background signal B for all wavelengths. The final measured radiance is simply the summation of the NO γ radiation, I_γ, and the background:

$$I(\lambda) = I_\gamma(\lambda) + B. \tag{3.22}$$

Normalization is performed using the peak of the $\gamma(0,1)$ vibrational band of the measured signal. The measured normalized spectrum can be written as:

$$\frac{I(\lambda)}{I(\lambda_{0,1})} = \frac{I_\gamma(\lambda) + B}{I_\gamma(\lambda_{0,1}) + B}. \tag{3.23}$$

Define the scaling factor a as the following:

$$a = \frac{1}{I_\gamma(\lambda_{0,1}) + B}. \tag{3.24}$$

Equation 3.23 can be rewritten to the following expression for the normalized intensity:

$$\frac{I(\lambda)}{I(\lambda_{0,1})} = 1 + a\Big[I_\gamma(\lambda) - I_\gamma(\lambda_{0,1})\Big]. \tag{3.25}$$

Figure 3.4 illustrates the effect of background signal on a normalized spectrum. A temperature of $T_v = T_r = 7000$ K is used with a uniform background level of 15% of the $\gamma(0,1)$ peak as an example. Background signal serves to artificially

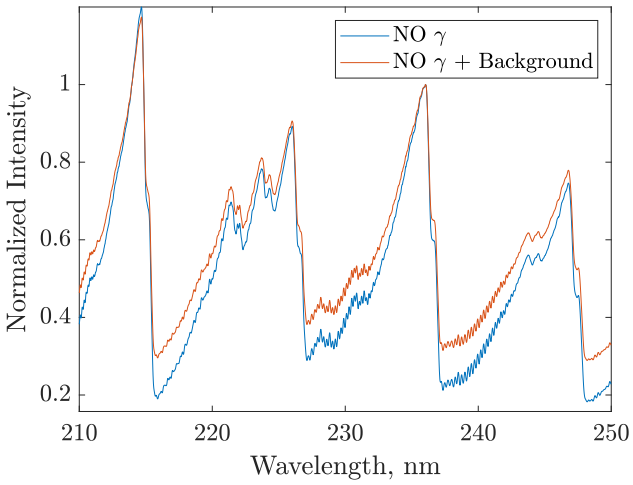

Figure 3.4: Normalized synthetic spectra for $T_v = T_r = 7000$ K with and without uniform background included. A uniform background level of 15% of the $\gamma(0,1)$ intensity is used.

increase the FWHM of the vibrational bands after normalization. Later in Chapter 4 and Chapter 5, experimental spectra are fit with computed synthetic spectra to extract quantitative properties of the gas. As the synthetic spectra are normalized beforehand, comparisons are made using the following expression:

$$I_{\text{compare}}(\lambda) = 1 + a\Big[I_{\text{synthetic}}(\lambda) - 1\Big], \tag{3.26}$$

where the scaling factor a is selected to reduce a residual. The use of a scaling factor has been implemented by Glumac et al. [27] and Sharma et al. [87] for fitting experimental spectra.

3.2 Radiative Transfer

Ideally, photons emitted from electronic transitions are all collected by optics for a given steradian and dispersed into wavelengths using a grating or prism. However, not all emitted photons leave a slab of radiating gas. Photons can be reabsorbed by other ground state molecules, exciting the absorbing molecule to an energy level equivalent to the frequency of the photon. Since an electronically excited molecule can have a finite lifetime, the photon can be re-emitted at a different wavelength as a result of energy transfer within the excited state. The emission and absorption of photons is an important aspect of radiative processes in gases, as this process heavily affects the shape of a measured spectrum. Accurate predictions

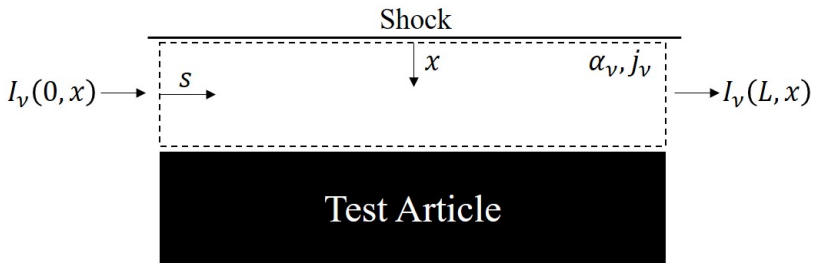

Figure 3.5: Coordinates used for spectral radiance along a slab of gas.

of the extent of self-absorption will ultimately determine the types of strategies used in extracting quantitative information from spectra. This section discusses the treatment of radiating gases that exhibit self-absorption. A good reference for radiative transfer is Rybicki and Lightman [83]. Discussion from sections on quantitative absorption from Hanson, Spearrin, and Goldenstein [33] are also useful in reviewing topics in radiative transport.

The radiative transport equation

Spectral radiance I_ν describes the energy per unit area of light for a given solid angle. Consider a slab of radiating gas with length L and no scattering present. The radiation transport along the slab coordinate s for collimated light at frequency ν is given by:

$$\frac{dI_\nu}{ds} = -\alpha_\nu I_\nu + j_\nu, \tag{3.27}$$

where α_ν and j_ν are the absorption and emission coefficients respectively. The radiative transport equation describes the change in final spectral radiance from emitters contributing to the intensity and absorbing molecules reducing the spectral radiance. Once α_ν and j_ν are known along the slab, the equation can be solved to find the spectral radiance for a given frequency ν. A commonly used quantity to describe the cumulative intensity for the entire spectral range is the integrated radiance:

$$I = \int_{\nu_0}^{\nu_1} I_\nu d\nu. \tag{3.28}$$

When evaluating the integral for different wavelength intervals, integrated radiance provides a measurement of how certain transitions contribute to the overall intensity

of a detector. This relationship will be used later to describe the spatial and temporal behavior of ultraviolet radiation without the need of plotting multiple spectra.

Emission and Absorption Coefficient

The Einstein coefficients describe the three important processes involved in radiation: spontaneous emission, absorption, and stimulated emission. Consider a lower energy level 1 and upper level 2 where transitions can occur. The first process is known as spontaneous emission, where the system transitions from level 2 to level 1 by emitting a photon. The Einstein A-coefficient, denoted as A_{21}, is the transition probability per unit time for spontaneous emission. A_{21} has units of s^{-1} and is typically tabulated for electronic transitions. The second process is absorption, where the system consumes a photon of energy $h\nu$ to transition from level 1 to level 2. The probability constant for absorption is denoted the coefficient B_{12} and has units $m^3J^{-1}s^{-2}$. Finally, the third process is known as stimulated emission. The coefficient for stimulated emission is denoted as B_{21} and is typically included in the absorption coefficient. Relations between the three Einstein coefficients can be derived through wave mechanics, so any one of the Einstein coefficients can be used to determine the other two.

The relation between the A_{21} and the emission coefficient is given by:

$$j_\nu = \frac{h\nu}{4\pi}\phi N_2 A_{21}, \tag{3.29}$$

where N_2 is the number of molecules or atoms at upper level for a specific transition and ϕ is line profile. In similar fashion, the absorption coefficient is related to the Einstein coefficients through the following relation:

$$\alpha_\nu = \frac{h\nu}{4\pi}\phi(N_1 B_{12} - N_2 B_{21}). \tag{3.30}$$

Stimulated emission is commonly thought of as negative absorption, as it serves to reduce the value of α_ν. Absorption coefficients are obtained from using values presented by Luque and Crosley [60].

When applying the absorption and emission coefficient to electronic transitions, the number density must be evaluated for a specific energy level involved in the transition and not the total number density of molecules in an electronic state. If the number density of the ground and the first excited state are known, the Boltzmann

fraction can be used to compute the density for a specific energy level with the following:

$$N_1 = N_X\left(\frac{e^{\frac{-hcG(v'')}{kT_v}}}{Q''_v}\cdot\frac{(2J''+1)e^{\frac{-hcF(J'')}{kT_r}}}{Q''_r}\right), \tag{3.31}$$

$$N_2 = N_A\left(\frac{e^{\frac{-hcG(v')}{kT_v}}}{Q'_v}\cdot\frac{(2J'+1)e^{\frac{-hcF(J')}{kT_r}}}{Q'_r}\right). \tag{3.32}$$

Line Profile

Ideally, a molecule will only absorb a photon at a specific frequency. Likewise, a molecule in the excited state will ideally emit a photon at a discrete frequency. These processes are complicated by the broadening of absorption and emission lines. The line profile ϕ describes the non-discrete nature of emission and absorption. This section will describe broadening mechanisms from internal processes of the molecules. The integral of the line profile is defined to be equal to 1 for the entire frequency range.

$$\int_0^\infty \phi d\nu = 1. \tag{3.33}$$

There are three mechanisms that determine the line profile of gases: Doppler shift, thermal broadening, and collisional broadening. Doppler shift does not broaden the line profile, but instead shifts the frequency of the transition through the Doppler effect. Recall that the Doppler effect can be written as:

$$\Delta\nu_0 = -\nu_0\left(\frac{U_m}{c}\right), \tag{3.34}$$

where ν_0 is the center frequency of the transition, U_m is the velocity of the molecule relative to the observer, and c is the speed of light. Depending on the wavelength range of interest or the velocity of the gas, the Doppler effect can shift the observed wavelength of the transition. However, the ratio of the velocity to the speed of light is insignificant in most cases. Assuming a maximum velocity of 4 km/s and a wavelength of $\lambda = 230$ nm, the shift in wavelength is $\Delta\lambda_d = 4\times10^{-3}$ nm, or $\Delta\nu = 1.74\times10^{10}$ s^{-1} in terms of frequency. Since all emission measurements are performed downstream of a shock, the velocity of the gas will be significantly lower than 4 km/s. In addition, the maximum wavelength resolution for the intensified camera is 4×10^{-2} nm for the grating used in experiments, meaning the Doppler shift

in wavelength will not be resolved. Doppler shift will not be taken into account in all reported measurements and calculations.

Thermal broadening (also known as Doppler broadening) is another form of the Doppler effect, but results from the thermal velocity of molecules. The change in FWHM of a line shape is given as:

$$\Delta\nu = \nu_0\sqrt{\frac{8kT_{tr}\ln 2}{mc^2}}, \tag{3.35}$$

where m is the mass of the molecule and T_{tr} is the translational temperature. If thermal broadening is the dominant contributor of the FWHM, the line shape can be approximated with the normalized form of the Gaussian distribution.

Collisional broadening (also referred to as pressure broadening) describes change in emitted frequency from the energy exchange that occur between colliding molecules. Collisions can cause a transition to a neighboring energy state in the excited molecule, interrupting the emission process and shifting the frequency of the emitted photon. When excited molecules with an associated cross section collides with other molecules, the effect on the absorption and emission profile can be estimated. Typically, the effects of pressure broadening can be estimated through tabulated collision broadening coefficients, such as the tabulation by Almodovar et al. [5]. The approximation for pressure broadening used in this work is taken from Hanson, Spearrin and Goldenstein [33]:

$$\Delta\nu = p\sum X_A 2\gamma_{B-A}, \tag{3.36}$$

where X is the species mole fraction and $2\gamma_{B-A}$ are tabulated broadening coefficients. If pressure broadening is the dominant contributor to the FWHM, then the normalized Lorentz profile can be used to approximate the line shape.

To take into account contributions from both thermal and collisional broadening, the convolution of the Gaussian and Lorentzian can be performed, resulting in the Voigt function. The line shape for both thermal and collisional broadening is derived by Hanson, Spearrin and Goldenstein [33]:

$$\phi(\nu) = \frac{2}{\Delta\nu_{\text{Doppler}}}\sqrt{\ln 2/\pi}V(a,w), \tag{3.37}$$

where w is the position along the Voigt profile V and the Voigt parameter is

$$a = \sqrt{\ln 2}\frac{\Delta\nu_{\text{Collision}}}{\Delta\nu_{\text{Doppler}}}. \tag{3.38}$$

Optical Depth

A common quantity used in describing the absorption of a gas is the optical depth τ_ν, defined as:

$$\tau_\nu(s) = \int_{s_0}^{s} \alpha_\nu(s')ds'. \tag{3.39}$$

The optical depth describes how far a photon can travel through a medium on average before being reabsorbed by a molecule. When $\tau_\nu << 1$, it is said that the gas is *optically thin*. In the optically thin limit, a photon can travel through the medium without being absorbed. When $\tau_\nu >> 1$, this describes the *optically thick* limit. In this limiting case, the photon cannot travel through the medium without being absorbed and re-emitted. The optically thick limit describes black-body radiation, where the radiation is in thermal equilibrium. Although the concept of optical depth is useful in describing self-absorption of a gas, classifying a gas with τ_ν to be either $\tau_\nu << 1$ and $\tau_\nu >> 1$ is generally arbitrary. The full radiative transport equation ultimately determines the final spectral radiance for a given optical depth.

Solution to the Radiative Transport Equation

We now have the tools to model the radiation for an emission spectroscopy experiment. Recall that collection optics are oriented perpendicular to the freestream velocity, collecting the cumulative radiance along the span of a gas. Assume that the emission and absorption coefficient are only a function of the post-shock streamwise coordinate x shown in Fig.3.5. Therefore, α_ν and j_ν are constant along s. In addition, it is assumed that the focal length of the collection optics are large relative to length scale of the slab of the gas. Therefore, collimated rays traveling along the span of the gas are only considered. With these assumptions, Equ. 3.27 simplifies to a first order ordinary equation. The general solution to this differential equation is

$$I_\nu(s) = \mathrm{c}_1 e^{-\alpha_\nu s} + \frac{j_\nu}{\alpha_\nu}. \tag{3.40}$$

To solve the unknown constant, we assume that no external spectral radiance enters the slab of gas (laser radiation for example). Setting $I_\nu(0) = 0$, we obtain the final result for spectral radiance as a function of slab length:

$$I_\nu(s) = \frac{j_\nu}{\alpha_\nu}\Big(1 - e^{-\alpha_\nu s}\Big). \tag{3.41}$$

Using the assumption of constant α_ν, it is recognized that Equ. 3.39 simplifies to:

$$\tau_\nu(s) = \alpha_\nu s. \tag{3.42}$$

Equation 3.41 shows that the final radiance at the end of the slab is described by the ratio of the emission and absorption coefficient, with an inverse exponential dependence in optical depth τ_ν. For an infinitely long slab of gas, the expected spectral radiance is simply $I_\nu = \frac{j_\nu}{\alpha_\nu}$. It is often useful to write the intensity in terms of number density of the upper and lower states. Assuming that the line shapes for emission and absorption are equal, spectral radiance simplifies to:

$$I_\nu = \frac{N_2 A_{21}}{N_1 B_{12} - N_2 B_{21}}\Big(1 - e^{-\tau_\nu}\Big). \tag{3.43}$$

Since the Einstein coefficients for absorption and stimulated emission differ by the ratio of degeneracies and for most cases $N_2 << N_1$, the denominator of Equ. 3.43 can be approximated as $N_1 B_{12}$, resulting in a relationship between the spectral radiance and the ratio of number densities. If Equ.3.43 is used with a post-shock relaxation calculation, a radiation profile downstream of the shock wave can be generated using the computed number densities of the ground and electronic state.

Criterion for Spectrum Fitting: The Ratio of Intensities

Calculations of synthetic spectra in Section 3.1 neglect the effects of absorption of the gas, meaning the gas is optically thin. However, many applications of emission spectroscopy involve measurements of high density gases that exhibit self absorption. Despite this mismatch in physics modeling, it is often desired to extract quantitative properties of a radiating gas that may not be optically thin. If a criterion is met, it is still possible to perform temperature fits using optically thin synthetic spectra for experiments with self-absorption present.

Consider a standard calculation of an emission spectrum without absorption. Assuming a constant j_ν along the slab of gas and no external radiation, Equ. 3.27 can be solved for the following:

$$I_{\nu,\text{thin}} = j_\nu s. \tag{3.44}$$

In the optically thin limit, the final intensity of a slab of gas is simply proportional to the slab length. When written in terms of the Einstein coefficients, emission intensity is also directly proportional to the number density of the electronically excited molecule. Therefore, if a gas can be approximated as optically thin, the spatial intensity profile is a direct measurement of the number density of a molecule in the excited state. A measurement corrected for absolute intensity can provide quantitative values for the emission coefficient, which is useful in determining the distribution between the X and A electronic states. When used in combination with a quasi-steady state approximation of the concentration, intensity profiles can also be used as markers for the other species in the flow.

Relative intensity is only required for spectrum fitting, as the absolute radiance only determines the population distribution between the ground and upper electronic states. If absorption occurs uniformly over all wavelengths, information is not lost as the spectrum shape is still preserved after normalization. In reality, certain bands can exhibit different levels of absorption, adding unwanted contributions to the spectrum shape. If the ratio of $I_{\nu,\text{Thin}}$ to $I_{\nu,\text{Total}}$ is the same between two adjacent bands, spectrum shape is still preserved after normalization. Introducing the ratio of intensities, the ratio of the optically thin intensity to the full radiative transport intensity simplifies to

$$Ri_\nu = \frac{I_{\nu,\text{thin}}}{I_{\nu,\text{total}}} = \frac{\tau_\nu}{1 - e^{-\tau_\nu}}. \tag{3.45}$$

Equation 3.45 is a more useful quantity to report than optical depth, since it is based on the solution of the radiative transport equation instead of the product of the path length and absorption coefficient alone. In addition, there are frequent situations where the local optical depth is $\tau_\nu \approx 1$, lying in between the traditional definition of optically thin and optically thick. The interpretation of Ri is more straightforward, as it is a measurement of the departure from the optically thin case. It can be observed that in the optically thin case, $\lim_{\tau_\nu \to 0} Ri(\tau_\nu) = 1$. As $Ri_\nu > 1$, more self-absorption is present in the slab of gas.

The criterion for fitting an experimental spectrum using optically thin synthetic spectra is

$$Ri_{\gamma(v_1', v_1'')} \approx Ri_{\gamma(v_2', v_2'')}. \tag{3.46}$$

For every vibrational band of the NO γ emission, Equ. 3.45 must be computed and checked to see if Equ. 3.46 is satisfied between adjacent vibrational bands. Equation 3.46 is always satisfied for optically thin cases.

3.3 Kinetics of Electronically Excited NO

There are several mechanisms that lead to the formation of electronically excited NO. These include thermal excitation of the ground state, collisional processes with neutrals or charged particles, and direct formation from chemical reactions. In addition to the spontaneous emission, there are non-radiative pathways for NO(A) to relax to the ground state, generally referred to as electronic quenching. In order to link NO(A) transitions with the chemical non-equilibrium present in the flow, a kinetic model must be used to estimate the amount of excitation and quenching of electronic states for a given gas. With this final description, it is possible to estimate the population of NO(A) from thermochemical processes and use the models of emission and absorption to provide the final expected radiance for a given post-shock state.

Before implementing a kinetic model with NO(A) as a separate species, thermodynamic properties of the electronic states of NO are required. Thermodynamic properties can be computed using statistical mechanics with spectroscopic constants. Routines from the Shock and Detonation Toolbox [51] are used for computing the thermodynamic properties of molecules and converting them into the form of the NASA9 polynomials, allowing for implementation through Cantera's routines. Typically, all possible electronic states are included in the computation of the partition functions for the standard NASA9 polynomial representation of NO [63, 64]. However, this does not serve as an accurate representation of the thermodynamics for individual electronic states. Thermodynamics of NO(X) and NO(A) are computed separately by considering only one electronic state in the computation of the partition functions. Spectroscopic constants presented in Section 3.1 are used in the calculation. Upper limits for vibrational and rotational quantum number are determined by the energy for dissociation of the molecule. Using the well depths tabulated in Park [76] and a $J = 0$, the highest vibrational level of NO(X) is $v_{\max} = 45$ and the highest vibrational level of NO(A) is $v_{\max} = 13$. For $v = 0$, the rotational quantum number limits are $J_{\max} = 185$ for NO(X) and $J_{\max} = 120$ for NO(A). Figure 3.6 plots the resulting specific heat at constant pressure from statistical mechanics. At low temperatures, the heat capacity at constant pressure of NO(X) is similar to the McBride, Zehe, and Gordon calculation of NO including all electronic states

[64]. However, at temperatures larger than 5000 K, the heat capacity of NO(X) is substantially lower than the NO thermodynamics using all electronic states. The profile of the NO(A) heat capacity is substantially different from the ground state due to the spacing of energy levels and the smaller well depth of NO(A). The final NASA9 polynomials are stored in a .cti file for use with Cantera.

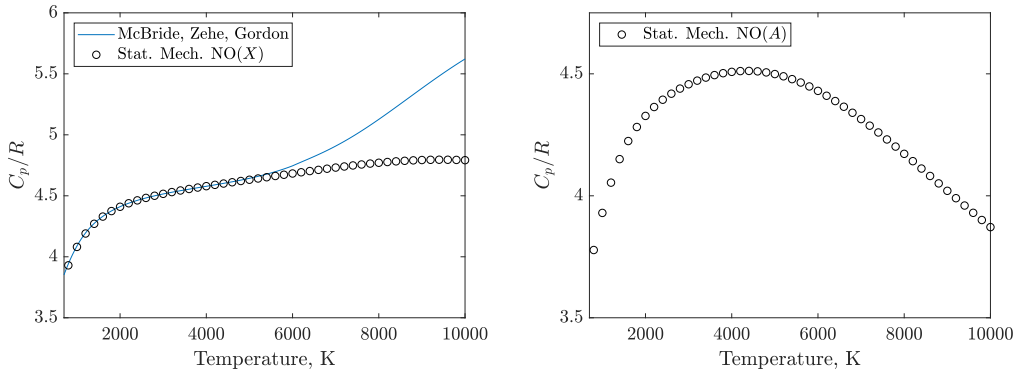

(a) NO(X) Heat Capacity

(b) NO(A) Heat Capacity

Figure 3.6: Computed heat capacity using statistical mechanics. Blue curve is NASA9 tabulation by McBride, Zehe and Gordon [64] that considers all electronic states.

Two-Temperature Reactive Landau-Teller Model

A two-temperature reactive Landau-Teller relaxation model implemented in the Shock and Detonation Toolbox [51] is used for computing post-shock conditions with NO(A) and NO(X) kinetics. Vibrational relaxation of molecules is modeled by Landau and Teller [52] with the expression

$$\frac{dE_{\text{vib}}}{dt} = \frac{E^*_{\text{vib}} - E_{\text{vib}}(t)}{\tau_{\text{vib}}}, \tag{3.47}$$

where $E_{\text{vib}}(t)$ is the vibrational energy at time t and E^*_{vib} is the equilibrium vibrational energy assuming translational-rotational-vibrational equilibrium. Coefficients used for the characteristic vibrational relaxation time, τ_{vib}, are taken from correlations developed by Millikan and White [66]. The empirical relation used by Millikan and White for vibrational relaxation time is given as

$$\tau_{\text{vib}} = \frac{(1.16 \times 10^{-3})\mu^{\frac{1}{2}}\theta^{\frac{4}{3}}(T^{-\frac{1}{3}} - 0.015\mu^{\frac{1}{4}}) - 18.42}{p}, \tag{3.48}$$

where τ_{vib} is in units of seconds, p is the pressure in units of atm, μ is the reduced mass in atomic units, and θ is the characteristic vibrational temperature for a species in units of K. The routine uses a two-temperature model of chemical reaction rates proposed by Park [76] with an effective vibrational-electronic temperature and a translational-rotational temperature. Chemical kinetics for neutral species are taken from Johnston and Brandis [44]. This includes the kinetics for the formation NO(X), given as

$$\mathrm{O} + \mathrm{N}_2 \leftrightarrows \mathrm{N} + \mathrm{NO}(X). \tag{3.49}$$

$$\mathrm{N} + \mathrm{O}_2 \leftrightarrows \mathrm{O} + \mathrm{NO}(X). \tag{3.50}$$

The above reactions are commonly referred to as the Zel'dovich mechanism [98], which describes the pathways NO(X) is created after the initial dissociation of O_2 and N_2. The Arrhenius form of the kinetics from Johnston and Brandis were developed to be used with two-temperature simulations of hypervelocity flows. For specified reactions, the geometrically averaged temperature proposed by Park [75] is used:

$$T_a = \sqrt{T_v T}, \tag{3.51}$$

where T_v is the bulk vibrational-electronic temperature and T is the translational-rotational temperature used in the calculation. The reaction rates for NO(A) are taken from Park [77], which also contains kinetics for other electronic states. Heavy particle electronic excitation is modeled using these rates, given as

$$\mathrm{NO}(X) + M \leftrightarrows \mathrm{NO}(A) + M, \tag{3.52}$$

where M is a colliding partner. The coefficient for spontaneous emission is taken from a followup paper by Hyun, Park, and Chang [40] for NO γ emission. The spontaneous emission of a photon is written as

$$\mathrm{NO}(A) \rightarrow \mathrm{NO}(X) + h\nu. \tag{3.53}$$

These Arrhenius expressions are tabulated in .cti files for thermochemical calculations of post-shock gas. The calculation can be configured to run for a standard shock tube calculation or as a stagnation streamline calculation. In addition, a non-equilibrium gas can be used as an input to the reaction zone calculation. This allows for calculations to be performed through multiple shocks.

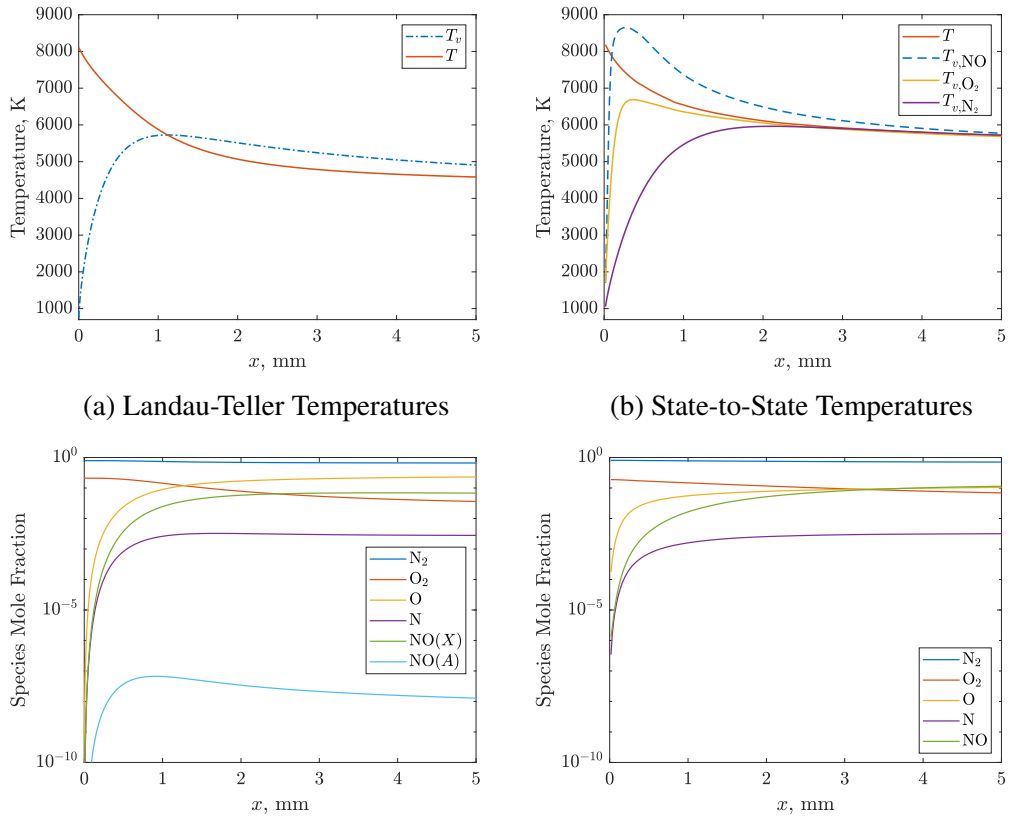

(a) Landau-Teller Temperatures

(b) State-to-State Temperatures

(c) Landau-Teller Mole Fractions

(d) State-to-State Mole Fractions

Figure 3.7: Reaction zone calculations of the M7-H8-A freestream using two thermochemical models. Horizontal axis is distance downstream a normal shock.

A zero-dimensional state-to-state model of Adamovich [3, 4, 61] with modifications in implementation (Massa and Austin [62]) is also used to compute the post-shock relaxation region. Energy transfer rates are computed using a forced-harmonic oscillator model with free-rotating molecule trajectories from Adamovich and Rich [4]. Molecule-molecule rates were extended to higher collisional energies for all possible O_2, N_2, and NO transfers from the work of Massa and Austin [62]. Molecule-atom rates are taken from the three-dimensional collisional model of Adamovich and Rich [4]. Chemical reaction rates are taken from the work of Bose and Candler [13, 14]. Only NO(X) is considered in the thermochemical model. Boltzmann distributions are assumed for NO(X) produced through the first Zel'dovich reaction, shown in Equ. 3.49. In contrast, non-Boltzmann vibrational distributions are modeled for NO(X) generated through the second Zel'dovich reaction [14]. The state-to-state model computes an effective vibrational temperature of each of the diatomic species

using the first two vibrational energy levels. A translational temperature is also computed in the model.

In Fig. 3.7, a comparison between the two relaxation models is made using the M7-H8-A as the freestream condition. The inviscid, perfect gas calculation of the expansion tube process is used as the inflow condition for the calculations. The translational-rotational temperature of the two-temperature model and the translational temperature of the state-to-state model both start at the thermally and chemically frozen value of 8105 K. This temperature limit assumes that the vibrational energy and chemistry is frozen across the shock, while translational-rotational equilibrium is assumed for the shock jump condition. The state-to-state model predicts a slower relaxation to equilibrium for translational temperature when compared to the Landau-Teller bulk translational-rotational temperature. The two-temperature Landau-Teller model treats all diatomic species with a common vibrational temperature, which is different from the state-to-state description of vibrational temperature for an individual species. In addition, the state-to-state model predicts an overshoot in NO(X) vibrational temperature from the thermally and chemically frozen value of 8105 K. This overshoot is associated with the formation of NO(X) in a non-Boltzmann distribution amongst the vibrational levels. Due to the capability of computing non-Boltzmann behavior of the species, the state-to-state model is used in comparing measured temperatures of the post-shock gas. However, the state-to-state model does not treat NO(A) as a separate species, critical for interpreting radiation intensity. When studying integrated intensity from the ultraviolet emission, the two-temperature reactive Landau-Teller model is used instead of the state-to-state model. Number density calculations of NO(A) from the Landau-Teller model can be used to compare with measured integrated radiance through Equ. 3.43.

Chapter 4

UV RADIATION OF HYPERVELOCITY FLOW OVER CIRCULAR CYLINDERS

Hypervelocity stagnation flows are a characteristic feature of planetary reentry vehicles and sounding rockets. Figure 4.1 shows a schematic of the various features in this flow field. This flow features a bow shock with a standoff distance Δ away from the surface of the vehicle. Stagnation of the gas occurs, where a streamline in the post-shock region decreases to zero velocity at the surface of the body, denoted as the stagnation point in Fig. 4.1. Along the stagnation streamline, dissociation of the freestream gas occurs, where minor species radiate in the ultraviolet wavelengths. A portion of the post-shock gas is subsonic and is bounded by the sonic line. Streamlines outside of the sonic line are supersonic due to the added curvature of the bow shock. For high enthalpy conditions, the gas remains in thermochemical non-equilibrium for the majority of the shock layer. Shock standoff distance and shock curvature are sensitive to thermochemical non-equilibrium in the post-shock gas, allowing for macroscopic flow features to be linked with microscopic processes of the gas. Hypervelocity flow of circular cylinders are a canonical example of blunt body flows that provide a good benchmark for computational models of thermochemical non-equilibrium. Due to the steady nature of these flows, experiments with cylinders can be used to judge the capabilities of new spectroscopic techniques without the need to decouple fluid dynamics from the measurement. In this chapter, measurements of NO rovibronic emission will be performed along the stagnation streamline of circular cylinders. Spectroscopic imaging will be performed at multiple freestream conditions and compositions to study changes in optical depth, thermochemical non-equilibrium, and electronic transitions. Paired with high resolution schlieren imaging, these spectroscopic measurements provide data used for modeling radiative processes and thermodynamic non-equilibrium.

4.1 Single Shot Schlieren

A camera exposure of 700 ns is used for single shot schlieren imagery. Shutter exposure occurs 120 µs after the arrival of the contact surface measured by a pitot probe mounted underneath the model. This ensures that the bow shock has fully established. Figure 4.2 shows schlieren images of the M7-H8-A and M5-

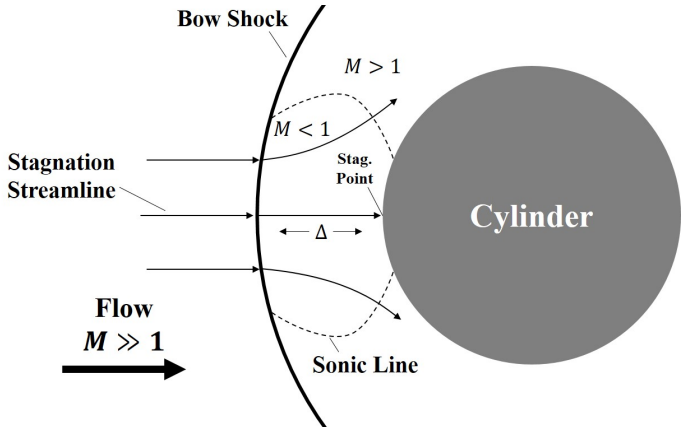

Figure 4.1: Schematic of hypervelocity flow over a cylinder.

H6-A conditions with an air and nitrogen test gas. Images are mirrored about the stagnation streamline for comparison between test gases. The field of view is large enough to observe the majority of the bow shock curvature. Along the surface of the cylinder model, image distortion due to the boundary layer is visible in the images. The presence of the boundary layer was confirmed by orienting the schlieren cutoff horizontally and visualizing the boundary layer for the upper half of the cylinder. The largest standoff distance occurs with nitrogen as the test gas for both freestream conditions. In addition, the radius of curvature of the bow shock is largest with nitrogen. For the highest enthalpy freestream, chemiluminescence is observed in Fig. 4.2a downstream the bow shock. As the pco camera collects broadband light, the chemiluminescence can only be used to indicate regions of high chemical activity. The peak in luminescence is found to occur further downstream for the nitrogen freestream as opposed to the air case. This indicates that the induction time for the post-shock nitrogen to radiate is longer than in the air case. The presence of chemiluminescence is not captured in the images of M5-H6-A due to the lower freestream enthalpy. The image of the shock contains a larger gradient in pixel intensities for M5-H6-A, indicating higher post-shock densities. These schlieren observations will later be confirmed with the spectroscopy measurements, as the standoff distance is indicated by the appearance of radiation.

Using the method outlined in Leibowitz and Austin [55], standoff distance can be measured along the stagnation streamline by extracting pixel intensities. A region 17 pixels wide is binned at the centerline of the cylinder and a profile of pixel intensity versus streamwise distance is generated. The minimum intensity is selected as the location of the shock. As the boundary layer distorts the cylinder

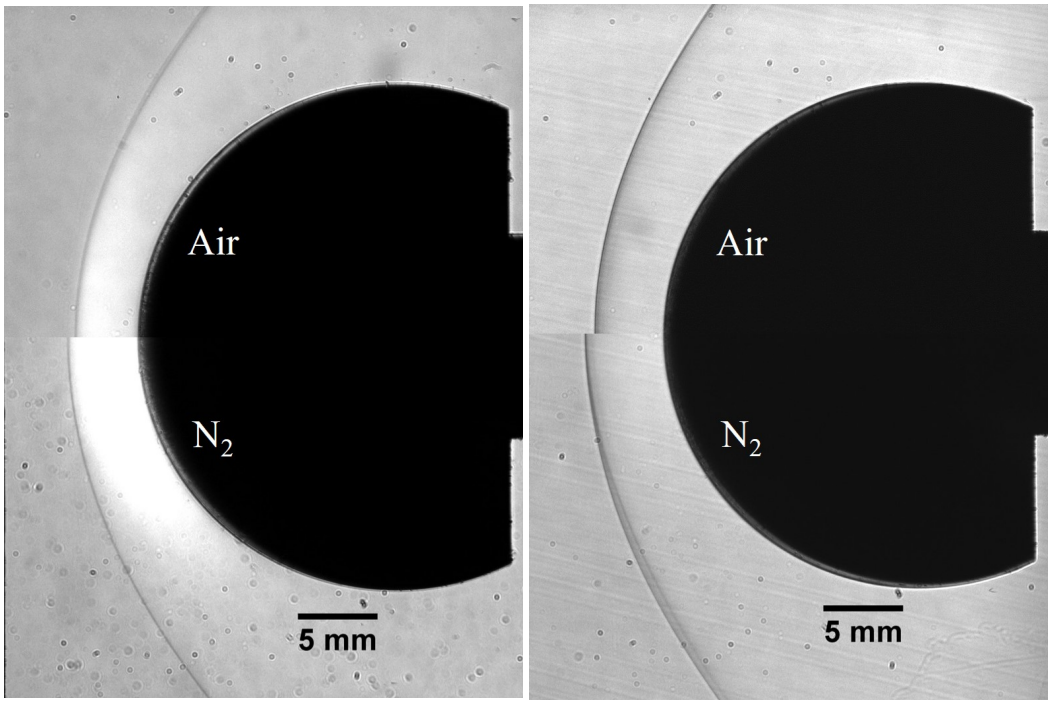

(a) M7-H8-A Freestream (b) M5-H6-A Freestream

Figure 4.2: Single-shot schlieren of a 31.75 mm diameter cylinder in different freestream enthalpy and gas compositions. Boundary layer effects are present in the near surface of the cylinder.

surface, a flat mounting surface located 22.86 mm behind the cylinder tip serves as a reference for measurements. To estimate the uncertainty in the shock standoff distance measurement, an error propagation analysis is performed. The uncertainty in standoff distance is given as

$$\sigma_\Delta^2 = 2c^2\left(\frac{x_{\text{shock}} - x_{\text{body}}}{x_1 - x_2}\right)^2 \sigma_{x_2}^2 + c^2(\sigma_{x_{\text{shock}}}^2 + \sigma_{x_{\text{body}}}^2), \tag{4.1}$$

where Δ is the standoff distance, c is the millimeter-to-pixel conversion in units of mm/pixel, and x_i are the location of features along the stagnation streamline in units of pixels. An uncertainty of $\sigma_x = \pm 1$ pixel is used. The cylinder mount geometry is used as a reference to obtain x_1 and x_2 for converting pixels to distance, which is typically $c = 0.03$ mm/pixel for cylinder images. If the shock location is measured relative to the cylinder surface, the value $x_{\text{shock}} - x_{\text{body}}$ would be small and the first term can be neglected. Since the measurement of the shock standoff distance is performed relative to the mounting surface far downstream, this adds a non-negligible contribution to the error. The uncertainty in measured Δ is calculated to be ± 0.05 mm from the error propagation analysis.

Mixture	$\Delta_{\text{M7-H8-A}}$, mm	$\Delta_{\text{M5-H6-A}}$, mm
N_2	4.79	5.18
$X_{O_2} = 0.063$	4.59	5.00
$X_{O_2} = 0.105$	4.24	4.76
$X_{O_2} = 0.137$	4.21	4.70
Air	4.14	4.56
$X_{O_2} = 0.273$	4.02	4.48

Table 4.1: Measured standoff distance for each freestream condition and mixture. An uncertainty of ±0.05 mm is used for all reported values.

Schlieren experiments are carried out for various mixtures of O_2 and N_2. To vary the composition of the test gas, a 37 L mixing tank is used. The uncertainty in the individual partial pressures of N_2 and O_2 is ±0.05 kPa. Each mixture is referenced by the oxygen mole fraction used in the driven section. The measured standoff distances can be found in Table 4.1, where air is taken as $X_{O_2} = 0.210$. For decreasing oxygen content, the standoff distance is observed to increase. This is expected, as the standoff distance scales as the ratio of the freestream density to the post-shock density. Hornung [38] proposed a scaling of the form

$$\frac{\Delta}{a} = 2.14\frac{\rho_\infty}{\bar{\rho}}\left(1 + \frac{1}{2}\frac{\rho_\infty}{\bar{\rho}}\right), \tag{4.2}$$

where a is the radius of the cylinder, and $\bar{\rho}$ is the mean post-shock density. Chemically frozen and equilibrium post-shock calculations are performed using the Shock and Detonation Toolbox for each of the mixture cases, assuming a perfect gas freestream, and are presented in Table 4.2. The chemically frozen calculation assumes translational-rotational-vibrational equilibrium in the post-shock state and results in a lower post-shock temperature than the thermally and chemically frozen case. Using the post-shock conditions in Table 4.2, the chemically frozen and equilibrium post-shock density is observed to decrease with decreasing oxygen content, thereby increasing the density ratio. To obtain an estimate of the mean density along the shock layer, the two-temperature reactive Landau-Teller model is used to compute the density profile along the stagnation streamline. Figure 4.3 plots the non-dimensional standoff distances from all schlieren experiments as a function of the computed $\frac{\rho_\infty}{\bar{\rho}}$ using the two-temperature calculation. It is observed that the non-dimensional standoff distance varies linearly as a function of density ratio, agreeing with the linear dependence of the scaling for standoff distance. Equation 4.2 is plotted alongside the data points. Agreement is observed at low density ratios, cor-

responding to the two largest X_{O_2} mixtures of M7-H8-A. However, the scaling over predicts the non-dimensional standoff distance compared to experiment. This suggests that the kinetic model used in the two-temperature Landau-Teller calculation underpredicts the amount of dissociation occurring in the shock layer.

Mixture			Frozen Chemistry			Equilibrium		
Condition	X_{O_2}	X_{N_2}	T, K	p, kPa	ρ, g/m^3	T, K	p, kPa	ρ, g/m^3
M7-H8-A	0.063	0.937	6487	49.5	25.9	5049	50.9	31.6
	0.105	0.895	6497	49.8	26.2	4822	51.4	32.7
	0.137	0.863	6506	50.0	26.4	4614	51.8	34.0
	0.210	0.790	6524	50.6	26.9	4127	52.9	37.8
	0.273	0.727	6539	51.1	27.4	3883	53.7	40.4
M5-H6-A	0.063	0.937	5145	99.1	65.5	4332	101.5	75.3
	0.105	0.895	5154	99.8	66.2	4017	103.2	81.2
	0.137	0.863	5161	100.3	66.7	3860	104.2	84.8
	0.210	0.790	5179	101.4	67.9	3674	106.0	90.5
	0.273	0.727	5192	102.4	69.0	3592	107.3	93.9

Table 4.2: Calculated post-shock conditions for varying oxygen content and freestream condition.

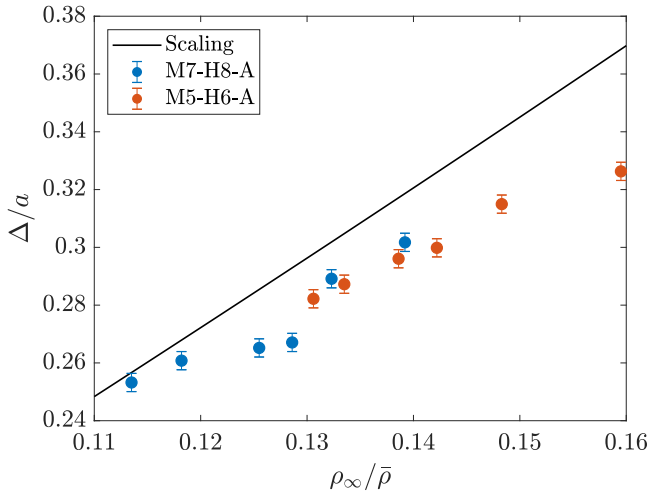

Figure 4.3: Non-dimensional standoff distance of experiment compared with scaling proposed by Hornung [38]. Mean density along the stagnation streamline is computed using a two-temperature reactive Landau-Teller model.

4.2 Radiation Along Stagnation Streamline for an Air Test Gas

Collection optics of the spectrometer are aligned such that the field of view is approximately 8 mm upstream of the cylinder surface and along the stagnation streamline shown in Fig. 4.1. For the M7-H8-A cases, the intensifier was set to a

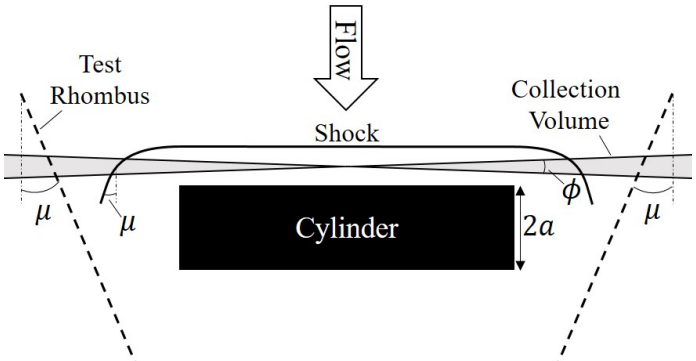

Figure 4.4: Planar view of a stagnation streamline measurement illustrating integration through three-dimensional features. Rays originating from a point source along the stagnation streamline is shown to demonstrate the collection volume of the optics.

gain of 14 and an exposure time of 90 µs. The start of exposure occurs 57 µs after the contact surface arrival. As signals dramatically decrease for the lower enthalpy condition, the camera settings for the M5-H6-A condition use a gain of 12 and an exposure time of 180 µs, with exposure starting 65 µs after the contact surface. Slit width is maintained between all experiments.

A planar view of the experiment is shown in Fig. 4.4. Away from the span, the bow shock curves and approaches the limit of a Mach wave with wave angle μ. The spectroscopy optics contain an effective collection volume that interrogates through a large portion of the shock layer and through the curvature of the shock. For rays emanating from the centerline of the cylinder geometry, the collection volume can be represented by a cone with an opening angle of $\phi = 2.9°$. Although the measurement integrates through this three-dimensional curvature of the bow shock, the gas is colder in the oblique portion of the shock, where signals are expected to drop significantly relative to the shock layer directly upstream of the cylinder surface. Therefore, effects of shock curvature are assumed to be negligible in all measurements. An additional consideration is the effective test rhombus of the facility, bounded by Mach waves emanating from the exit of the tube. The M5-H6-A condition results in the largest Mach wave angle of $\mu = 11.8$ deg. To maintain the cylinder within the test rhombus, the tube is positioned 10 mm away from the surface of the cylinder. Although the collection volume integrates through a portion of the freestream, the freestream contains a negligible amount of radiation. This is further confirmed with freestream measurements upstream of the cylinder.

Figure 4.5a shows an example detector image of radiation downstream of the bow

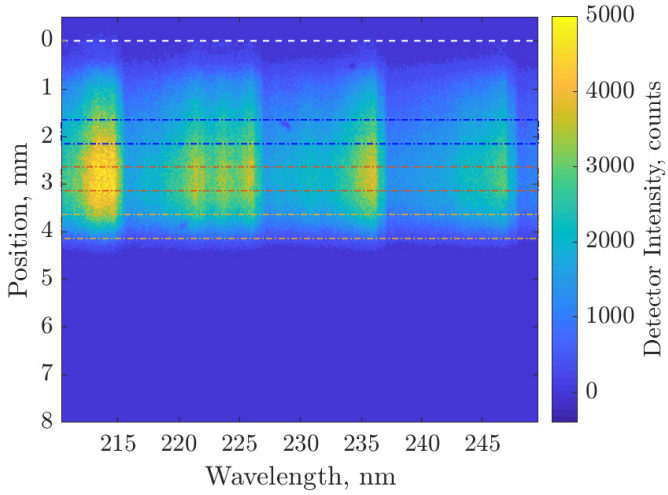

(a) Detector Image of Radiation

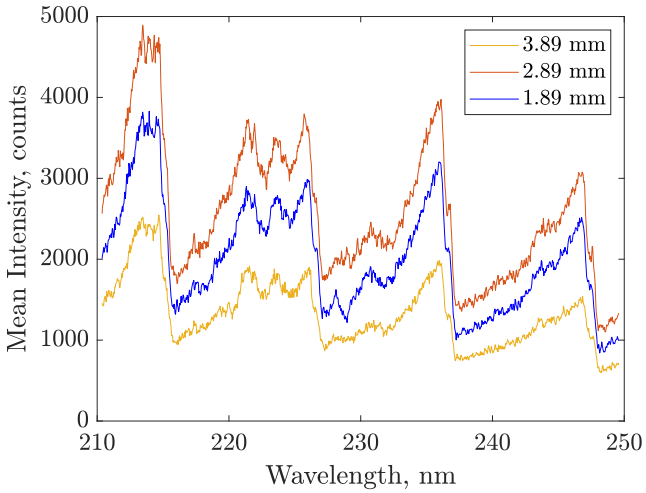

(b) Binned Spectra

Figure 4.5: Ultraviolet radiation along the stagnation streamline for a M7-H8-A freestream with air as the test gas. Figure 4.5a is a corrected detector image of the emission. The origin of the position axis is set to the cylinder surface and is indicated by a white dashed line. Three marked regions represent examples of how data binning is performed. The extracted spectra corresponding to the regions are shown in Fig. 4.5b.

shock along the stagnation streamline for the high enthalpy air condition. The image is corrected for streamwise position, wavelength, and relative intensity. Streamwise position is referenced relative to the cylinder surface. No radiation is observed upstream of the shock, as the freestream temperature is cold relative to the post shock gas. The location of the shock is indicated by the start of the NO emission. The radiation ends at the location of the cylinder surface, which is set as the origin

in the detector image. Spectra are extracted from the corrected image by binning data points along the streamwise axis. Binning is performed in 0.50 mm increments as a compromise between obtaining enough pixels to extract a clean spectrum and to limit averaging over a large portion of the flow. Three example regions for binning are shown in Fig. 4.5a and the corresponding binned spectra are plotted in Fig. 4.5b. Using the convention of (v',v"), the four dominant vibrational band transitions of γ(1,0), γ(0,0), γ(0,1), and γ(0,2) are clearly visible as strong transitions on the detector and binned spectra. Vibrational bands of γ(1,1) and γ(2,2) are also observable between 220-225 nm. The relative peaks in intensity between vibrational bands change as a function of streamwise distance, as well as the general rotational structure of the spectra. These streamwise changes in spectrum shape are directly related to changes in internal temperatures of the NO(A) species.

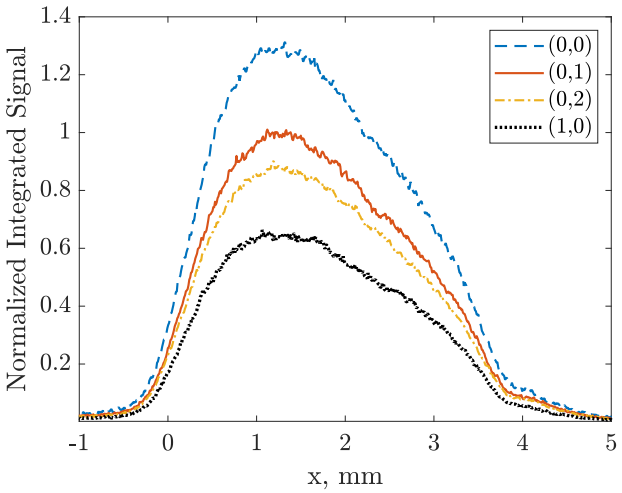

Figure 4.6: Integrated intensity behind a bow shock in a M7-H8-A air freestream. Labels represent the most dominant vibrational band in the range of wavelengths used in integration. Horizontal axis is referenced to the measured shock location. Data are normalized to the γ(0,1) peak intensity.

Vibrational band intensities can be plotted as a function of streamwise distance by integrating intensity for a given wavelength range. Figure 4.6 plots the intensity profile of several vibrational bands as a function of distance downstream of the shock. Integration is performed in four wavelength ranges: 211.65 nm - 215.80 nm, 215.80 nm - 227.24 nm, 227.24 nm - 237.20 nm, and 237.20 nm - 248.00 nm. These regions contain the major vibrational bands of the NO γ emission in the experiment. Wavelengths between 211.65 nm to 215.80 nm contain contributions from both γ(1,0) and the upper electronic transitions of NO. Wavelengths between

215.80 nm to 227.24 nm contain the dominant $\gamma(0,0)$ vibrational band, as well as contributions from the $\gamma(1,1)$ and $\gamma(2,2)$ vibrational bands. Regions of 227.24 nm - 237.20 nm and 237.20 nm - 248.00 nm are primarily dominated by the $\gamma(0,1)$ and $\gamma(0,2)$ bands, respectively. The measured standoff distance in Table 4.1 is used in plotting the integrated intensity profile as a function of downstream distance. Along a vibrational band, intensity is initially seen to increase in the downstream direction, indicating an increased production of NO(A). After the intensity reaches a peak, the emission decreases until it reaches the cylinder surface, where no radiation is measured. This behavior is shared amongst the major vibrational bands. However, peak intensities and rate of change in radiance vary between vibrational bands. As this flow field is optically thin, profiles of intensity are proportional to the number density of the NO(A) molecule formed in the flow. After transforming to the stagnation line coordinate system, some signal is typically measured upstream of the known shock location. This is due to imaging radiation with a finite span, where a point source at the far ends of the span is imaged as a spot in the slit plane shown in Fig. 2.8.

Figure 4.7a is a detector image of radiation for the M5-H6-A condition with an air freestream. Emission intensities from the lower enthalpy condition are considerably less than the M7-H8-A condition, despite twice the exposure time used in the measurement. The trends in radiation intensity are very similar to the M7-H8-A case, where intensity initially peaks, but then drops off as the gas moves downstream to the cylinder surface. Binning at 0.5 mm increments, the extracted spectra in Fig. 4.7b reveals that the more ultraviolet transitions of $\gamma(1,0)$, $\gamma(1,1)$, and $\gamma(2,2)$ are less intense compared to the $\gamma(0,1)$ band peak. This is an indicator of lower post-shock temperatures, since there are fewer high energy photons entering the detector. Due to the higher post shock density and lower temperatures, portions of the stagnating gas are not optically thin. Therefore, vibrational bands have different optical depths and can be studied by using the peak heights of the vibrational bands.

Plotting the vibrational band profiles, Fig. 4.8 shows a quicker rise in intensity for the NO γ emission close to the shock. The integrated signal of $\gamma(0,1)$ peaks approximately $x = 0.85$ mm downstream of the measured shock location. After peak NO γ radiation, the profile of all vibrational bands decrease linearly up to the surface of the cylinder. This results in a different shape of vibrational band intensity when compared to the higher enthalpy condition. The integrated intensities of the $\gamma(0,1)$ and $\gamma(0,2)$ bands are observed to have approximately the same intensity

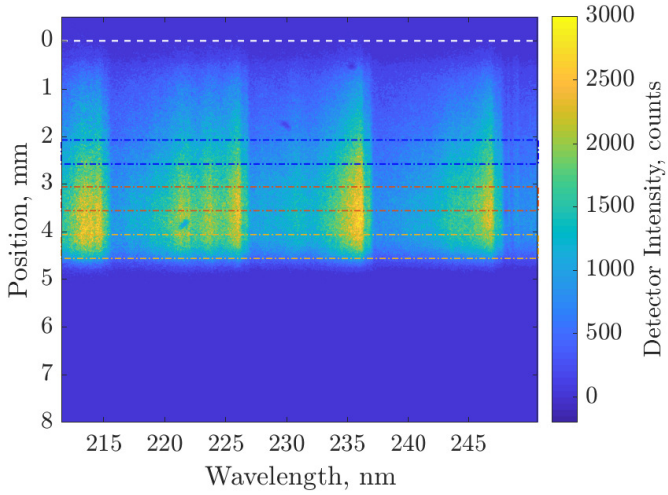

(a) Detector Image of Radiation

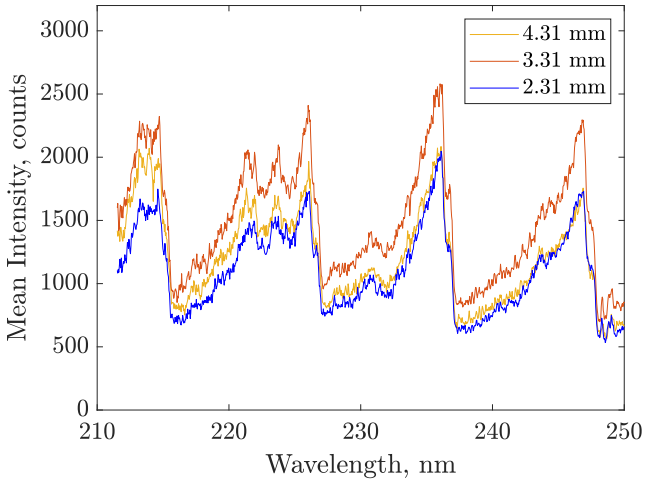

(b) Binned Spectra

Figure 4.7: Ultraviolet radiation along the stagnation streamline for a M5-H6-A freestream with air as the test gas. The origin of the position axis is set to the cylinder surface, indicated by a white dashed line.

throughout the stagnation streamline. Unlike the M7-H8-A case, self-absorption of the M5-H6-A can determine the shape of the intensity profile, as it is no longer a direct measure of the number density of NO(A) molecules.

4.3 Spectrum Fitting For NO A-X Transitions

Through the use of computed synthetic spectra, it is possible to extract quantitative information on the measured spectra to obtain a relaxation profile downstream of the bow shock. Spectrum fitting is the selected technique used for extracting

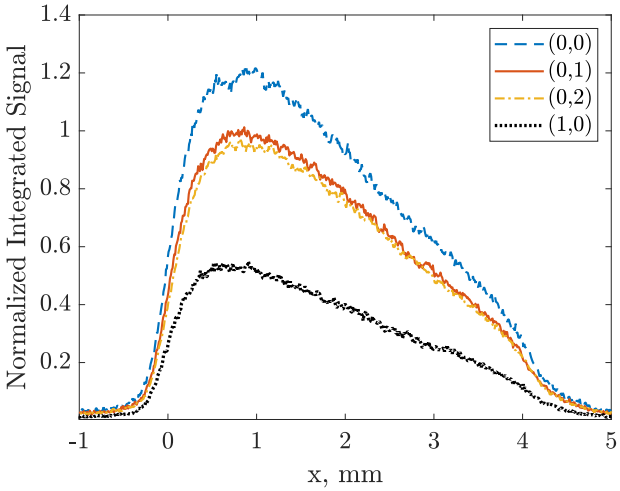

Figure 4.8: Integrated intensity behind a bow shock in a M5-H6-A air freestream. Labels represent the most dominant vibrational band in the range of wavelengths used in integration. Horizontal axis is referenced to the measured shock location. Data are normalized to the $\gamma(0,1)$ peak intensity.

temperatures from an experimental spectrum. A number of physical processes can affect the quality of the fit for a spectrum, including self-absorption, uncertainty in measured signals, and contributions of other species to the radiation. Strategies for fitting will be discussed in the context of cylinder radiation measurements of an air test gas. Techniques presented in this section will later be used for interpreting radiation of a shock-wave/boundary-layer interaction.

Least-Squares Fitting of Spectra

Define I to be the normalized spectrum measured from experiment and I_{syn} to be the normalized computed spectrum. The quality of a fit is quantified using the χ^2 parameter:

$$\chi^2 = \sum \left(\frac{1}{\sigma_I^2(\lambda)} \Big[I(\lambda) - I_{\text{syn}}(\lambda) \Big]^2 \right), \tag{4.3}$$

where σ_I^2 is the uncertainty in the intensity values from experiment. The summation is performed over the pixel range of the detector relevant for the wavelengths used in the fitting. Typically, a large χ^2 represents a poor fit between the experimental spectrum and the computed spectrum. To obtain the best representation of an experimental spectrum, it is desired to minimize the χ^2 parameter for a best estimate of the temperature.

It is possible to quantify the uncertainties in the recorded intensities values as a function of wavelength. For ICCD measurements of ultraviolet radiation, Jacobs estimates an uncertainty of $\pm(\text{counts})^{\frac{1}{2}}$ for the detector response [42]. In addition, uncertainties from the intensity calibration determine the final uncertainty of the measurement. The propagation of errors must also take into account normalization of quantities. For all comparisons using the $A-X$ system, normalization is performed using the peak value of the $\gamma(0,1)$ transition. This transition is selected due to its strong signal in the emission. The error associated with the normalized intensity values can be derived to be of the form

$$\sigma_I^2 = \left(\frac{I}{C}\right)^2 \sigma_C^2 + \frac{I^2}{S} + \left(\frac{I}{C_{(0,1)}}\right)^2 \sigma_{C_{(0,1)}}^2 + \frac{I^2}{S_{(0,1)}}. \tag{4.4}$$

Recall that C is the correction for relative intensity, σ_C^2 is the uncertainty in the intensity calibration shown in Equ. 2.1, and S is the true signal in units of counts. The first two summed terms in Equ. 4.4 are the contributions from the relative intensity calibration and detector response to the uncertainty in the measured intensity. The last two summation terms are a result of the normalization that is performed using $\gamma(0,1)$. χ^2 values are computed with this error representation. In situations where σ_I^2 is not known beforehand, the form of the variance in Equ. 2.2 can serve as a good approximation. It is found that the uncertainty in the final temperature does not change dramatically when using this assumption.

When possible, two forms of fitting error are used in the reporting of temperatures. The first form uses the curvature of the χ^2 statistic. The error for the least squares fitting of independent parameters is given in Bevington [12] as

$$\sigma_T^2 = \frac{2}{\frac{\partial^2 \chi^2}{\partial T^2}}. \tag{4.5}$$

The second derivative in the χ^2 distribution is approximated by fitting a polynomial to the χ^2 values and computing the derivatives. Equation 4.5 represents the fitting uncertainty that arises from the sensitivity of χ^2 to changes in the fitting parameter T. If two temperatures T_i and T_j are used as fitting parameters and the fitting errors are correlated, the expression for the uncertainty in temperature T_i is given as

$$\sigma_{T_i}^2 = \frac{2\frac{\partial^2\chi^2}{\partial T_j^2}}{\frac{\partial^2\chi^2}{\partial T_i^2}\cdot\frac{\partial^2\chi^2}{\partial T_j^2} - \frac{\partial^2\chi^2}{\partial T_i\partial T_j}\cdot\frac{\partial^2\chi^2}{\partial T_j\partial T_i}}. \tag{4.6}$$

If the two fitting parameters are independent, the above expression simplifies to Equ. 4.5. In the context of NO γ spectra, it is a measure of how sensitive the shape of the spectrum is to changes in rotational or vibrational temperature.

The second method for quantifying fitting uncertainty is based on the method proposed by Tibère-Inglesse et al. [92] for fitting the ultraviolet emission of a nitrogen plasma. After the best fit is obtained for a given experimental spectrum, noise is applied to the final synthetic spectrum. Random numbers from a Gaussian distribution with a standard deviation of σ_I are used as noise for the synthetic spectrum. Afterwards, the fitting algorithm is run 100 times using different seeding for the number generator. A distribution of 100 fit temperatures are generated, where the standard deviation σ_N is taken as the uncertainty. This method describes the sensitivity of the fitting algorithm to experimental noise.

An alternative metric for fitting quality is used to compare with the χ^2 statistic. The residual is defined to be the sum of differences between the spectra for the fit wavelength range, written as

$$R = \sum \left| I(\lambda) - I_{\text{syn}}(\lambda) \right|. \tag{4.7}$$

The synthetic spectrum that minimizes the residual is selected as the best fit. This fitting metric was used by Sharma et al. [87] for extracting temperatures from NO γ emission. With χ^2, pixel intensities containing lower uncertainties are weighted more in the fit compared to other pixels. However, the use of the residual allows for all pixel intensities to be weighted equally when determining the quality of the fit. Fitting with χ^2 or R often result in different final temperatures. Results from both metrics of fitting will be presented to illustrate variations in fitting technique.

M7-H8-A Condition: Two Temperature Fitting Strategies

The most dominant vibrational bands in the wavelength of interest include the $\gamma(0,0)$, $\gamma(0,1)$, and $\gamma(0,2)$ bands, which are transitions from the v'=0 state to the ground state v" levels. As a result, wavelengths between 227.50 nm - 250.00 nm are insensitive to distributions of the A-state vibrational levels and can be used to determine T_r from

fitting the spectrum. Below a wavelength of 227.50 nm, vibrational bands from upper levels become prevalent. As seen in Fig. 4.5b, wavelengths below 215 nm contain both the γ(1,0) transition and contributions of the NO δ system as indicated by an undefined peak.

Fitting the entire range of wavelengths with synthetic spectra of the NO γ system results in estimates in T_r well above the frozen temperature of 8105 K and poor fits with experimental spectra. Although NO γ is the dominant radiator, contributions of other electronic transitions such as the NO δ emission influence the background radiation and add intensity to bands below 227.50 nm, contributing to the overall shape of the spectrum. As a result, fitting the entire spectral range with NO γ produces an inflated T_r and T_v in order to compensate for the additional radiation from other electronic transitions.

To limit the effect of other electronic transitions on the fitting, an approach of fitting two separate regions is implemented. As the wavelength region containing γ(0,1) and γ(0,2) bands is a strong function of T_r, the 227.50 nm - 250.00 nm range wavelengths are selected as one fitting region. Wavelengths between 214.20 nm - 227.50 nm are used as the second fitting region. Wavelengths below 214.20 nm are ignored in the analysis, as this is primarily dominated by the NO δ(0,3) transition and will provide unwanted uncertainties in the fitting. The procedure begins with synthetic spectra computed for a matrix of T_r and T_v at 100 K increments. For each candidate synthetic spectrum, wavelengths are interpolated between experiment and simulation to match up points in the wavelength axis. Normalization is performed with respect to the γ(0,1) peak of each spectrum. For each of the two regions, a scaling factor is applied to the synthetic spectrum that reduces the goodness of fit. Two matrices of χ^2 representing each region are summed together and a surface fit is applied to the final sum. A surface polynomial with degree of three in T_r and T_v is used in fitting the contour of χ^2. The T_r and T_v pair that minimizes χ^2 is selected as the fit rotational and vibrational temperature for a given experimental spectrum. The result is a two temperature profile that describes the NO γ spectrum.

Figure 4.9 provides an example two-temperature fit of an experimental spectrum extracted 1.75 mm downstream of the bow shock. For the longer wavelength range in Fig. 4.9b, an excellent match is seen between experiment and computation. For the shorter wavelength range in Fig. 4.9a, agreement is generally good between experiment and computation. The peak intensity of the γ(2,2) is not captured by the synthetic spectrum. This is possibly a result of the NO δ system, which shares

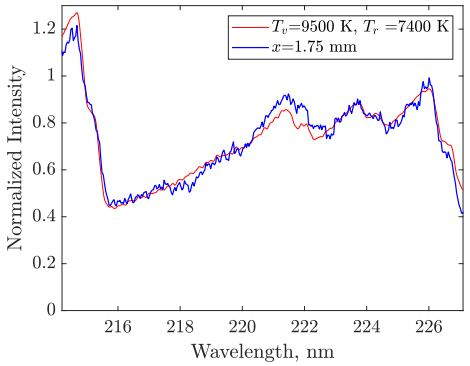

(a) Fit of γ(1,0), γ(2,2), γ(1,1), γ(0,0)

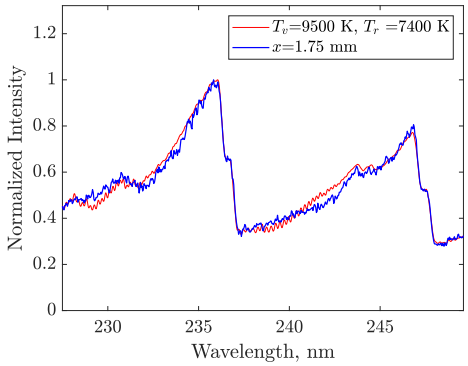

(b) Fit of γ(0,1), γ(0,2)

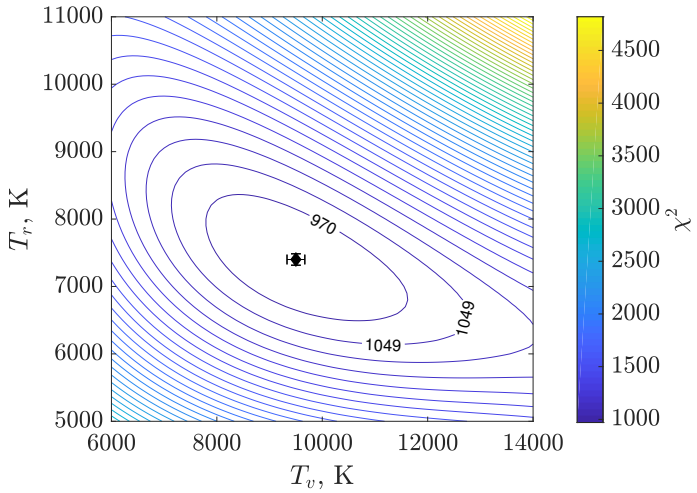

(c) Contour of χ^2

Figure 4.9: Two-temperature fit of a x = 1.75 mm experimental spectrum using NO γ synthetic spectra. Freestream condition is M7-H8-A with air as the test gas. Diamond symbol in χ^2 contour represents the minimum χ^2 value, with error bars taken from χ^2 statistics.

a transition at this wavelength. Figure 4.9c shows a surface fit of χ^2 values for the T_r and T_v matrix. The diamond symbol marks the minimum χ^2 value. At a fixed T_r, it is observed that neighboring fits with varying T_v result in very similar residual values. There is a larger uncertainty in selecting the fit T_v due to the shape of the contour plot. This is to be expected, as the only transition that contains useful information of the A-state vibrational levels is the γ(1,0) vibrational band. However, since other electronic transitions are present, only a small portion of γ(1,0) can be used, adding uncertainty in extracting T_v. Table 4.3 lists the final two-temperature fits for an experiment of M7-H8-A. It is observed that the final temperature pair depends on whether the residual or χ^2 statistic is used as a metric for fitting quality.

Typically, fits using χ^2 result in slightly higher temperatures than using the residual. The least-squares fitting reveals that vibrational temperature uncertainty is nearly double that of the rotational temperature. This further demonstrates the insensitivity of the wavelength range to vibrational temperature.

x, mm	T_v^R, K	T_r^R, K	$T_v^{\chi^2}$, K	$T_r^{\chi^2}$, K	χ^2	σ_{T_v}, K	σ_{T_r}, K
0.25	10100	6900	10200	7200	707	234	105
0.75	10500	7500	10500	7800	776	202	93
1.25	9500	7100	9900	7400	865	177	85
1.75	9300	7000	9500	7400	891	169	85
2.25	8200	6800	8400	7200	823	158	84
2.75	8700	6700	9200	6800	915	170	81
3.25	8400	6500	8700	6600	772	178	87
3.75	8400	5600	8600	5400	892	258	122

Table 4.3: Two-temperature fits of an example data set of M7-H8-A with air as the test gas. Uncertainties are based on the least-squares fit.

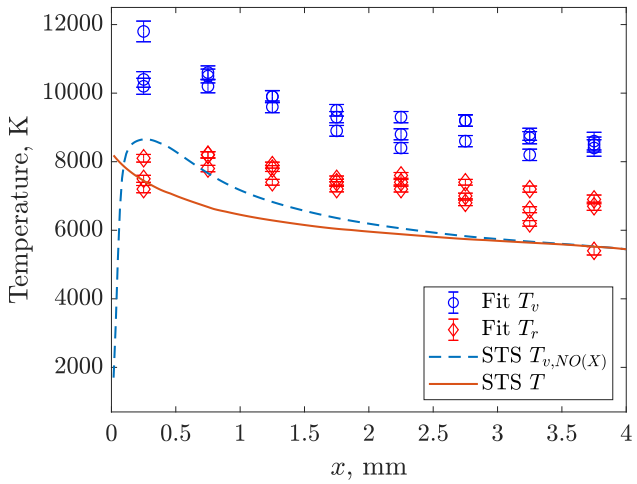

Figure 4.10: Two-temperature profile from repeat experiments of M7-H8-A compared with a state-to-state computation.

Figure 4.10 is the temperature profile of post shock air for the M7-H8-A condition. Three repeat experiments are plotted together to demonstrate shot-to-shot variation with the error bars taken from the uncertainty in the least-squares fit. Rotational temperatures at the shock are measured to be close to the thermally frozen limit of 8105 K. A slow relaxation is then observed downstream of the bow shock for T_r. The extracted T_v shows temperatures well above the frozen limit, which relaxes over downstream distance. The measured T_r and T_v do not reach equilibrium for the entire

stagnation streamline. A state-to-state calculation is shown alongside the resulting fits. Although the state-to-state computation is only structured for normal shocks and is not representative of stagnating flow, it is possible to map the calculation along the stagnation streamline. Stulov shows that a good approximation for stagnating flow is for the mass flux, ρu, to decrease linearly between the shock and the body [89]. Using this assumption, it is possible to derive the relationship between the streamwise distance x of a stagnation point flow to the post-shock distance x_s in a shock tube:

$$\frac{x}{\Delta} = 1 - \exp\left(- \frac{x_s}{\Delta} \right). \tag{4.8}$$

The exponential relationship in Equ. 4.8 describes the state of the gas as it approaches to zero velocity. This transformation allows quantitative comparisons between shock tube type calculations and stagnating flows. The state-to-state computation shows that the gas has achieved thermodynamic equilibrium at a streamwise position of x = 3 mm. In addition, the state-to-state model predicts a substantially lower vibrational temperature than what is extracted from the two temperature method. Despite taking additional measures to limit the contributions of other electronic states, estimates in T_v continue to be extremely large.

M7-H8-A Condition: Single Temperature Fitting Strategies

Attempts to perform two-temperature fitting reveal that rotational temperature contains higher sensitivity to changes in spectrum shape than vibrational temperature for the range of wavelengths of interest. Therefore, an alternate approach is used for an approximate estimate of T_r while limiting the effect of other electronic transitions influencing the fits. In the single temperature approach, fitting is performed using the vibrational bands of γ(0,1) and γ(0,2) of NO γ emission. The vibrational bands of γ(0,1) and γ(0,2) have previously been used for estimates of T_r from experimental work by Park et al. [78] and γ(0,1) in Laux et al. [53] due to the band's insensitivity to T_v. Fits of the γ(0,1) and γ(0,2) vibrational bands are performed for wavelengths between 227.50 nm - 250.00 nm using synthetic spectra computed with $T_v = T_r$. Although NO γ spectrum calculations are performed using T_v/T_r equilibrium, the wavelength range does not contain major transitions from the upper vibrational levels of NO(A). Interpretation of single temperature fits must be made with the understanding that it is a good approximation of T_r. The methodology is similar to the one used by Sharma et al. [87], where the authors used synthetic spectra

computed assuming $T_v = T_r$ and fitted with NO γ emission to obtain an effective temperature. Single temperature comparisons are performed in 20 K increments. For each candidate synthetic spectrum, wavelengths are interpolated between experiment and simulation to match up points in the wavelength axis. Normalization is performed with respect to the $\gamma(0,1)$ peak of each spectrum. At each $T_v = T_r$ increment, a scaling factor is applied to the synthetic spectrum that reduces the goodness of fit. The temperature that minimizes the residual or χ^2 is selected as the fit temperature for a given experimental spectrum.

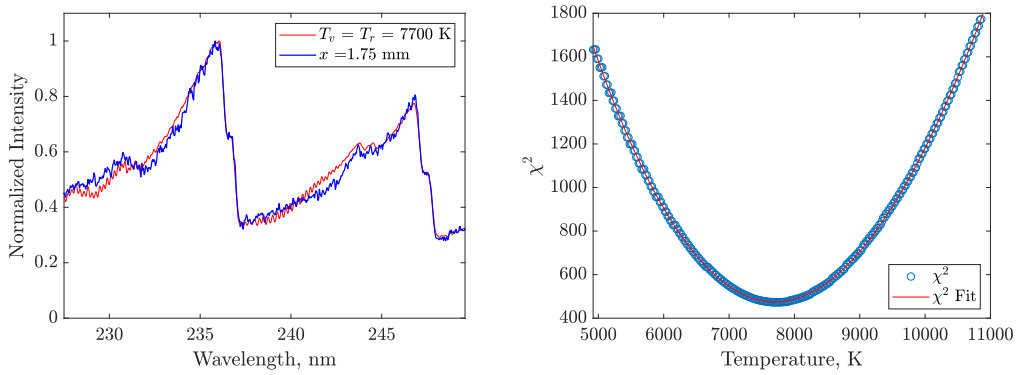

(a) Single temperature fit

(b) χ^2 distribution

Figure 4.11: Single temperature fit of M7-H8-A air radiation at a streamwise location of x=1.75 mm. χ^2 values for a range of $T_v = T_r$ values show the quality of the fits.

Figure 4.11a presents an example of an extracted experimental spectrum compared against a synthetic $T_v = T_r$ spectrum that minimized the χ^2 profile, and Fig. 4.11b plots the final χ^2 values as a function of temperature. An excellent fit is seen between the computed spectrum and experiment. Table 4.4 provides the final single temperature fits for the same experiment used in the two-temperature strategy. In addition to the least-squares description of uncertainty, the uncertainty proposed by Tibère-Inglesse et al. is also computed and labeled as σ_N. Final temperatures from χ^2 fitting again are slightly larger than using the residual. The uncertainty of the least-squares fitting is of the order of 100 K for a majority of the data set. When using the Tibère-Inglesse et al. method, uncertainties are approximately 7% of the final fit temperature.

From the resulting fits, a relaxation profile can be generated from the extracted temperatures. A plot of the final $T_v = T_r$ fits is shown in Fig. 4.12. Symbols represent repeats from three experiments and the error bars represent the uncertainty using the Tibère-Inglesse et al. method. To demonstrate shot-to-shot repeatability,

x, mm	T^R, K	T^{χ^2}, K	χ^2	σ_T, K	σ_N, K
0.25	7800	7840	359	107	603
0.75	8060	8260	482	93	603
1.25	7780	7920	580	86	550
1.75	7540	7700	472	84	566
2.25	7040	7300	440	80	521
2.75	7160	7220	557	81	510
3.25	6920	6920	434	85	529
3.75	6260	6020	627	119	593

Table 4.4: Comparison of $T_v = T_r$ fits of an example M7-H8-A cylinder data set with different fitting strategies and error analysis.

x, mm	$\bar{T}^R$, K	σ_S^R, K	$\bar{T}^{\chi^2}$, K	$\sigma_S^{\chi^2}$, K
0.25	8120	439	8227	477
0.75	8060	35	8393	122
1.25	7760	35	8040	104
1.75	7513	162	7647	205
2.25	7273	202	7513	186
2.75	7147	343	7273	304
3.25	6833	352	6920	320
3.75	6860	489	6667	560

Table 4.5: Mean $T_v = T_r$ and standard deviation σ_S from three repeat experiments of M7-H8-A with air. The residual and χ^2 definition of goodness of fit are compared.

Table 4.5 lists the mean $T_v = T_r$ from fitting and the standard deviation amongst the repeat experiments. The standard deviation in the mean temperature is largest at the shock location and locations close to the cylinder surface, corresponding to regions where detector signals are low. Immediately downstream of the shock location, the temperature reaches a value of 8120 K. This agrees with the theoretical frozen translational temperature of 8105 K, providing evidence that this is a good representation of translational-rotational temperature. A slow relaxation in $T_v = T_r$ is measured along the stagnation streamline, where the last data point never approaches the theoretical equilibrium value of 4127 K computed in Table 4.2. A state-to-state computation of M7-H8-A is mapped into stagnation line coordinates and presented in Fig. 4.12. Translational temperature and NO(X) vibrational temperature show that the gas has reached thermal equilibrium between the two temperatures at a streamwise location of $x = 3$ mm. When compared to the experimental temperature profile, the computation predicts a faster relaxation in T_r and T_v. Lower post-shock densities in the experiment could lead to the slow temperature relaxation

observed. Therefore, a combination of freestream uncertainty and uncertainty in thermochemical modeling could result in this discrepancy.

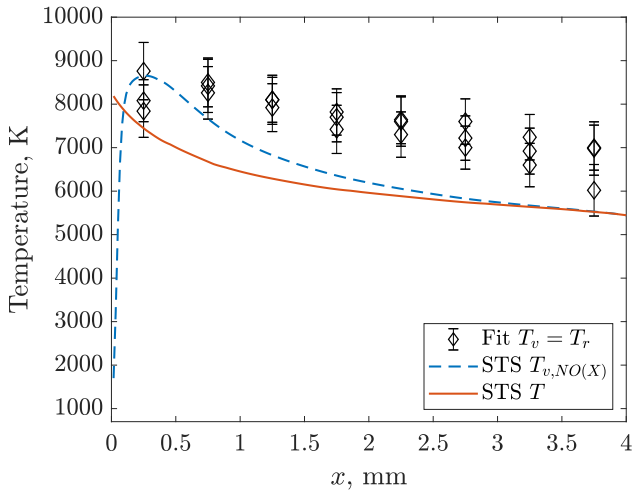

Figure 4.12: Mean temperature profile from repeat experiments of M7-H8-A air compared with a state-to-state computation.

M5-H6-A Condition: Single Temperature Fitting with Self Absorption

For conditions that are not optically thin, fitting spectra requires prior knowledge of the amount of absorption within each vibrational band. As a result, fitting an experimental spectrum that is not optically thin requires additional treatment to reduce uncertainty from fitting. Immediately behind the shock, translational temperatures are at the frozen limit and the number density of NO(X) is low due to the frozen chemistry. As a result, it is possible to approximate the region immediately behind the shock as optically thin. The methodology used in the M7-H8-A cases can be readily applied in the first 1 mm downstream of the shock. However, as the production of NO increases, self absorption becomes more significant.

Cases where $\tau >> 1$ can still be fitted using an optically thin calculation if the ratio of intensity between optically thin case and the full radiation transport case is the same between two or more vibrational bands. Along the span of the cylinder, the absorption and emission coefficients are assumed to be constant at a fixed streamwise coordinate.

As an example calculation, *Ri* factors are computed for the Q1 branch, N" = 33 level for the major vibrational bands in the NO γ system. Absorption coefficients are obtained from using values presented by Luque and Crosley [60]. In Fig. 4.13a, it can be observed that the bands that satisfies Equ. 3.46 throughout the entire shock

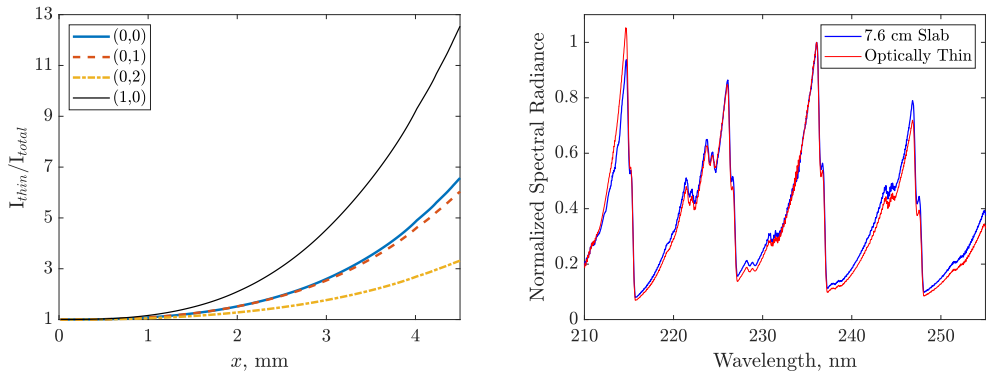

(a) *Ri* values for the major vibrational bands (b) Specair calculation

Figure 4.13: Effects of optical depth for stagnation flow of M5-H6-A, air. Specair 3.0 is used for computing spectra for a finite slab of gas and an optically thin case.

layer are the $\gamma(0,0)$ and $\gamma(0,1)$ bands. For confirmation, a calculation of the NO γ radiance is performed using Specair 3.0 for an optically thin and optically thick case. Figure 4.13b is a Specair radiance calculation using gas temperatures and number densities from a state-to-state calculation of M5-H6-A at x = 3 mm. A slab length of 7.6 cm is selected to represent the span of the cylinder and is compared against the optically thin calculation. It is easily observed that after normalization, the $\gamma(0,0)$ and $\gamma(0,1)$ bands preserve their shape, while the other bands are heavily influenced by absorption. The use of *Ri* provides a simple method of selecting wavelength ranges for spectrum fitting in situations where computing the full radiation transport is not possible.

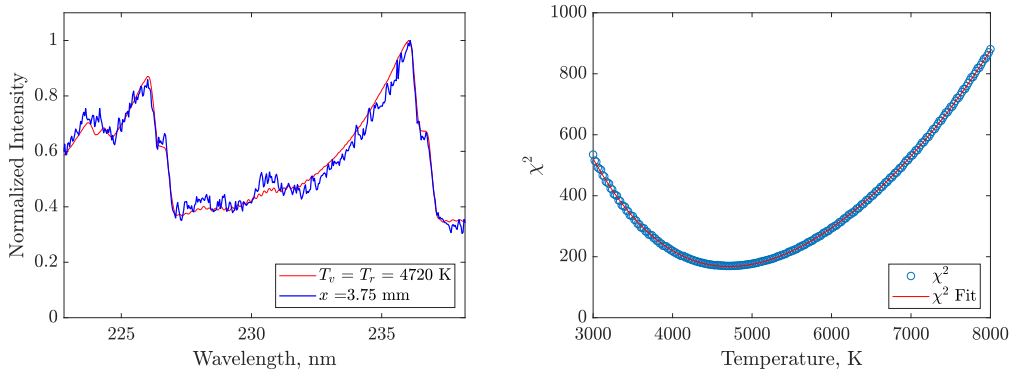

(a) Single temperature fit (b) χ^2 distribution

Figure 4.14: Single temperature fit of M5-H6-A air radiation at a streamwise location of x = 3.75 mm. χ^2 values for various $T_v = T_r$ are presented in 4.14b.

From the analysis, temperature fitting is performed in the wavelength range of

x, mm	T^R, K	T^{χ^2}, K	χ^2	σ_T, K	σ_N, K
0.25	5540	5720	304	102	723
0.75	5180	5480	289	90	603
1.25	5400	5740	253	96	667
1.75	5060	5440	260	93	670
2.25	4600	4900	346	84	513
2.75	4860	5020	235	89	636
3.25	5300	5540	225	111	720
3.75	4600	4720	170	104	597

Table 4.6: Single temperature fits of an example M5-H6-A cylinder data set with air as a test gas. Strategies for fitting with self-absorption present in experiment are implemented.

x, mm	$\bar{T}^R$, K	σ_S^R, K	$\bar{T}^{\chi^2}$, K	$\sigma_S^{\chi^2}$, K
0.25	5440	28	5580	198
0.75	5310	42	5470	14
1.25	5400	170	5570	240
1.75	5400	28	5430	14
2.25	4850	14	4940	57
2.75	4800	28	5050	42
3.25	4990	71	5340	283
3.75	4540	198	4810	127

Table 4.7: Mean $T_v = T_r$ and standard deviation σ_S from two repeat experiments of M5-H6-A with air. The residual and χ^2 definition of goodness of fit are compared.

222.80 nm to 238.20 nm to maximize the amount of the experimental spectrum to fit while avoiding regions affected by self absorption. Only synthetic spectra computed for $T_v = T_r$ are used, as there are not enough transitions to be used for an accurate estimate of T_v. The procedure of single temperature fits is identical to the method used in the M7-H8-A, with the wavelength range now shifted and shortened. Figure 4.14a shows an example fit of an experimental spectrum with a synthetic spectrum that minimized χ^2. Figure 4.14b plots the final χ^2 values from $T_v = T_r$ fits. Excellent agreement is observed between experiment and the synthetic spectrum. Table 4.6 displays the resulting single temperature fits for an example data set. Once again, fits using χ^2 result in higher temperatures than the residual method.

Figure 4.15 shows the temperature relaxation behind a bow shock for M5-H6-A condition with air as a test gas. Error bars of the two repeat experiments represent the fitting uncertainty from experimental noise using the Tibère-Inglesse et al.

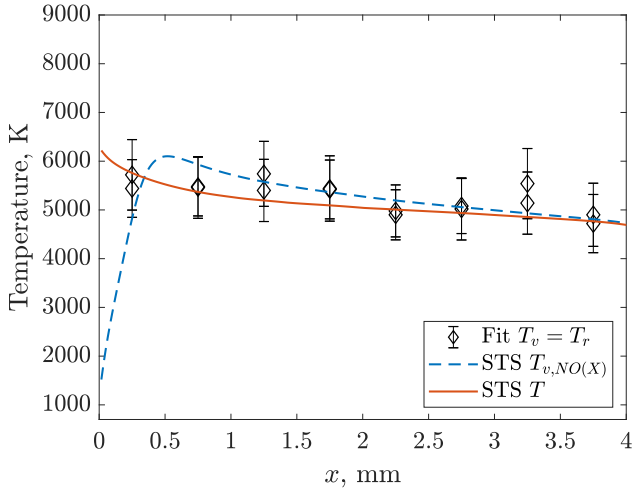

Figure 4.15: Temperature profile from repeat experiments of M5-H6-A air compared with a state-to-state computation.

method. Statistics of the shot-to-shot repeatability is shown in Table 4.7. State-to-state calculations of bulk translational temperature and vibrational temperature of NO are also plotted. For the first 1 mm, excitation temperature fits show that the gas approaches the frozen temperature. This is confirmed with the state-to-state calculation, which shows that the vibrational and rotational/translational temperature are within 500 K of one another. After 1 mm, the computation shows that the gas is in thermal equilibrium. Extracted temperatures agree with the mean T_v and T_r profile of the state-to-state calculation, providing evidence that the single temperature fitting procedure can be used to gauge the relaxation of the gas in cases where radiation is not optically thin.

4.4 Radiation Measurements of Oxygen/Nitrogen Mixtures

Emission measurements varying the mole fraction O_2 and N_2 are performed at the same wavelength range as the air cases, with the exception of nitrogen tests. Exposure time, intensifier gain, slit width, and shutter delay are maintained between tests to observe changes in intensity.

Silicon and Air Contamination

An experiment was performed using N_2 as a test gas for the M7-H8-A condition at the same camera settings used for all other tests. Under perfect experimental conditions, NO is not formed in the flow due to the complete lack of oxygen. Figure 4.16 displays the resulting detector images of an experiment with nitrogen as a

test gas. Radiation is measured in the experiment, with lines identified as the Si I electronic transitions. Similar to the radiation of the iron hollow cathode lamp, atomic radiation is formed as discrete lines in the spectrum. In the case of silicon, strong signals are observed in the lines, with intensities approaching as high as 7000 counts on the detector. A likely source of the silicon contamination is the vacuum grease used for preparing the o-rings for a vacuum seal. The sealant used for the facility is Dow Corning high vacuum grease, which is a silicone based lubricant.

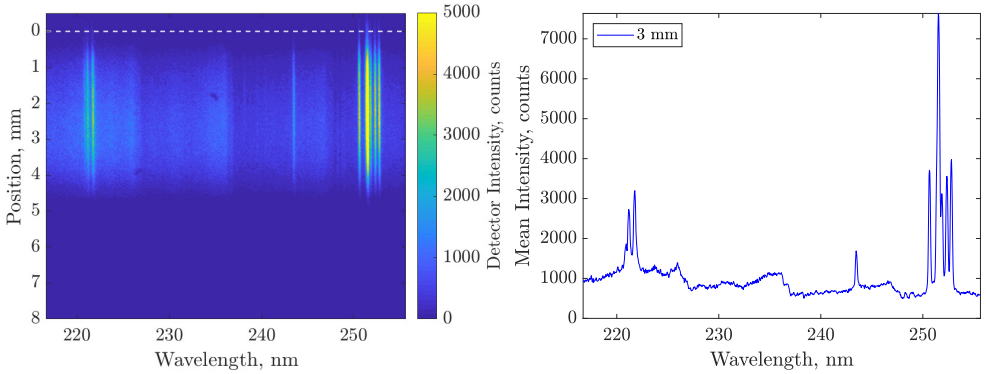

(a) Detector Image of Contaminants

(b) Extracted Spectrum

Figure 4.16: Detector image of silicon atomic lines and residual NO γ radiation for a N_2 test gas experiment of M7-H8-A. White dashed line indicates surface of cylinder.

In addition, some residual NO γ signal is observable on the detector. The maximum signal of the $\gamma(0,1)$ is measured to be 1144 counts. This is likely due to a combination of leaking in the driven section and air remaining from the flushing procedure. Figure 4.17 plots the integrated radiance for the entire wavelength range of the experiment. Primarily consisting of Si I transitions, the radiation profile is measured to peak approximately 2 mm downstream of the location of the shock.

Radiation of Oxygen/Nitrogen Mixtures

Figure 4.18a shows emission spectra extracted at the $x = 0.75$ mm streamwise location for four test gas mixtures in the M7-H8-A freestream. Normalization is performed using the $\gamma(0,1)$ peak of air. Overall detector intensity is observed to increase from the $X_{O_2} = 0.273$ case to the $X_{O_2} = 0.105$ case. The change in detector intensity is due to the reduced quenching of the excited states by other species such as O_2. As the oxygen mole fraction is reduced further, detector intensity drops, as seen in the $X_{O_2} = 0.063$ mixture. In this limiting case, there is not enough oxygen

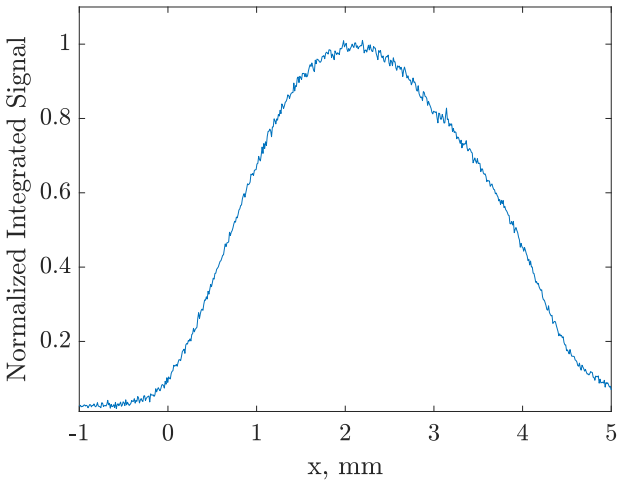

Figure 4.17: Integrated intensity of detector image of silicon radiation. Standoff distance for N_2 is taken from Table 4.1.

present to produce NO molecules in both the X and A states, effectively reducing the amount of radiation for the extremely low oxygen cases.

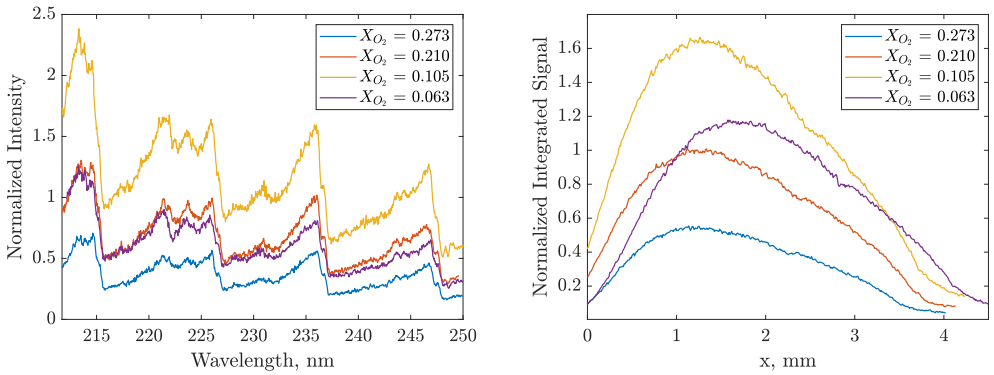

(a) Spectra at x = 0.75 mm

(b) Integrated Signal of $\gamma(0,1)$

Figure 4.18: Post-shock radiation of M7-H8-A for various mixtures. Figure 4.18a are spectra extracted at x = 0.75 mm downstream of the shock. Figure 4.18b are integrated signal profiles for the $\gamma(0,1)$ vibrational band. Normalization is performed using the peak value of the $\gamma(0,1)$ vibrational band for air in both plots.

In addition to changes in radiance, the vibrational band profiles change dramatically. Figure 4.18b contains the integrated radiance profile of the $\gamma(0,1)$ vibrational band for each test gas mixture for the M7-H8-A condition. As oxygen mole fraction is reduced, the peak of vibrational band intensity pushes downstream. This is related to the reduced rate of chemical reactions occurring, as nitrogen dissociation rates are typically slower than that of oxygen. Similar to Fig. 4.18a, intensities are also

observed to increase from the $X_{O_2} = 0.273$ case to the $X_{O_2} = 0.105$ case. The mole fraction of $X_{O_2} = 0.063$ experiences a decrease in radiance, confirming observations in Fig 4.18a. As integration was performed for only the $\gamma(0,1)$ vibrational band of an optically thin gas, the intensity profiles represent the number density of NO(A) along the shock layer. Identical trends in overall detector intensity and vibrational band profiles were observed in the M5-H6-A data set. It is to be noted that optical depth is affected as oxygen is removed. The equilibrium number density of NO species for $X_{O_2} = 0.063$ is computed to be $N_{\mathrm{NO}} = 2.18 \times 10^{16}$ cm^{-3}, an order of magnitude lower than $N_{\mathrm{NO}} = 1.04 \times 10^{17}$ cm^{-3} for $X_{O_2} = 0.210$ of M5-H6-A. Therefore, post-shock gas of M5-H6-A approaches the optically thin limit as oxygen is removed.

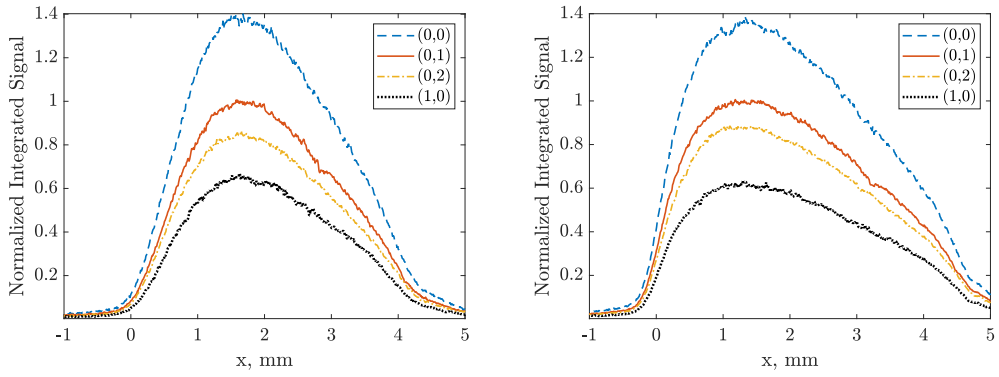

(a) M7-H8-A (b) M5-H6-A

Figure 4.19: Integrated intensity profile of the dominant vibrational bands for X_{O_2}= 0.063 freestream mixtures.

The integrated radiance of other vibrational bands can be plotted for the lowest oxygen mole fraction to study variations of the population of electronically excited NO. Figure 4.19 shows extracted profiles of X_{O_2}= 0.063 for both freestream conditions. The most notable difference between air and X_{O_2}= 0.063 is the increase in radiance for the $\gamma(0,0)$ band compared to the $\gamma(0,1)$ peak intensity. For M5-H6-A, dramatic changes in profiles are observed, where peak radiance now occurs at x = 1.25 mm and $\gamma(0,2)$ no longer shares the intensity levels as $\gamma(0,1)$. The shifts in peak intensities between the wavelength regions are also caused by the contributions of additional electronic transitions for low oxygen cases.

4.5 Spectrum Fitting For A-X, B-X, and C-X Systems

Attempts to use the NO γ synthetic spectra for fitting low oxygen experiments resulted in extremely large temperatures and poor matches with experiment. Not

only is oxygen responsible for quenching NO(A), but it also quenches the other electronic states of the NO molecule. Reducing oxygen in the freestream increases the radiance from the upper electronic levels of the spectra. This is evidenced by comparing the $X_{O_2} = 0.210$ and $X_{O_2} = 0.063$ spectra for the same streamwise position in Fig. 4.18a. The γ(0,1) and γ(0,2) vibrational band intensities have different peak intensities between the air and the $X_{O_2} = 0.063$ case. However, relative intensities are approximately identical at wavelengths below 225 nm for both mixtures. Below a wavelength of 215 nm, $X_{O_2} = 0.063$ no longer has the γ(1,0) band of the NO as the dominant transition. Instead, the NO δ(0,3) transition becomes identifiable. As a result, it is not possible to extract a T_v and T_r using only NO γ synthetic spectra.

To accurately match the experiment, the addition of electronic excitation temperature, T_{ex}, is necessary to describe the distribution of the upper electronic states of NO. Specair version 3.0 is used to compute the convolved radiation of NO γ, β, and δ of the NO molecule, with T_{ex} used to describe the Boltzmann distribution of the excited states. Features of the NO β transitions cannot be identified in the experimental spectra. However, the addition of NO β allows for an approximate representation of background radiance within Specair. Typically, residuals were found to be smaller for fits including the NO β system. The NO δ system produces additional transitions below 215 nm. It is also possible to include the NO ϵ system, which contributes radiance below 215 nm. In an arcjet study by Hyun, Park and Chang, contributions of the upper electronic states of NO were investigated [40]. It was found that the NO ϵ total band intensity was weaker than those of the NO δ and γ band systems. In addition, it was shown that NO(A) is likely in quasisteady state with NO(C) and can be described by an electronic excitation temperature. As a result, the ϵ band is neglected in this analysis.

Fitting with synthetic spectra of NO γ, β, and δ is performed using Specair's internal fitting routine. The root-finding algorithm implemented is Brent's method for minimizing the residual, defined as the root-mean square of the difference between the experimental spectrum and the synthetic spectrum. Normalization is performed with the peak intensity of the spectra. The software is limited to iterating one temperature at a time and cannot fit an entire parameter space of T pairs. To alleviate the challenge of fitting a large parameter space of (T_{ex}, T_v, T_r), an approach of fitting extracted spectra for $x = 0.25$ mm is made, with the assumption that T_r is the thermally frozen temperature for a given freestream condition. An initial guess

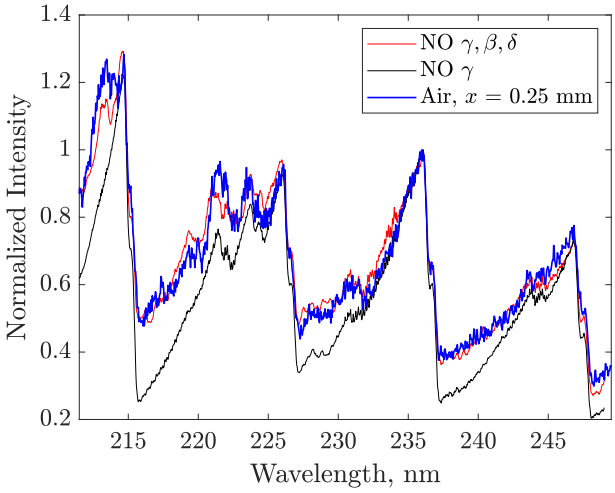

(a) Specair Calculation and Experiment

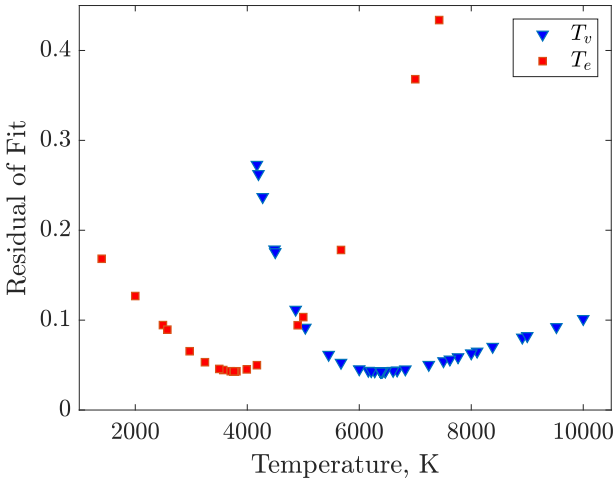

(b) Specair Residuals

Figure 4.20: Specair fit of a M7-H8-A experimental spectrum at $x = 0.25$ mm. A solution of $T_{ex} = 3757$ K and $T_v = 6388$ K is obtained from fitting the NO γ β δ convolved transitions, assuming $T_r = 8105$ K. A NO γ spectrum calculated at the same temperatures is shown for comparison. Residuals in Fig. 4.20b are extracted by fixing the final T_{ex} or T_v and looping through the free temperature.

of $T_{ex} = T_v = T_r$ is made, with an initial step size of 30% and an accuracy of 0.01% made to the algorithm. Six iterations between T_{ex} and T_v are made to allow for a convergent solution. For the T_{ex}, T_v pair that minimized the residual, two plots of residual versus T_{ex} and T_v are generated by fixing one temperature and cycling the free temperature parameter. Uncertainties are not reported within the Specair software and must be inferred using Specair's definition of residual. To convert Specair's residual to a χ^2, the uncertainty in the signal intensity σ_I is assumed to

be constant throughout the wavelength range. The conversion to χ^2 is given by

$$\chi^2 = \frac{N}{\sigma_I^2}\left(R_{\text{Specair}}\right)^2, \tag{4.9}$$

where N is the number of pixels used in the fitting and R_{Specair} is Specair's definition of residual. The value of σ_I^2 is taken to be the mean value throughout the wavelength range involved in the fit. Attempts to perform noise uncertainty analysis resulted in non-convergent solutions within Specair's fitting algorithm. As a result, fitting uncertainty from the method of Tibère-Inglesse et al. will not be reported and only σ_{χ^2} will be shown.

The procedure is applied to the first extracted spectrum of the air case of M7-H8-A condition. Figure 4.20 shows a comparison of a $x = 0.25$ mm experimental spectrum and Specair fits of T_{ex} and T_v that minimized the residual. An experimental spectrum can now be compared along side a synthetic spectrum for the entire wavelength range. For air as the test gas, the optimal solution is $T_{ex} = 3757$ K and $T_v = 6388$ K. Table 4.8 lists the resulting statistics from the fit. A larger uncertainty is found in T_v, suggesting that the shape of the spectra is a stronger function of T_{ex}. In the literature, $T_{ex} = T_{v,bulk}$ and $T_{ex} = T_{tr}$ have been typical assumptions in describing the distribution of electronic states [18, 26]. However, the final Specair fit for air reveals that the optimum solution is for $T_{ex} \neq T_v$ for an experimental spectrum immediately behind the shock. As the number density of NO(X) is not measured and absolute radiance is not obtained, it is unknown how well T_{ex} describes the relationship between NO(X) and its upper electronic states. In terms of describing the relationship between NO A, B, and C, the best solution is to assume all three temperatures are in non-equilibrium with one another.

R_{Specair}	χ^2	$\bar{\sigma_I}$	σ_{T_v}, K	$\sigma_{T_{ex}}$, K
0.043	911	0.045	46	27

Table 4.8: Fitting parameters of a Specair T_{ex} and T_v fit of a M7-H8-A experimental spectrum at $x = 0.25$ mm. An assumed value of $T_r = 8105$ K is used in computing synthetic spectra.

Performing fits with independent T_{ex} and T_v for reduced oxygen experiments results in a non-convergent solution using Specair's internal fitting routine. As a matrix of T_{ex} and T_v, calculations for fitting cannot be made through the user interface of Specair 3.0, fitting with T_{ex} and T_v pairs will be investigated as part of future work. To arrive at a compromise, an assumption of $T_{ex} = T_v$ is made in computing spectra

for investigating the low oxygen cases. This prevents iterations from either diverging or arriving at a local minimum in the residual plane. Although the assumption of $T_{ex} = T_v$ is made, it is emphasized that spectra computed using this assumption may not best represent experimental results. As discussed in the M7-H8-A fits with air, an inflated T_v is typically found when attempting fits using only the NO γ system. Depending on the initial T_v, estimates in T_{ex} may also be affected.

Figure 4.21 shows experimental spectra extracted at x = 0.25 mm along with synthetic spectra of the NO γ β and δ bands assuming T_r = 8105 K and optimizing $T_{ex} = T_v$. The corresponding statistics are shown in Table 4.9. The procedure is identical to the Specair fit in Fig. 4.20, with the exception that the algorithm is run without alternating between T_{ex} and T_v. A synthetic spectrum can represent the entire wavelength range of the experimental spectrum, a feature that could not be achieved using NO γ alone. As oxygen mole fraction is decreased, the effective $T_{ex} = T_v$ fits increase, indicating the increased population of upper electronic states of NO. This provides evidence that experimental spectra for low oxygen cases can be better represented by including other electronic transitions of NO.

X_{O_2}	$T_{ex} = T_v$, K	R_{Specair}	χ^2	$\bar{\sigma}_I$	σ_T, K
0.063	5699	0.498	8.639×10^4	0.053	10
0.105	5620	0.834	3.624×10^5	0.044	3
0.137	5542	0.112	5.508×10^3	0.047	13
0.210	4951	0.124	7.548×10^3	0.045	8

Table 4.9: Results of a Specair $T_{ex} = T_v$ fit for M7-H8-A mixtures. Fits are performed with experimental spectra at x = 0.25 mm and an assumed T_r=8105 K.

4.6 Two-Temperature Calculation of Integrated Intensity for Mixtures

It is possible to compare computed number densities of NO(A) with measured profiles of integrated radiance along the stagnation streamline. Reaction zone calculations are performed using the reactive Landau-Teller relaxation model with a two-temperature model of chemical reaction rates. This will assess the predictive capability of the model using the selected kinetic rates and the model for thermal non-equilibrium. With the addition of the high density case of M5-H6-A, it is also possible to understand the effects of self-absorption along the profile of integrated intensity.

To study the effect of oxygen quenching, post shock conditions are computed for M7-H8-A with varying oxygen mole fractions in the freestream. Figure 4.22 shows

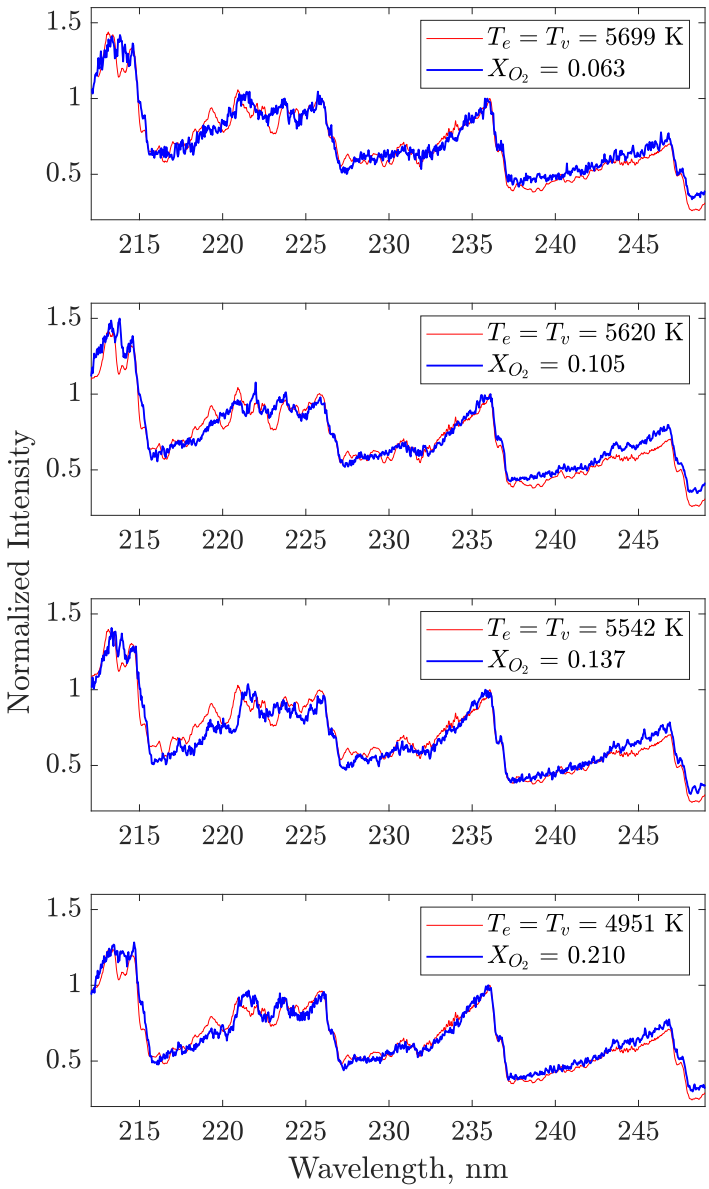

Figure 4.21: Specair fits of M7-H8-A experimental spectra at $x = 0.25$ mm with the NO γ, β, and δ transitions. Synthetic spectra are computed assuming $T_{ex} = T_v$ and T_r=8105 K.

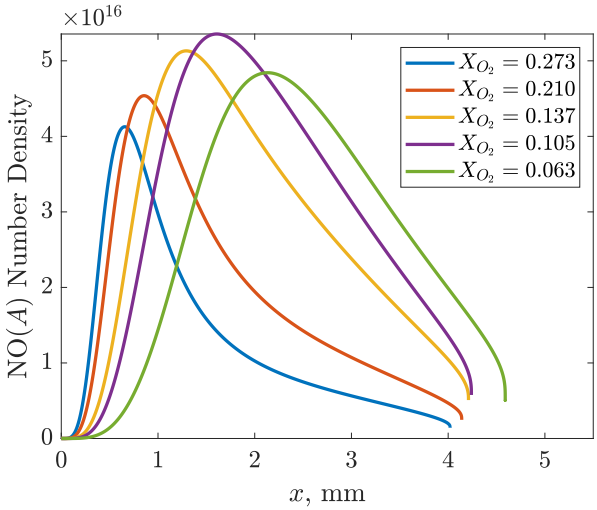

Figure 4.22: Calculated number density profiles of NO(A) for varying oxygen mole fraction of a M7-H8-A freestream. Standoff distances are taken from Table 4.1.

profiles of NO(A) number density for the M7-H8-A freestream along the stagnation streamline. The normal shock calculation is mapped into stagnation streamline coordinates, where Table 4.1 is used for the standoff distance. Recall that number density is directly proportional to spectral radiance for optically thin gases. Therefore, number density of NO(A) is an indicator for the amount of radiance expected in an optically thin gas. As mole fraction decreases from $X_{O_2} = 0.273$ to $X_{O_2} = 0.105$, the number density of NO(A) increases. The increase in NO(A) is primarily caused by the reduced quenching of oxygen. The calculation agrees with the trend observed in the experiment in Fig. 4.18b, where signals initially increase for decreasing oxygen mole fractions. When reducing the oxygen mole fraction further, the calculation predicts a drop in NO(A) number density for the case of $X_{O_2} = 0.063$. In this situation, the amount of oxygen is too low to form NO in both the ground and the electronically excited states. As a result, the reduced quenching of oxygen cannot compete with the reduced formation of NO, resulting in a drop in NO(A). This prediction also agrees with the observations from experiment, where the case of $X_{O_2} = 0.063$ resulted in a drop in signal from the $X_{O_2} = 0.105$ case. Overall, the reaction zone calculation accurately predicts the effects of oxygen quenching for electronically excited states.

It is possible to directly compare the measured signal of the experiment to the predicted number density of NO(A). Figure 4.23 contains integrated intensities of $\gamma(0, 1)$ from four mixture experiments of M7-H8-A compared with simulation. The black curves are the integrated radiance in the 227.24 nm - 237.20 nm range

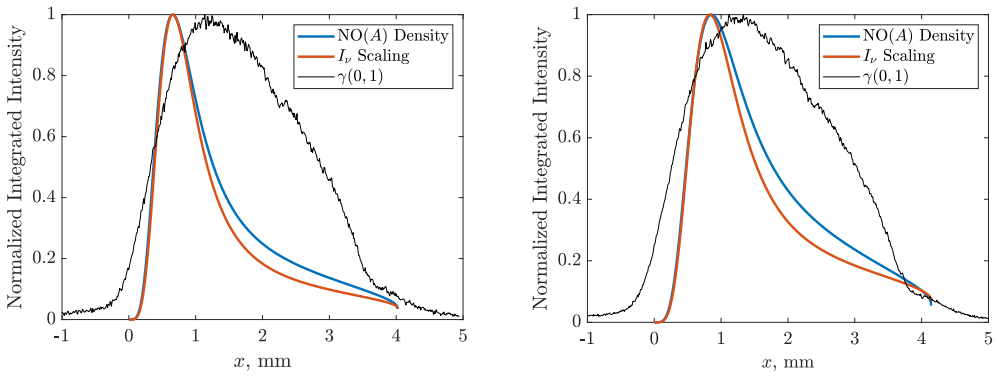

(a) $X_{O_2} = 0.273$ (b) $X_{O_2} = 0.210$

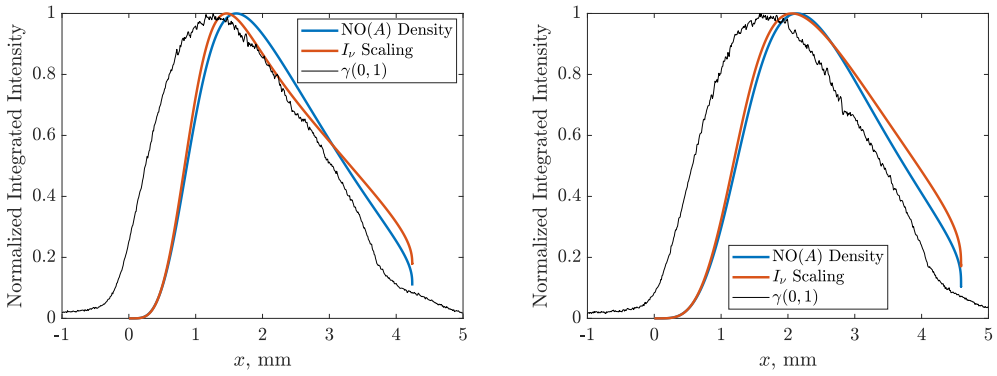

(c) $X_{O_2} = 0.105$ (d) $X_{O_2} = 0.063$

Figure 4.23: Integrated intensity profiles of $\gamma(0,1)$ from the M7-H8-A condition compared with a two-temperature reactive Landau-Teller calculation of number density and intensity scaling. Normalization is performed using the peak value of each profile.

of wavelengths, while the blue curves are the calculated number density of NO(A) normalized with respect to the maximum value. The red curve is the proposed scaling for spectral radiance shown in Equ. 3.43, where the assumption of $N_{\mathrm{NO}(A)} << N_{\mathrm{NO}(X)}$ is made. The scaling for I_ν takes into account the effects of self absorption in the profile. In all calculations of M7-H8-A, the number density profile of NO(A) and the scaling for I_ν is approximately the same, demonstrating that this flow field can be approximated as optically thin. Signal is present upstream of the measured stand-off distance, while the calculations start at $x = 0$. Recall that the finite collection volume of the optics causes the slab of gas to be imaged with span effects present as described by the spot diagram in Fig. 2.8. As a result, measured signal is expected to occur at most 1 mm upstream of the shock location. Span effects also play a role in signal close to the cylinder surface, where not all rays reach the collection optics and are clipped against the cylinder surface. Measured signals

are expected to drop close to the surface of the test article. The comparisons of the M7-H8-A condition generally show poor agreement for the $X_{O_2} = 0.273$ and $X_{O_2} = 0.210$ (air) test gas mole fractions. The two-temperature reactive Landau-Teller calculation predicts a peak in NO(A) number density closer to the shock location, with a sudden drop in NO(A) production up to the body. In contrast, the experiment peaks at approximately 1.25 mm downstream of the shock with radiance still present throughout the shock layer. When oxygen is reduced further, better agreement occurs between experiment and the calculation for the $X_{O_2} = 0.105$ and $X_{O_2} = 0.063$ cases. The increasing gradient at the shock location agrees well between experiment and simulation, while the location of peak intensity also improves. Unlike the higher oxygen cases, the simulation accurately predicts the profile of NO(A) downstream the peak intensity. These results indicate that the kinetic rates and the relaxation model allows for a higher de-excitation rate of electronic states than what is measured in the experiment. Possible causes for this disagreement at higher oxygen content include a faster relaxation in translational-rotational temperature in the calculation or that the kinetic rates associated with quenching are inappropriate for this flow condition.

Comparisons of two-temperature reactive Landau-Teller calculations with M5-H6-A data are shown in Fig. 4.24 for various mixtures. For the $X_{O_2} = 0.273$ and $X_{O_2} = 0.210$ cases, self-absorption is expected to heavily affect the intensity profile measured by the spectrometer. It is observed that the scaling for intensity pushes the peak radiance upstream compared to the optically thin case, resulting in better agreement with the experiment. Downstream of the peak, the experimental profiles of $X_{O_2} = 0.273$ and $X_{O_2} = 0.210$ are bounded by the optically thin profile and the I_ν profile. It is possible that absorption from NO(X) is overpredicted in the calculation. For the reduced oxygen cases, poor agreement is observed for both computed profiles. Although the scaling of I_ν provides a slight improvement in the peak location and the intensity profile compared to the optically thin case, the production in NO(A) is heavily delayed compared to experiment. The delay in NO(A) is most notable in the calculation of $X_{O_2} = 0.063$, where the number density and I_ν remains below 20% of the peak value at a streamwise location of $x = 1$ mm. This suggests that the computed population NO(X) is underpredicted, as the production of NO(X) also determines the production of NO(A). The kinetic rates used in the model may need to be reevaluated for the low Mach number conditions, as the production of NO(A) is extremely low. For all comparisons with measured integrated radiance, ray tracing may also provide better comparisons with

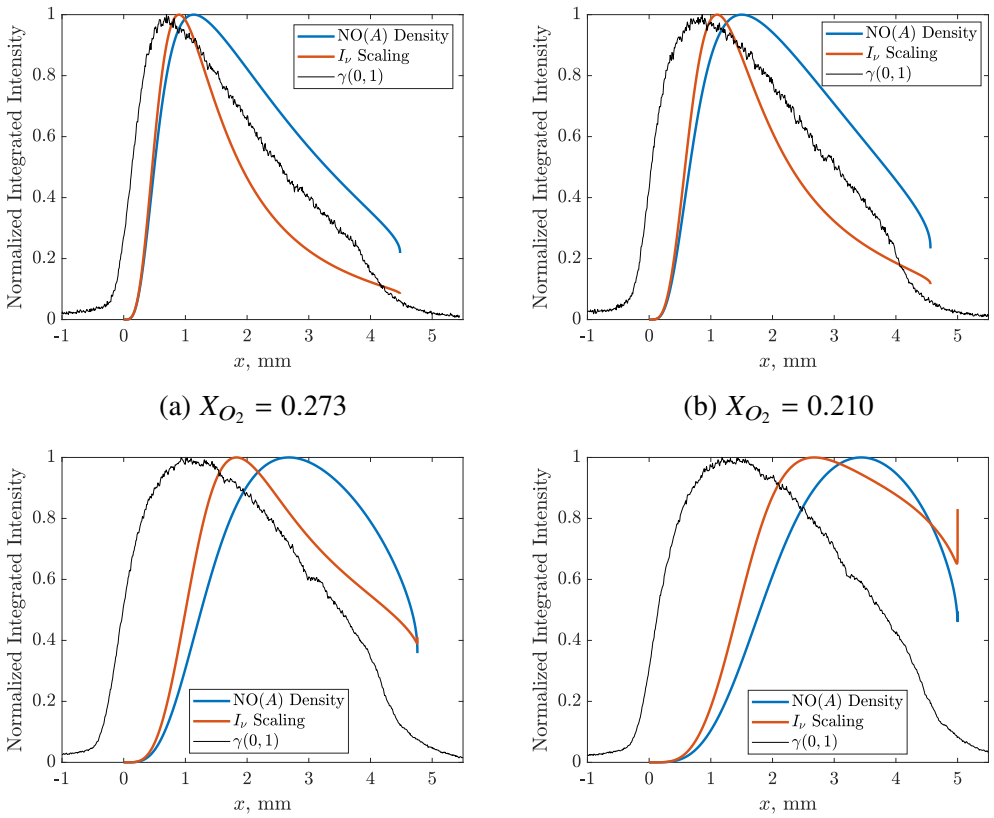

(a) $X_{O_2} = 0.273$ (b) $X_{O_2} = 0.210$

(c) $X_{O_2} = 0.105$ (d) $X_{O_2} = 0.063$

Figure 4.24: Integrated intensity profiles of $\gamma(0,1)$ from the M5-H6-A condition compared with a two-temperature reactive Landau-Teller calculation of number density and intensity scaling. Normalization is performed using the peak value of each profile.

experiment, as the measured radiance can either be mapped along the stagnation streamline or computations can be transformed to the image plane of the collection optics.

4.7 Concluding Remarks

The case study of stagnation flow allows for a better understanding of the capabilities of the spectroscopic technique and the physical processes involved in ultraviolet radiation transport. In the case of high Mach number, high total enthalpy flow, strong emission of NO γ is present within the shock layer. For a given vibrational band of the NO γ system, radiance is observed to peak at 1.25 mm downstream of the shock for an air freestream. Attempts to fit the experimental data with NO γ synthetic spectra resulted in extremely high vibrational temperatures beyond the thermally and chemically frozen limit of 8105 K. Contributions of other electronic

transitions are found to be the cause of inflated vibrational temperatures. Specair 3.0 is selected to simulate spectra of multiple electronic transitions, since spin multiplicity is not treated explicitly in NEQAIRv14.0. Including the NO β and NO δ systems in Specair 3.0 improves the fits with spectra, but require a heavy amount of optimization amongst three temperatures to minimize the goodness of fit. The alternative approach is to fit NO γ bands that are a strong function of rotational temperature and at longer wavelengths that are not influenced by other transitions. Fitting data with synthetic spectra for $T_v = T_r$ using the vibrational bands of $\gamma(0,1)$ and $\gamma(0,2)$ allows for an approximate estimate in T_r without being heavily influenced by other transitions. Temperature fits of $T_v = T_r$ are compared with a state-to-state calculation of NO(X) for the high enthalpy condition, where a slower temperature relaxation is measured compared to the simulation.

For higher density conditions, considerations of self absorption becomes critical in fitting spectra and interpreting integrated intensities. As the extent of self absorption is a strong function of NO(X) number density, gas immediately downstream of the shock can still be approximated as optically thin until the production of NO(X) increases. For the remainder of the gas, temperature fits are performed using portions of the $\gamma(0,0)$ and $\gamma(0,1)$ bands based on Ri factors and Specair 3.0 calculations of the radiation transport. These bands exhibit similar self absorption and can be used for an estimate of rotational temperature after normalization. Good agreement is observed for $T_v = T_r$ fits and the output of a state-to-state calculation for M5-H6-A.

Varying the composition of the test gas influences the standoff distance and the measured radiation. Measured signals increase when oxygen mole fraction is reduced from the value of air. The increase in radiance is due to the reduced quenching of excited states from oxygen. When the test gas mole fraction reaches the value of $X_{O_2} = 0.063$, intensity is observed to drop due to the lack of NO produced in the gas. These trends in electronic quenching are confirmed by two-temperature reactive Landau-Teller calculations of the peak NO(A) number density for mixtures. In addition to NO(A), measured spectra show increased contribution of other electronic states of NO, increasing the effective electronic excitation temperature. Spectrum fits of M7-H8-A mixtures using NO γ, β, and δ transitions demonstrate that the effective $T_{ex} = T_v$ increases as oxygen is reduced in the test gas. Landau-Teller computations of the radiation profile shows that additional work is required for correctly modeling the kinetics of electronically excited NO and the thermal non-equilibrium present in the flows. Modeling of radiation and kinetics of electronically excited

states continues to be an active area of research [26, 45]. As a result, the measured emission spectra of cylinder flows will serve as valuable validation data for radiation modeling of hypervelocity flows.

Chapter 5

OPTICAL MEASUREMENTS IN A SHOCK/BOUNDARY-LAYER INTERACTION

Shock/boundary-layer interactions are known to lead to high thermal and aerodynamic loads on the surfaces of hypersonic vehicles. A canonical example of this phenomenon is hypersonic flow over a double wedge geometry, where the interaction of a shock wave and a boundary layer results in flow separation. The consequence of this separation is a modified shock structure that alters the state of the gas downstream of the separation region. As a result, a feedback behavior occurs until an established flow configuration is reached. To gain insight into the thermochemical relaxation profiles during flow development, a series of NO emission measurements are made in strategic locations with 10 µs and 25 µs acquisition windows to compile a time series. In addition, schlieren imaging will serve to link the emission measurements to changes in the flow field throughout test time. Finally, post-shock calculations of the flow will aid in understanding the role of thermochemical non-equilibrium to the development of a shock/boundary-layer interaction.

5.1 High Speed Schlieren Imaging

Four test conditions are used for imaging double wedge flow using air as a test gas. Two conditions are repeat tests from the work of Swantek [90] with new optics and upgrades to the facility. Videos are taken with a Shimadzu Hyper Vision HPV-X2 camera at a frame rate of 400,000 fps and an exposure time of 200 ns. Frames presented are only during test time. However, images of the acceleration gas were captured and used to indicate start of test time in the videos. For experiments with M5-H4-A and M5-H6-A, the transmitted shock in the acceleration gas can be captured in the videos and can be used as a potential measurement for shock speed. The flash lamp is triggered using a wall mounted PCB113B26 trace and the camera is delayed 0.2 ms after the flash lamp trigger. A total of 256 frames is collected with zero pre-trigger images. A pitot probe is mounted underneath the test article and within the core flow of the test gas. Events recorded by the camera are synced with the pitot pressure trace to locate the arrival of the contact surface. For all double wedge experiments, the start of test time (t = 0 µs) is defined by the arrival of the contact surface in the pitot trace. The pitot probe is mounted 11.0 mm below the

model and 3.0 mm downstream of the leading wedge tip.

M5-H4-A Double Wedge

The M5-H4-A condition is the lowest enthalpy condition of all present experiments with the double wedge. The condition also contains the largest unit Reynolds number of all experiments. In terms of driven and acceleration section fill pressures, this is equivalent to the former M5_4 condition ran by Swantek [90] and serves as a repeat with the upgraded facility. Unlike the former measurement, the burst pressure has increased from 2500 kPa to 3300 kPa. Figure 5.1 shows schlieren images taken during the startup process of the flow field. A time increment of 2.5 μs is recorded between frames. However, only 10 μs increments will be presented here. A full description of the flow development process and separation scaling analysis has been discussed by Swantek [90]. From the description of Swantek, the M5-H4-A condition initially starts as a two-shock system before the separation region increases in length. However, the present experiment reveals that the flow field fully establishes after $t = 63$ μs with separation already present and highly three-dimensional. At the arrival of the contact surface ($t = 0$ μs), the separation region nearly extends 10 mm upstream the hinge location along the first wedge. The initial separation is caused by the development of post-shock acceleration gas 100 μs prior to the arrival of the contact surface. With the exception of this new observation, the flow field is identical to the data presented by Swantek.

M5-H6-A Double Wedge

The M5-H6-A is a new condition run with the double wedge that serves to maintain the Mach number of M5-H4-A while increasing the stagnation enthalpy. Static pressure, density, and unit Reynolds number are reduced compared to the previous M5-H4-A condition. Figure 5.2 contains frames of the high speed establishment of M5-H6-A flow over the double wedge. At the arrival of the test gas, the lead oblique shock is formed with an initial separation of 5.5 ± 0.3 mm already present. From the pitot probe underneath the model, the duration of the acceleration gas is measured to be 71 μs. The high speed camera also captures the development of the acceleration gas, initially forming a two shock system, akin to inviscid supersonic flow. Afterwards, separation of the post-shock acceleration gas forms and moves downstream along the wedge. The final separation length of the acceleration gas is carried over to the test gas and is observed in Fig. 5.2 at $t = 18$ μs. The separation region contains some three-dimensionality, indicated by multiple separation shocks,

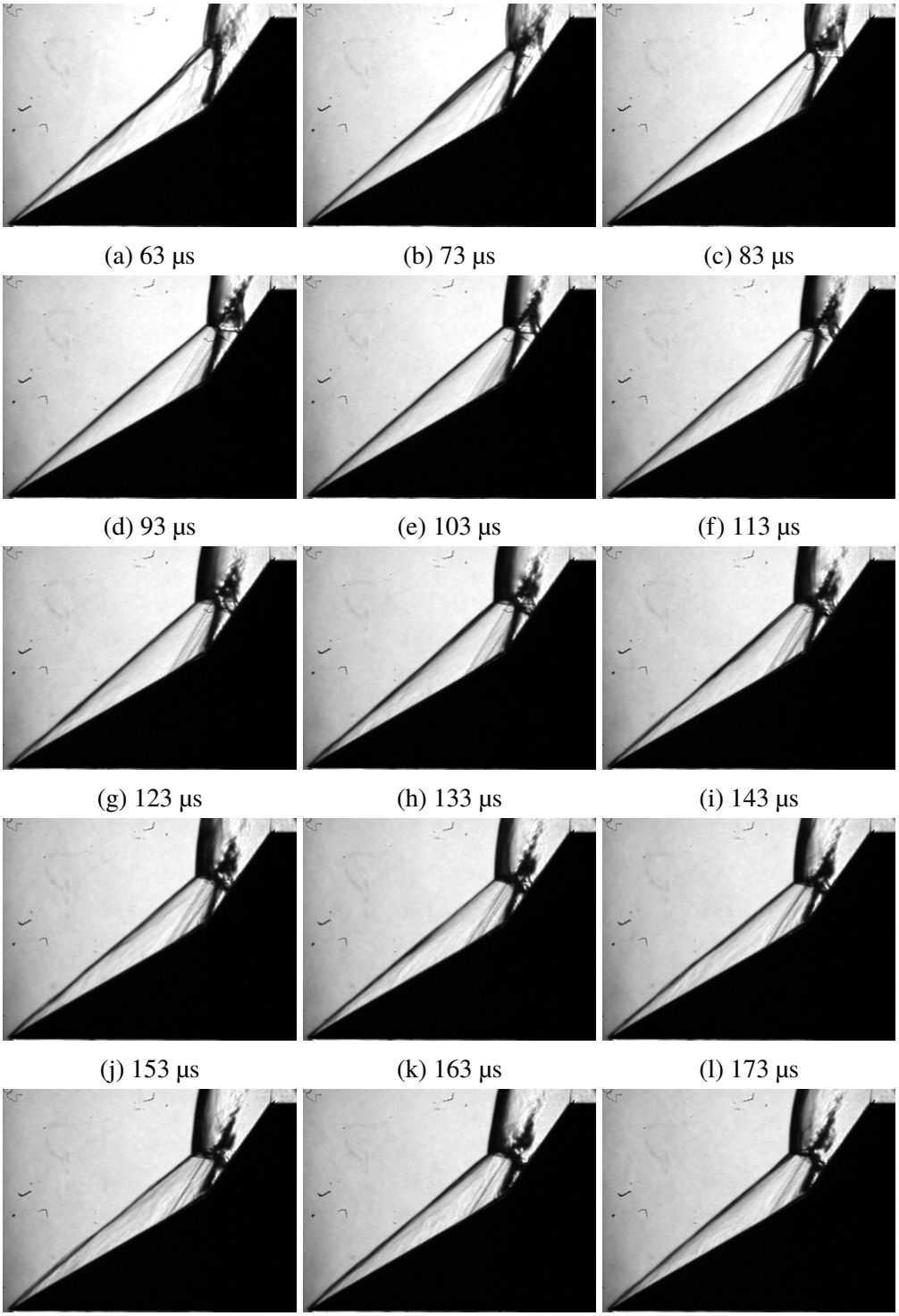

(a) 63 µs (b) 73 µs (c) 83 µs

(d) 93 µs (e) 103 µs (f) 113 µs

(g) 123 µs (h) 133 µs (i) 143 µs

(j) 153 µs (k) 163 µs (l) 173 µs

(m) 183 µs (n) 193 µs (o) 203 µs

Figure 5.1: High speed schlieren images of M5-H4-A. Time interval between frames is 10 µs.

and persists for the entire startup process. After the flow has established, the separation region increases in length throughout test time.

The triple point forms immediately after the start of test time and is initially located downstream of the hinge. Similar to other examples of double wedge flow, the triple point moves upstream past the hinge location and downward as time progresses. The reattachment shock location at the wedge surface is maintained during startup and experiences changes in shock β angle. Behind the bow shock, the shear layer and system of shock waves forms above the surface of the second wedge. As the flow develops, the system of turning waves moves upstream along the second wedge surface until $t = 88$ µs, where the waves exhibit three dimensionality. As with other examples, shear layer oscillations and shedding vortices are observed throughout test time.

M7-H8-He Double Wedge

A repeat of Swantek's former M7_8 condition is performed with a faster frame rate and upgraded facility. Figure 5.3 contains a series of high speed schlieren images of the startup process of M7-H8-He flow over the double wedge geometry. An in-depth discussion of the flow features and behavior can be found in Swantek [90]. Images of the flow features are clearer and sharper than the older data set, making it easier to identify waves in each frame. Similar to the previously presented cases, the test gas arrives with an initial separation length. Due to the low density of the helium, the establishment of the acceleration gas cannot be captured by the schlieren optics. However, the pitot pressure measures an acceleration gas duration of 60 µs, allowing enough time for separation to develop and have initial length of 3.9 ± 0.3 mm before the arrival of the test gas.

M7-H8-A Double Wedge

From Chapter 2, a condition identical to M7-H8-He was created to study the effects of acceleration gas on the state of the final test gas. The M7-H8-A was developed to have the same perfect gas freestream as the previous M7-H8-He, but using air as the accelerator gas. The driver and driven pressures were maintained in this condition, while the acceleration section was filled to 28 mTorr of room air. This is in contrast to the M7-H8-He helium fill pressure of 173 mTorr. The creation of this condition allows for the study of acceleration gas effects over the double wedge geometry before the arrival of the contact surface.

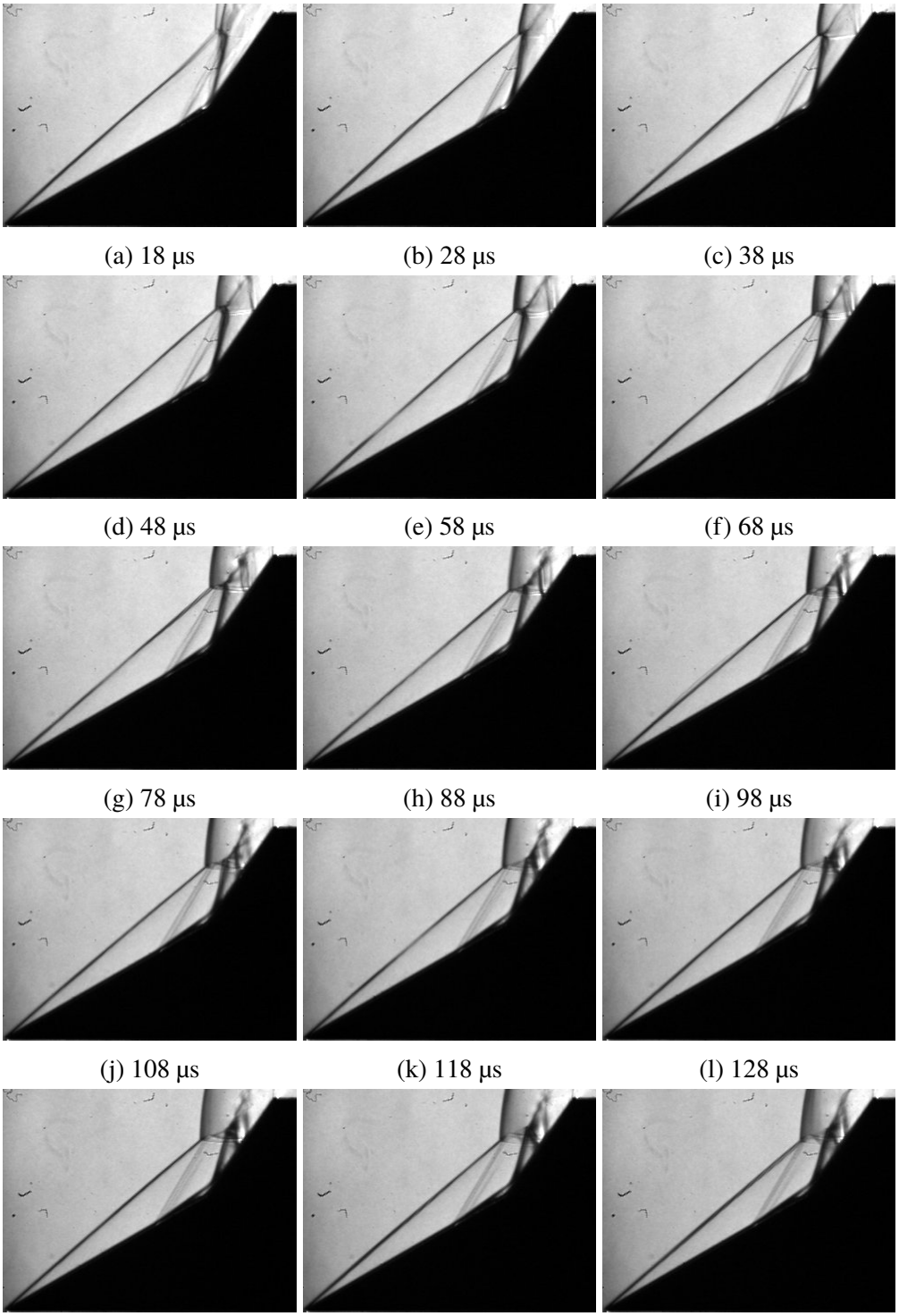

(a) 18 µs (b) 28 µs (c) 38 µs

(d) 48 µs (e) 58 µs (f) 68 µs

(g) 78 µs (h) 88 µs (i) 98 µs

(j) 108 µs (k) 118 µs (l) 128 µs

(m) 138 µs (n) 148 µs (o) 158 µs

Figure 5.2: High speed schlieren images of M5-H6-A. Time interval between frames is 10 µs.

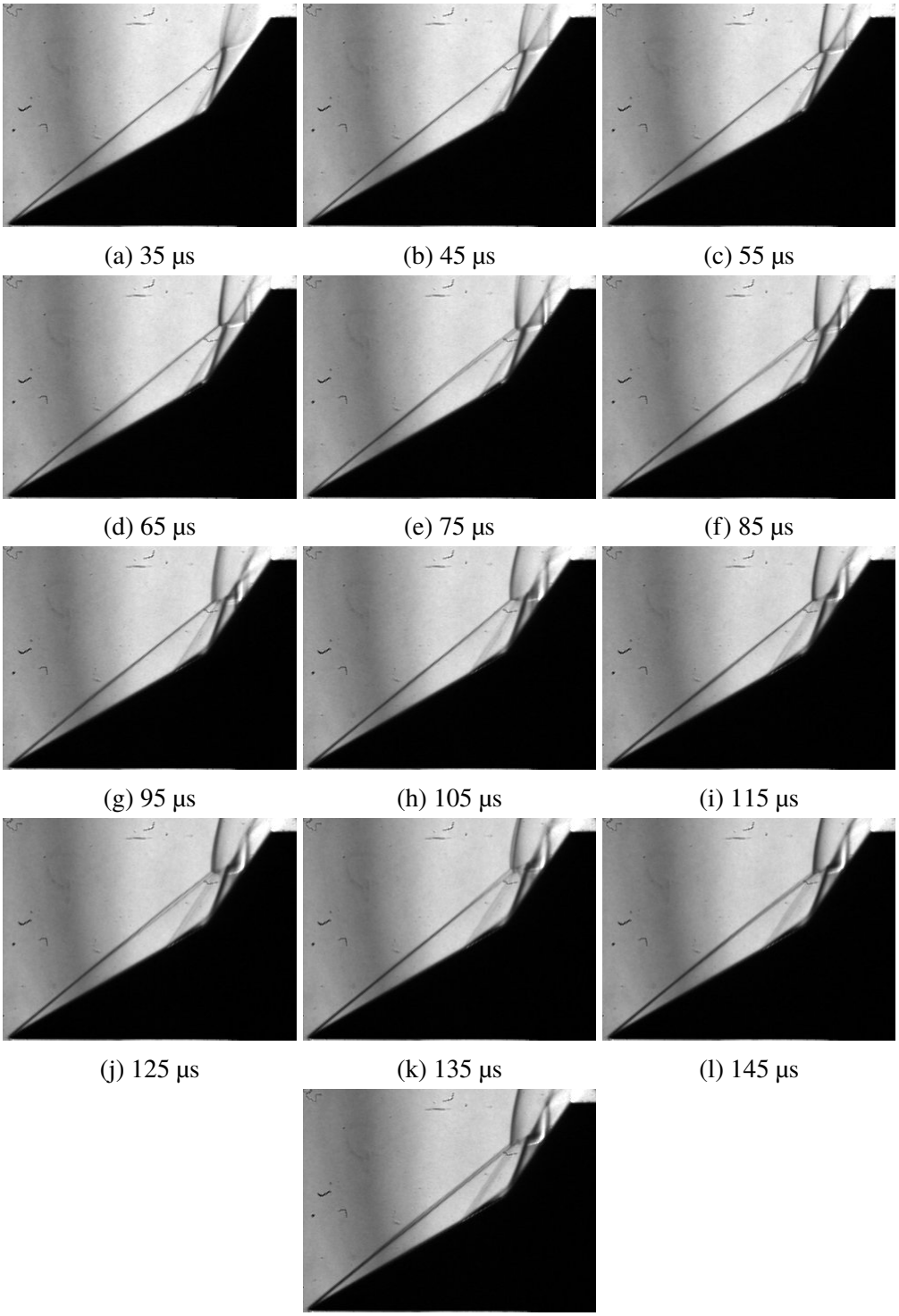

(a) 35 µs (b) 45 µs (c) 55 µs

(d) 65 µs (e) 75 µs (f) 85 µs

(g) 95 µs (h) 105 µs (i) 115 µs

(j) 125 µs (k) 135 µs (l) 145 µs

(m) 155 µs

Figure 5.3: High speed schlieren images of M7-H8-He, with helium used as an acceleration gas. Time interval between frames is 10 µs.

Figure 5.4 contains frames of a high speed schlieren of M7-H8-A flow over a double wedge geometry. Out of all past and present experiments of the double wedge in the expansion tube, M7-H8-A is the only condition where the test gas arrives with minimal initial separation. In Fig. 5.4, the test gas begins as a two-shock system, where separation starts at the hinge. As time progresses, the separation shock becomes visible and the separation length grows, moving upstream along the first wedge. Development of other flow features is qualitatively similar to what was described by Swantek [90]. However, the positioning of the separation shock and the triple point occur at different points in test time than in the M7-H8-He case.

Effect of Facility Startup on Double Wedge Flow

Figure 5.5 compares two frames from the M7-H8-He and the M7-H8-A condition at $t = 45$ µs after the arrival of the contact surface. Background images are subtracted from the raw images to highlight the important features of the shock structure. Although the perfect gas freestream conditions are similar between the cases, the location of flow features have shifted. Define L_{sep} as the length of the separation region and x_1 as the distance of the separation front from the wedge tip. The non-dimensional length of the separation region is $\frac{L_{sep}}{x_1} = 5.2 \times 10^{-2} \pm 0.6 \times 10^{-2}$ for the M7-H8-A case compared to $\frac{L_{sep}}{x_1} = 9.3 \times 10^{-2} \pm 0.7 \times 10^{-2}$ for the M7-H8-He condition at the same period in test time. This is likely due to the initial separation present in the M7-H8-He case. In addition, the series of waves behind the bow shock is further upstream in the helium case when compared to the air acceleration case. These changes in the evolution of the flow field are critical when comparing time resolved heat flux data to simulations, since flow separation and shock impingement heavily determine where peak heat flux occurs on the test article. Careful attention must be placed in correctly modeling the startup processes of any high enthalpy facility, as this will modify the initial conditions of such a time sensitive flow.

5.2 Tracking of Major Features in Schlieren Videos

Using similar techniques for extracting the standoff distance of cylinder flow, it is possible to measure the temporal changes in locations of various features of the shock/boundary-layer interaction. Although the spectroscopic technique also doubles as an imaging technique, quantities such as wave angle cannot be inferred from the radiation measurement alone. As changes in radiation intensity are directly correlated to the movement of the bow shock, shear layer, reattachment shock, and separation shock, it is critical to locate the position of the waves beforehand. From

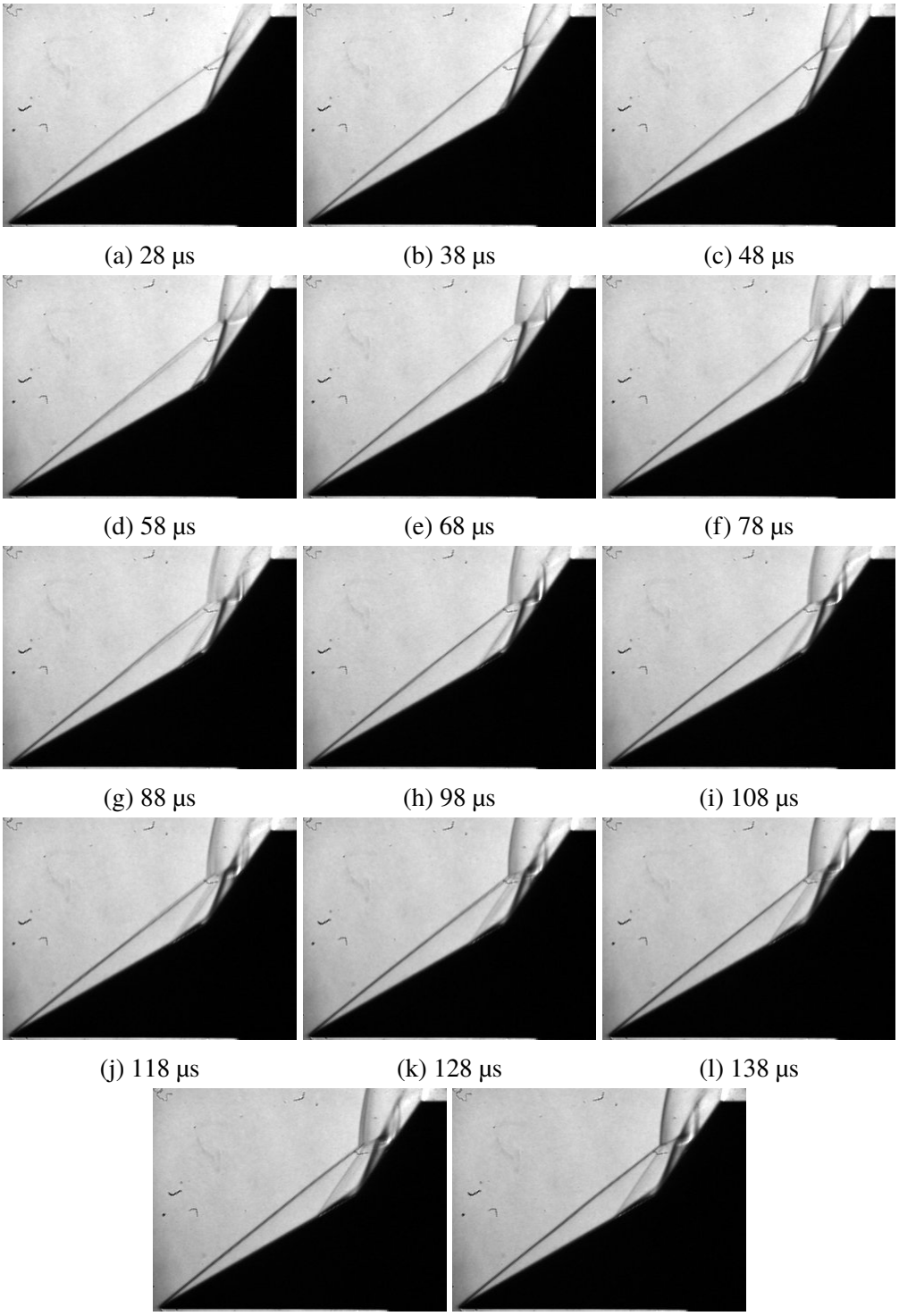

(a) 28 µs (b) 38 µs (c) 48 µs

(d) 58 µs (e) 68 µs (f) 78 µs

(g) 88 µs (h) 98 µs (i) 108 µs

(j) 118 µs (k) 128 µs (l) 138 µs

(m) 148 µs (n) 158 µs

Figure 5.4: High speed schlieren images of M7-H8-A, with air used as an acceleration gas. Time interval between frames is 10 µs.

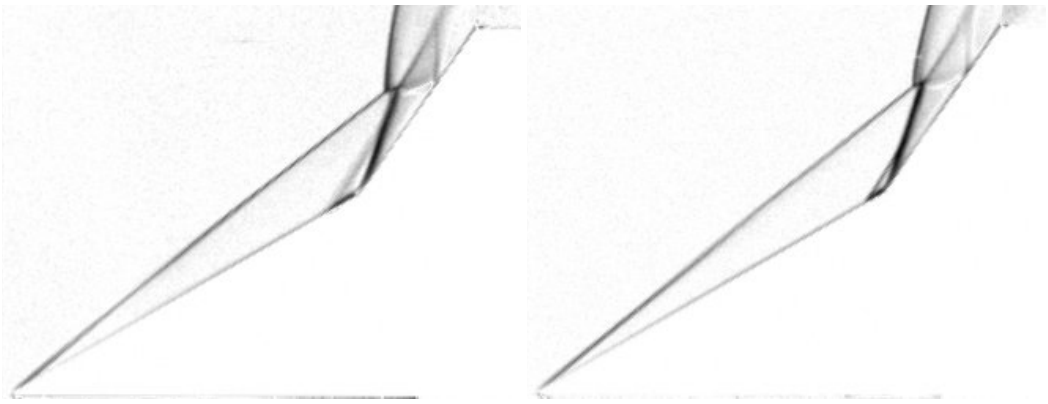

(a) M7-H8-He (b) M7-H8-A

Figure 5.5: Background subtracted frames of two freestream conditions taken 45 µs after the contact surface.

the knowledge gained from radiation measurements of cylinder flow, it is expected that the M7-H8-A freestream will provide the strongest ultraviolet signal in the post-bow shock region. Spectroscopic measurements will only be performed with this high enthalpy condition, providing the best case scenario for short exposure measurements. As a result, the focus of discussion will be on the analysis of M7-H8-A schlieren images.

Before every experiment, a background video is recorded at the same camera settings as the test with no flow present. The light source of the flash lamp diminishes in intensity over time and will result in global changes in pixel intensities. The image processing software ImageJ is used to perform mathematical operations on the series of images. The raw schlieren videos are subtracted with background videos using the subroutine "difference" in the image calculator of ImageJ. This allows for imperfections from optics to be removed and to minimize the intensity variations of the light source during test time. Figure 5.6 is a background subtracted frame with all flow features labeled. The origin of the coordinate system is selected to be at the location of the tip of the first wedge.

Bow shock standoff distance is measured using the same method outlined for analyzing cylinder schlieren images. The procedure is applied to a series of background subtracted images along a horizontal line y_t = 42.62 mm above the leading wedge tip. Later on, this will be one of two locations used for emission measurements. Figure 5.7 is the x_t bow shock location along y_t = 42.62 mm. Vertical lines represent the establishment time and the end of theoretical test time. As observed in Fig. 5.4, the bow shock travels upstream early in the flow development process. At

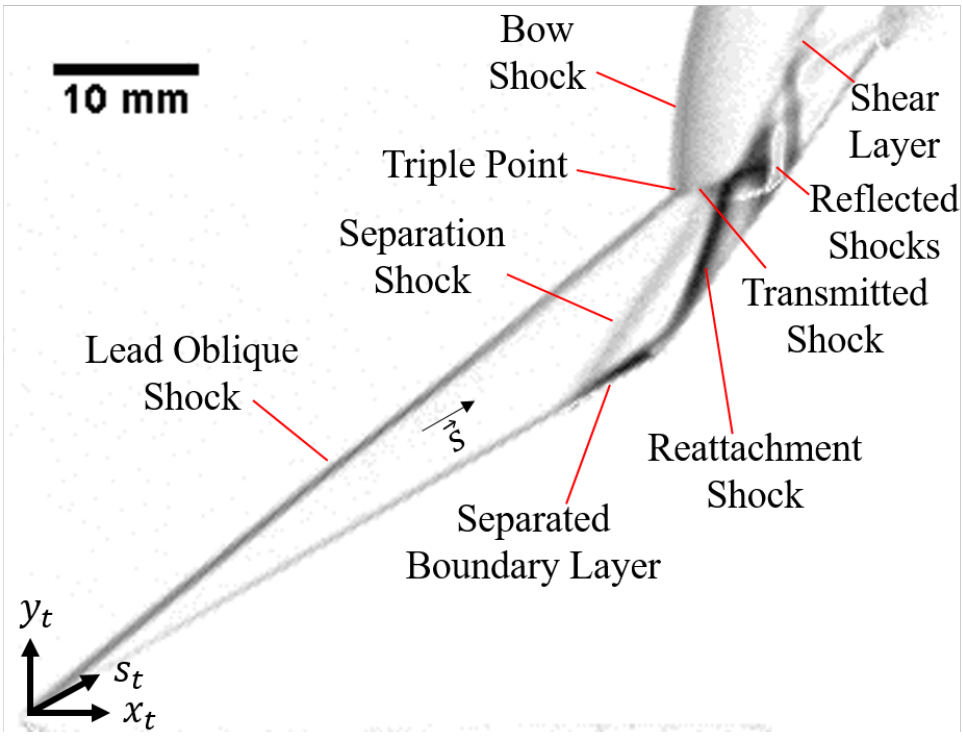

Figure 5.6: Labeled diagram of major features in a shock/boundary-layer interaction. A M7-H8-A freestream is shown with the frame taken t = 100 µs after the contact surface.

t = 70 µs, the bow shock arrives at a mean location with oscillations present. After approximately t = 137 µs, the bow shock reverses direction and partially moves downstream until the theoretical test time ends. The location of the shock is plotted beyond the theoretical test time, where the bow shock moves upstream a second time.

The temporal evolution of the bow shock location demonstrates the potential for smearing on the detector throughout test time. This is of great concern early in test time, where the bow shock travels with a mean horizontal velocity of 83 ± 6 m/s. In addition, oscillations of the shock can generate peak-to-peak movement of approximately 1.5 mm, a displacement large enough for observable changes on a detector. It is the movement of the bow shock that ultimately governs the selected exposure time for emission measurements.

The other defining feature of the double wedge flow is the separation of the boundary layer. Swantek [90] and Knisely [48] have performed measurements of the separation length for double wedge flows in both the HET and the Caltech T5 reflected shock tunnel. However, the location of separation was only measured using still schlieren

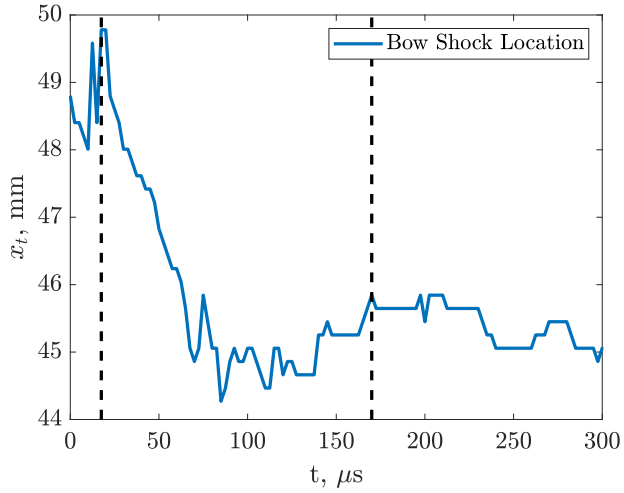

Figure 5.7: Measured bow shock location along a horizontal line located y_t = 42.62 mm as a function of test time. Background subtracted images are used for measurements.

images. With background subtracted images such as Fig. 5.6, the separation zone can be easily identified in the movies and tracked using similar methods applied to bow shocks. Through ImageJ, the background subtracted images are rotated 30 degrees using a bilinear interpolation to orient the leading wedge horizontally. A region 0.79 mm thick (equivalent to 4 pixels) is binned along the wedge surface to obtain average pixel intensity versus the streamwise coordinate s_t. The separation of the boundary layer is indicated by a region of low pixel intensity in the images. The upstream location of the separation region is measured by setting a threshold in pixel intensity from the background value. The threshold is set to 80% of the mean pixel intensity where no flow is present in the images. The location where binned pixel intensity drops below the threshold is selected as the upstream location of the separation zone.

Figure 5.8 plots the streamwise location of the start of the separation region as a function of time. As previously identified in the schlieren videos, the separation of the boundary layer starts approximately 1.9 mm from the hinge location after the flow has established and propagates upstream throughout test time. Outside test time, the boundary layer separation continues to grow until reaching a mean location 260 µs after the arrival of the contact surface. An important outcome from this measurement is the deceleration of the separation length motion over time. Because a shock is formed at the separation front, the movement of the separation shock also decays with time. The mechanism driving the decay of the separation

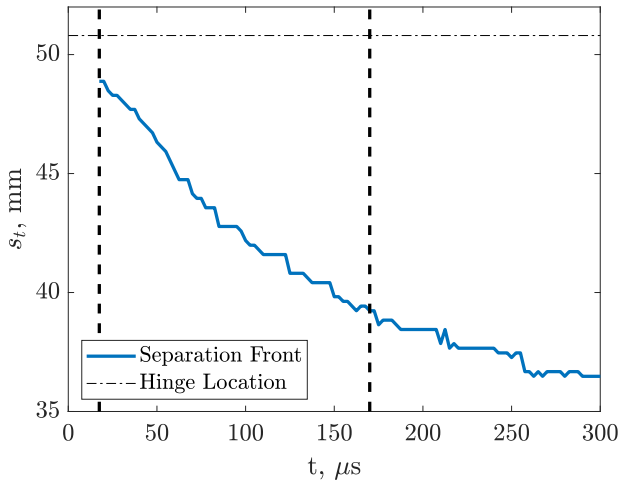

Figure 5.8: Front of separation region measured along leading wedge surface. Vertical lines mark the startup process and end of test time. Horizontal line marks the hinge location from the tip along the wedge face. Background subtracted images are used for measurements.

growth is likely to originate downstream. The most plausible flow feature to cause this deceleration is the reattachment shock behind the separation bubble. Based on the wake model of Roshko, the post-reattachment state of the gas determines the pressure downstream of the separation bubble, ultimately governing the growth of the region [82].

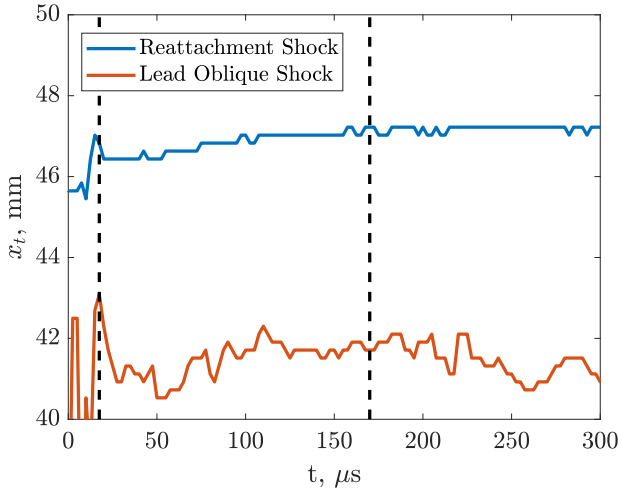

Figure 5.9: Measured lead oblique shock and reattachment shock locations along a horizontal line at y_t = 33.91 mm as a function of test time. Background subtracted images are used for measurements.

The last remaining features that can be readily tracked are the lead oblique shock and the reattachment shock. A horizontal line of pixels located $y_t = 33.91$ mm are binned, intersecting the oblique shock features in the background subtracted images. This is chosen as the second location used for emission measurements. The procedure for locating shocks is applied to the line. Figure 5.9 plots the x_t locations of the lead oblique shock and the reattachment shock at a fixed $y_t = 33.91$ mm line. During startup, the lead oblique shock experiences extreme oscillations. Once the flow has established, the oblique shock exhibits movement throughout test time. This is confirmed in the series of images in Fig. 5.4, where a frame corresponding to $t = 58$ µs captures unsteadiness of the downstream portion of the lead oblique shock. This movement is likely due to freestream disturbances. Movement of the reattachment shock is measured, where the shock location propagates downstream with time relative to the horizontal line. This is due to the combination of wave angle change and the streamwise moment of the shock itself.

5.3 Emission Measurements in the Post-Bow Shock and Shear Layer Region

Emission measurements of the post-bowshock region of double wedge flow have been performed in a previous work by Swantek [90]. Although these measurements provided the first recorded attempt of measuring NO γ emission in a shock/boundary-layer interaction, the greatest limitation was the exposure time used in the former measurements, set to 110 µs. Not only did this exposure time allow for an extreme amount of smearing from flow unsteadiness, a portion of the exposure occurred outside the theoretical test time, as a 90 µs delay was set after the arrival of the contact surface. Measurements used short focal length fused silica lenses, allowing for chromatic aberrations to possibly affect the measurement. Extracted temperatures were reported as NO vibrational temperature. However, fits were done in the range of 220 nm - 255 nm assuming $T_v = T_r$, which makes the measurement a closer approximation to rotational temperature based on the discussion in Chapter 3.

Using the knowledge gained from ultraviolet emission of stagnating flow, numerous improvements can be made in the measurement through the use of better optical design and analysis tools. Methods outlined in Chapter 4 can readily be applied to the post-bow shock region of double wedge flow. Collection optics, calibration sources, and calibration procedure are identical to the ones used in cylinder measurements. For bow shock measurements, optics are aligned such that the image of the slits are oriented $y_t = 42.62$ mm above the tip of the leading wedge. The sting of the double wedge model is designed to allow for streamwise movement by adding or removing

shims. This allows for investigations to be performed through the shear layer and up to the surface of the test article.

Considerations for Short Exposure Times and Low Signal

Shock smearing presents a new challenge to emission measurements of an unsteady flow. Exposure times must be kept low to limit smearing, but long enough to minimize the signal-to-noise ratio of extracted spectra. To serve as a compromise, an exposure time of 10 µs is selected for emission behind the bow shock. Trigger repeatability also becomes a new concern, as the National Instruments DAQ system is prone to a jitter of ±4 µs. For all emission measurements with the double wedge, triggering of the camera is performed using a YOKOGAWA DL850E oscilloscope from the pitot signal. Therefore, the pitot trace was recorded using both the NI DAQ and the YOKOGAWA for redundancy. The oscilloscope was set to a sample rate of 2 MHz with a bandwidth of 640 kHz.

In addition to increasing the gain of the intensifier, improving the signal of the radiation can be achieved by increasing the slit width. As discussed in Chapter 3, the instrument line shape is a strong function of the slit width. Increasing the slit width has the consequence of increasing the FWHM of the instrument line shape, reducing the overall resolution of the spectral features. As rotational temperature determines the FWHM of the vibrational bands in NO γ emission, a change in instrument FWHM can lead to an unwanted loss in sensitivity in T_r. To verify that temperature fits can still be performed on low resolution spectra, synthetic spectra are computed using a FWHM of 40 cm^{-1} and 80 cm^{-1} for convolving transitions. A target synthetic spectrum of $T_r = T_v = 7000$ K was selected and the fitting routine was ran for a range of temperatures. Using the χ^2 metric as a way of quantifying sensitivity, an assumed $\sigma_I = 0.05$ was used for computing χ^2 profiles. A fit uncertainty of $\sigma_T = 55$ K was obtained for both FWHM values, verifying that $T_r = T_v$ fits can still be performed on low resolution spectra without loss of sensitivity.

Slit width was increased while recording the radiation of a Hg-Ar lamp. Radiation of the Hg-Ar lamp is shown in Fig. 5.10 alongside proposed instrument functions. A new FWHM of 59 cm^{-1} (0.38 nm) was measured. In contrast to the cylinder measurements with a shorter FWHM, the proposed instrument line-shapes show a poorer fit to the measured radiation, with some asymmetry present in the line. Nevertheless, the square-root of the Voigt function still provided the best coefficient

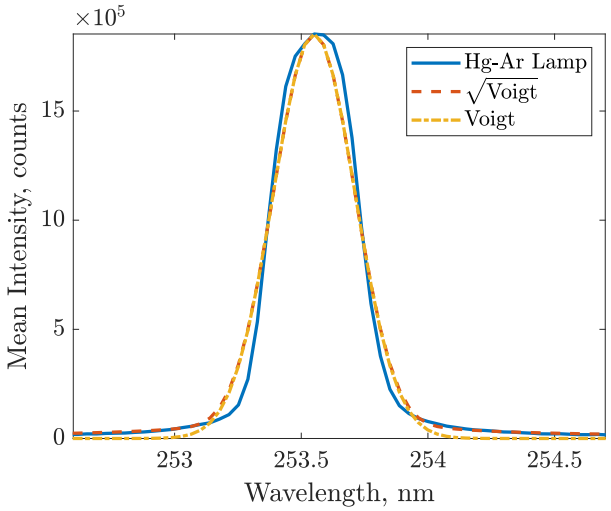

Figure 5.10: Mercury-Argon lamp radiation plotted alongside proposed instrument line-shapes. This line-shape is used for all double wedge experiments.

of determination and is used in computing synthetic spectra for all double wedge emission results.

Post-Bow Shock Radiation of Double Wedge Flow

To study radiation immediately downstream the bow shock, optics are aligned such that the field of view is approximately 6 mm downstream of the mean shock location. Similar to the cylinder data set, the system is triggered and delayed relative to the arrival of the contact surface, which is indicated by a trigger voltage of 0.25 V. This voltage is equivalent to 17.14 kPa when using the conversion for a PCB 112A22 (SN: 36883). Radiation is collected in seven intervals: 35-45 µs, 55-65 µs, 70-80 µs, 90-100 µs, 110-120 µs, 135-145 µs, and 150-160 µs. Five experiments were performed with varying exposure time, slit width, and camera gain to find the optimal settings for clean signals. Finally, an additional two tests were performed to investigate the effect of flow unsteadiness on measurement repeatability.

The time evolution of radiation downstream the bow shock is shown in Fig. 5.11. The vertical axis is referenced as the downstream position from leading wedge tip. The contour height range is fixed to observe relative changes in detector intensity. From the high speed schlieren videos, unsteadiness in the location of the bow shock is present for the majority of frames. The greatest displacement of the bow shock occurs at the start of test time. This is confirmed in the detector images of radiation, where the shock location moves approximately 2 mm upstream between the 35-45 µs interval and the 55-65 µs interval. For the first 100 µs of test time, overall detector

intensities are similar with some variations in shock location from the oscillatory nature of the flow. Features of the detector images are similar to the post-shock radiation of stagnation flow, where radiance peaks downstream of the bow shock before decreasing in intensity. After 100 µs, a dramatic drop in intensity is observed. At the final interval of 150-160 µs, the recorded signals are the lowest amongst the data set. It is also observed that the bow shock begins to move downstream near the end of test time, confirming schlieren measurements of the bow shock location in Fig. 5.7.

The $\gamma(0,1)$ vibrational band can again be used to study the number density profile of NO(A) that is formed downstream of the shock. Figure 5.12 plots the integrated radiance of the $\gamma(0,1)$ vibrational band for seven time intervals throughout test time. Similar to the cylinder data set, no radiation is measured in the freestream. The unsteady nature of the bow shock is highlighted in Fig. 5.12, where the location of the peak in integrated radiance is not commonly shared among the time intervals. It is observed that the bow shock position moves in the upstream direction with some oscillations about a mean. Within the 150-160 µs portion of test time, the bow shock begins to move downstream along the slit location. The profiles of integrated radiance share several traits found in the cylinder data set, where peak intensities occur approximately 1.5 mm downstream of the location of the shock. However, the shock layer is no longer terminated by the surface of the test article, now located $x_t = 56.05$ mm along the image of the slits. Instead, the shear layer determines the end of the shock layer. From the schlieren videos, the mean shear layer location amongst the time intervals is $x_t = 51.0 \pm 0.3$ mm with fluctuations about the mean. The $\gamma(0,1)$ vibrational band experiences a drop at approximately $x_t = 51$ mm in Fig. 5.12, coinciding with the formation of the shear layer.

Post-Shear Layer Radiation

Repeat experiments were performed at the same seven time intervals to investigate radiation within the shear layer and downstream of the system of oblique waves. In order to change the field of view, shims were added to the sting to position the model an additional 4 mm upstream. Figure 5.13 shows the resulting detector image of the flow field at the 35-45 µs interval. The position axis is now shifted downstream, where radiation is measured up to the surface of the second wedge located at $x_t = 56.05$ mm. From using the schlieren videos, the location of features are identified within the time interval of the emission measurement. Figure 5.13b shows the resulting binned spectra downstream of the shear layer in yellow and

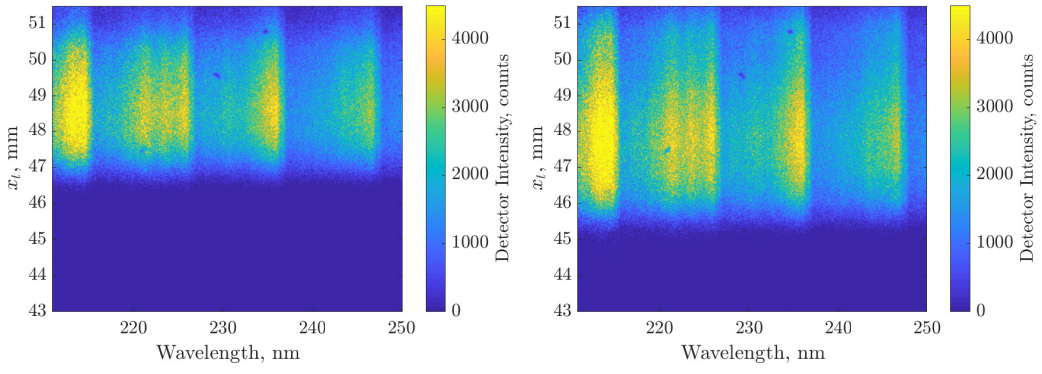

(a) 35-45 µs

(b) 55-65 µs

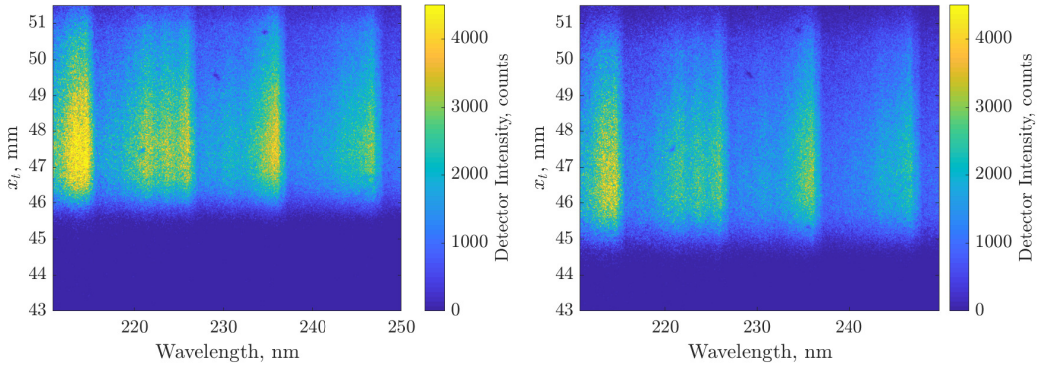

(c) 90-100 µs

(d) 110-120 µs

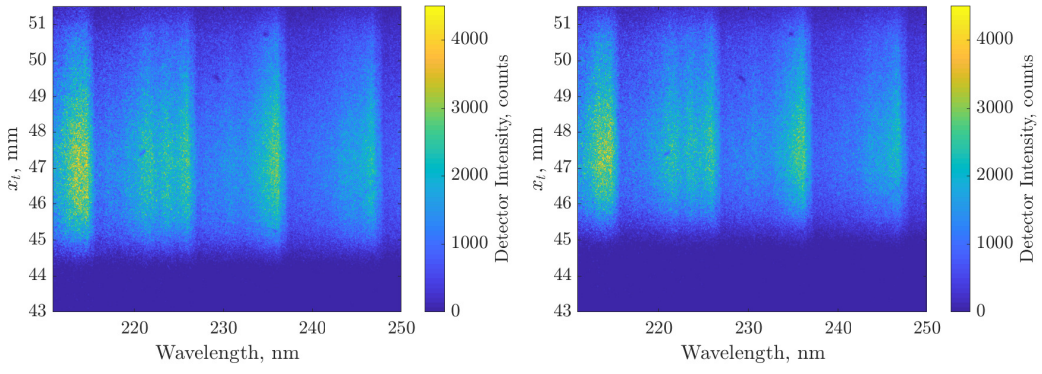

(e) 135-145 µs

(f) 150-160 µs

Figure 5.11: UV emission downstream of bow shock at select intervals in test time.

downstream of the reflected shock in red. Signals dramatically decrease downstream of the shear layer, with more binning required to extract clean spectra. Close to the surface of the wedge, signals drop further, with the quality of the binned spectra becoming poor. Similar to the cylinder results, near surface measurements are prone to a loss in signal due to clipping of rays by the model geometry. Regardless, it is still possible to fit synthetic spectra to these near surface measurements. More

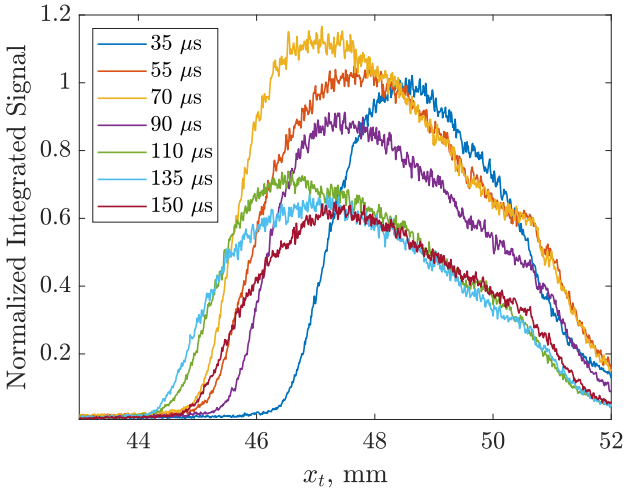

Figure 5.12: Profiles of $\gamma(0,1)$ integrated band intensity for exposure times of 10 µs. Profiles are referenced to the start of exposure within test time. Normalization was performed using the 35-45 µs peak counts. Position axis is measured relative to the location of the leading wedge tip.

details on the binning procedure will be shown in a later subsection on temperature measurements.

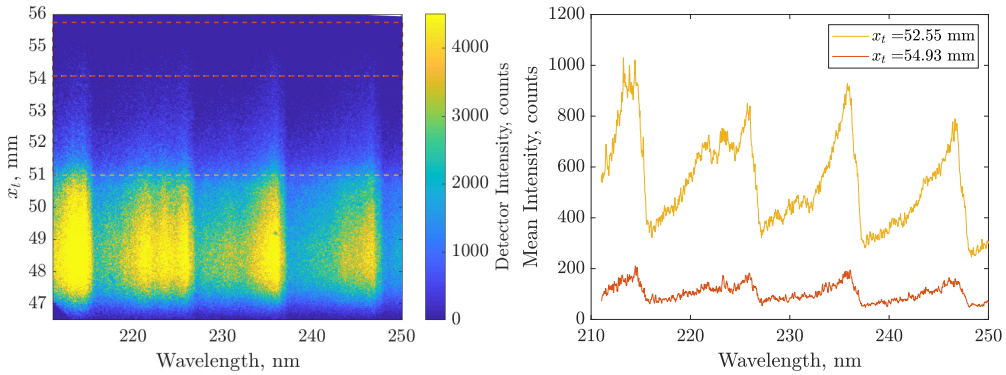

(a) Radiation To Model Surface

(b) Binned Spectra

Figure 5.13: Detector image of radiation of bow shock gas and downstream of shear layer at an interval of 35-45 µs. Dashed lines represent regions used in binning spectra downstream of the measured shear layer location.

Similar to the bow shock data, it is possible to compare the integrated intensities of the $\gamma(0,1)$ vibrational band for different times at locations up to the surface of the second wedge. Figure 5.14 displays the time evolution of radiation downstream of the post-bow shock gas. As observed previously in Fig. 5.12, radiation dramatically decreases after x_t = 51 mm and approaches to zero at the wedge surface. At a

fixed coordinate of x_t = 53 mm, signals are the highest early in test time with a gradual decrease in intensity with time. The proximity of the post-bow shock gas may influence the intensity of signals early in test time, as the bow shock initially starts downstream of the hinge location before propagating upstream.

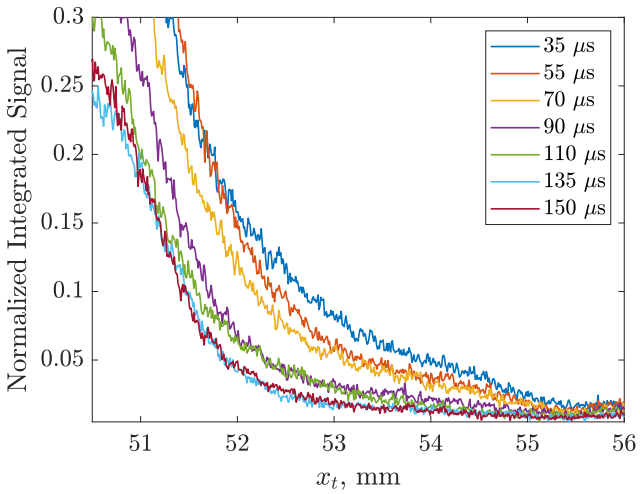

Figure 5.14: Integrated band intensity of γ(0,1) for exposure times of 10 µs along a line at y_t = 42.62 mm. Normalization was performed using the 35-45 µs peak intensity upstream the shear layer location. Second wedge surface is located at x_t = 56.05 mm.

Single Temperature Fits of Post-Bow Shock Region

As double wedge flow features a strong bow shock, techniques for temperature extraction of stagnation flow can be readily applied to the post-shock region of the bow shock. The primary difference between the cylinder bow shock and the double wedge bow shock the non-stagnant nature of the gas downstream of the double wedge bow shock. Due to the existence of the second wedge, streamlines are forced to turn upward after the bow shock. As a result, movement along a horizontal line corresponds to movement between streamlines. The appearance of the shear layer and reflected waves also adds complexity to the measurement. Videos are used to locate the features of the flow field for the seven snap shots. The locations of the features determine the extent of binning that is performed on the detector. Experimental spectra are fitted using NO γ synthetic spectra for $T_v = T_r$ in the 227.50 nm - 250.00 nm range of wavelengths. Recall from Chapter 3 that these wavelengths are dominated by $\gamma(0,1)$ and $\gamma(0,2)$, which allow sensitivity to rotational temperature.

In the first 70 µs of test gas, three distinct regions are formed along the y_t = 42.62 mm horizontal line. The areas are bounded by the bow shock, shear layer, and reflected shock from the surface of the second wedge. Between the bow shock and shear layer, binning is performed at 1 mm increments to obtain the best signal from the spectra. Although measurements of the bow shock location have been obtained from the schlieren images, there are cases where the start of radiation does not coincide with the measured bow shock position. Therefore, the detector images are used to indicate the start of binning for spectra downstream of the bow shock. The start of binning occurs at the x_t location corresponding to 20% of the peak radiance on the detector images. Using the 35 − 45 µs profile in Fig. 5.12 as an example, binning starts at x_t = 46.8 mm with 1 mm increments on the detector. For the second region downstream of the shear layer, binning is performed between the location of the shear layer and the reflected wave measured in the schlieren images. Finally, the third region is binned between the position of the reflected wave and model surface. Due to the low signals downstream of the shear layer, averaging across a large region allows for better spectrum fits.

Figures 5.15 and Fig. 5.16 show the temperature profile along a line through the various features of double wedge flow. The frame corresponding to the end of the time interval is shown with a red line 12 mm long from the surface of the second wedge. Temperature profiles consist of two repeat experiments, each interrogating a different portion of the flow along the horizontal line. Error bars are the uncertainties from experimental noise following the method of Tibère-Inglesse et al. [92]. Within the post-bow shock region, the gas is initially at the thermally frozen temperature of 8105 K with a slow relaxation. Similar to the cylinder, the temperature never reaches the equilibrium value of 4127 K before the location of the shear layer. Between the shear layer and the location of the reflected wave, the temperature dramatically decreases. This region corresponds to streamlines that have been processed by three oblique shocks. After the reflected wave, another drop in temperature is measured. Due to extremely low signals, spectrum fits are poor near the surface of the second wedge, with fits resulting in values of χ^2 = 247. In Fig. 5.16, the shear layer and reflected shock moves upstream between 55-65 µs, decreasing the volume of gas that can be imaged between these features. Nevertheless, measured temperatures are observed to decrease downstream of the shear layer similar to the 35-45 µs interval.

After 80 µs, the reflected shock at the second wedge surface begins to exhibit three dimensionality. As this portion of the flow is complex, it is difficult to

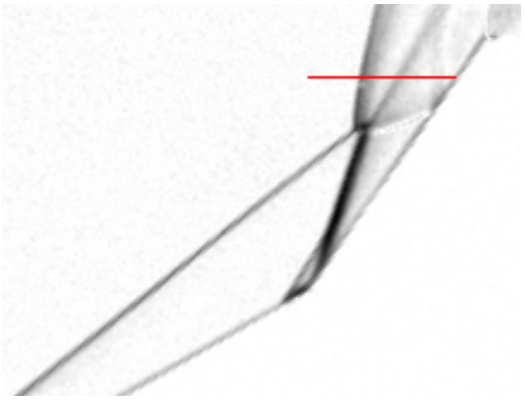

(a) Schlieren Image $t = 45\mu s$

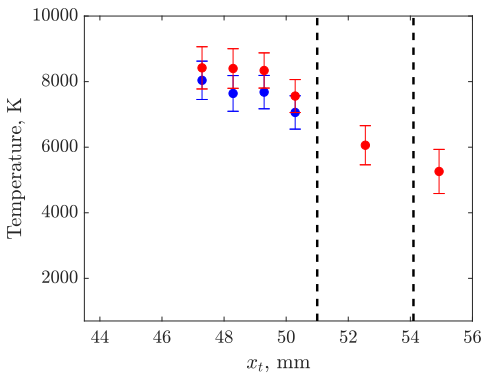

(b) $T_v = T_r$ Profile

Figure 5.15: Temperature profile at $t = 35-45$ µs along a horizontal line located $y_t = 42.62$ mm above the wedge tip. A red line 12 mm long shows the interrogation region of the spectroscopy optics in the schlieren image. Multiple colors in temperature plot represent repeat experiments at different x_t ranges, while vertical dashed lines are the measured locations of features.

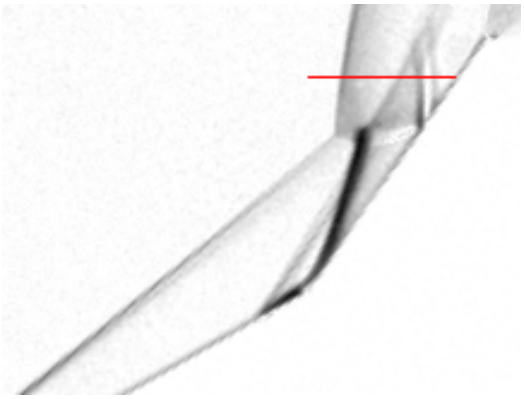

(a) Schlieren Image $t = 65$ µs

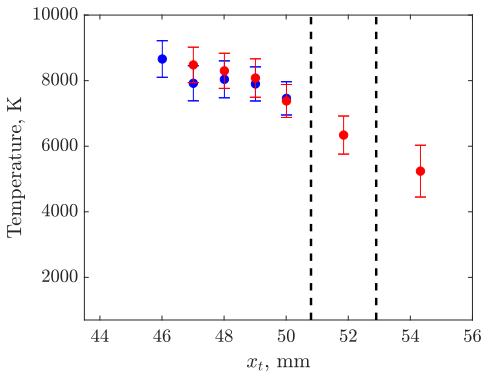

(b) $T_v = T_r$ Profile

Figure 5.16: Temperature profile at $t = 55-65$ µs along a horizontal line located $y_t = 42.62$ mm above the wedge tip. A red line 12 mm long shows the interrogation region of the spectroscopy optics in the schlieren image. Multiple colors in temperature plot represent repeat experiments at different x_t ranges, while vertical dashed lines are the measured locations of features.

interpret emission from this section of the flow without the aid of three-dimensional simulations. Binning of the second region is performed within the boundaries of the three dimensional waves and shear layer. Within the first 100 µs of test gas, the bow shock portion of the flow continues to initially start at the frozen limit with no relaxation to the calculated equilibrium value. Within the three dimensional feature, emission shows a drop in temperature. The near surface region continues to be

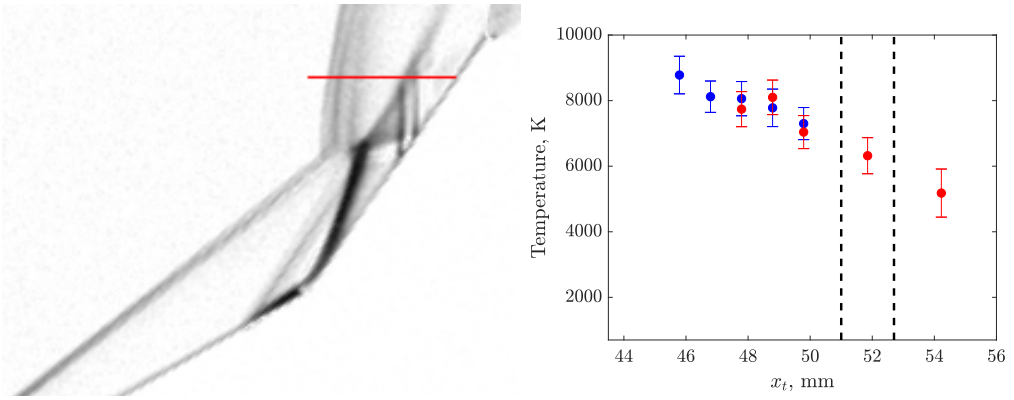

(a) Schlieren Image $t = 80\mu s$ (b) $T_v = T_r$ Profile

Figure 5.17: Temperature profile at $t = 70-80$ µs along a horizontal line located $y_t = 42.62$ mm above the wedge tip. A red line 12 mm long shows the interrogation region of the spectroscopy optics in the schlieren image. Multiple colors in temperature plot represent repeat experiments at different x_t ranges. Vertical dashed lines mark the three-dimensional feature of shear layer and reflected waves.

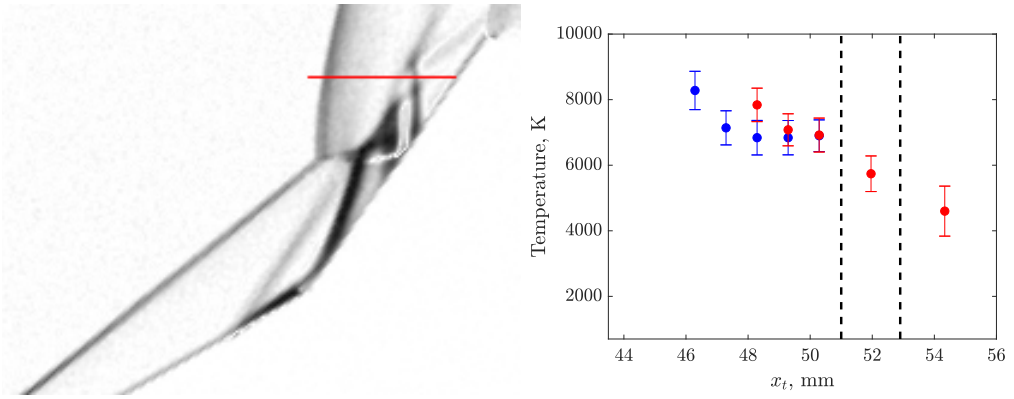

(a) Schlieren Image $t = 100\mu s$ (b) $T_v = T_r$ Profile

Figure 5.18: Temperature profile at $t = 90 - 100$ µs along a horizontal line located $y_t = 42.62$ mm above the wedge tip. A red line 12 mm long shows the interrogation region of the spectroscopy optics in the schlieren image. Multiple colors in temperature plot represent repeat experiments at different x_t ranges. Vertical dashed lines mark the three-dimensional feature of shear layer and reflected waves.

the coldest portion of the gas along the horizontal line. Bow shock movement is observed to increase in the upstream direction in the radiation images, increasing the number of spectra to fit.

After $t = 100$ µs, the temperature immediately downstream of the bow shock location begins to drop below the frozen value. Figure 5.19 shows the decrease in measured temperature in the post-bow shock gas using an exposure time within $110 - 120$ µs

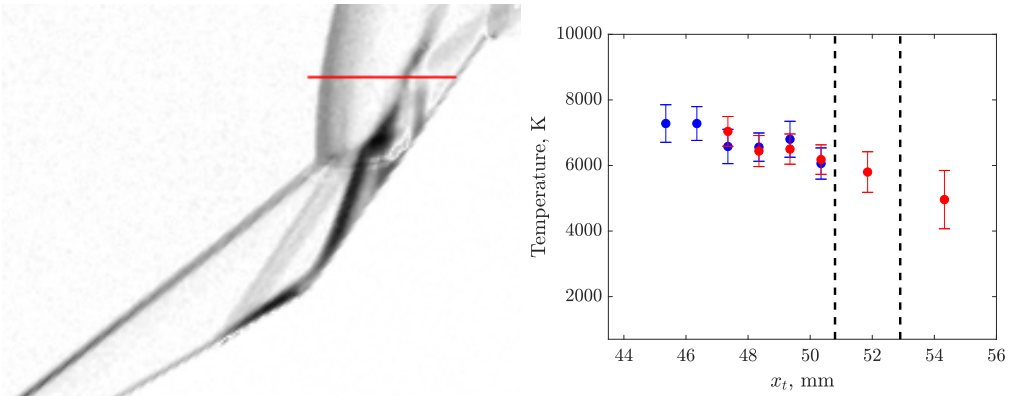

(a) Schlieren Image $t = 120\mu s$ (b) $T_v = T_r$ Profile

Figure 5.19: Temperature profile at $t = 110 - 120$ µs along a horizontal line located $y_t = 42.62$ mm above the wedge tip. A red line 12 mm long shows the interrogation region of the spectroscopy optics in the schlieren image. Multiple colors in temperature plot represent repeat experiments at different x_t ranges. Vertical dashed lines mark the three-dimensional feature of shear layer and reflected waves.

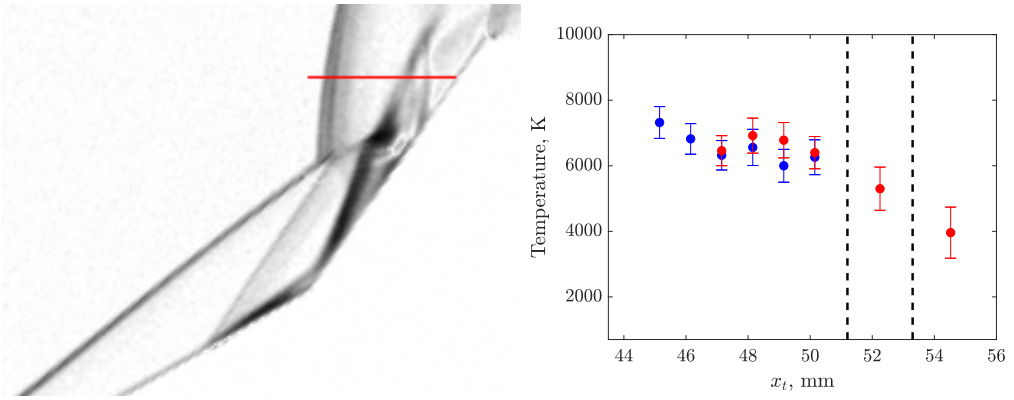

(a) Schlieren Image $t = 145\mu s$ (b) $T_v = T_r$ Profile

Figure 5.20: Temperature profile at $t = 135 - 145$ µs along a horizontal line located $y_t = 42.62$ mm above the wedge tip. A red line 12 mm long shows the interrogation region of the spectroscopy optics in the schlieren image. Multiple colors in temperature plot represent repeat experiments at different x_t ranges. Vertical dashed lines mark the three-dimensional feature of shear layer and reflected waves.

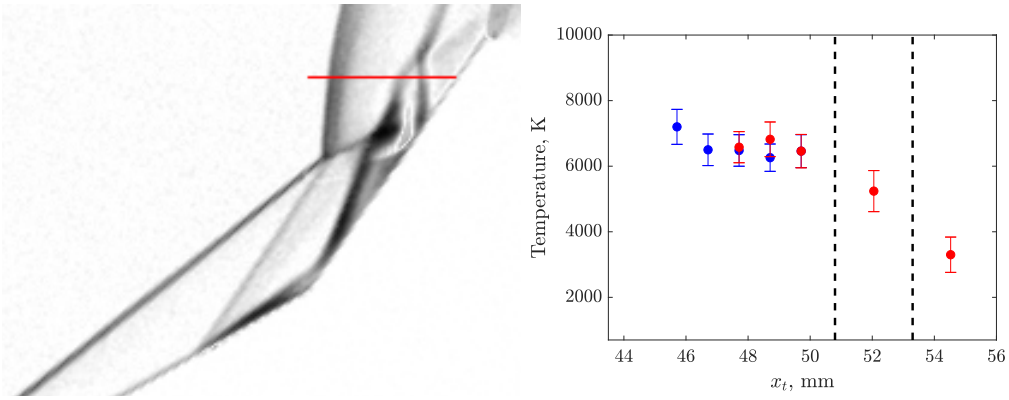

(a) Schlieren Image $t = 160\mu s$ (b) $T_v = T_r$ Profile

Figure 5.21: Temperature profile at $t = 150 - 160$ µs along a horizontal line located $y_t = 42.62$ mm above the wedge tip. A red line 12 mm long shows the interrogation region of the spectroscopy optics in the schlieren image. Multiple colors in temperature plot represent repeat experiments at different x_t ranges. Vertical dashed lines mark the three-dimensional feature of shear layer and reflected waves.

of the test gas. The frame corresponding to the end of this exposure time shows that the bow shock has moved upstream with the triple point location further below the horizontal line. In the schlieren image, the bow shock is observed to remain approximately as a normal shock. For the remainder of the test gas, the post-shock temperature continues to be measured below the frozen value of 8105 K, indicating that the gas is becoming colder with time. The decrease in gas temperatures explains the reduction in the measured signal intensity in Fig. 5.11, which indicates a drop in NO(A) production.

Based on the temporal changes of detector signals and extracted temperatures, there is strong evidence indicating that post-bow shock gas is decreasing in temperature for the later portion of test time. Three phenomena could explain a drop in temperature: the increased relaxation along the streamlines, three-dimensionality of the bow shock, and unsteadiness of the freestream state. Recall that streamlines turn upward after being processed by the bow shock as indicated by the orientation of the shear layer. As a result, the relaxation of a streamline is determined by the distance traveled from where the streamline originated along the bow shock and its frozen state. Since streamlines originating from the triple point have the longest progression, it is likely that the downward movement of the triple point will result in colder measured temperatures. In addition, downward movement of the triple point introduces additional curvature of the bow shock at the location of the slits. To aid in answering the question of streamline relaxation, computations of double

wedge flow from other groups can be studied to determine if a drop of approximately 900 K is due to the positioning of flow features. A two-dimensional computation of the M7-H8-He condition in the HET was performed by Tumuklu et al. using a direct simulation Monte Carlo method [93]. A different approach was taken by Khraibut and Gai, where a reactive Navier-Stokes solver US3D is used to perform two-dimensional calculations of the same freestream condition and model geometry [46]. In the computation of Tumklu et al., the time evolution of streamlines and temperature distribution is shown in Fig. 17 of the paper. A streamline originating at $y_t = 40$ mm is shown in the reference, closely approximating the location of the slits in the present experiment. The DSMC calculation does not predict a dramatic decrease in post shock temperature between $t = 80$ µs, $t = 300$ µs, and $t = 400$ µs. A similar plot is shown in the two-dimensional CFD computation by Khraibut and Gai in Fig. 16 of the reference. Contours of translational-rotational temperature were shown for 70 µs, 120 µs, and 160 µs. However, no decrease in post-shock temperature is observed along $y_t = 40$ mm due to the movement of the triple point and added curvature of the shock. Therefore, the drop in measured temperature may not be due to the positioning of flow features at later times. It is important to note that current high enthalpy simulations of double wedge flow contain discrepancies in the location of some flow features such as separation [47]. Therefore, some caution must be used when comparing simulation with experiment.

Three-dimensional effects may also play a role in the drop in post-shock temperatures and signals. For example, Fig. 5.17a shows three-dimensionality of the bow shock as indicated by the presence of multiple shocks. This image corresponds to a time of $t = 80$ µs, where three-dimensionality in the reflected shocks is also observed. The effect of three-dimensionality is to smear radiation about the mean shock location relative to the slit, reducing the measured post-shock temperature. This is shown schematically in Fig. 4.4, where the collection volume of the optics integrates through any curvature of the shock wave.

Freestream unsteadiness is another candidate in explaining the reduction in measured signals and post-shock temperatures. Due to the lack of time of arrival measurements, the state of the freestream can only be inferred indirectly through the pitot trace during emission experiments. Figure 5.22 is a pitot measurement during a M7-H8-A experiment. The arrival of the contact surface corresponds to $t = 0$ µs, where a rise in stagnation pressure is measured. In this example, the pitot trace continuously rises in pressure throughout test time. This is in contrast to a constant

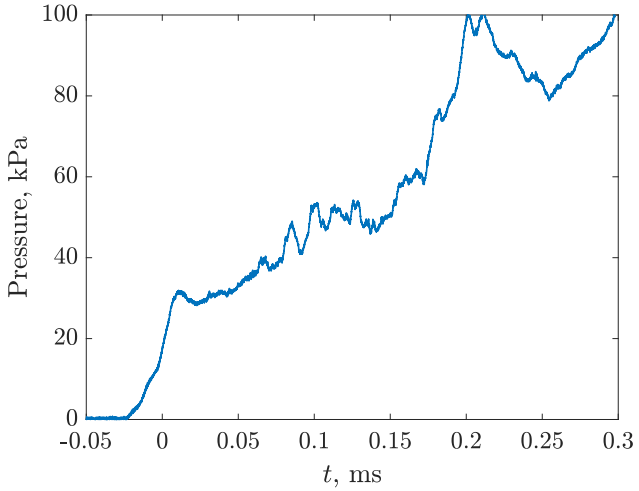

Figure 5.22: Example pitot trace of M7-H8-A. A PCB 113B26 transducer mounted at the centerline and within the tube is used for the measurement. Arrival of the contact surface is defined to be $t = 0$ µs

pressure value predicted by inviscid calculations. The test time of 163 µs does not account for viscous effects in the operation of the tube. In an experimental study by James et al., the effective test times in the X2 expansion tube can be as short as 45% of the total test time for certain conditions, with all measured test times lower than calculations [43]. Therefore, it is possible that the freestream state is unsteady for later test times. Until diagnostics are developed to accurately determine the freestream condition, a viscous simulation of the M7-H8-A condition is required to assess the extent of unsteadiness.

5.4 Two-Temperature Calculations of Oblique Shock System

Streamlines traveling through a system of multiple oblique shocks experience thermal non-equilibrium due to the long time scales for vibrational relaxation compared to the local flow time. In addition, the temporal evolution of the system of oblique shocks causes changes to the extent of temperature relaxation. To understand the effects of thermal non-equilibrium in the oblique shock portion of the flow, the Landau-Teller calculation with a two temperature model of chemical reaction rates can be used to compute flow properties. Within the Shock and Detonation Toolbox [51], the Landau-Teller relaxation calculation is only configured for normal shocks. In order to solve for the reaction zone along streamlines in an oblique shock system, a mapping of the normal shock calculation is applied assuming no curvature exists in the shock and no viscosity. For each wave, the normal component of the gas

velocity relative to the shock is used for the jump condition. The upstream condition can be in thermochemical non-equilibrium. The resulting reaction zone calculation is mapped to lab frame coordinates by assuming that the velocity component parallel to the wave is conserved after the shock jump. Geometry of the oblique shock system is measured from schlieren videos of M7-H8-A presented in Fig. 5.4.

Two-Shock System

Early in test time, double wedge flow forms as a two-shock system consisting of the lead oblique shock and the reattachment shock at the location of the hinge. From the schlieren movies, $t = 45$ µs is used to obtain measurements of the wave angles for a two-temperature reactive Landau-Teller calculation. The lead oblique shock is measured to have a wave angle of $\beta_L = 38.6° \pm 0.5°$ and the reattachment shock is measured to be $\beta_R = 42.1° \pm 0.5°$. The perfect gas freestream condition is used as the inflow state for the lead oblique shock wave.

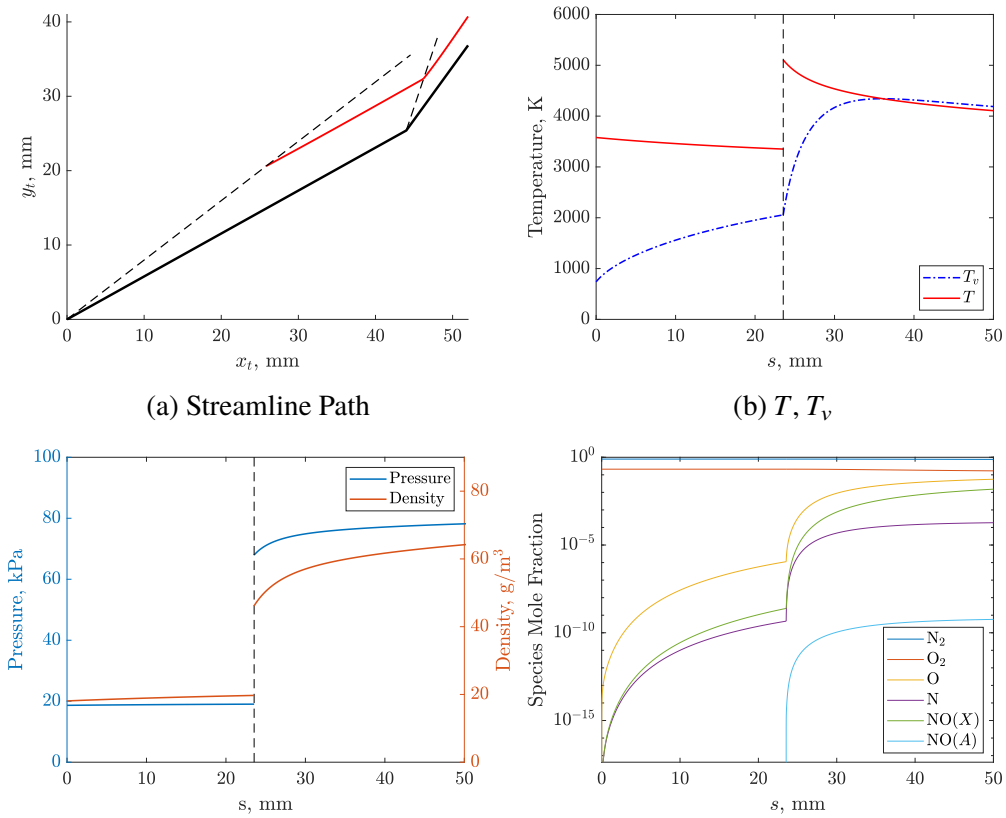

(a) Streamline Path

(b) T, T_v

(c) Pressure and Density

(d) Mole Fractions

Figure 5.23: Calculation of a two-shock system using a two-temperature reactive Landau-Teller relaxation model. Wave angles are taken from $t = 45$ µs in schlieren images.

Figure 5.23 shows a calculation of the reaction zone along a streamline for a two-shock system. In this calculation, the selected streamline originates 33 mm along the length of the lead oblique shock. The path of the streamline is shown alongside the geometry of the double wedge in Fig. 5.23a, where the shocks are represented as dashed lines and the wedge surface is shown as solid black lines. In the immediate vicinity of the shock wave, curvature of the streamline occurs due to the endothermic relaxation of the gas. Further downstream, the streamlines become approximately straight. In Fig. 5.23b, the two-temperature profile is shown along a streamline. Due to the supersonic velocity of the gas, it is observed that the gas remains in thermal non-equilibrium before arriving at the reattachment shock. Once another shock jump occurs, the translational-rotational temperature increases a second time to a value of 5106 K. Vibrational temperature rises faster after the second oblique shock, eventually becoming in equilibrium with T approximately 10 mm downstream the second shock. A plot of pressure and density is also shown, where pressure jumps to a calculated value of 68.0 kPa immediately downstream of the reattachment. Finally, a plot of the species mole fraction is shown in Fig. 5.23d. As expected, little dissociation occurs downstream of the lead oblique shock due to low post-shock temperatures. Calculated values of NO(A) mole fraction are on the order of $X = 10^{-16}$ in this region. At the reattachment shock, species dissociation begins to occur, as the mole fractions of minor species begin to increase. Values of NO(A) reach over $X = 10^{-10}$ downstream the reattachment shock, over two orders of magnitude lower than the normal shock case with M7-H8-A. Therefore, it is expected that measurements behind the reattachment shock will require more exposure time and camera gain for low signals.

Three-Shock System

After flow startup, the boundary layer separates and the separation region grows in length. This generates an additional separation shock to the geometry, turning the flow a second time before arriving to the reattachment shock. It is possible to extend the calculation to add a third shock wave. To represent the final state of the shock structure at the end of test time, a frame taken at a time $t = 150$ µs will be used to extract the wave angles. Measured wave angles of $\beta_L = 38.6° \pm 0.5°$, $\beta_S = 26.5° \pm 0.5°$, and $\beta_R = 40.0° \pm 0.7°$ were obtained for the lead, separation, and reattachment shocks, respectively. This will serve as a representation for the final time interval used in radiation measurements downstream the reattachment shock.

Figure 5.24 shows a two-temperature reactive Landau-Teller calculation of a stream-

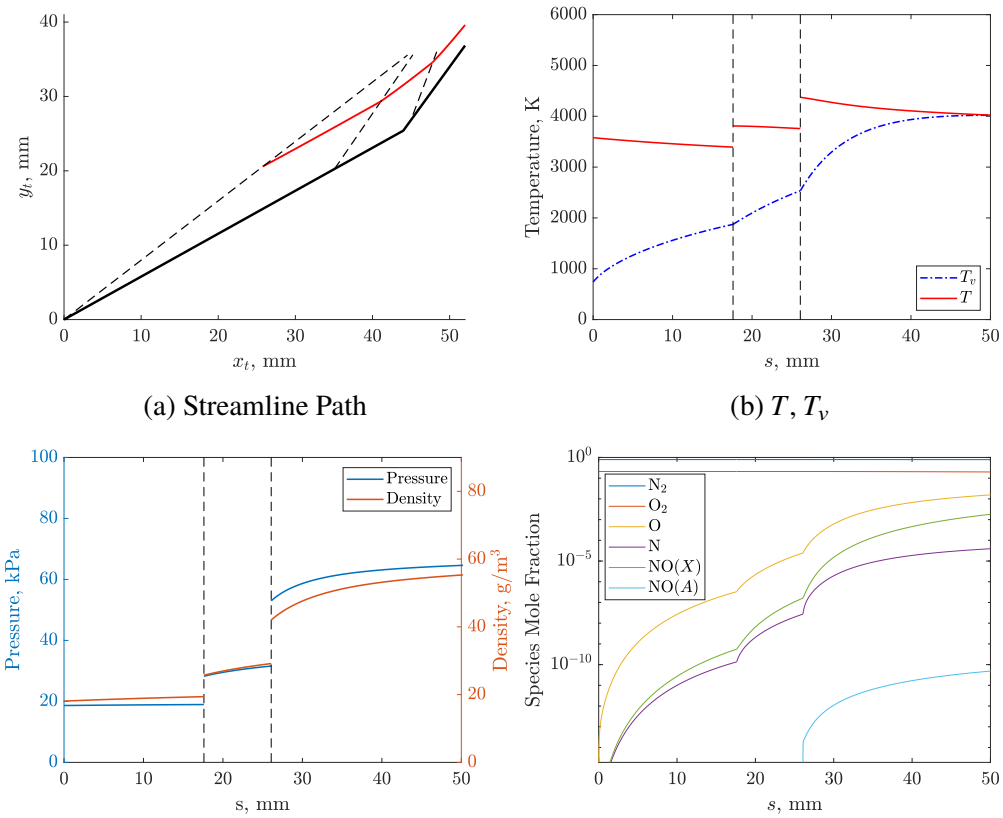

(a) Streamline Path

(b) T, T_v

(c) Pressure and Density

(d) Mole Fractions

Figure 5.24: Calculation of a three-shock system using a two-temperature reactive Landau-Teller relaxation model. Wave angles are taken from $t = 150$ µs in schlieren images.

line processed by three oblique shocks. The same initial conditions for the streamline are used in this calculation to compare with the two-shock case. Similar to the two-shock calculation, curvature in the streamline is observed in the immediate vicinity of the lead oblique shock before becoming approximately straight. At the separation shock location, the flow turns upward. A jump in translational-rotational temperature of 3809 K is observed, while pressure jumps to 28.2 kPa. Once the gas is processed by the reattachment shock, the flow turns a third time upward. The frozen translational-rotational temperature is calculated to be 4373 K, while pressure jumps to 53.0 kPa. The mole fractions of the minor species show that little dissociation continues to occur downstream of the separation shock, meaning the reattachment shock is expected to have the most NO γ signal in this portion of the flow. However, the magnitude of NO(A) mole fraction is considerably less than in the two-shock case.

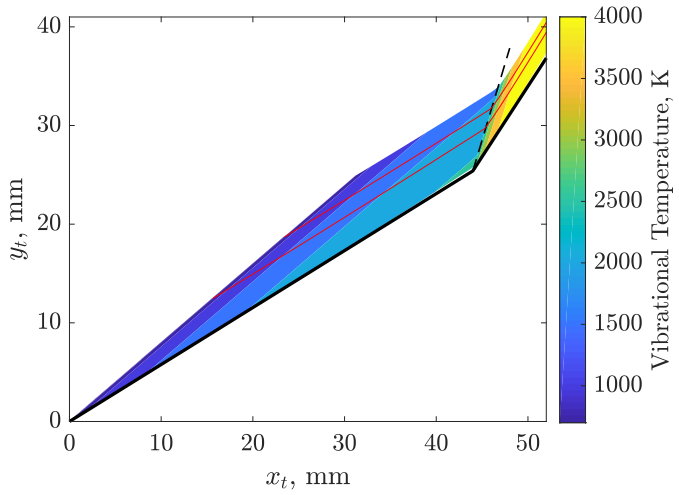

(a) Two-Shock Contour of T_v

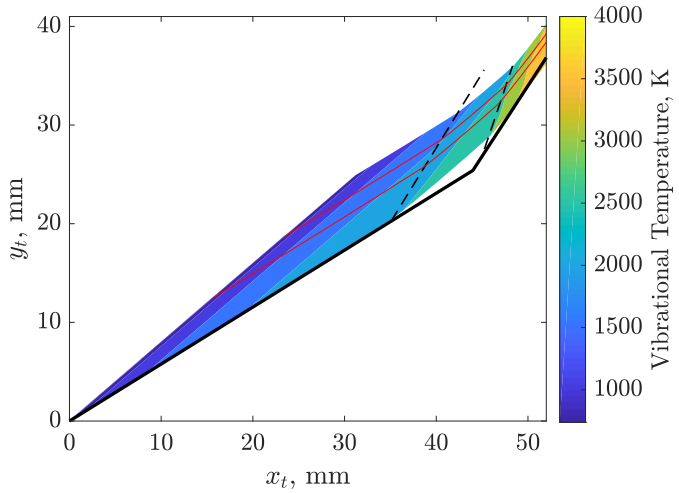

(b) Three-Shock Contour of T_v

Figure 5.25: Contours of vibrational temperature for a two-shock and three-shock system. Streamlines are shown as solid red lines, shock locations are dashed lines, and wedge geometry is shown as solid black lines.

For a comparison, multiple streamlines have been computed for both the two-shock and three-shock systems. Figure 5.25 shows the contours of the vibrational temperature of multiple streamlines. Red solid lines are two representative streamline paths with the same initial coordinates between the two cases. It can be observed that the rate of vibrational relaxation is different with the addition of the separation shock. In the three-shock case, the streamline originating at the origin shows a region representing the separation bubble, indicated by the absence of contour color. The separation region ends at the surface of the second wedge. Note that viscosity is

not taken into account in these calculations and may not represent the true behavior of the unsteady separation region. In both cases, the streamlines are spaced 10 mm along the lead shock wave. After multiple compressions, the streamlines eventually coalesce and are spaced close together downstream of the reattachment shock. Gradients in T_v occur perpendicular to the streamline direction. This is a result of streamlines being processed by the shock waves at different times in the relaxation of the gas.

The most notable differences between the two-shock and three-shock cases are the translational-rotational temperature and pressure immediately downstream of the reattachment shock. With the addition of the separation zone, the flow is allowed to gradually turn a second time upstream of the hinge. As a result, both the frozen translational-rotational temperature and pressure downstream of the reattachment shock decrease later in test time.

From the experimental studies of Davis and Sturtevant [20], a scaling for the separation length was proposed to be of the form:

$$\frac{L_{sep}}{x_1} \propto \left(\frac{p_3 - p_2}{p_1}\right)^{3/2}, \tag{5.1}$$

where L_{sep}/x_1 is the normalized separation length and p_1, p_2, p_3 are the post shock pressure of the lead, separation, and reattachment shock, respectively. Recall that the scaling is based on a momentum balance proposed by Roshko [82] for supersonic base flows. A rise in pressure p_3 requires a longer separation length to impart the necessary shear stress along the dividing streamline to maintain the momentum balance. The scaling shows that the separation length is proportional to $(p_3 - p_2)^{3/2}$. From Fig 5.8, the measured separation front shows a decrease in upstream velocity with time. Within the same time frame, the reattachment shock experiences a reduction in β_R that slows in the later portions of test time in Fig. 5.9. We observe similar time scales in the evolution of the separation and reattachment shock, consistent with the idea that these features are linked, as described in the base flow model of Roshko. In addition, the dissociation behind the reattachment shock leads to a reduction in shock angle. A perfect gas calculation of the reattachment shock results in a shock angle of $\beta_R = 48.0°$, significantly larger than what was measured. Due to the larger wave angle, the perfect gas pressure is 89.1 kPa downstream of the reattachment shock. Therefore, the two-temperature reactive Landau-Teller calculation shows that dissociation behind the reattachment

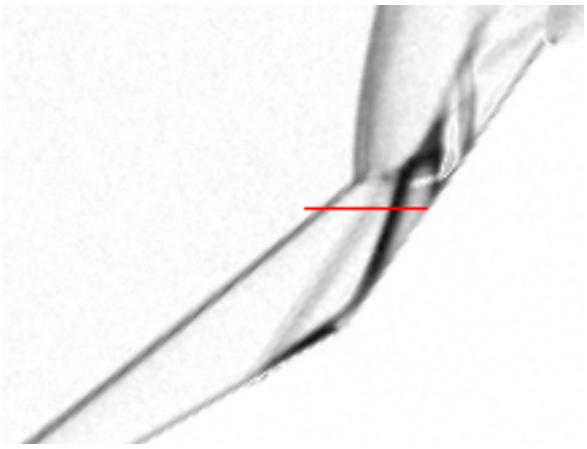

Figure 5.26: Schlieren image at t = 110 µs. A red line 9 mm long represents the orientation of the spectrometer slits in the flow.

shock decreases the post-shock pressure relative to the perfect gas case due to the reduction in shock angle. These observations will later be confirmed with emission experiments, where direct measurements of the NO(A) species will interrogate the state of the gas.

5.5 Emission Measurements in Post-Lead Oblique Shock and Reattachment Shock Region

Previous heat flux measurements indicate that peak heating of double wedge flow occurs at the location of the reattachment shock. In addition, the state of the gas downstream of the reattachment shock may determine the growth of the separation region in double wedge flow. Due to interest in understanding how the reattachment shock plays a role in flow development and unsteadiness, the post-shock reattachment region will be investigated through ultraviolet radiation measurements. Optics are aligned such that the image of the horizontal slits are oriented y_t =33.91 mm above the leading wedge tip. This vertical location is selected based on the schlieren videos for providing the maximum volume for emission measurements. The field of view is set approximately 8 mm upstream of the second wedge surface. Along this line, emission from the reattachment shock and a portion of the post-oblique/separation shock is recorded.

Optical Depth Effects of Post-Reattachment Shock Gas

Recall from Section 3.2 that optical depth of a gas is a strong function of the number density of NO(X) absorbers at the relevant vibrational levels for UV transitions. As the wavelength range of interest is dominated by transitions from NO(A) v'=

0 vibrational levels to v" levels in the ground state, colder temperatures push the population of NO(X) to v" = 0 levels as described by the Boltzmann fraction. The result is increased optical depth for electronic transitions to lower vibrational levels of the ground state in the 225-250 nm range of wavelengths. Based on calculations of the oblique shock system, reattachment shock temperatures are expected to be lower than the bow shock flow and gas density is significantly higher, meaning the extent of self absorption must be investigated before spectrum fitting is performed.

The oblique shock system was calculated in Shock and Detonation Toolbox assuming an equilibrium process and a two-temperature reactive Landau-Teller calculation. For the equilibrium calculation, the measured separation shock wave angle from high speed schlieren videos is used for computing the post-separation shock state, while all other wave angles are calculated. Assuming equilibrium processes, Table 5.1 lists the ratio of optically thin to full transport intensities for the post-reattachment shock gas using Equ. 3.45. A significant deviation from the optically thin limit is observed, meaning that the equilibrium assumption will require fitting strategies to take into account gases with self absorption present. Similar to cylinder measurements of M5-H6-A air, the best pair of vibrational bands that can be used with optically thin synthetic spectra are γ(0,0) and γ(0,1). However, there is now a non-negligible difference between the Ri factors of γ(0,0) and γ(0,1).

Vibrational Band	Ri
γ(1,0)	12.8
γ(0,0)	6.6
γ(0,1)	4.9
γ(0,2)	2.3

Table 5.1: Ratio of intensities computed for the post-reattachment shock state using an equilibrium three-shock system.

In reality, streamlines traveling through the oblique shock system remain in thermochemical non-equilibrium throughout the flow. Figure 5.24 shows that the mole fraction of NO(X) never achieves its equilibrium value within the double wedge geometry. The assumption of equilibrium provides an upper bound of $X = 4.71 \times 10^{-2}$ for the mole fraction of NO(X). To obtain an estimate of the extent of non-equilibrium at the slit location, a streamline originating from the wedge tip ($x_t = y_t = 0$ mm) is computed through three oblique shocks. This provides another bound on the progress of chemical reactions at the location of the horizontal slits. The two-temperature reactive Landau-Teller calculation shows that the mole fraction of

NO(X) is $X = 1.10 \times 10^{-4}$ with a translational-rotational temperature of 4131 K at the location of the slits. At these conditions, the amount of NO(X) is extremely low due to the lack of dissociation occurring within the time scales along the streamline.

For comparison, a Specair 3.0 calculation is performed using the equilibrium assumption and the thermochemical non-equilibrium calculation. Figure 5.27 shows the resulting spectra of an optically thin gas and a gas with self absorption present. A FWHM of 59 cm^{-1} is used to match the experimental settings. A slab of gas for 10 cm and an optically thin spectrum is calculated and compared, with normalization performed for the $\gamma(0,1)$ peak intensity. The Specair calculation confirms that the shape of the spectrum is affected by self absorption with the assumption of equilibrium processes. In addition, all peak heights relative to $\gamma(0,1)$ are not preserved after normalization, further confirming Table 5.1 estimates. If the gas achieves equilibrium, calculations solving the full radiation transport must be performed for accurate comparisons with experimental spectra. However, the two-temperature Landau-Teller calculation results in a spectrum that is unaffected by self-absorption. This is due to the low number density of ground state NO molecules present downstream of the reattachment shock. Since the Landau-Teller reactive calculation provides a more physical description of the flow downstream of the oblique shock, fits of experimental spectra will be performed assuming optically thin conditions. This will later be confirmed in the experimental results, where fits provide low χ^2 values.

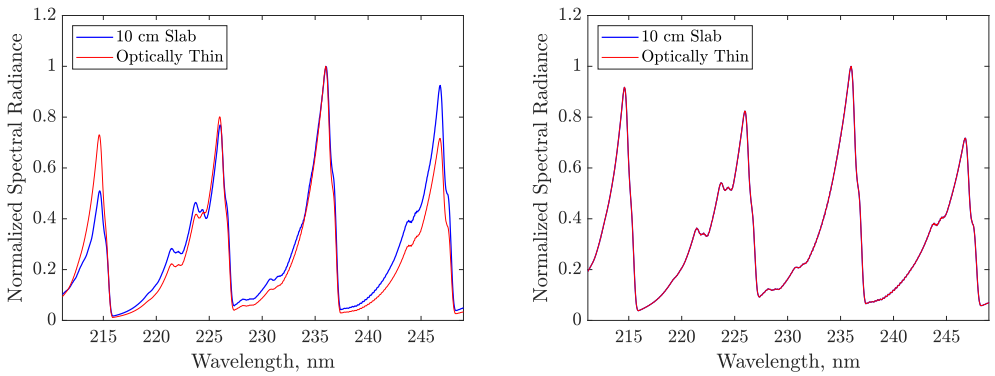

(a) Equilibrium

(b) Non-Equilibrium

Figure 5.27: Specair 3.0 calculation of a slab of gas 10 cm long using gas properties downstream the reattachment shock from an equilibrium calculation and a two-temperature reactive Landau-Teller calculation.

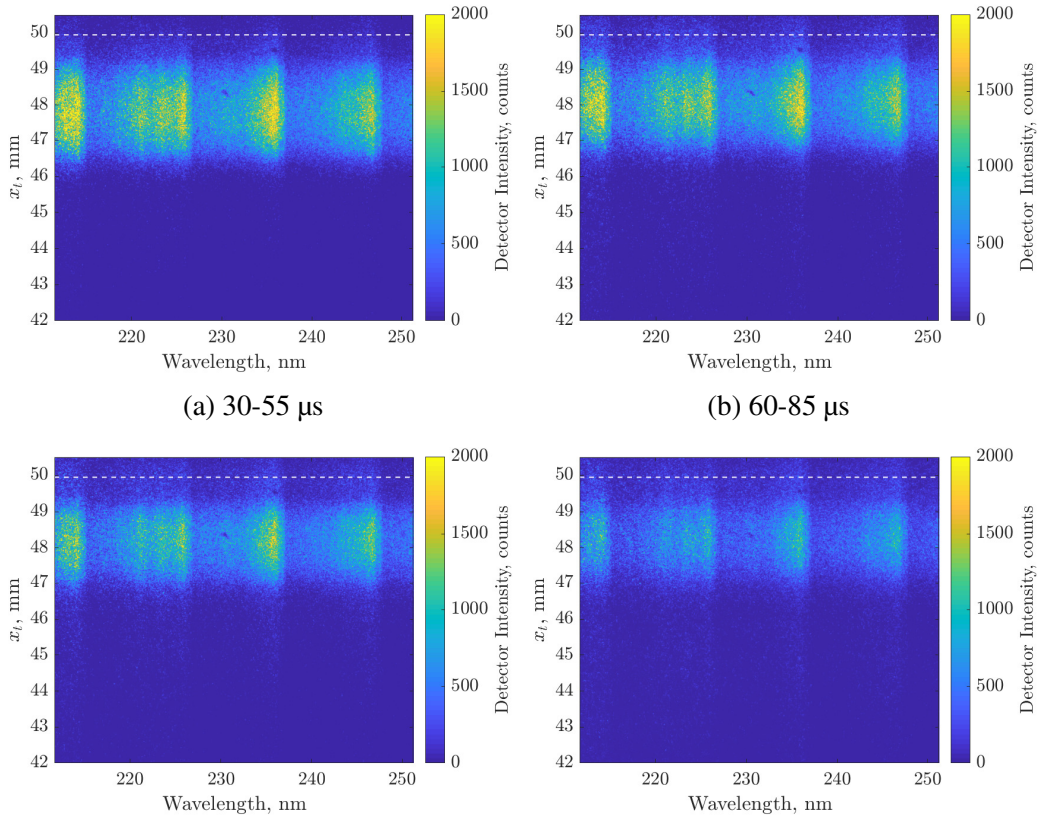

(a) 30-55 µs

(b) 60-85 µs

(c) 100-125 µs

(d) 125-150 µs

Figure 5.28: Emission of post-reattachment shock gas at four intervals throughout test time. Line measurement is performed 33.91 mm above the leading wedge tip. Horizontal distance is referenced to leading wedge tip and dashed lines indicate the location of model surface.

Time Evolution of UV Radiation in post-reattachment shock region

Initial radiation measurements using the camera settings listed in Section 5.3 revealed a cold region with very little production of NO(A), with only 350 counts recorded as the maximum intensity. The poor quality of extracted spectra forced exposure times to be longer than those used in the bow shock measurements. Fortunately, the high speed schlieren videos show that the reattachment shock is relatively stationary and does not experience large oscillation, with only the wave angle changing slightly throughout test time. Therefore, a longer exposure time can be used without concerns of the reattachment shock smearing the detector. A gain of 80 and an exposure time of 25 µs is selected for measurements of the reattachment shock radiation. Figure 5.26 shows an example schlieren frame with a red line 9 mm long indicating the orientation of the slits.

Radiation is measured at four intervals throughout test time: 30-55 μs, 60-85 μs, 100-125 μs, and 125-150 μs. Figure 5.28 contains detector images of the radiation along a line through the post separation and post reattachment shock region of the double wedge flow. The location of the test article surface is indicated by a dashed white line and the position is referenced from the leading wedge tip. The location of the reattachment shock is indicated by region of signal on the images. The start of signal agrees well with the measured reattachment shock location from the high speed schlieren in Fig 5.9. Despite an increase in the exposure time, gas downstream of the reattachment shock have counts much lower than the bow shock measurements. Signal upstream of the reattachment shock is extremely low and within the background noise. However, the faint signal of the post-oblique shock region can be binned to extract a noisy spectrum. Several temporal changes are observed in the data. Overall intensities behind the reattachment shock decrease with time, with the lowest signal occurring in the 125-150 interval. In addition, spatial variations in radiation occur, with radiating gas moving downstream over test time. This is consistent with the movies and Fig. 5.9, where the reattachment shock moves slightly downstream with time along the line. Because the reattachment shock has some three dimensionality in the schlieren videos, it is difficult to determine changes in wave angle. However, the detector images provide evidence that the wave angle is decreasing, as lower detector counts indicate reduced electronic excitation and a colder gas.

Signal-to-noise of the spectra become poor when binning data at 1 mm, especially for later time intervals where intensities are typically below 1000 counts. As a result, binning is increased to 2 mm on the spatial axis of the detector to extract better quality spectra. The region behind the reattachment shock is already on the order of 3 mm, meaning that a temperature profile cannot be generated. However, a larger binning area allows for better confidence in spectrum fitting with a trade-off in spatial resolution. Figure 5.29a plots the time evolution of the emission spectrum downstream of the reattachment shock. The mean shock location in Fig. 5.9 is used to define the start of 2 mm binning. The extracted spectra confirm observations in the detector image, where intensities drop with increasing test time. For the first time, it is now possible to identify the $\gamma(1,0)$ band at λ=215 nm without contributions of other electronic transitions. Figure 5.29b plots the integrated band intensity of $\gamma(0,1)$ for the four time intervals. The horizontal axis is referenced to the wedge tip coordinate system. The vibrational bands also confirm the downstream movement of the reattachment shock along the measurement line and an overall decrease of

signal with time. Similar to cylinder post-shock data, NO γ emission is seen to peak downstream of the shock before decreasing in intensity. As the measurement can be approximated as optically thin, the profile of integrated intensity is directly proportional to the number density of NO(A). The decrease in signal with time indicates colder gas temperatures for the later portions of theoretical test time.

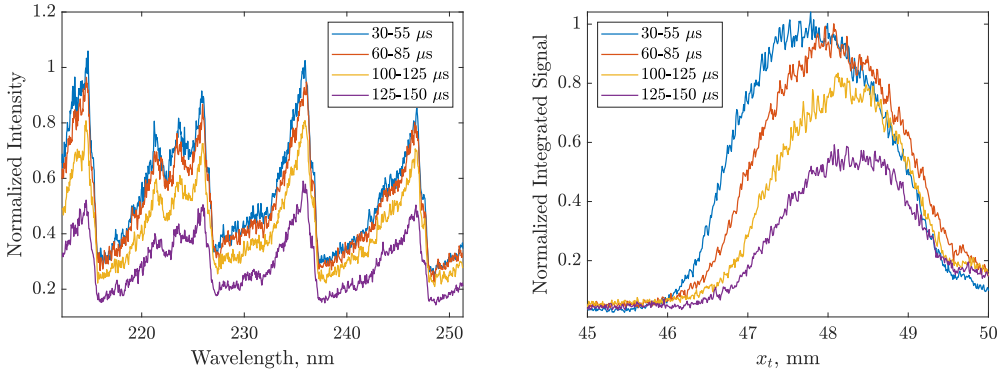

(a) Spectra 1mm downstream of reattachment (b) $\gamma(0,1)$ Vibrational Band Profiles

Figure 5.29: Cross sections of radiation downstream of reattachment shock. All signals are normalized using the 30-55 μs $\gamma(0,1)$ peak to compare relative intensities between time intervals.

Temperature Fits Downstream of Reattachment Shock

Spectrum fits using the NO γ system can be performed using the same procedures used in the bow shock data. Fits are performed in the wavelength range of 227.50 nm -250.00 nm using synthetic spectra computed for $T_v = T_r$ and a FWHM of 59 cm^{-1}. Figure 5.30 plots the effective temperature profile of the post-reattachment shock gas for the four intervals of time. Error bars are the uncertainties from experimental noise following the method of Tibère-Inglesse et al. [92], and vertical lines are the average reattachment shock location measured from high speed schlieren images. The slow movement of the reattachment shock along the slits can be easily observed in Fig. 5.30, where the reattachment shock is relatively stationary only for the last 50 μs of test time. With increasing time, spectrum fits show a general decrease in temperature. The last 50 μs shows that the temperature has stabilized to approximately 4900 K, corresponding to when the reattachment shock is approximately stationary. Table 5.2 lists the extracted temperatures for multiple experiments. Similar to observations in the cylinder data set, the χ^2 method results in slightly higher temperature fits compared to the residual method.

Three pieces of evidence point to a steadily colder gas downstream of the reattach-

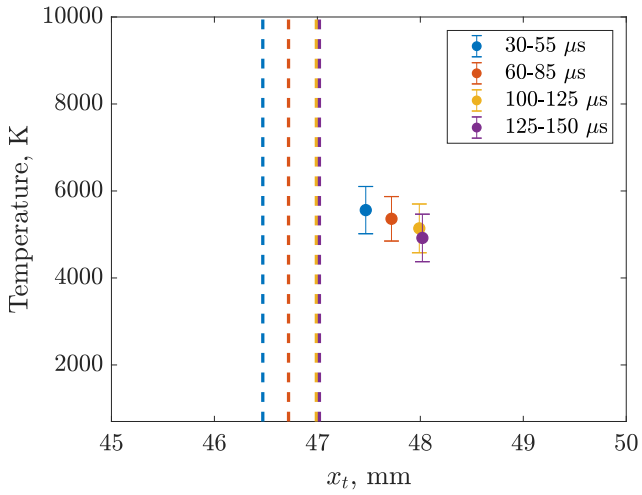

Figure 5.30: Single temperature fits downstream of reattachment shock for different time intervals. Vertical lines are measured reattachment shock locations averaged over each time interval.

Interval, µs	Shot #	T^R, K	T^{χ^2}, K	χ^2	σ_T, K	σ_N, K
30-55	1693	5700	5920	443	81	453
30-55	1698	5360	5560	324	78	543
60-85	1697	5160	5360	307	81	511
100-125	1699	4940	5140	291	82	560
125-150	1694	4340	4640	227	118	647
125-150	1700	4860	4920	290	83	546

Table 5.2: $T_v = T_r$ fits of spectra collected downstream of the reattachment shock for varying time intervals.

ment shock: a reduction in oblique shock angle, reduced emission of NO γ, and lower temperatures from fits. The reduction in signal and temperature is confirmed with the two-shock and three-shock system calculations of the flow field. With the addition of the separation shock, number densities of NO(A) are predicted to decrease downstream of the reattachment shock. In addition, a reduction in post shock temperature is predicted for the reattachment shock in the three-shock calculation. Therefore, trends in the calculations are consistent with the experiment.

Measurement of post-oblique and separation shock region

Gas downstream of the lead oblique shock and the separation shock contains the lowest UV emission out of every region investigated by the current technique. The combination of low post-shock temperatures and low density require long exposures for post-oblique shock measurements. An experiment is performed with an exposure

time of 100 µs and a gain of 99 to obtain the maximum possible counts in the region upstream of the reattachment shock. As separation length grows throughout test time, smearing from the separation shock is likely for an exposure time of 100 µs. However, from calculations of the three-shock system, the separation shock slightly increases the temperature by 230 K. Therefore, smearing of the separation will only contribute a minor increase in the measured temperature.

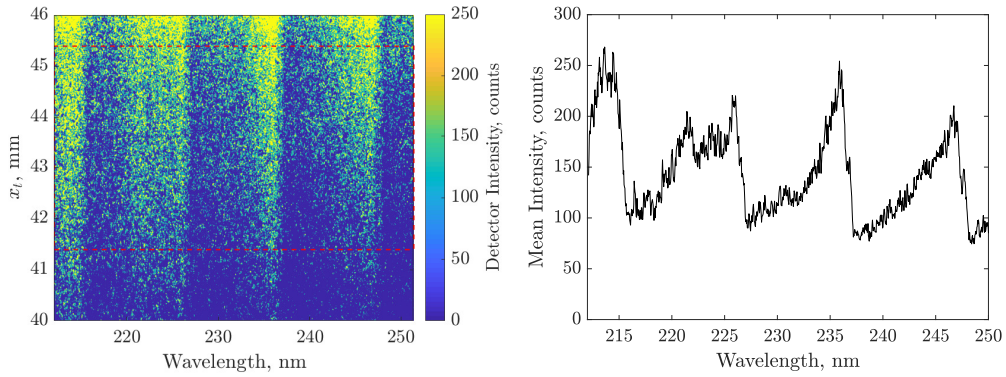

(a) Post-Oblique Shock Radiation (b) Extracted Spectrum

Figure 5.31: Detector image of radiation downstream of the lead oblique shock. An exposure time of 100 µs was used in obtaining radiance. Rectangle represents region used for binning.

Figure 5.31 shows a detector image of radiation downstream of the lead oblique shock with the exposure occurring 30-130 µs in test time. The maximum counts in the contour levels is selected to be 250 counts in order to visualize the region of interest, saturating the signal downstream of the reattachment shock. The red dashed lines represent the region in which binning was performed, starting at the mean lead oblique shock location of x_t = 41.4 mm measured from the schlieren videos. To obtain the best quality spectrum for these low signals, binning was performed with an increment of 4 mm on the spatial axis of the detector. The result of the large binning provides a spectrum in Fig. 5.31b with favorable signal-to-noise. A Specair 3.0 calculation of a frozen temperature and equilibrium number density of NO shows that the region can be assumed to be optically thin. Therefore, fits in this region will be performed using the optically thin method applied in the bow shock of M7-H8-A for double wedge flow and cylinder flow. When performing the optically thin fitting procedure on the extracted spectrum, a temperature of 4520 K was obtained with χ^2 = 180, σ_T = 157 K, and $\sigma_N = 577K$.

Additional experiments using an exposure of 50 µs and a gain of 80 were performed

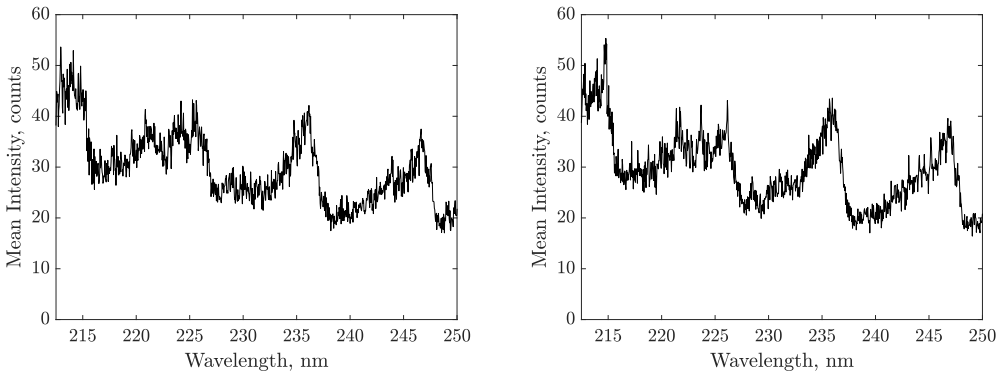

(a) 50-100 µs (b) 100-150 µs

Figure 5.32: Extracted spectra downstream of lead oblique shock region for an exposure time of 50 µs. Two intervals in test time are presented and detector binning was done with a 4 mm region on the position axis.

to investigate any possible temporal changes in the post-oblique shock region. Figure 5.32 shows the extracted spectra of the post-oblique shock region at two different intervals in test time. Binning was performed using the same 4 mm region from the 100 µs case for comparison. Signals are substantially lower than Fig. 5.31b due to the reduced exposure time and gain. Unlike the reattachment shock region, signal intensities downstream of the lead oblique shock are similar in the two time intervals.

5.6 Concluding Remarks

A new set of emission measurements have been performed of a shock/boundary-layer interaction that provides a direct measurement of the thermochemical non-equilibrium present in the flow. To complement the spectroscopic technique, schlieren imaging is performed at higher frame rates and improved resolution compared to previous measurements. New videos reveal the effects of facility startup, where the post-shock acceleration gas initializes the separation length before the arrival of the test gas. Two freestreams with identical conditions, but different acceleration gases, show that development of flow features occurs at shifted times depending on the initial separation before the test gas. As a result, the M7-H8-A condition is selected for emission measurements due to the lack of separation at $t = 0$ µs.

Emission measurements downstream of the bow shock show temperatures approaching the thermally and chemically frozen limit of 8105 K and relaxing to values well above the equilibrium temperature. Radiation is measured in the post-shear layer

region as well, revealing colder temperatures relative to the post-bow shock gas. Later portions of test time result in colder post-bow shock temperatures below the thermally frozen limit. Unsteadiness in the freestream, three-dimensionality of the bow shock, and increased relaxation along streamlines are considered to be likely causes for the drop in post-shock temperatures.

Another set of emission measurements were performed in the post-lead oblique shock and reattachment shock region of the double wedge flow. Detector images and spectrum fits reveal a cold region with low signals of NO γ. Similar to the bow shock data, post-reattachment shock gas becomes colder with increasing test time. This is likely a result of the feedback between the separation shock and the reattachment shock angle. These measurements are confirmed with two-temperature calculations of the shock system, which also indicate a colder gas downstream of the reattachment shock for a shock system later in test time.

Chapter 6

CONCLUSIONS

A diagnostic for measuring spatially resolved emission spectra has been successfully designed and implemented in the Hypervelocity Expansion Tube facility. Spatially resolved emission in the post-shock relaxation region for Mach 7.2 and Mach 4.9 flow over a cylinder have been measured for freestream mixtures with varying O_2/N_2 mole fractions. High resolution schlieren images of the cylinder flow were obtained for accurate measurements of standoff distance. For the higher enthalpy air condition, temperature profiles have been obtained through spectrum fitting of NO $\gamma(0,1)$ and $\gamma(0,2)$ transitions, which are shown to be a strong function of T_r. Measured temperatures immediately downstream of the shock agree with the thermally frozen limit of 8105 K. However, a slow relaxation of the post-shock gas is observed when compared to a state-to-state calculation of translational-rotational temperature. For the low enthalpy condition, a portion of the stagnation streamline cannot be approximated as optically thin, leading to the development of a procedure to check what vibrational bands can be used in fitting synthetic spectra. It was found that the $\gamma(0,0)$ and $\gamma(0,1)$ bands in the experiment can be fit with optically thin synthetic spectra if self absorption is present. Single temperature profiles for lower enthalpy air conditions agree with the state-to-state calculation, providing evidence that the fitting method is reliable.

The presence of other electronic states prevents full comparisons of NO γ computations to be made with the entire wavelength range of experimental spectra. The inclusion of NO β and NO δ through the use of the electronic excitation temperature T_{ex} was shown to dramatically improve fits with the cylinder data. A three temperature fit of a spectrum immediately downstream of a shock for the Mach 7.2 air freestream revealed that all three temperatures are not in equilibrium with one another, with $T_{ex} = 3750$ K and $T_v = 6390$ K. This is in contrast to the typical $T_{ex} = T_{v,bulk}$ and $T_{ex} = T_{tr}$ assumptions in the literature [18, 26]. Based on the distribution of χ^2 for multi-temperature fits, the 210-250 nm range of wavelengths remains insensitive to T_v, with higher sensitivity found in T_{ex} followed by T_r. It was shown that the population of upper electronic states increases as oxygen is removed in the freestream from fits of T_{ex}. Calculated NO(A) number density profiles from a two-temperature reactive Landau-Teller model correctly predict an increase

in NO(A) peak production when reducing freestream oxygen mole fraction from $X_{O_2} = 0.273$ to $X_{O_2} = 0.105$, matching observations in the experiment. However, poor agreement was observed in the profile of NO(A) when compared to measured integrated radiance of $\gamma(0,1)$, suggesting that further work in kinetic rates for oxygen quenching and ray tracing methods are required for better predictions.

A new set of experiments were performed using a 30-55 degree double wedge at Mach 7.2 with stagnation enthalpy of 8.1 MJ/kg. High resolution schlieren images were recorded at a frame rate of 400 kHz for detailed measurements of flow features. Facility startup was revealed to heavily determine initial separation length, where post-shock acceleration gas separates the flow before the arrival of the test gas. Two freestreams with identical calculated conditions, but different acceleration gases were ran with the double wedge geometry. A shift of approximately $\Delta\left(\frac{L_{sep}}{x_1}\right) = 4.1 \times 10^{-2}$ in separation length is observed when operating with an air acceleration gas versus a helium acceleration gas for the same period in test time. Tracking of major features have been performed, where the separation front is observed to decrease in velocity with time. Oscillations in the bow shock location and shear layer were observed throughout the theoretical test time of 163 µs.

Emission measurements in the post-bow shock region were taken at seven time intervals throughout test time. Post-bow shock gas shares similar features early in test time with post-shock radiation of cylinder flow, where signals peak downstream of the shock location and measured temperatures approach the thermally-chemically frozen limit of 8105 K. Radiation is measured downstream of the shear layer and reflected shock location, where a drop in temperature is measured compared to the bow shock gas. Spatial variations in the measured ultraviolet radiation coincide with observed features in the schlieren videos. After 100 µs, a dramatic drop in signals was observed for the NO γ emission. This point of time also coincides with a drop in measured temperatures downstream of the bow shock, where post-shock temperatures fall approximately 900 K compared to early in test time. Increased relaxation along streamlines from the downward movement of the triple point and unsteadiness in the freestream were discussed as possible causes. Additional characterization of the freestream using time of arrival measurements or other spectroscopic methods is required to determine freestream steadiness.

Emission measurements in the post-reattachment shock region were also performed for the double wedge flow. Signals and measured temperatures were observed to be significantly lower than in the bow shock flow. Data were collected in four time

intervals, revealing a continuous drop in signals and temperatures. The cooling of the gas was confirmed with two-temperature reactive Landau-Teller calculations of the flow field. It was shown that dissociation behind the reattachment shock decreases the post-shock pressure relative to the perfect gas case through the reduction in shock wave angle. The reduction in post-shock pressure is likely linked to the slowdown in separation length observed in the schlieren videos based on the scaling proposed by Davis and Sturtevant [20]. Finally, radiation measurements of the post-lead oblique shock were attempted, but low signals prevented accurate temperature fits.

This work provided the first spatially resolved measurement of NO γ radiation in a hypervelocity double wedge flow. Strategies developed for extracting quantitative properties of a radiating gas also provide a valuable contribution to the field of hypersonics, as there are frequent situations where a gas can contain multiple electronic transitions and exhibit self-absorption. The results from this work highlight the importance of three-dimensional, unsteady calculations of double wedge flows. This includes modeling flow startup processes and time accurate comparisons between simulations and experiments. Overall, emission spectroscopy remains an effective tool for measuring molecular processes in hypervelocity flows.

6.1 Future Work

Freestream characterization continues to be a priority for future experimental work in the expansion tube, as flow measurements are sensitive to inflow conditions. To investigate the possibility of freestream unsteadiness, bow shock emission measurements of cylinders can be performed with shorter exposure times. Due to the simplicity of stagnation flow compared to double wedge flow, it will allow the radiation measurement to be decoupled from the fluid dynamics involved. Diagnostics are being developed to measure time of arrival of shocks generated from processes in the expansion tube. Viscous simulations, such as the ones previously carried out by McGilvray et al. [65], are in progress for all freestream conditions. This will provide better confidence in the freestream conditions and may resolve discrepancies found in comparisons between experiments and computations.

Absolute radiance measurements can significantly help in understanding the relationship between the ground state and electronic states of NO. When combined with absorption measurements of ground state NO, absolute radiance provides an experimental measurement of T_{ex} and the number density of NO(A). Comparisons between freestream conditions or spatial locations also benefit from measurements

corrected for absolute radiance, as camera settings often have to be changed to increase signal levels. Corrections for absolute radiance require special considerations and equipment during calibration. If a UV calibration source generates radiance on the same order as the experiment, then absolute radiance calibration only requires a measurement of the source at the camera settings used in experiment. If a light source is too dim to use with the experimental camera settings, a second approach is to determine the reciprocity factor of the intensified camera. In the current work, exposure times of the deuterium lamp are on the order of 100 ms, several orders of magnitude larger than in the experiment. Determining the reciprocity can convert counts in one camera setting to W/(cm^2-sr-μm) in another camera setting. If a grating is used for coarse measurements, it is also possible to use multiple calibration lamps to anchor dimmer light sources to other sources with known radiance.

The emission measurements made in this work are valuable validation data for modelers to use in comparing with simulations. To effectively use these data, simulations must be implemented with chemical kinetics of electronic states, radiative transport, and a model for thermal non-equilibrium. Although comparisons can be made with the single temperature fits, direct comparisons with the experimental spectra is the ideal method for judging the capability of simulations. An emission spectrum contains the distribution of excited NO molecules amongst the electronic, vibrational, and rotational energy states. In addition, information on self-absorption is also contained in an experimental spectrum for cases that are not optically thin. Coupling the radiative transport to the fluid mechanics is then required to accurately model the spatial and temporal dependence of the emission. A simulation that can model these physical processes can directly compare with the experimental spectra through the χ^2 metric for goodness of fit.

The capabilities of the emission spectroscopy diagnostic can be further expanded by investigating other wavelength ranges and measuring additional species. The best candidates for future emission work would be OH and N_2^+, which are readily accessible with the present setup. Varying the magnification of the collection optics can allow for imaging a larger portion of the flow. Changing the grating type can also allow for course measurements of the radiation, where tools such as NEQAIR are better suited for computing large wavelength ranges.

Results from the integrated intensities indicate additional improvements can be made to either the kinetics of NO(A) or the thermal non-equilibrium model used in post-shock calculations. To improve on comparisons, ray tracing can be performed to

transform a slab of radiating gas to a stagnation streamline profile. Three temperature fitting of an entire profile remains a possibility for all optically thin measurements. Computing arrays of synthetic spectra for NO γ, β, and δ transitions can allow for contours of residual or χ^2 values to be generated. Optimization routines can then be developed to extract quantitative information of the other transitions.

Work with double wedge flows can be extended to additional locations and freestream conditions. Similar to the cylinder experiments, varying the oxygen content of the freestream can be performed with double wedge flows with emission measurements performed at wavelengths where electronic transitions other than NO γ are weak. Although spectrum fits of low oxygen cases still require additional considerations, integrated intensity profiles can remain useful for directly measuring chemical non-equilibrium in the flow. With the development of a quasi-steady model of NO(A), there is also an additional possibility of linking the measured integrated radiance to other dissociating species in the flow. Using this, NO(A) can be interpreted as a marker for other species.

Finally, other spectroscopic techniques such as tunable diode laser absorption spectroscopy (TDLAS) can serve to complement emission techniques by probing the ground state of NO. It is currently unknown how well NO(A) represents the bulk of the gas. Measurements of NO(X) number density and absolute radiance can serve to link both electronic states in a hypervelocity flow. The advantage of absorption techniques also allows measurements of rotational and vibrational temperature measurements of NO [5]. As the current spectroscopic technique is insensitive to vibrational temperature, this can provide better estimates of vibrational non-equilibrium present in the flow.

BIBLIOGRAPHY

[1] K. Abe, H. Kihara, T. Uchida, and M. Nishida. Experimental and numerical studies of rotational relaxation behind a strong shock wave in air. *Shock Waves*, 11(6):413–421, 2002.

[2] K. Abe, T. Kameyama, H. Kihara, M. Nishida, K. Ito, and H. Tanno. Computation and experiment of a nonequilibrium nozzle flow of arc-heated air. *Journal of Thermophysics and Heat Transfer*, 19(4):428–434, 2005. doi: 10.2514/1.13603.

[3] I. V. Adamovich. Three-dimensional analytic model of vibrational energy transfer in molecule-molecule collisions. *AIAA Journal*, 39(10):1916–1925, 2001.

[4] I. V. Adamovich and J. W. Rich. Three-dimensional nonperturbative analytic model of vibrational energy transfer in atom–molecule collisions. *The Journal of Chemical Physics*, 109(18):7711–7724, 1998. doi: 10.1063/1.477417.

[5] C. A. Almodovar, W. Su, C. L. Strand, and R. K. Hanson. R-branch line intensities and temperature-dependent line broadening and shift coefficients of the nitric oxide fundamental rovibrational band. *Journal of Quantitative Spectroscopy and Radiative Transfer*, 239:106612, 2019. doi: https://doi.org/10.1016/j.jqsrt.2019.106612.

[6] C. Amiot. The infrared emission spectrum of NO: Analysis of the $\Delta v = 3$ sequence up to $v = 22$. *Journal of Molecular Spectroscopy*, 94:150–172, 1982.

[7] J. D. Anderson Jr. *Hypersonic and High-Temperature Gas Dynamics*. American Institute of Aeronautics and Astronautics, Reston, second edition, 2006.

[8] D. Andrienko and I. D. Boyd. Molecular dynamics simulation of nitric oxide formation and extinction. *AIAA Scitech 2019 Forum*, 2019. doi: 10.2514/6.2019-0791.

[9] J. O. Arnold, E. E. Whiting, and G. C. Lyle. Line by line calculation of spectra from diatomic molecules and atoms assuming a Voigt line profile. *Journal of Quantitative Spectroscopy and Radiative Transfer*, 9(6):775–798, 1969. ISSN 0022-4073. doi: https://doi.org/10.1016/0022-4073(69)90075-2.

[10] D. S. Babikian, N. Gopaul, and C. Park. Measurement and analysis of nitric oxide radiation in an arcjet flow. *Journal of Thermophysics and Heat Transfer*, 8(4):737–743, 1994. doi: 10.2514/3.606.

[11] R. D. Banner and A. E. Kuhl. A summary of X-15 heat transfer and skin friction measurements. *Progress of the X-15 Research Airplane Program*, pages 17–26, 1965.

[12] P. R. Bevington. *Data Reduction and Error Analysis for the Physical Sciences*. McGraw-Hill, New York, 1969.

[13] D. Bose and G. V. Candler. Thermal rate constants of the N_2+O→NO+N reaction using ab initio ^3A" and ^3A' potential energy surfaces. *The Journal of Chemical Physics*, 104(8):2825–2833, 1996. doi: 10.1063/1.471106.

[14] D. Bose and G. V. Candler. Thermal rate constants of the O_2+N→NO+O reaction based on the A^2' and A^4' potential-energy surfaces. *The Journal of Chemical Physics*, 107(16):6136–6145, 1997. doi: 10.1063/1.475132.

[15] D. Bose and G. V. Candler. Advanced model of nitric oxide formation in hypersonic flows. *Journal of Thermophysics and Heat Transfer*, 12(2):214, 222, 1998. doi: 10.2514/2.6324.

[16] B. Cruden. Absolute radiation measurements in Earth and Mars entry conditions. RTO-EN-AVT-218, Von Karman Institute for Fluid Dynamics, Rhode Saint Genese, Belgium, 2014. NATO TR RTO-EN-AVT-218.

[17] B. Cruden and A. M. Brandis. Updates to the NEQAIR radiation solver. Number ARC-E-DAA-TN19271, NASA, 2014. Technical Report, 20150022164.

[18] B. Cruden and A. M. Brandis. Measurement and prediction of radiative nonequilibrium for air shocks between 7-9 km/s. *AIAA Aviation*, (20170007384), 2017.

[19] J. Danielak, U. Domin, R. Kepa, M. Rytel, and M. Zachwieja. Reinvestigation of the emission γ band system ($A^2\Sigma^+ - X^2\Pi$) of the NO molecule. *Journal of Molecular Spectroscopy*, 181:394–402, 1997.

[20] J. Davis and B. Sturtevant. Separation length in high-enthalpy shock/boundary-layer interaction. *Physics of Fluids*, 12(10):2661–2687, 2000. doi: 10.1063/1.1289553.

[21] M. Druguet, G. V. Candler, and I. Nompelis. Effects of numerics on Navier-Stokes computations of hypersonic double-cone flows. *AIAA Journal*, 43(3): 616–623, 2005. doi: 10.2514/1.6190.

[22] A. Dufrene, M. Sharma, and J. M. Austin. Design and characterization of a hypervelocity expansion tube facility. *Journal of Propulsion and Power*, 23 (6):1185, 1193, 2007.

[23] B. Edlén. The refractive index of air. *Metrologia*, 2(2):71–80, 1966. doi: 10.1088/0026-1394/2/2/002.

[24] P. W. Erdman, E. C. Zipf, L. C. Howlett, D. A. Levin, R. J. Collins, and G. V. Candler. Flight measurements of low-velocity bow shock ultraviolet radiation. *Journal of Thermophysics and Heat Transfer*, 7(1):37, 41, 1993. doi: 10.2514/3.11566.

[25] P. W. Erdman, E. C. Zipf, P. Espy, L. C. Howlett, D. A. Levin, R. J. Collins, and G. V. Candler. Measurements of ultraviolet radiation from a 5-km/s bow shock. *Journal of Thermophysics and Heat Transfer*, 8(3):441, 446, 1994.

[26] S. F. Gimelshein and I. J. Wysong. Validation of high-temperature air reaction and relaxation models using emission data. *Journal of Thermophysics and Heat Transfer*, 33(3):606–616, 2019. doi: 10.2514/1.T5555.

[27] N. Glumac, H. Krier, T. Bazyn, and R. Eyer. Temperature measurements of aluminum particles burning in carbon dioxide. *Combustion Science and Technology*, 177(3):485–511, 2005. doi: 10.1080/00102200590909030.

[28] D. G. Goodwin, R. L. Speth, H. K. Moffat, and B. W. Weber. Cantera: An object-oriented software toolkit for chemical kinetics, thermodynamics, and transport processes. 2018. doi: 10.5281/zenodo.1174508.

[29] V. Gorelov, M. Gladyshev, A. Kireev, I. Yegorov, Y. Plastinin, and G. Karabadzhak. Nonequilibrium shock-layer radiation in the systems of molecular bands NO and N2(+)(1-) - experimental study and numerical simulation. *31st AIAA Thermophysics Conference*, 1996. doi: 10.2514/6.1996-1900.

[30] V. Gorelov, M. Gladyshev, A. Kireev, I. Yegorov, Y. Plastinin, and G. Karabadzhak. Experimental and numerical study of nonequilibrium ultraviolet NO and N emission in shock layer. *Journal of Thermophysics and Heat Transfer*, 12(2):172–179, 1998.

[31] J. Grinstead, M. Wilder, J. Olejniczak, D. Bogdanoff, G. Allen, K. Dang, and M. Forrest. Shock-heated air radiation measurements at lunar return conditions. *46th AIAA Aerospace Sciences Meeting and Exhibit*, 2008. doi: 10.2514/6.2008-1244.

[32] J. Hank, J. Murphy, and R. Mutzman. The X-51A scramjet engine flight demonstration program. *15th AIAA International Space Planes and Hypersonic Systems and Technologies Conference*, 2008. doi: 10.2514/6.2008-2540.

[33] R. K. Hanson, R. M. Spearrin, and C. S. Goldenstein. *Spectroscopy and Optical Diagnostics for Gases*. Springer, Cham, 2016. ISBN 978-3-319-23251-5.

[34] J. Hao, C. Wen, and J. Wang. Numerical investigation of hypervelocity shock-wave/boundary-layer interactions over a double-wedge configuration. *International Journal of Heat and Mass Transfer*, 138:277–292, 2019. doi: https://doi.org/10.1016/j.ijheatmasstransfer.2019.04.062.

[35] G. Herzberg. *Molecular Spectra and Molecular Structure*. D. Van Nostrand Company, Inc., New York, second edition, 1950.

[36] M. S. Holden. Theoretical and experimental studies of the shock wave-boundary layer interaction on compression surfaces in hypersonic flow. Technical Report AD0706135, Cornell Aeronautical Lab Inc., Buffalo, NY, 1970.

[37] M. S. Holden. Boundary-layer displacement and leading-edge bluntness effects on attached and separated laminar boundary layers in a compression corner. ii-experimental study. *AIAA Journal*, 9(1):84–93, 1971.

[38] H. Hornung. Hypersonic flow over a wedge in the detached shock range. *arXiv*, (1906.06604), 2019.

[39] H. Hornung and R. J. Sandeman. Interferometric measurements of radiating ionizing argon flow over blunt bodies. *Journal of Physics D: Applied Physics*, 7:920–934, 1974.

[40] S. Hyun, C. Park, and K. Chang. Rate parameters for electronic excitation of diatomic molecules: No radiation. *Journal of Thermophysics and Heat Transfer*, 23(4):641–650, 2009. doi: 10.2514/1.42686.

[41] K. R. Jackson, M. R. Gruber, and S. Buccellato. Mach 6–8+ hydrocarbon-fueled scramjet flight experiment: the hifire flight 2 project. *Journal of Propulsion and Power*, 31(1):36–53, 2014.

[42] C. Jacobs. *Radiation in low density hypervelocity flows*. PhD thesis, The University of Queensland, 2011.

[43] C. M. James, T. G. Cullen, H. Wei, S. W. Lewis, S. Gu, R. G. Morgan, and T. J. McIntyre. Improved test time evaluation in an expansion tube. *Experiments in Fluids*, 59(5):87, 2018. doi: 10.1007/s00348-018-2540-1.

[44] C. O. Johnston and A. M. Brandis. Modeling of nonequilibrium CO fourth-positive and CN violet emission in CO_2–N_2 gases. *Journal of Quantitative Spectroscopy and Radiative Transfer*, 149:303 – 317, 2014. ISSN 0022-4073. doi: https://doi.org/10.1016/j.jqsrt.2014.08.025.

[45] I. N. Kadochnikov and I. V. Arsentiev. Kinetics of nonequilibrium processes in air plasma formed behind shock waves: state-to-state consideration. *Journal of Physics D: Applied Physics*, 51(37):374001, 2018.

[46] A. Khraibut and S. Gai. Flow steadiness over a double wedge at Mach 7 including effect of trailing edge expansion. *22nd AIAA International Space Planes and Hypersonics Systems and Technologies Conference*, 2018. doi: 10.2514/6.2018-5388.

[47] D. Knight, O. Chazot, J. Austin, M. A. Badr, G. V. Candler, B. Celik, D. Rosa, R. Donelli, J. Komives, A. Lani, D. Levin, I. Nompelis, M. Panesi, G. Pezzella, B. Reimann, O. Tumuklu, and K. Yuceil. Assessment of predictive capabilities for aerodynamic heating in hypersonic flow. *Progress in Aerospace Sciences*, 90:39, 53, 2017. doi: 10.1016/j.paerosci.2017.02.001.

[48] A. M. Knisely. *Experimental investigation of nonequilibrium and separation scaling in double-wedge and double-cone geometries*. PhD thesis, University of Illinois at Urbana-Champaign, 2016.

[49] K. Kossi and I. Boyd. Detailed computation of ultraviolet spectra in rarefied hypersonic flow. *Journal of Spacecraft and Rockets*, 35(5):653, 659, 1998. doi: 10.2514/2.3381.

[50] I. Kovacs. *Rotational Structure in the Spectra of Diatomic Molecules*. American Elsevier, New York, 1969.

[51] Explosion Dynamics Laboratory. SDToolbox: Numerical tools for shock and detonation wave modeling. California Institute of Technology, Pasadena, CA, 2020. GALCIT Report FM2018.001. URL `https://shepherd.caltech.edu/EDL/PublicResources/sdt/`.

[52] L. Landau and E. Teller. Theory of sound dispersion. *Physikalische Zeitschrift der Sowjet-Union*, 10:34, 1936.

[53] C. O. Laux, T. G. Spence, C. H. Kruger, and R. N. Zare. Optical diagnostics of atmospheric pressure air plasmas. *Plasma Sources Science and Technology*, 12(2):125–138, feb 2003. doi: 10.1088/0963-0252/12/2/301.

[54] J. M. Lawson and J. M. Austin. Design of conventional and detonation-driven hypervelocity expansion tubes. *2018 Aerodynamic Measurement Technology and Ground Testing Conference*, (3566), 2018. doi: 10.2514/6.2018-3566.

[55] M. G. Leibowitz and J. M. Austin. Assessment of reflected shock tunnels for Mars entry vehicle ground testing. *2018 AIAA Aerospace Sciences Meeting*, 2018. doi: 10.2514/6.2018-1721.

[56] D. A. Levin, G. V. Candler, R. J. Collins, P. W. Erdman, E. Zipf, P. Espy, and C. Howlett. Comparison of theory with experiment for the bow shock ultraviolet rocket flight. *Journal of Thermophysics and Heat Transfer*, 7(1): 30, 36, 1993.

[57] D. A. Levin, M. Braunstein, G. V. Candler, R. J. Collins, and G. P. Smith. Examination of theory for bow shock ultraviolet rocket experiments - II. *Journal of Thermophysics and Heat Transfer*, 8(3):453, 459, 1994.

[58] D. A. Levin, G. V. Candler, R. J. Collins, P. W. Erdman, E. C. Zipf, and L. C. Howlett. Examination of theory for bow shock ultraviolet rocket experiments - i. *Journal of Thermophysics and Heat Transfer*, 8(3):447, 452, 1994.

[59] Z. Li, I. Sohn, and D. A. Levin. Modeling of Nitrogen monoxide formation and radiation in nonequilibrium hypersonic flows. *Journal of Thermophysics and Heat Transfer*, 28(3):365–380, 2014. doi: 10.2514/1.T3940.

[60] J. Luque and D. R. Crosley. Transition probabilities and electronic transition moments of the $A^2\ \Sigma^+$-$X^2\ \Pi$ and $D^2\ \Sigma^+$-$X^2\ \Pi$ systems of nitric oxide. *The Journal of Chemical Physics*, 111(16):7405–7415, 1999.

[61] S. O. Macheret and I. V. Adamovich. Semiclassical modeling of state-specific dissociation rates in diatomic gases. *The Journal of Chemical Physics*, 113 (17):7351–7361, 2000. doi: 10.1063/1.1313386.

[62] L. Massa and J. M. Austin. Spatial linear stability of a hypersonic shear layer with nonequilibrium thermochemistry. *Physics of Fluids*, 20(8):84–104, 2008.

[63] B. J. McBride and S. Gordon. Computer program for calculation of complex chemical equilibrium compositions and applications II. Users' Manual and Program Description. Technical Report RTOP 505-62-52, NASA, 1996.

[64] B. J. McBride, M. J. Zehe, and S. Gordon. NASA Glenn coefficients for calculating thermodynamic properties of individual species. Technical Report RTOP 708-87-13, NASA, 2002.

[65] M. McGilvray, J. M. Austin, M. Sharma, P. A. Jacobs, and R. G. Morgan. Diagnostic modelling of an expansion tube operating condition. *Shock Waves*, 19(1):59–66, April 2009.

[66] R. C. Millikan and D. R. White. Systematics of vibrational relaxation. *The Journal of Chemical Physics*, 39(12):3209–3213, 1963. doi: 10.1063/1.1734182.

[67] Ioannis N., G. V. Candler, M. MacLean, T. P. Wadhams, and M. S. Holden. Numerical investigation of double-cone flow experiments with high-enthalpy effects. *48th AIAA Aerospace Sciences Meeting Including the New Horizons Forum and Aerospace Exposition*, 2010. doi: 10.2514/6.2010-1283.

[68] I. Nompelis, G. V. Candler, and M. S. Holden. Effect of vibrational nonequilibrium on hypersonic double-cone experiments. *AIAA Journal*, 41(11):2162–2169, 2003. doi: 10.2514/2.6834.

[69] H. Nubbermeyer and B. Wende. Instrumental functions of a 5-m echelle spectrometer with diffraction-limited resolving power. *Applied Optics*, 16 (10):2708, 2710, 1977.

[70] J. Olejniczak, G. V. Candler, M. Wright, H. Hornung, and I. Leyva. High enthalpy double-wedge experiments. *Advanced Measurement and Ground Testing Conference*, 1996. doi: 10.2514/6.1996-2238.

[71] J. Olejniczak, G. V. Candler, and H. Hornung. Computation of double-cone experiments in high enthalpy Nitrogen. *32nd Thermophysics Conference*, 1997. doi: 10.2514/6.1997-2549.

[72] J. Olejniczak, G. V. Candler, M. J. Wright, I. Leyva, and H. Hornung. Experimental and computational study of high enthalpy double-wedge flows. *Journal of Thermophysics and Heat Transfer*, 13(4):431–440, 1999.

[73] H. A. Ory, A. P. Gittleman, and J. P. Maddox. Franck-condon factors for the no beta and gamma band systems. *The Astrophysical Journal*, 139:346, 1964.

[74] M. Panesi, T. E. Magin, A. Bourdon, A. Bultel, and O. Chazot. Electronic excitation of atoms and molecules for the FIRE II flight experiment. *Journal of Thermophysics and Heat Transfer*, 25(3):361–374, 2011. doi: 10.2514/1.50033.

[75] C. Park. Assessment of a two-temperature kinetic model for dissociating and weakly ionizing nitrogen. *Journal of Thermophysics and Heat Transfer*, 2(1):8–16, 1988. doi: 10.2514/3.55.

[76] C. Park. *Nonequilibrium Hypersonic Aerothermodynamics*. John Wiley & Sons, New York, 1990.

[77] C. Park. Rate parameters for electronic excitation of diatomic molecules II. heavy particle-impact processes. *46th AIAA Aerospace Sciences Meeting and Exhibit*, 2008. doi: 10.2514/6.2008-1446.

[78] C. S. Park, M. E. Newfield, D. G. Fletcher, T. Gokcen, and S. P. Sharma. Spectroscopic emission measurements within the blunt-body shock layer in an arcjet flow. *Journal of Thermophysics and Heat Transfer*, 12(2):190–197, 1998.

[79] C. S. Park, M. E. Newfield, D. G. Fletcher, and T. Gokcen. Spectroscopic measurements of shock-layer flows in an arcjet facility. *Journal of Thermophysics and Heat Transfer*, 13(1):60–67, 1999.

[80] V. N. Patil, D. A. Levin, S. F. Gimelshein, and J. M. Austin. Study of shock-shock interactions for the HET facility double wedge configuration using the DSMC approach. *43rd AIAA Fluid Dynamics Conference*, 2013. doi: 10.2514/6.2013-3202.

[81] J. D. Reinert, S. Gs, G. V. Candler, and J. R. Komives. Three-dimensional simulations of hypersonic double wedge flow experiments. *47th AIAA Fluid Dynamics Conference*, 2017. doi: 10.2514/6.2017-4125.

[82] A. Roshko. Free shear layers, base pressure and bluff-body drag. *Symposium on Developments in Fluid Dynamics and Aerospace Engineering*, (ADA286316), 1993.

[83] G. B. Rybicki and A. P. Lightman. *Radiative Processes in Astrophysics*. John Wiley & Sons, Weinheim, 1979.

[84] T. B. Settersten, B. D. Patterson, and C. D. Carter. Collisional quenching of NO $A^2\,\Sigma^+$ (v'= 0) between 125 and 294 K. *The Journal of Chemical Physics*, 130(20):204302, 2009. doi: 10.1063/1.3138178.

[85] G. S. Settles. *Schlieren and shadowgraph techniques: visualizing phenomena in transparent media*. Springer Science & Business Media, 2012.

[86] M. Sharma. *Post-shock thermochemistry in hypervelocity CO_2 and air flow*. PhD thesis, University of Illinois at Urbana-Champaign, 2010.

[87] M. Sharma, J. M. Austin, N. Glumac, and L. Massa. NO and OH spectroscopic vibrational temperature measurements in a postshock relaxation region. *AIAA Journal*, 48(7):1434, 1443, 2010. doi: 10.2514/1.J050047.

[88] K. Stewartson and P. G. Williams. Self-induced separation. *Proceedings of the Royal Society of London. A. Mathematical and Physical Sciences*, 312(1509): 181–206, 1969. doi: 10.1098/rspa.1969.0148.

[89] V. P. Stulov. Similarity law for supersonic flow past blunt bodies. *Fluid Dynamics*, 4(4):93–96, 1969.

[90] A. B. Swantek. The role of aerothermochemistry in double cone and double wedge flows. University of Illinois at Urbana-Champaign, 2012. Ph.D. thesis.

[91] A. B. Swantek and J. M. Austin. Flowfield establishment in hypervelocity shock-wave/boundary-layer interactions. *AIAA Journal*, 53(2):311–320, 2015. doi: 10.2514/1.J053104.

[92] A. C. Tibère-Inglesse, S. D. McGuire, P. Mariotto, and C. O. Laux. Experimental study of recombining nitrogen plasmas: I. vibronic population distributions and nonequilibrium molecular radiation. *Plasma Sources Science and Technology*, 28(7):075018, July 2019. doi: 10.1088/1361-6595/ab2cc4.

[93] O. Tumuklu, D. A. Levin, and J. M. Austin. Shock-shock interactions for a double wedge configuration in different gases. *53rd AIAA Aerospace Sciences Meeting*, 2015. doi: 10.2514/6.2015-1520.

[94] O. Tumuklu, D. A. Levin, and V. Theofilis. Modal analysis with proper orthogonal decomposition of hypersonic separated flows over a double wedge. *Physical Review Fluids*, 4:033403, Mar 2019.

[95] E. E. Whiting, C. Park, Y. Liu, J. O. Arnold, and J. A. Paterson. Neqair96, nonequilibrium and equilibrium radiative transport and spectra program: user's manual. 1996.

[96] W. Wurster, C. Treanor, and M. Williams. Nonequilibrium UV radiation and kinetics behind shock waves in air. *20th Fluid Dynamics, Plasma Dynamics and Lasers Conference*, 1989. doi: 10.2514/6.1989-1918.

[97] H. W. Yoon, J. E. Proctor, and C. E. Gibson. FASCAL 2: a new NIST facility for the calibration of the spectral irradiance of sources. *Metrologia*, 40(1): S30–S34, February 2003. doi: 10.1088/0026-1394/40/1/308.

[98] Y. B. Zel'dovich and Y. P. Raizer. *Physics of Shock Waves and High-Temperature Hydrodynamic Phenomena*, volume 2. Academic Press, New York, 1966.

Appendix A

ADDITIONAL CYLINDER EMISSION DATA

Spectra are extracted by binning 0.5 mm increments of the detector image, with normalization performed with respect to the $\gamma(0,1)$ peak of the x = 0.25 mm spectrum. Integration is performed in four wavelength ranges: 211.65 nm - 215.80 nm, 215.80 nm - 227.24 nm, 227.24 nm - 237.20 nm, and 237.20 nm - 248.00 nm. Integrated radiance data are normalized to the $\gamma(0,1)$ peak intensity in the profile. Downstream position is referenced using the measured Δ in Table 4.1.

M7-H8-A

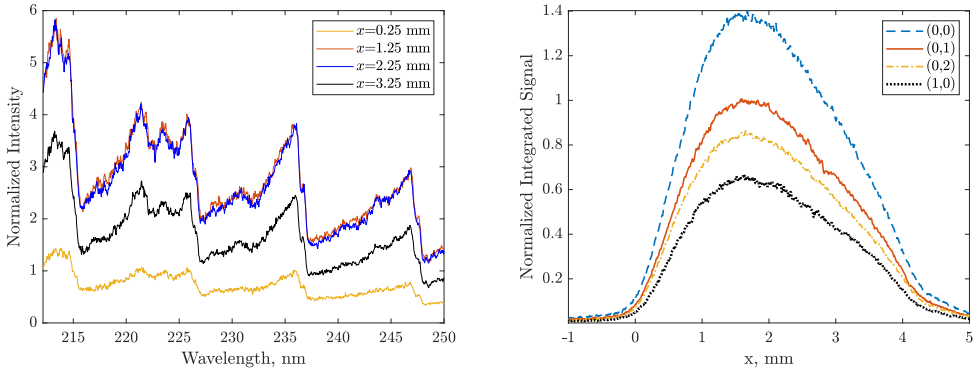

X_{O_2}= 0.063

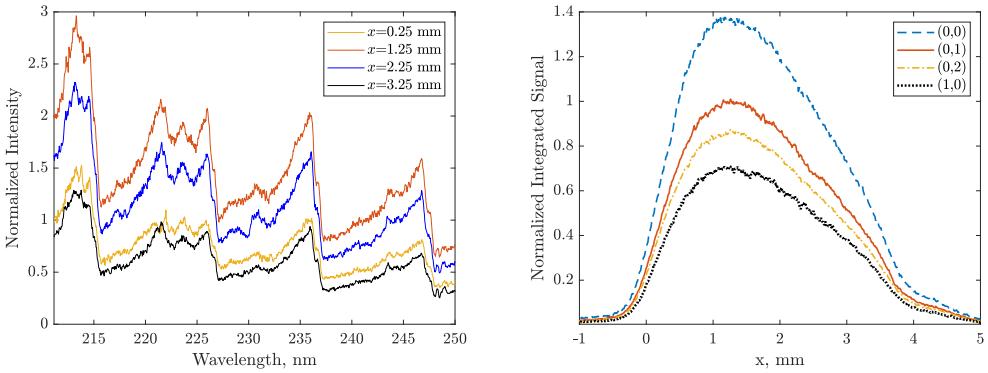

X_{O_2}= 0.105

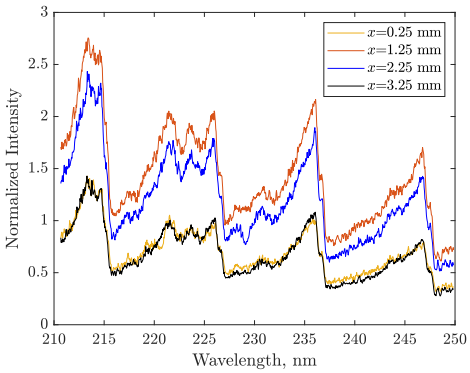

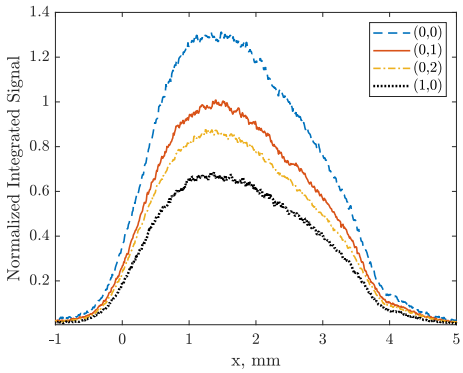

$X_{O_2} = 0.137$

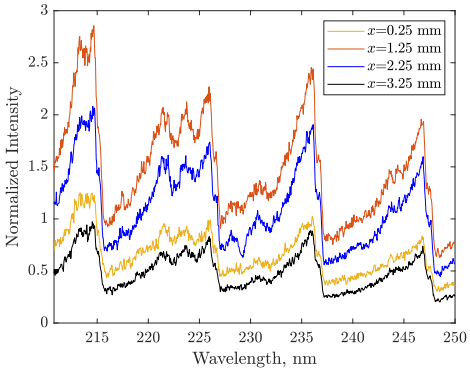

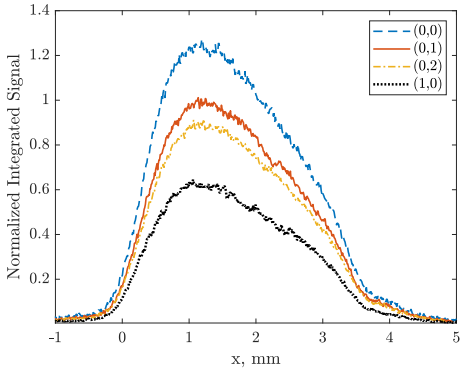

$X_{O_2} = 0.273$

M5-H6-A

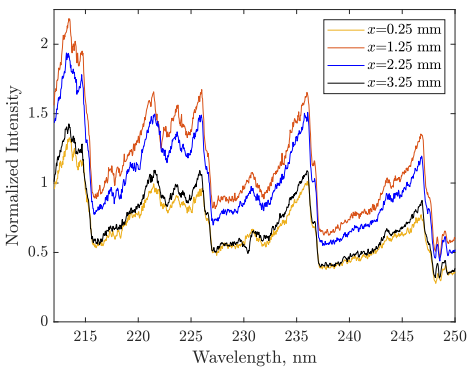

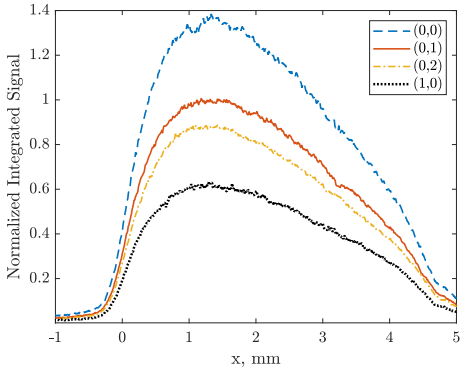

X_{O_2}= 0.063

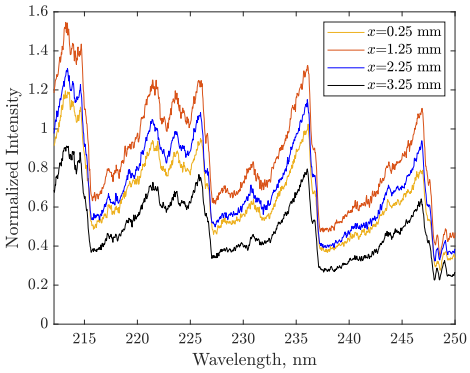

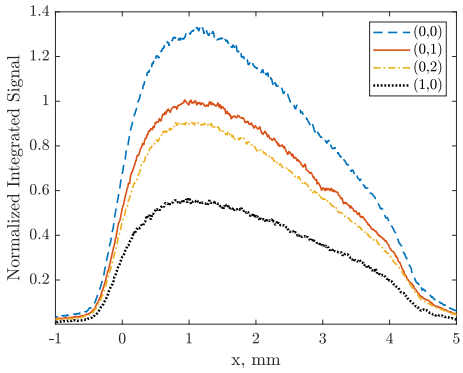

X_{O_2}= 0.105

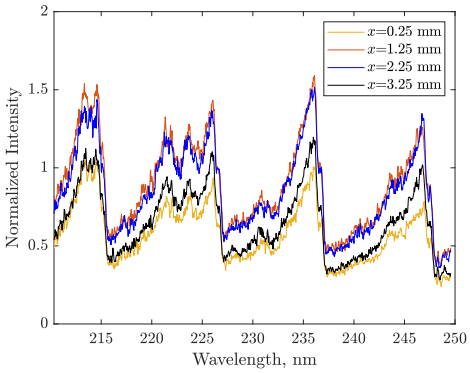

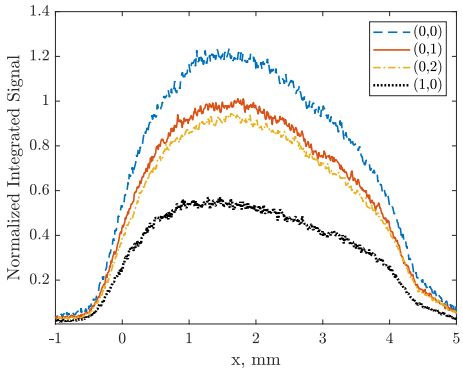

X_{O_2}= 0.137

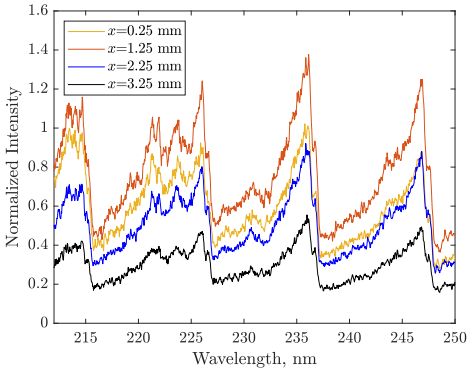

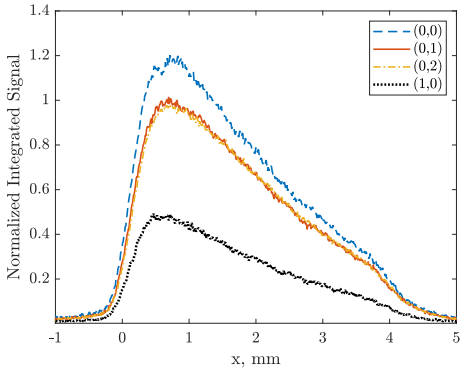

X_{O_2}= 0.273

Appendix B

ADDITIONAL DOUBLE WEDGE EMISSION DATA

Spectra at y_t = 42.62 mm are extracted by binning 1 mm increments of the detector image downstream of the bow shock. A separate experiment is used to extract spectra downstream of the measured shear layer location and downstream of the reflected shock. Binning is performed at variable increments for locations downstream of the shear layer and the interval of the detector binned is shown. Integration is performed in four wavelength ranges: 211.65 nm - 215.80 nm, 215.80 nm - 227.24 nm, 227.24 nm - 237.20 nm, and 237.20 nm - 248.00 nm. Integrated radiance data are normalized to the $\gamma(0,1)$ peak intensity in the profile. Downstream position is referenced to the tip of the first wedge.

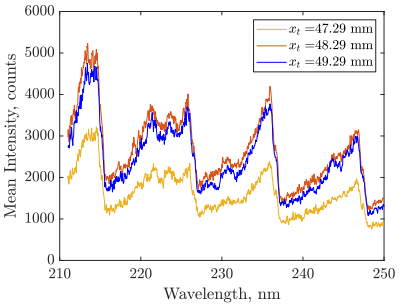

Post-bow shock

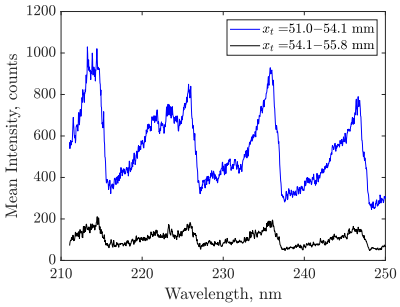

Post-shear layer

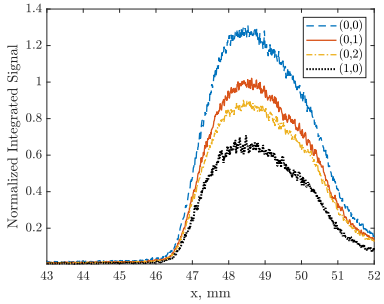

Integrated intensity

t = 35 − 45 μs

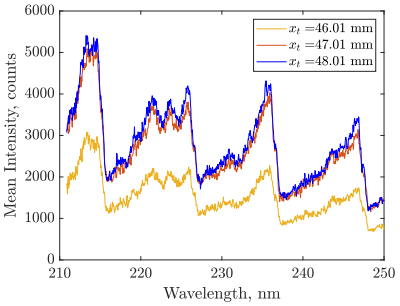

Post-bow shock

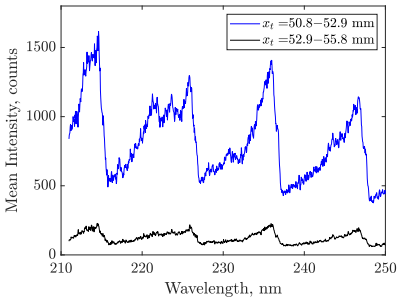

Post-shear layer

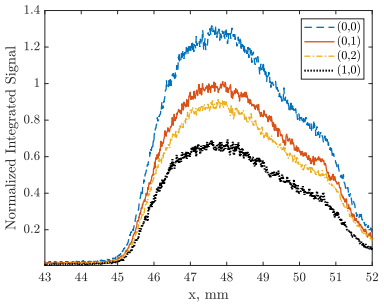

Integrated intensity

t = 55 – 65 μs

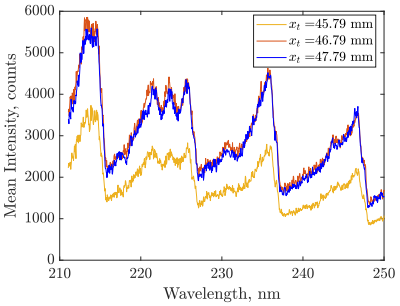

Post-bow shock

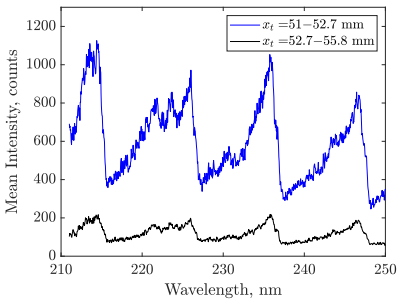

Post-shear layer

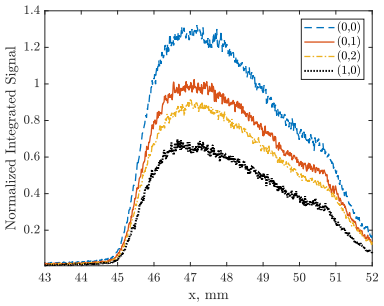

Integrated intensity

t = 70 – 80 μs

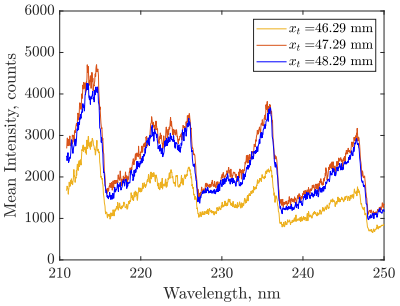

Post-bow shock

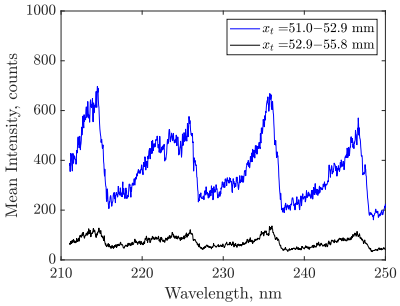

Post-shear layer

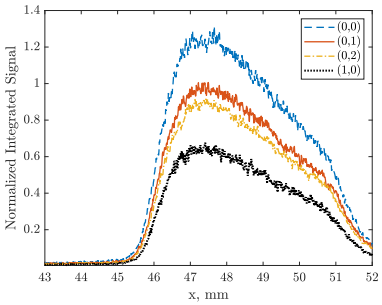

Integrated intensity

t = 90 – 100 μs

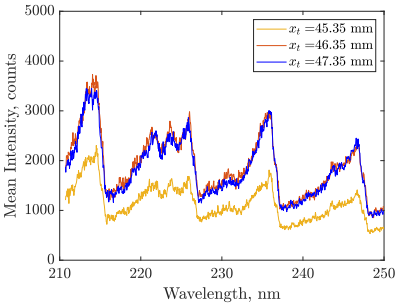

Post-bow shock

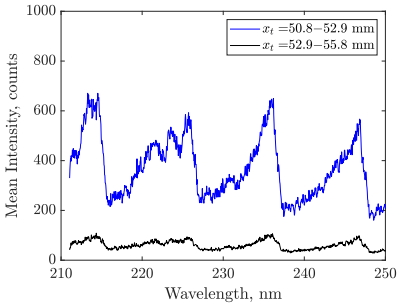

Post-shear layer

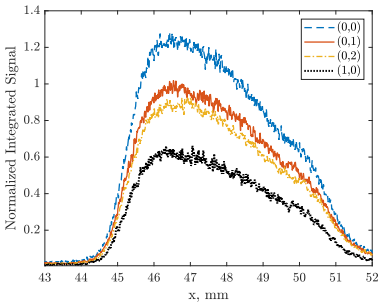

Integrated intensity

t = 110 – 120 μs

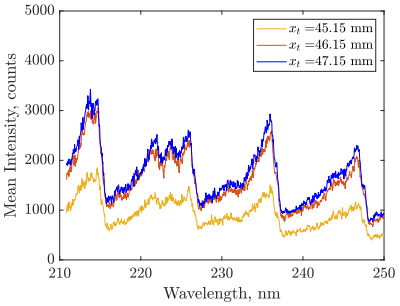

Post-bow shock

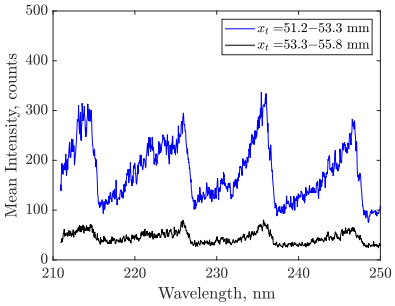

Post-shear layer

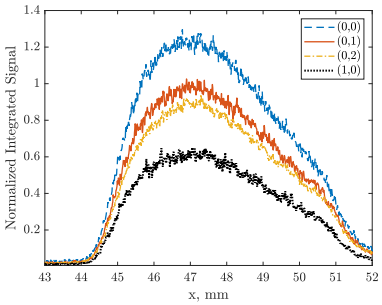

Integrated intensity

t = 135 – 145 μs

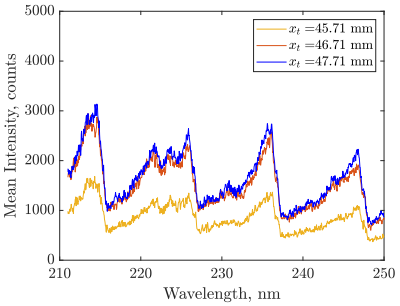

Post-bow shock

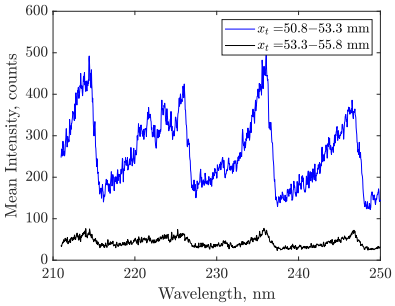

Post-shear layer

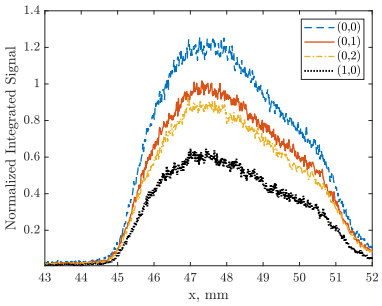

Integrated intensity

t = 150 – 160 μs

Appendix C

NO A-X SPECTRUM CODE

The software used for computing the NO γ spectrum is MATLAB. The scripts are confirmed to be compatible with MATLAB versions R2015a through R2018a. To run the code, place all scripts in one directory and modify the directory for saved results. A text file of Frank-Condon factors is also required.

NO_Gamma_two_temp_v0.m

Table of Contents


```
%This code outputs the line spectrum data for the NO A-X transition
 for a
%given set of temperatures and a line width of interest. This code is
 used
%for computing a large array of spectra for a given matrix of Tr/Tv
 pairs.
%Functions are required to run this main code and can be found in the
 same
%directory. They include "HL_NO.m", "umin.m", "upos.m", "Cmin.m",
 "Cpos.m",
%and "Voigt.m". The structure of the code is as follows: Input of
%spectroscopic constants, input of temperature/linewidth/wavelength
 ranges,
%calculation of upper and lower state energies, calculation of
 Boltzmann
%fraction for each possible state, calculation of Honl-London factors,
 line
%shape computation, and corrections to air wavelengths. An effort will
 be
%made to cite the appropriate references throughout the code. The book
%"Spectroscopy and Optical Diagnostics for Gases" (Hanson, Spearrin,
%Goldenstein) provides a good overview of some of the calculations
 made in
%this code. It is highly recommended to read the book and review the
 OH
%case study.

%In this version, a two-temperature model will be assumed in computing
 the
%Boltzmann fractions. This allows for the rotational and vibrational
%populations to be independent of each other.

%Last Modified: 8/19/2018
%Nelson J Yanes
```

INPUT PARAMETERS & INITIALIZING VARIABLES

```
clear all
Tv = [4000]; %[K] Folders in Tv increments
Tr = [2000]; %[K]

%File Output Location
out_loc = 'C:\Users\nelson\Documents\Caltech\';

%Range of wavenumbers we are interested
wvn_start = 38450;            %[cm-1] 255.5 nm = 39138 cm-1
wvn_end = 47620;              %[cm-1] 219.0 nm = 45663 cm-1
inc = 3;                      %[cm-1] Resolution value
w = [wvn_start:inc:wvn_end];  %[cm-1]

%Instrumental Linewidth (Full Width, Half Max):
%This must be obtained from either Hg or Fe lamp spectrum. Need FWHM,
 and
%"a" value that best represent the instrument lineshape. In this code,
 I am
%using the square-root of the Voigt function.
FWHM = 59; %[cm-1]
a = 0.01;  %Ratio of Lorentz to Doppler widths
thresh = 3*FWHM; %Threshold for convolving transitions

%Find correct coefficient for finding the FWHM of the square-root of
 voigt
%line shape. This is used for getting the right scaling of this shape.
fun = @(b) sqrt(Voigt(b*FWHM/2, a))/sqrt(Voigt(0,a)) - 1/2;
sv_const = fzero(fun,0.1);

%Indexing information
num_branches = 12;
v_upper = 13;  %Number of upper vibrational states (limited by FC
 factors)
v_lower = 21;  %Number of lower vibrational states (also limited by
 FC's)
rot_max = 250; %Max rotation quantum number (starting at zero quantum
 #)
vib_max = v_lower - 1; %Max Vibrational Quantum number (starting at
 zero)

%Initialize variables
fc = zeros(v_upper,v_lower);
E1_pp = zeros(vib_max+1,rot_max+3);
E1_p = zeros(vib_max+1,rot_max+3);
E2_pp = zeros(vib_max+1,rot_max+3);
E2_p = zeros(vib_max+1,rot_max+3);
boltz_frac = zeros(v_upper, rot_max+3);
wvn = zeros(v_upper,v_lower,num_branches,rot_max+2);
str = zeros(v_upper,v_lower,num_branches,rot_max+2);
```

```
intensity = zeros(1,length(w));
lambda_air = zeros(1,length(w));
```

SPECTROSCOPIC CONSTANTS AND FRANK-CONDON FACTORS

```
%These constants were taken from a variety of sources. Please refer to
 the
%original sources before making updates. NOTATION: p = upper
 electronic
%state A, pp (or dp) = ground state X.

%Electronic Term Energy of the A State (J. Danielak et al)
Te = 43906.191; %[cm-1]

%Constants for rotational distortion (Bv) [cm-1]
%All pp's -> C. Amoit p.168 ; All p's -> J. Danielak et al
Be_p = 1.995586;        %0th order
Be_pp = 1.70488847;
alpha_p = 1.8714*10^-2; %1st order
alpha_pp = 0.01754158;
gamma_p = -4.78*10^-5;  %2nd order
gamma_pp = -1.4886*10^-5;
delta_p = 0;            %3rd order
delta_pp = 0;
Y41_p = 0;              %4th order
Y41_pp = -4.7275*10^-8;
Y51_p = 0;              %5th order
Y51_pp = 1.0108*10^-9;
Y61_p = 0;              %6th order
Y61_pp = -6.0557*10^-11;%NOTE:LIFBASE HAS THIS LISTED INCORRECTLY!


%Anharmonicity Corrections (omega's) For Vib. Energy [cm-1]
%All pp's -> C. Amoit p.168 ; All p's -> J. Danielak et al
we_p = 2374.372;     %1st order
we_pp = 1904.13455;
wxe_p = 16.159;      %2nd order
wxe_pp = 14.088358;
wye_p = -3.73*10^-2; %3rd order
wye_pp = 0.0100467;
wze_p = 0;           %4th order
wze_pp = -1.5331*10^-4;
wae_p = 0;           %5th order
wae_pp = -9.769*10^-6;
wbe_p = 0;           %6th order
wbe_pp = -1.9142*10^-7;
wce_p = 0;           %7th order
wce_pp = -5.2734*10^-9;

%Constants for centrifrugal distortion (Dv) [cm-1]
De_p = 5.64*10^-6;        %0th order (J. Danielak et al)
```

```
De_pp = 5.46616*10^-6;    %(C. Amoit)

beta_p = 2.55*10^-8;      %1st order (J. Danielak et al)
beta_pp = 1.7032*10^-8;   %(C. Amoit)
Y22_p = 0;
Y22_pp = 1.4651*10^-10;   %2nd order (C. Amoit)


%Spin splitting constant (J. Danielak has some values to pick) [cm-1]
%See also "The beta and gamma bands of nitric oxide..." R. Engleman,
 P.
%Rouse (1971) for additional values.
gamma_s_p =0; %-2.765*10^-3; %J. Danielak gamma_3.

%Read in Frank-Condon Factors. Reference: "Frank-Condon Factors for
 the NO
%Beta and Gamma band systems" H. Ory, A. Gittleman, J.Maddox. This
 data
%must be in a separate .txt file named "FC_NO.txt". Note that quantum
%numbers should be corrected to start at zero.
%FILE FORMAT: v', v'', fc
FC_filename = 'FC_njy.txt';
fc_data = importdata(FC_filename);
x=0;
%Read in FC data
for p = 1:v_upper
    for dp = 1:v_lower
        fc(p,dp) = fc_data(x+dp,3);
    end
    x = x +21;
end
```

CALCULATE ENERGIES FOR UPPER & LOWER STATES IN BOTH 1,2 CONFIGS.

```
%Recall that NO's two electornic levels are doublets. Therefore, we
 denote
%two spin-split levels with the same J, but different spin. Denote
 angular
%momentum term energies F1 and F2. NOTATION: F1 => N=J-1/2, F2 => N=J
+1/2.
%See Kovacs pg. 63,65 "Rotational structure in the spectra of diatomic
%molecules" section 2.1.3.

%Spin/rotation correction was not made, because I do not
%have gamma for the ground state (gamma_s_pp). Recall that vibrational
%quantum number starts at 0.

for dp = 0 : vib_max
    v = (dp + 1/2); %Vibrational quantum number + 0.5

    %Constant for rotational distortion
```

```
    Bv_p = Be_p - alpha_p*v + gamma_p*v^2 + delta_p*v^3 ...
        +Y41_p*v^4 + Y51_p*v^5 + Y61_p*v^6;
    Bv_pp = Be_pp - alpha_pp*v + gamma_pp*v^2 + delta_pp*v^3 ...
        + Y41_pp*v^4 + Y51_pp*v^5 +Y61_pp*v^6;

    %Constant for centrifugal distortion
    Dv_p = De_p + beta_p*v + Y22_p*v^2;
    Dv_pp = De_pp + beta_pp*v + Y22_pp*v^2;

    %Vibrational Term Energy
    G_p = we_p*v - wxe_p*v^2 + wye_p*v^3 + wze_p*v^4 + wae_p*v^5 ...
        + wbe_p*v^6 + wce_p*v^7;
    G_pp = we_pp*v - wxe_pp*v^2 + wye_pp*v^3 + wze_pp*v^4 ...
        + wae_pp*v^5 + wbe_pp*v^6 + wce_pp*v^7;

    %Spin Orbit Coupling Constant (pg 168, C. Amoit)
    Av_pp = 123.252407 - 0.235702*v - 4.0762*10^-3*v^2 ...
        -1.8629*10^-4*v^3 + 0*v^4 - 2.5207*10^-7*v^5 -2.386*10^-9*v^6;
    Y_pp = Av_pp/Bv_pp;

    %Energy calculations
    for N = 0 : (rot_max+2)
        %Upper state total energy
        E1_p(dp+1,N+1) = Te + G_p + Bv_p*N*(N+1)...
            -Dv_p*( N*(N+1) )^2 + (1/2)*gamma_s_p*N;
        E2_p(dp+1,N+1) = Te + G_p + Bv_p*N*(N+1)...
            -Dv_p*( N*(N+1) )^2 - (1/2)*gamma_s_p*(N+1);

        %Lower State total energy
        if N ~= 0
        E1_pp(dp+1,N+1) = G_pp + Bv_pp*((N+1)^2 ...
            -1^2-0.5*sqrt(Y_pp*(Y_pp-4)*1^2+4*(N+1)^2))...
            -Dv_pp*( N*(N+1)-1^2 )^2;
        E2_pp(dp+1,N+1) = G_pp + Bv_pp*(N^2-1^2 ...
            +0.5*sqrt(Y_pp*(Y_pp-4)*1^2+4*N^2)) ...
            -Dv_pp*( N*(N+1)-1^2 )^2;
        end

    end


end

% %%%START LOOPS HERE%%% %
for tv=1:length(Tv)
    mkdir(strcat(out_loc,num2str(Tv(tv))))
    for tr=1:length(Tr)

    %Text file output. Put in the form Tr, Tv for later use
    f_out =
 fopen(strcat(out_loc,num2str(Tv(tv)),'\Tr_',num2str(Tr(tr))...
        ,'_Tv_',num2str(Tv(tv)),'.txt'),'w');
```

BOLTZMANN FRACTION COMPUTATION

```
%Calculate Boltzmann fractions for v' and J'. Recall that the
 intensity for
%a spectral line is dependent on the transition from the initial state
 n',
%v', J' to the state n'', v'', J''. This is dependent of the number of
%molecules in the initial state N'. This section will focus on the
 fraction
%of molecules at the A state (aka N'). Later on, these values will be
 used
%for computing the intensities of the 12 branches. For absorption
%computations, computations of the fractions in the ground state (N'')
 are
%needed instead.

hc_k = 1.43877; %Radiation Constant [k/(cm-1)]

    for p = 1 : v_upper              %Upper state v. Limited by FC
 factors.
        v = (p-1)+1/2; %current v'

        %Constant for rotational distortion (upper state only!)
        B_p = Be_p - alpha_p*v + gamma_p*v^2 + delta_p*v^3 ...
            +Y41_p*v^4 + Y51_p*v^5 + Y61_p*v^6;

        %Rotational partition function (rigid rotor approximation)
        Qr = Tr(tr) / (B_p *hc_k);

        %Vibrational partition function
        qsum = 0;
        for dp = 0 : (v_upper-1)
            v_p = dp + 1/2;
            G = we_p*v_p - wxe_p*v_p^2 + wye_p*v_p^3 + wze_p*v_p^4 ...
                + wae_p*v_p^5 + wbe_p*v_p^6 + wce_p*v_p^7;
            qsum = qsum + exp( -hc_k*G/Tv(tv) );
        end
        Qv = qsum; %sum of all possible states

        %Vibration fraction for quantum number v' of initial state
        G_vp = we_p*v - wxe_p*v^2 + wye_p*v^3 + wze_p*v^4 +
 wae_p*v^5 ...
            + wbe_p*v^6 + wce_p*v^7;
        f_vib = exp( -hc_k*G_vp/Tv(tv) ) / Qv;

        %Rotation fraction & total fraction for each v' and J'
        for J = 0 : (rot_max+2)
            F = B_p*J*(J+1); %Rot. energy, w/o cent. dist. term
            f_rot = (2*J+1)*exp( -hc_k*F/Tr(tr) )/Qr;

        %Store boltzmann fraction for upper state
            boltz_frac(p,(J+1)) = f_vib * f_rot;
        end
```

```
    end
```

HONL-LONDON FACTORS AND LINE STRENGTH CALCULATION

```
%Calculate the Honl-London Factors for each N'' in the 12 branches in
 each
%band. There are the usual P,Q,R branches, with two different spin
 split
%states at each electronic level. Use formulas from Kovacs's
 "Rotational
%Structure in the Spectra of Diatomic Molecules", table 3.7, column
%del_Lambda = -1 for sigma-pi transitions.
%(remember Sigma ->0, Pi ->1. So Sigma - Pi is negative 1).
%Note comment from Kovacs: "Lambda values always mean the
%smaller of the two Lambda's involved in the transition." In this
 case, all
%lambda's in his expressions are zero! This computation
%will be done in a separate function to reduce clutter.


%Outer loop is limited by FC factors computed (only first 13
 vibrational
%states were considered at the upper level). See H. Ory, A. Gittleman,
%J.Maddox paper on FC factors computation for NO gamma system.

scale = 30000; %Normalize wavenumber by this value to get near ~1.
%This normalization is arbitrary, since I am interested in relative
%intensity between peaks.

for p = 1 : v_upper        %OUTER LOOP: UPPER VIBRATION (index at 1)

    for dp = 1 : v_lower   %MIDDLE LOOP: LOWER VIBRATION (index at 1)

        v_pp = (dp-1) + 1/2; %Vibrational quantum number + 0.5

        %Constant for rotational distortion (ground state)
        Bv_pp=Be_pp - alpha_pp*v_pp + gamma_pp*v_pp^2 +
 delta_pp*v_pp^3 ...
                  + Y41_pp*v_pp^4 + Y51_pp*v_pp^5 +Y61_pp*v_pp^6;

        %Spin Orbit Coupling Constant (ground state)
        Av_pp = 123.252407 - 0.235702*v_pp - 4.0762*10^-3*v_pp^2 ...
            -1.8629*10^-4*v_pp^3 + 0*v_pp^4 - 2.5207*10^-7*v_pp^5
 -2.386*10^-9*v_pp^6;
        Y_pp = Av_pp/Bv_pp;


        for n = 4 : (rot_max+1)  %INNER LOOP: ROTATION (index at 1)
            %Will go down to n-2, so minimum n is 3 in this case.
            %Rotation starts at N = 0;
```

```
            N = n-1;


%%%%%%%%%%%%% R1 Branch: N = J - 1/2 Transition #1 %%%%%%%%%%%%%%%%%%
%%%%%%
    trans = 1;
    J = N + 1/2;
    hl = HL_NO(trans,N,Y_pp);
    boltz = boltz_frac(p,n+1);
    wvn(p,dp,trans,n) = E1_p(p,n+1) - E1_pp(dp,n);
    str(p,dp,trans,n) = hl * fc(p,dp)...
        *(wvn(p,dp,trans,n)/scale)^4 * boltz/(2*(J+1)+1);

%%%%%%%%%%%%% Q1 Branch: N = J - 1/2 Transition #2 %%%%%%%%%%%%%%%%%%
%%%%%%
    trans = 2;
    J = N + 1/2;
    hl = HL_NO(trans,N,Y_pp);
    boltz = boltz_frac(p,n);
    wvn(p,dp,trans,n) = E1_p(p,n) - E1_pp(dp,n);
    str(p,dp,trans,n) = hl * fc(p,dp)...
        *(wvn(p,dp,trans,n)/scale)^4 * boltz/(2*J+1);

%%%%%%%%%%%%% P1 Branch: N = J - 1/2 Transition #3 %%%%%%%%%%%%%%%%%%
%%%%%%
    trans = 3;
    J = N + 1/2;
    hl = HL_NO(trans,N,Y_pp);
    boltz = boltz_frac(p,n-1);
    wvn(p,dp,trans,n) = E1_p(p,n-1) - E1_pp(dp,n);
    str(p,dp,trans,n) = hl * fc(p,dp)...
        *(wvn(p,dp,trans,n)/scale)^4 * boltz/(2*(J-1)+1);

%%%%%%%%%%%%% R12 Branch: N = J + 1/2 Transition #4 %%%%%%%%%%%%%%%%%%
%%%%%%
    trans = 4;
    J = N - 1/2;
    hl = HL_NO(trans,N,Y_pp);
    boltz = boltz_frac(p,n);
    wvn(p,dp,trans,n) = E1_p(p,n) - E2_pp(dp,n);
    str(p,dp,trans,n) = hl * fc(p,dp)...
        *(wvn(p,dp,trans,n)/scale)^4 * boltz/(2*(J+1)+1);

%%%%%%%%%%%%% Q12 Branch: N = J + 1/2 Transition #5 %%%%%%%%%%%%%%%%%%
%%%%%%
    trans = 5;
    J = N - 1/2;
    hl = HL_NO(trans,N,Y_pp);
    boltz = boltz_frac(p,n-1);
    wvn(p,dp,trans,n) = E1_p(p,n-1) - E2_pp(dp,n);
    str(p,dp,trans,n) = hl * fc(p,dp)...
        *(wvn(p,dp,trans,n)/scale)^4 * boltz/(2*(J)+1);
```

```
%%%%%%%%%%%%% P12 Branch: N = J + 1/2 Transition #6 %%%%%%%%%%%%%%%%%%%%
%%%%%%
    trans = 6;
    J = N - 1/2;
    hl = HL_NO(trans,N,Y_pp);
    boltz = boltz_frac(p,n-2);
    wvn(p,dp,trans,n) = E1_p(p,n-2) - E2_pp(dp,n);
    str(p,dp,trans,n) = hl * fc(p,dp)...
        *(wvn(p,dp,trans,n)/scale)^4 * boltz/(2*(J-1)+1);

%%%%%%%%%%%%% R21 Branch: N = J - 1/2 Transition #7 %%%%%%%%%%%%%%%%%%%%
%%%%%%
    trans = 7;
    J = N + 1/2;
    hl = HL_NO(trans,N,Y_pp);
    boltz = boltz_frac(p,n+2);
    wvn(p,dp,trans,n) = E2_p(p,n+2) - E1_pp(dp,n);
    str(p,dp,trans,n) = hl * fc(p,dp)...
        *(wvn(p,dp,trans,n)/scale)^4 * boltz/(2*(J+1)+1);

%%%%%%%%%%%%% Q21 Branch: N = J - 1/2 Transition #8 %%%%%%%%%%%%%%%%%%%%
%%%%%%
    trans = 8;
    J = N + 1/2;
    hl = HL_NO(trans,N,Y_pp);
    boltz = boltz_frac(p,n+1);
    wvn(p,dp,trans,n) = E2_p(p,n+1) - E1_pp(dp,n);
    str(p,dp,trans,n) = hl * fc(p,dp)...
        *(wvn(p,dp,trans,n)/scale)^4 * boltz/(2*(J)+1);

%%%%%%%%%%%%% P21 Branch: N = J - 1/2 Transition #9 %%%%%%%%%%%%%%%%%%%%
%%%%%%
    trans = 9;
    J = N + 1/2;
    hl = HL_NO(trans,N,Y_pp);
    boltz = boltz_frac(p,n);
    wvn(p,dp,trans,n) = E2_p(p,n) - E1_pp(dp,n);
    str(p,dp,trans,n) = hl * fc(p,dp)...
        *(wvn(p,dp,trans,n)/scale)^4 * boltz/(2*(J-1)+1);

%%%%%%%%%%%%% R2 Branch: N = J + 1/2 Transition #10 %%%%%%%%%%%%%%%%%%%%
%%%%%%
    trans = 10;
    J = N - 1/2;
    hl = HL_NO(trans,N,Y_pp);
    boltz = boltz_frac(p,n+1);
    wvn(p,dp,trans,n) = E2_p(p,n+1) - E2_pp(dp,n);
    str(p,dp,trans,n) = hl * fc(p,dp)...
        *(wvn(p,dp,trans,n)/scale)^4 * boltz/(2*(J+1)+1);

%%%%%%%%%%%%% Q2 Branch: N = J + 1/2 Transition #11 %%%%%%%%%%%%%%%%%%%%
%%%%%%
    trans = 11;
    J = N - 1/2;
```

```
    hl = HL_NO(trans,N,Y_pp);
    boltz = boltz_frac(p,n);
    wvn(p,dp,trans,n) = E2_p(p,n) - E2_pp(dp,n);
    str(p,dp,trans,n) = hl * fc(p,dp)...
        *(wvn(p,dp,trans,n)/scale)^4 * boltz/(2*J+1);

%%%%%%%%%%%%% P2 Branch: N = J + 1/2 Transition #12 %%%%%%%%%%%%%%%%%%
%%%%%%
    trans = 12;
    J = N - 1/2;
    hl = HL_NO(trans,N,Y_pp);
    boltz = boltz_frac(p,n-1);
    wvn(p,dp,trans,n) = E2_p(p,n-1) - E2_pp(dp,n);
    str(p,dp,trans,n) = hl * fc(p,dp)...
        *(wvn(p,dp,trans,n)/scale)^4 * boltz/(2*(J-1)+1);
        end

    end

end
```

LINE SHAPE COMPUTATION AND CONVERTING TO AIR WAVELENGTHS

```
%Following B. Cruden in the paper "Absolute Radiation Measurements in
 Earth
%and Mars Entry Conditions," a lineshape of the form of sqrt(Voigt
%function) will be used to approximate the instrument lineshape. I
 have
%also did other fits (Gaussian, Lorentzian, Voigt, Sine Squared) and
 found
%that this best matches my current setup. You can change the lineshape
%to best represent your experiment. At
%each wavelength, we have to cycle through all computed line strengths
 for
%every lower rotational level, 12 possible branch transitions, every
 upper
%vibrational level, and every lower vibrational level.

%For ease, let wvn and str become a long row vector for use with Voigt
%function. I will use vector operations to speed this part up.
wvn_vec = reshape(wvn,[1,numel(wvn)]);
str_vec = reshape(str,[1,numel(str)]);
sqrt_v_max = sqrt(Voigt(0,a)); %Used to normalize lineshape


for k = 1:length(w)
    vsum = 0;
    diff_tot = abs(wvn_vec - w(k));

    %Threshold criterion
    th_index = find(diff_tot < thresh);
```

```
     %Square-root of Voigt Function (normalized)
     factor = sqrt(Voigt_vect(sv_const*(w(k)-
wvn_vec(th_index)),a))/...
         sqrt_v_max;
     vsum = str_vec(th_index).*factor;

%To convert to vacuum wavelengths to air wavelengths, use the
 expresion
%found in "The Refractive Index of Air" B. Edlen (1965)

    I = sum(vsum);
    lambda_vac = 10^7/w(k);
    sigma = 10^3/lambda_vac;
    dlx = (8342.13+2406030/(130-sigma^2) + 15997/(38.9-
sigma^2))*10^-8;
    air = lambda_vac/(1+dlx);

    %Output text file
    fprintf(f_out,'%d %d\n',[air I]);
end
fclose(f_out);

    end
end
```

Published with MATLAB® R2018a

HL_NO.m

```
%Function: "HL_NO.m"

%This function is used to compute the Honl - London factors for branch
%strengths in the gamma transition for NO (2 Sigma -> 2 Pi). This is
 used
%in combination with the script "NO_Gamma_njy.m" to compute the
%contributions of the 12 branches. The original expression can be
 found in
%the book "Rotational Structure in the Spectra of Diatomic Molecules"
 by I.
%Kovacs (1969, New York), in table 3.7 (section 3.2.2).Keep in mind
 that in
%table 3.7, we are using the second del_Lambda = -1 column and that
 Lambda
%in all expressions are zero, since "Lambda values always mean the
 smaller
%of the two Lambda's involved" written by Kovacs.

%The input required is the transition number (labeled from 1 to 12
 going
%from top down the list), the current N (1 => N=J-1/2, 2 => N=J+1/2),
 and
%the fraction Ypp = Av_pp / Bv_pp computed for the current vibrational
%quantum number v. The functions umin.m, upos.m, Cpos.m, Cmin.m are
 all
%required to compute the factors.

%Last Modified: 1/16/2018
%Nelson J Yanes

function hl_factor = HL_NO (transition , N , Ypp)
p = 0; %Prime state Lambda (Sigma configuration for upper state)
pp = 1; %Double prime state Lambda (Pi configuration in lower state)
Y = Ypp; %Redefine as it may confuse some of the p's later


%%%%%%%%%%%%% R1 Branch: N = J - 1/2 Transition #1 %%%%%%%%%%%%%%%%%%
%%%%%%
if transition == 1
    J = N + 1/2;
    R1 = ((J-1/2)*(J+1/2)/(8*(J+1)*Cmin(p,J,Y)*Cmin(pp,J+1,Y)))...
        *(umin(p,J,Y)*umin(pp,J+1,Y)+4*(J+3/2)*(J+3/2))^2;

    hl_factor = R1;
end


%%%%%%%%%%%%% Q1 Branch: N = J - 1/2 Transition #2 %%%%%%%%%%%%%%%%%%
%%%%%%
if transition == 2
```

```
    J = N + 1/2;
    Q1 =( (J-1/2)*(J+1/2)*(J+3/2)/(4*J*(J
+1)*Cmin(p,J,Y)*Cmin(pp,J,Y)) )...
        *(umin(p,J,Y)*umin(pp,J,Y)+4*(J+1/2)^2)^2;

    hl_factor = Q1;
end


%%%%%%%%%%%%% P1 Branch: N = J - 1/2 Transition #3 %%%%%%%%%%%%%%%%%
%%%%%%
if transition == 3
   J = N + 1/2;
   P1 = ( (J+1/2)*(J+3/2)/(8*J*Cmin(p,J,Y)*Cmin(pp,J-1,Y)) )...
       *(umin(p,J,Y)*umin(pp,J-1,Y)+4*(J-1/2)^2)^2;

   hl_factor = P1;
end


%%%%%%%%%%%%% R12 Branch: N = J + 1/2 Transition #4 %%%%%%%%%%%%%%%%%
%%%%%%
if transition == 4
    J = N - 1/2;
    R12 = ( (J-1/2)*(J+1/2)/(8*(J+1)*Cpos(p,J,Y)*Cmin(pp,J+1,Y)) )...
        *(upos(p,J,Y)*umin(pp,J+1,Y)-4*(J+3/2)^2)^2;

    hl_factor = R12;
end


%%%%%%%%%%%%% Q12 Branch: N = J + 1/2 Transition #5 %%%%%%%%%%%%%%%%%
%%%%%%
if transition == 5
    J = N - 1/2;
    Q12 =((J-1/2)*(J+1/2)*(J+3/2)/(4*J*(J
+1)*Cpos(p,J,Y)*Cmin(pp,J,Y)))...
        *(upos(p,J,Y)*umin(pp,J,Y)-4*(J+1/2)^2)^2;

    hl_factor = Q12;
end


%%%%%%%%%%%%% P12 Branch: N = J + 1/2 Transition #6 %%%%%%%%%%%%%%%%%
%%%%%%
if transition == 6
    J = N - 1/2;
    P12 = ( (J+1/2)*(J+3/2)/(8*J*Cpos(p,J,Y)*Cmin(pp,J-1,Y)) )...
        *(upos(p,J,Y)*umin(pp,J-1,Y)-4*(J-1/2)^2)^2;

    hl_factor = P12;
end
```

```
%%%%%%%%%%%%% R21 Branch: N = J - 1/2 Transition #7 %%%%%%%%%%%%%%%%%%
%%%%%%
if transition == 7
   J = N +1/2;
   R21 = ( (J-1/2)*(J+1/2)/(8*(J+1)*Cmin(p,J,Y)*Cpos(pp,J+1,Y)) )...
       *(umin(p,J,Y)*upos(pp,J+1,Y)-4*(J+3/2)^2)^2;

   hl_factor = R21;
end


%%%%%%%%%%%%% Q21 Branch: N = J - 1/2 Transition #8 %%%%%%%%%%%%%%%%%%
%%%%%%
if transition == 8
   J = N + 1/2;
   Q21 =((J-1/2)*(J+1/2)*(J+3/2)/(4*J*(J
+1)*Cmin(p,J,Y)*Cpos(pp,J,Y)))...
       *(umin(p,J,Y)*upos(pp,J,Y)-4*(J+1/2)^2)^2;

   hl_factor = Q21;
end


%%%%%%%%%%%%% P21 Branch: N = J - 1/2 Transition #9 %%%%%%%%%%%%%%%%%%
%%%%%%
if transition == 9
    J = N + 1/2;
    P21 = ( (J+1/2)*(J+3/2)/(8*J*Cmin(p,J,Y)*Cpos(pp,J-1,Y)) )...
        *(umin(p,J,Y)*upos(pp,J-1,Y)-4*(J-1/2)^2)^2;

    hl_factor = P21;
end


%%%%%%%%%%%%% R2 Branch: N = J + 1/2 Transition #10 %%%%%%%%%%%%%%%%%%
%%%%%%
if transition == 10
   J = N - 1/2;
   R2 = ( (J-1/2)*(J+1/2)/(8*(J+1)*Cpos(p,J,Y)*Cpos(pp,J+1,Y)) )...
       *(upos(p,J,Y)*upos(pp,J+1,Y)+4*(J+3/2)^2)^2;

   hl_factor = R2;
end


%%%%%%%%%%%%% Q2 Branch: N = J + 1/2 Transition #11 %%%%%%%%%%%%%%%%%%
%%%%%%
if transition == 11
    J = N - 1/2;
    Q2 = ((J-1/2)*(J+1/2)*(J+3/2)/(4*J*(J
+1)*Cpos(p,J,Y)*Cpos(pp,J,Y)))...
        *(upos(p,J,Y)*upos(pp,J,Y)+4*(J+1/2)^2)^2;

    hl_factor = Q2;
```

```
end


%%%%%%%%%%%%% P2 Branch: N = J + 1/2 Transition #12 %%%%%%%%%%%%%%%%%%
%%%%%%
if transition == 12
  J = N - 1/2;
  P2 = ( (J+1/2)*(J+3/2)/(8*J*Cpos(p,J,Y)*Cpos(pp,J-1,Y)) )...
      *(upos(p,J,Y)*upos(pp,J-1,Y)+4*(J-1/2)^2)^2;

  hl_factor = P2;
end


end
```

Published with MATLAB® R2018a

Voigt_vect.m

Table of Contents


```
function [W] = Voigt_vect(X,Y)

%VOIGT Normalized Voigt profile

%Nelson's Edits: This code is based on "Spectrosocopy and Optical
%Diagnostics for Gases" (Hanson, Spearrin, Goldenstein). The code is
%Heavily modified to work with vectors. This assumes X is an
%array and Y is only a scalar!

% [W]=Voigt(X,Y)
%
% Uses Humlicek’s algorithm for calculating the Voigt profile
%
% X = position/frequency
% Y= Voigt ‘‘a" parameter (ratio of Lorentz to Doppler widths)
% W = Voigt value
% area = sqrt(pi)
% width (FWHM) = (Y+sqrt(Y*Y+4*ln(2)))(approximation)
% linecenter is at X=0
% amplitude = Voigt(0,Y)
%
% To use with curve-fitting or for simulating absorption spectra,
% use this function the following way:
%
% Lineshape = amp* Voigt((2*sqrt(log(2))/WG)*(x-x0),a)
% amp = 2*(sqrt(ln(2))*S*P*xj/(sqrt(pi)*WG)
% log(2) = ln(2)
% WG = Doppler FWHM

% x = frequency position at which to calculate theVoigt function
% x0 = linecenter
% a = Voigt ‘‘a" parameter
%
% For calculating the amplitude, S is the integrated linestrength
% [cm^(-2)/atm], P is the pressure [atm], and xj is the
% molefraction of species of interest

T = complex(Y,-X); S = abs(X)+Y; %Complex function is a vector.
```

Region 1

```
index1 = find(S>=15);

    W(index1)= 0.5641896*T(index1)./(0.5+T(index1).*T(index1));
```

Region 2

```
index2 = find(S>=5.5 & S<15);
    T2 = T(index2);
        U2= T2.*T2;
        W(index2)= T2.*(1.410474+U2*0.5641896)./(0.75+U2.*(3+U2));
```

Region 3

Original Statement: Y >= (0.195*abs(X)-0.176)

```
index3 = find (S<5.5 & S<=(5.1282*(1.195*Y+0.176)));
        T3 = T(index3);
            Wnum= (16.4955+T3.*(20.20933+T3.*(11.96482+T3.*...
            (3.778987+T3*0.5642236))));
            Wden= (16.4955+T3.*(38.82363+T3.*(39.27121+T3.*...
            (21.69274+T3.*(6.699398+T3)))));
            W(index3) = Wnum./Wden;
```

Region 4

```
clear('Wnum')
clear('Wden')
index4 = find(S<5.5 & S>(5.1282*(1.195*Y+0.176)));
        T4 = T(index4);
            U4= T4.*T4;
            Wnum=T4.*(36183.31-U4.*(3321.9905-U4.*...
            (1540.787-U4.*( 219.0313-U4.*(35.76683-U4.*...
            (1.320522-U4*0.56419))))));
            Wden =(32066.6-U4.*(24322.84-U4.*(9022.228-U4.*...
            (2186.181-U4.*(364.2191-U4.*...
            (61.57037-U4.*(1.841439-U4)))))));
            Wtemp=Wnum./Wden;
            W(index4)= complex(exp(real(U4)).*cos(imag(U4)),0)-Wtemp;


W = real(W);
```

Published with MATLAB® R2018a

Cmin.m

```
%Function: "Cmin.m"

%This function computes the C minus expresion. This is Equation 6 in
%section 2.1.3 from the book "Rotational Sturcture in the Spectra of
%Diatomic Molecules" by I. Kovacs (1969, New York). This function
 requres
%the umin.m function as well. Lambda depends on the state of interest
%(upper state lambda versus lower state lambda). This function is used
 in
%computing the Honl-London factors for NO.

%Last Modified: 1/17/2018
%Nelson J Yanes

function c = Cmin(Lambda, J, Y)

c = (1/2)*(umin(Lambda,J,Y)^2 + 4*((J+1/2)^2 - Lambda^2));

end
```

Published with MATLAB® R2015a

Cpos.m

```
%Function: "Cpos.m"

%This function computes the C positive expresion. This is Equation 6
 in
%section 2.1.3 from the book "Rotational Sturcture in the Spectra of
%Diatomic Molecules" by I. Kovacs (1969, New York). This function
 requres
%the upos.m function as well. Lambda depends on the state of interest
%(upper state lambda versus lower state lambda). This function is used
 in
%computing the Honl-London factors for NO.

%Last Modified: 1/17/2018
%Nelson J Yanes

function c = Cpos(Lambda, J, Y)

c = (1/2)*(upos(Lambda,J,Y)^2 + 4*((J+1/2)^2 - Lambda^2));

end
```

Published with MATLAB® R2015a

umin.m

```
%Function: "umin.m"

%This function computes the u with the minus expression. Lambda used
%depends on the state (prime or double prime for upper and lower
 states
%respectively). This will be passed into the fuction via "Lambda"
%From the book "Rotational Sturcture in the Spectra of Diatomic
 Molecules"
%by I. Kovacs (1969, New York). Equation 6 in section 2.1.3 is used in
%Honl-London factor computation.

%Last Modified: 1/16/2018
%Nelson J Yanes

function u = umin(Lambda, J, Y)

u = sqrt( Lambda^2 * Y*(Y-4) + 4*(J+1/2)^2 ) - Lambda * (Y -2);

end
```

Published with MATLAB® R2015a

upos.m

```
%Function: "upos.m"

%This function computes the u with the positive expression. Lambda
 used
%depends on the state (prime or double prime for upper and lower
 states
%respectively). This will be passed into the fuction via "Lambda"
%From the book "Rotational Sturcture in the Spectra of Diatomic
 Molecules"
%by I. Kovacs (1969, New York). Equation 6 in section 2.1.3 is used in
%Honl-London factor computation.

%Last Modified: 1/16/2018
%Nelson J Yanes

function u = upos(Lambda, J, Y)

u = sqrt( Lambda^2 * Y*(Y-4) + 4*(J+1/2)^2 ) + Lambda * (Y -2);

end
```

Published with MATLAB® R2015a

Frank-Condon Factors

The constants computed by Ory et al. [73] are used in the present work. File format: v', v", $q_{v',v''}$.

```
1,1,0.16558
1,2,0.26393
1,3,0.23793
1,4,0.16062
1,5,0.090801
1,6,0.045607
1,7,0.021097
1,8,0.0092046
1,9,0.003851
1,10,0.0015637
1,11,0.00062187
1,12,0.00024395
1,13,9.49E-05
1,14,3.68E-05
1,15,1.43E-05
1,16,5.58E-06
1,17,2.19E-06
1,18,8.65E-07
1,19,3.46E-07
1,20,1.40E-07
1,21,5.63E-08
2,1,0.3295
2,2,0.10504
2,3,0.00079568
2,4,0.072245
2,5,0.13508
2,6,0.13405
2,7,0.098671
2,8,0.060824
2,9,0.033368
2,10,0.016886
2,11,0.0080682
```

2,12,0.0036991
2,13,0.0016464
2,14,0.00071762
2,15,0.00030852
2,16,0.00013157
2,17,5.59E-05
2,18,2.38E-05
2,19,1.01E-05
2,20,4.23E-06
2,21,1.71E-06
3,1,0.29093
3,2,0.01468
3,3,0.15473
3,4,0.075294
3,5,0.00054896
3,6,0.034387
3,7,0.088594
3,8,0.10576
3,9,0.090032
3,10,0.062969
3,11,0.038737
3,12,0.021801
3,13,0.011512
3,14,0.0058038
3,15,0.0028294
3,16,0.0013462
3,17,0.00062899
3,18,0.00028933
3,19,0.00013094
3,20,5.83E-05
3,21,2.58E-05
4,1,0.15051
4,2,0.19057
4,3,0.048775
4,4,0.037312
4,5,0.11318

```
4,6,0.051313
4,7,0.00059613
4,8,0.022915
4,9,0.065587
4,10,0.085584
4,11,0.0794
4,12,0.060427
4,13,0.040387
4,14,0.024652
4,15,0.014089
4,16,0.0076652
4,17,0.0040149
4,18,0.0020426
4,19,0.0010196
4,20,0.00050771
4,21,0.00025888
5,1,0.050764
5,2,0.23765
5,3,0.035495
5,4,0.12645
5,5,0.002554
5,6,0.054853
5,7,0.087917
5,8,0.034123
5,9,0.0001753
5,10,0.018413
5,11,0.052441
5,12,0.071262
5,13,0.069789
5,14,0.056386
5,15,0.0401
5,16,0.026062
5,17,0.015878
5,18,0.0092522
5,19,0.0052517
5,20,0.0029477
```

```
5,21,0.0016438
6,1,0.011753
6,2,0.13393
6,3,0.19787
6,4,0.0036686
6,5,0.10272
6,6,0.051258
6,7,0.0038666
6,8,0.062972
6,9,0.067945
6,10,0.022149
6,11,1.13E-08
6,12,0.016185
6,13,0.043791
6,14,0.060425
6,15,0.06135
6,16,0.051999
6,17,0.039181
6,18,0.027231
6,19,0.017822
6,20,0.011052
6,21,0.0064403
7,1,0.0019159
7,2,0.044347
7,3,0.19906
7,4,0.097177
7,5,0.057539
7,6,0.034399
7,7,0.088496
7,8,0.010858
7,9,0.017895
7,10,0.062905
7,11,0.051729
7,12,0.014166
7,13,0.0001218
7,14,0.014647
```

```
7,15,0.037611
7,16,0.052685
7,17,0.055426
7,18,0.04883
7,19,0.037805
7,20,0.026359
7,21,0.016878
8,1,0.00022206
8,2,0.0094975
8,3,0.094719
8,4,0.2116
8,5,0.019038
8,6,0.10587
8,7,0.00030332
8,8,0.073398
8,9,0.04773
8,10,4.09E-05
8,11,0.030809
8,12,0.057947
8,13,0.038895
8,14,0.0087483
8,15,0.0004855
8,16,0.01394
8,17,0.03281
8,18,0.044446
8,19,0.045884
8,20,0.040543
8,21,0.033098
9,1,1.83E-05
9,2,0.0013712
9,3,0.026462
9,4,0.14874
9,5,0.17106
9,6,0.0012457
9,7,0.10348
9,8,0.017766
```

```
9,9,0.030874
9,10,0.068463
9,11,0.016818
9,12,0.0040435
9,13,0.037657
9,14,0.04946
9,15,0.028692
9,16,0.0058447
9,17,0.00042484
9,18,0.010277
9,19,0.025444
9,20,0.038695
9,21,0.046903
10,1,1.05E-06
10,2,0.00013542
10,3,0.004716
10,4,0.054289
10,5,0.18873
10,6,0.10286
10,7,0.03187
10,8,0.062334
10,9,0.055681
10,10,0.0023771
10,11,0.056778
10,12,0.044888
10,13,0.0028695
10,14,0.01231
10,15,0.04233
10,16,0.046119
10,17,0.024785
10,18,0.0041322
10,19,0.0013292
10,20,0.015167
10,21,0.033008
11,1,4.14E-08
11,2,9.11E-06
```

```
11,3,0.00055497
11,4,0.011886
11,5,0.090884
11,6,0.20177
11,7,0.039452
11,8,0.075305
11,9,0.018399
11,10,0.076362
11,11,0.0056629
11,12,0.026471
11,13,0.054808
11,14,0.019588
11,15,0.00033358
11,16,0.021023
11,17,0.038097
11,18,0.029535
11,19,0.010986
11,20,0.00080708
11,21,0.0011331
12,1,1.06E-09
12,2,4.13E-07
12,3,4.33E-05
12,4,0.0016546
12,5,0.024459
12,6,0.13065
12,7,0.18417
12,8,0.0043962
12,9,0.10107
12,10,4.93E-05
12,11,0.067835
12,12,0.032243
12,13,0.0025622
12,14,0.041059
12,15,0.04103
12,16,0.0097536
12,17,0.00089437
```

12,18,0.016943
12,19,0.033612
12,20,0.036459
12,21,0.025575
13,1,1.45E-10
13,2,1.17E-08
13,3,2.20E-06
13,4,0.00015061
13,5,0.0040002
13,6,0.043278
13,7,0.16672
13,8,0.14167
13,9,0.0036829
13,10,0.093681
13,11,0.010905
13,12,0.041503
13,13,0.056148
13,14,0.0018754
13,15,0.026392
13,16,0.057432
13,17,0.030223
13,18,0.00074414
13,19,0.014696
13,20,0.045546
13,21,0.051112

Appendix D

LIST OF HET EXPERIMENTS

Shot #	Condition	Gas	Model	Diagnostic	Notes
1564	M5-H6-A	Air	Staggered Pitot Rake		
1565	M7-H8-A	Air	Staggered Pitot Rake		
1566	M7-H8-He	Air	Staggered Pitot Rake		
1567	M5-H4-A	Air	Staggered Pitot Rake		
1568	M5-H6-A	Air	Staggered Pitot Rake		
1569	M7-H8-A	Air	Staggered Pitot Rake		
1570	M5-H4-A	Air	Staggered Pitot Rake		
1571	M7-H8-A	Air	Staggered Pitot Rake		
1572	M7-H8-A	Air	1" Diameter Cylinder	High Speed Schlieren	
1573	M5-H6-A	Air	1" Diameter Cylinder	High Speed Schlieren	
1574	M5-H4-A	Air	1" Diameter Cylinder	High Speed Schlieren	
1575	M7-H8-He	Air	Staggered Pitot Rake		
1576	M5-H6-A	Air	Double Wedge	High Speed Schlieren	
1577	M7-H8-A	Air	Double Wedge	High Speed Schlieren	
1578	M7-H8-He	Air	Double Wedge	High Speed Schlieren	
1579	M5-H4-A	Air	Double Wedge	High Speed Schlieren	
1580	M7-H8-A	Air	Double Wedge	High Speed Schlieren	
1581	M7-H8-He	Air	Double Wedge	High Speed Schlieren	
1582	M7-H8-A	Air	1" Diameter Cylinder	High Speed Schlieren	
1583	M7-H8-A	Air	1" Diameter Sphere	High Speed Schlieren	
1608	M7-H8-A		1.25" Diameter Cylinder	Single Shot Schlieren	
1609	M7-H8-A	X_{O_2} 0 .063	1.25" Diameter Cylinder	Single Shot Schlieren	
1610	M7-H8-A	Air	1.25" Diameter Cylinder	Single Shot Schlieren	
1611	M7-H8-A	Air	1.25" Diameter Cylinder	Single Shot Schlieren	
1612	M7-H8-A	Air	1.25" Diameter Cylinder	Single Shot Schlieren	
1613	M7-H8-A	Air	1.25" Diameter Cylinder	Single Shot Schlieren	
1614	M7-H8-A	X_{O_2} 0 .105	1.25" Diameter Cylinder	Single Shot Schlieren	Crack found on weld for driver blades.
1633	M7-H8-A	Air	1.25" Diameter Cylinder	Single Shot Schlieren	New blades were tested between 1614 and 1633.
1634	M7-H8-A	X_{O_2} 0 .063	1.25" Diameter Cylinder	Single Shot Schlieren	
1635	M7-H8-A	X_{O_2} 0 .105	1.25" Diameter Cylinder	Single Shot Schlieren	
1636	M7-H8-A	X_{O_2} 0 .252	1.25" Diameter Cylinder	Single Shot Schlieren	
1637	M7-H8-A	X_{O_2} 0 .137	1.25" Diameter Cylinder	Single Shot Schlieren	
1638	M7-H8-A	Air	1.25" Diameter Cylinder	Single Shot Schlieren	
1639	M7-H8-A	X_{O_2} 0 .168	1.25" Diameter Cylinder	Single Shot Schlieren	
1640	M7-H8-A	Nitrogen	1.25" Diameter Cylinder	Single Shot Schlieren	

Shot #	Condition	Gas	Model	Diagnostic	Notes
1641	M7-H8-A	Air	1.25" Diameter Cylinder	Emission of Stagnation Line	
1642	M7-H8-A	Air	1.25" Diameter Cylinder	Emission of Stagnation Line	
1643	M5-H6-A	Air	1.25" Diameter Cylinder	Emission of Stagnation Line	
1644	M5-H6-A	Air	1.25" Diameter Cylinder	Emission of Stagnation Line	
1645	M5-H6-A	X_{O_2} 0 .063	1.25" Diameter Cylinder	Emission of Stagnation Line	
1646	M5-H6-A	X_{O_2} 0 .105	1.25" Diameter Cylinder	Emission of Stagnation Line	
1647	M5-H6-A	X_{O_2} 0 .168	1.25" Diameter Cylinder	Emission of Stagnation Line	
1648	M5-H6-A	X_{O_2} 0 .273	1.25" Diameter Cylinder	Emission of Stagnation Line	
1649	M5-H6-A	Air	1.25" Diameter Cylinder	Emission of Stagnation Line	
1650	M7-H8-A	Air	1.25" Diameter Cylinder	Emission of Stagnation Line	
1651	M7-H8-A	X_{O_2} 0 .105	1.25" Diameter Cylinder	Emission of Stagnation Line	
1652	M7-H8-A	Nitrogen	1.25" Diameter Cylinder	Emission of Stagnation Line	
1653	M7-H8-A	X_{O_2} 0 .063	1.25" Diameter Cylinder	Emission of Stagnation Line	
1654	M7-H8-A	X_{O_2} 0 .252	1.25" Diameter Cylinder	Emission of Stagnation Line	
1655	M7-H8-A	Air	1.25" Diameter Cylinder	Emission of Stagnation Line	
1656	M5-H6-A	Air	1.25" Diameter Cylinder	Emission of Stagnation Line	
1657	M5-H6-A	X_{O_2} 0 .137	1.25" Diameter Cylinder	Emission of Stagnation Line	
1658	M7-H8-A	X_{O_2} 0 .137	1.25" Diameter Cylinder	Emission of Stagnation Line	
1659	M7-H8-A	X_{O_2} 0 .273	1.25" Diameter Cylinder	Emission of Stagnation Line	
1670	M7-H8-A	Air	Double Wedge	Emission Downstream Bow Shock + Shear Layer	
1671	M7-H8-A	Air	Double Wedge	Emission Downstream Bow Shock + Shear Layer	
1672	M7-H8-A	Air	Double Wedge	Emission Downstream Bow Shock + Shear Layer	
1673	M7-H8-A	Air	Double Wedge	Emission Downstream Bow Shock + Shear Layer	
1674	M7-H8-A	Air	Double Wedge	Emission Downstream Bow Shock + Shear Layer	
1675	M7-H8-A	Air	Double Wedge	Emission Downstream Bow Shock + Shear Layer	
1676	M7-H8-A	Air	Double Wedge	Emission Downstream Bow Shock + Shear Layer	
1677	M7-H8-A	Air	Double Wedge	Emission Downstream Bow Shock + Shear Layer	
1678	M7-H8-A	Air	Double Wedge	Emission Downstream Bow Shock + Shear Layer	
1679	M7-H8-A	Air	Double Wedge	Emission Downstream Bow Shock + Shear Layer	
1680	M7-H8-A	Air	Double Wedge	Emission Downstream Bow Shock + Shear Layer	
1681	M7-H8-A	Air	Double Wedge	Emission Downstream Bow Shock + Shear Layer	
1682	M7-H8-A	Air	Double Wedge	Emission Downstream Bow Shock + Shear Layer	
1683	M7-H8-A	Air	Double Wedge	Emission Downstream Bow Shock + Shear Layer	Data lost.

Shot #	Condition	Gas	Model	Diagnostic	Notes
1684	M7-H8-A	Air	Double Wedge	Emission Downstream Bow Shock + Shear Layer	Moved DW 4 mm upstream to measure up to 2nd wedge surface.
1685	M7-H8-A	Air	Double Wedge	Emission Downstream Bow Shock + Shear Layer	
1686	M7-H8-A	Air	Double Wedge	Emission Downstream Bow Shock + Shear Layer	
1687	M7-H8-A	Air	Double Wedge	Emission Downstream Bow Shock + Shear Layer	
1688	M7-H8-A	Air	Double Wedge	Emission Downstream Bow Shock + Shear Layer	
1689	M7-H8-A	Air	Double Wedge	Emission Downstream Bow Shock + Shear Layer	
1690	M7-H8-A	Air	Double Wedge	Emission Downstream Bow Shock + Shear Layer	
1691	M7-H8-A	Air	Double Wedge	Emission Downstream Bow Shock + Shear Layer	
1692	M7-H8-A	Air	Double Wedge	Emission Downstream Reattachment Shock	Realignment
1693	M7-H8-A	Air	Double Wedge	Emission Downstream Reattachment Shock	
1694	M7-H8-A	Air	Double Wedge	Emission Downstream Reattachment Shock	
1695	M7-H8-A	Air	Double Wedge	Emission Downstream Reattachment Shock	
1696	M7-H8-A	Air	Double Wedge	Emission Downstream Reattachment Shock	
1697	M7-H8-A	Air	Double Wedge	Emission Downstream Reattachment Shock	
1698	M7-H8-A	Air	Double Wedge	Emission Downstream Reattachment Shock	
1699	M7-H8-A	Air	Double Wedge	Emission Downstream Reattachment Shock	
1700	M7-H8-A	Air	Double Wedge	Emission Downstream Reattachment Shock	
1701	M7-H8-A	Air	Double Wedge	Emission Downstream Reattachment Shock	
1706	M5-H6-A	Air	1.25" Diameter Cylinder	Single Shot Schlieren	
1707	M5-H6-A	Nitrogen	1.25" Diameter Cylinder	Single Shot Schlieren	
1708	M5-H6-A	X_{O_2} 0 .063	1.25" Diameter Cylinder	Single Shot Schlieren	
1709	M5-H6-A	X_{O_2} 0 .105	1.25" Diameter Cylinder	Single Shot Schlieren	
1710	M5-H6-A	X_{O_2} 0 .137	1.25" Diameter Cylinder	Single Shot Schlieren	
1711	M5-H6-A	X_{O_2} 0 .273	1.25" Diameter Cylinder	Single Shot Schlieren	
1712	M7-H8-A	X_{O_2} 0 .273	1.25" Diameter Cylinder	Single Shot Schlieren	
1713	M7-H8-A	X_{O_2} 0 .273	1.25" Diameter Cylinder	Single Shot Schlieren	

Appendix E

MACHINE DRAWINGS

- Cylinder Model
- Cylinder Mount
- Cylinder Sting
- Universal Base for Stings
- Double Wedge Model
- Double Wedge Sting
- Cylinder Alignment Plate
- Double Wedge Alignment Plate
- Primary Diaphragm Cutting Blades
- Driver Section Flange

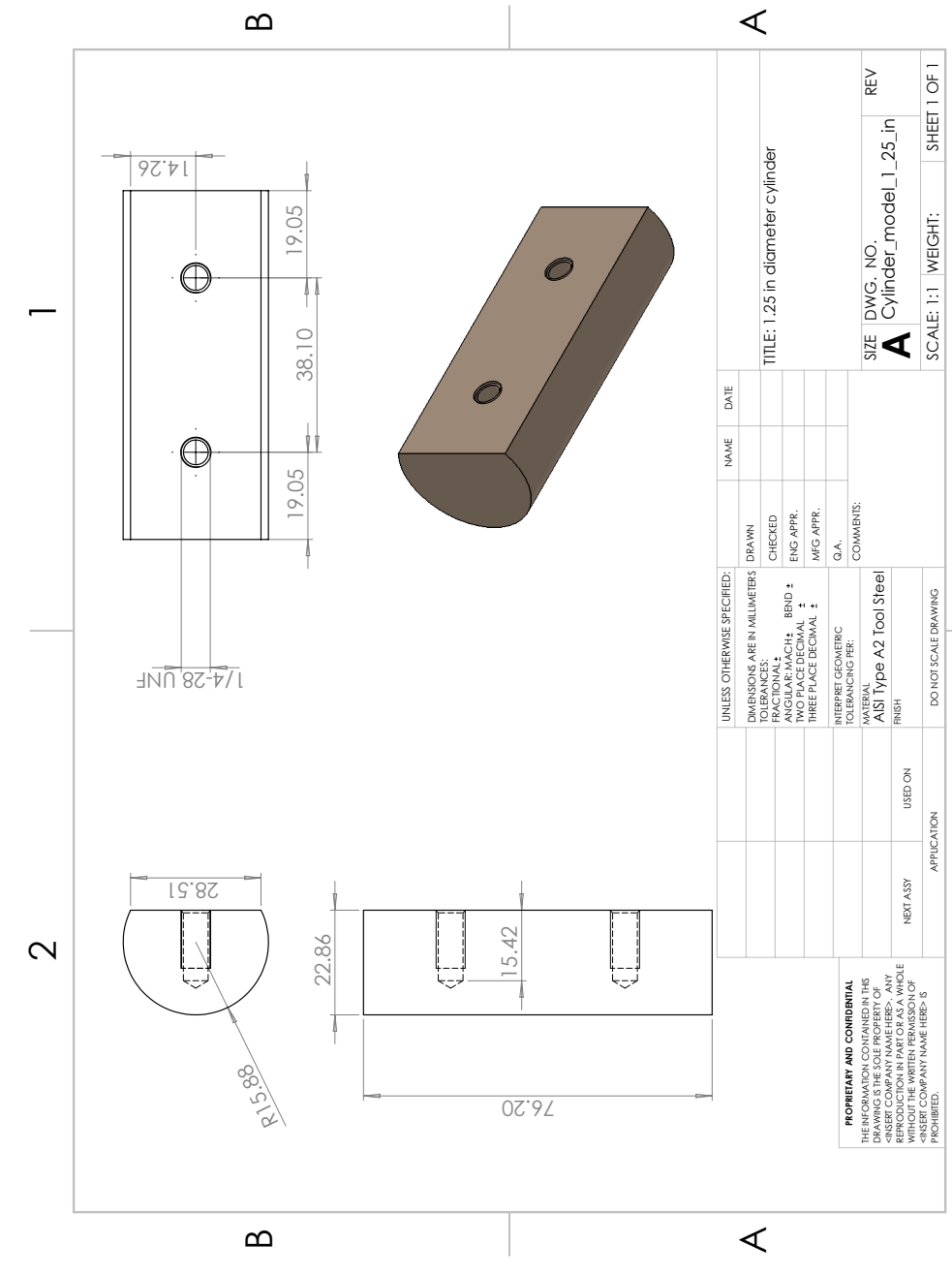
14.26
19.05
38.10
19.05
1/4-28 UNF
28.51
22.86
15.42
76.20
R15.88
TITLE: 1.25 in diameter cylinder
SIZE A
DWG. NO. Cylinder_model_1_25_in
REV
SCALE: 1:1
WEIGHT:
SHEET 1 OF 1
UNLESS OTHERWISE SPECIFIED:
DIMENSIONS ARE IN MILLIMETERS
TOLERANCES:
FRACTIONAL ±
ANGULAR: MACH ± BEND ±
TWO PLACE DECIMAL ±
THREE PLACE DECIMAL ±
INTERPRET GEOMETRIC TOLERANCING PER:
MATERIAL
AISI Type A2 Tool Steel
FINISH
DRAWN
CHECKED
ENG APPR.
MFG APPR.
Q.A.
COMMENTS:
NAME
DATE
NEXT ASSY
USED ON
APPLICATION
DO NOT SCALE DRAWING
PROPRIETARY AND CONFIDENTIAL
THE INFORMATION CONTAINED IN THIS DRAWING IS THE SOLE PROPERTY OF <INSERT COMPANY NAME HERE>. ANY REPRODUCTION IN PART OR AS A WHOLE WITHOUT THE WRITTEN PERMISSION OF <INSERT COMPANY NAME HERE> IS PROHIBITED.

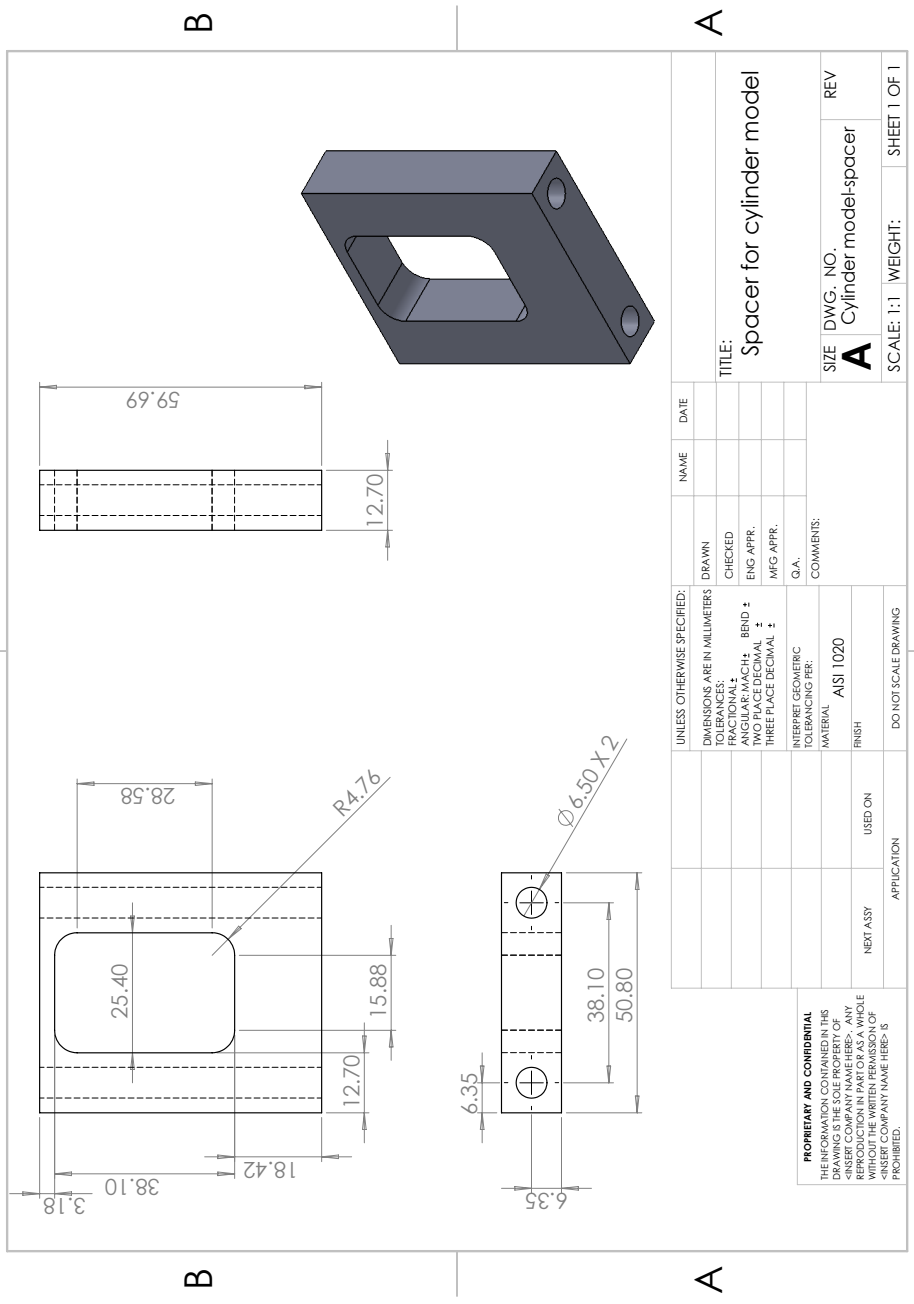
59.69
12.70
28.58
R4.76
25.40
15.88
12.70
18.42
38.10
3.18
Ø6.50 X 2
38.10
50.80
6.35
6.35
TITLE:
Spacer for cylinder model
SIZE
A
DWG. NO.
Cylinder model-spacer
REV
SCALE: 1:1
WEIGHT:
SHEET 1 OF 1
UNLESS OTHERWISE SPECIFIED:
DIMENSIONS ARE IN MILLIMETERS
TOLERANCES:
FRACTIONAL ±
ANGULAR: MACH ± BEND ±
TWO PLACE DECIMAL ±
THREE PLACE DECIMAL ±
INTERPRET GEOMETRIC
TOLERANCING PER:
MATERIAL
AISI 1020
FINISH
DRAWN
CHECKED
ENG APPR.
MFG APPR.
Q.A.
COMMENTS:
NAME
DATE
NEXT ASSY
USED ON
APPLICATION
DO NOT SCALE DRAWING
PROPRIETARY AND CONFIDENTIAL
THE INFORMATION CONTAINED IN THIS DRAWING IS THE SOLE PROPERTY OF <INSERT COMPANY NAME HERE>. ANY REPRODUCTION IN PART OR AS A WHOLE WITHOUT THE WRITTEN PERMISSION OF <INSERT COMPANY NAME HERE> IS PROHIBITED.
1
2
A
B

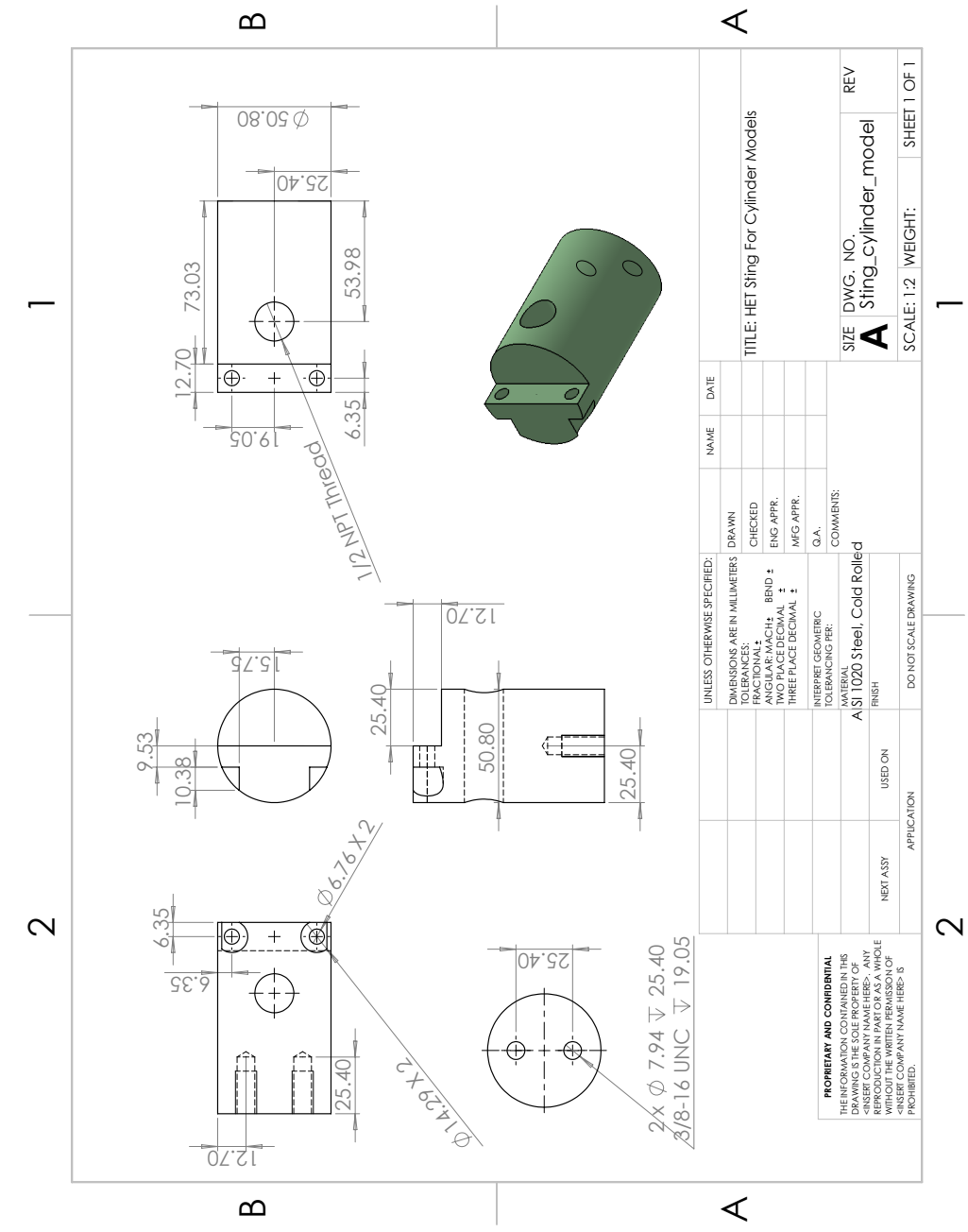
Ø50.80
25.40
73.03
53.98
12.70
19.05
6.35
1/2 NPT Thread
12.70
25.40
50.80
25.40
15.75
9.53
10.38
Ø6.76 X 2
6.35
6.35
25.40
12.70
Ø14.29 X 2
25.40
2X Ø 7.94 ↧ 25.40
3/8-16 UNC ↧ 19.05
UNLESS OTHERWISE SPECIFIED:
DIMENSIONS ARE IN MILLIMETERS
TOLERANCES:
FRACTIONAL ±
ANGULAR: MACH ± BEND ±
TWO PLACE DECIMAL ±
THREE PLACE DECIMAL ±
INTERPRET GEOMETRIC TOLERANCING PER:
MATERIAL
ASI 1020 Steel, Cold Rolled
FINISH
DO NOT SCALE DRAWING
DRAWN
CHECKED
ENG APPR.
MFG APPR.
Q.A.
COMMENTS:
NAME
DATE
TITLE: HET Sting For Cylinder Models
SIZE A
DWG. NO. Sting_cylinder_model
REV
SCALE: 1:2
WEIGHT:
SHEET 1 OF 1
NEXT ASSY
USED ON
APPLICATION
PROPRIETARY AND CONFIDENTIAL
THE INFORMATION CONTAINED IN THIS DRAWING IS THE SOLE PROPERTY OF <INSERT COMPANY NAME HERE>. ANY REPRODUCTION IN PART OR AS A WHOLE WITHOUT THE WRITTEN PERMISSION OF <INSERT COMPANY NAME HERE> IS PROHIBITED.
A
B
1
2

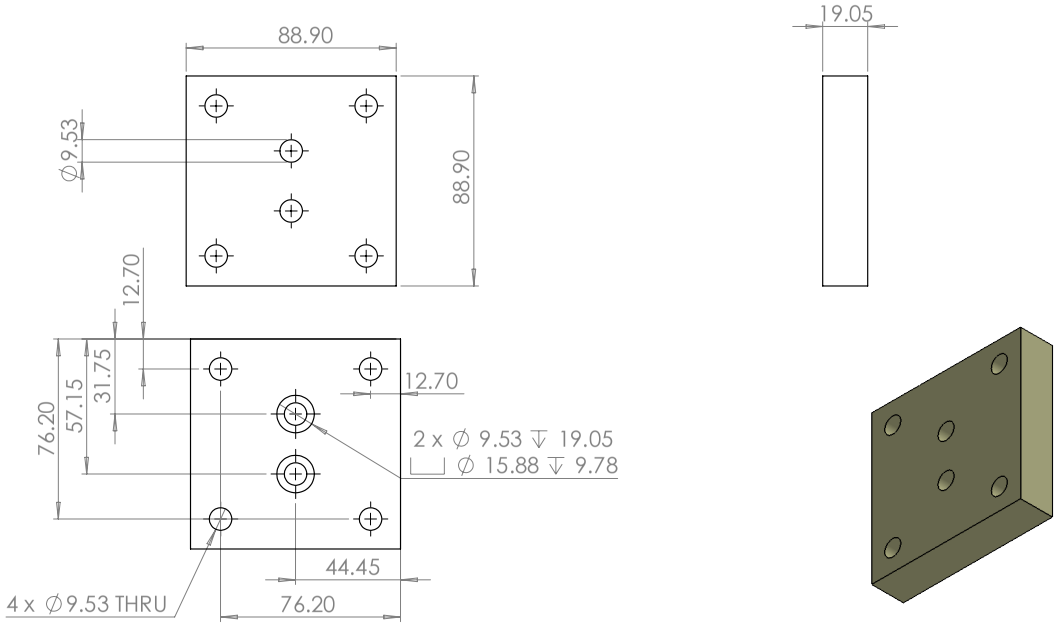

		UNLESS OTHERWISE SPECIFIED:		NAME	DATE
		DIMENSIONS ARE IN MILLIMETERS TOLERANCES: FRACTIONAL ± ANGULAR: MACH ± BEND ± TWO PLACE DECIMAL ± THREE PLACE DECIMAL ±	DRAWN		
			CHECKED		
			ENG APPR.		
			MFG APPR.		
		INTERPRET GEOMETRIC TOLERANCING PER:	Q.A.		
		MATERIAL AISI 1020 Steel, Cold Rolled	COMMENTS:		
NEXT ASSY	USED ON	FINISH			
APPLICATION		DO NOT SCALE DRAWING			

TITLE:Universal Base for Stings

SIZE	DWG. NO.	REV
A	Sting_Base	
SCALE: 1:1	WEIGHT:	SHEET 1 OF 1

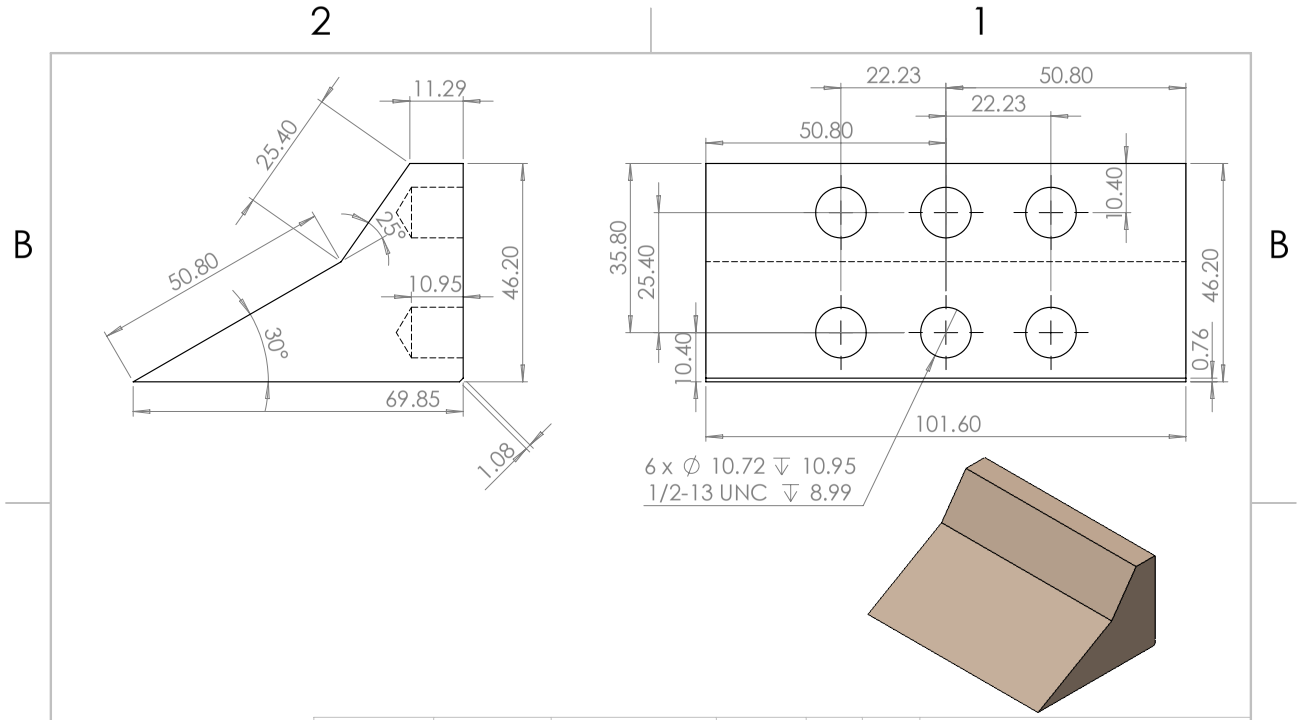

		UNLESS OTHERWISE SPECIFIED:		NAME	DATE
		DIMENSIONS ARE IN MILLIMETERS TOLERANCES: FRACTIONAL ± ANGULAR: MACH ± BEND ± TWO PLACE DECIMAL ± THREE PLACE DECIMAL ±	DRAWN		
			CHECKED		
			ENG APPR.		
			MFG APPR.		
		INTERPRET GEOMETRIC TOLERANCING PER:	Q.A.		
		MATERIAL	COMMENTS:		
NEXT ASSY	USED ON	FINISH			
APPLICATION		DO NOT SCALE DRAWING			

TITLE: Double Wedge Geometry

SIZE	DWG. NO.	REV
A	Double_wedge	
SCALE: 1:2	WEIGHT:	SHEET 1 OF 1

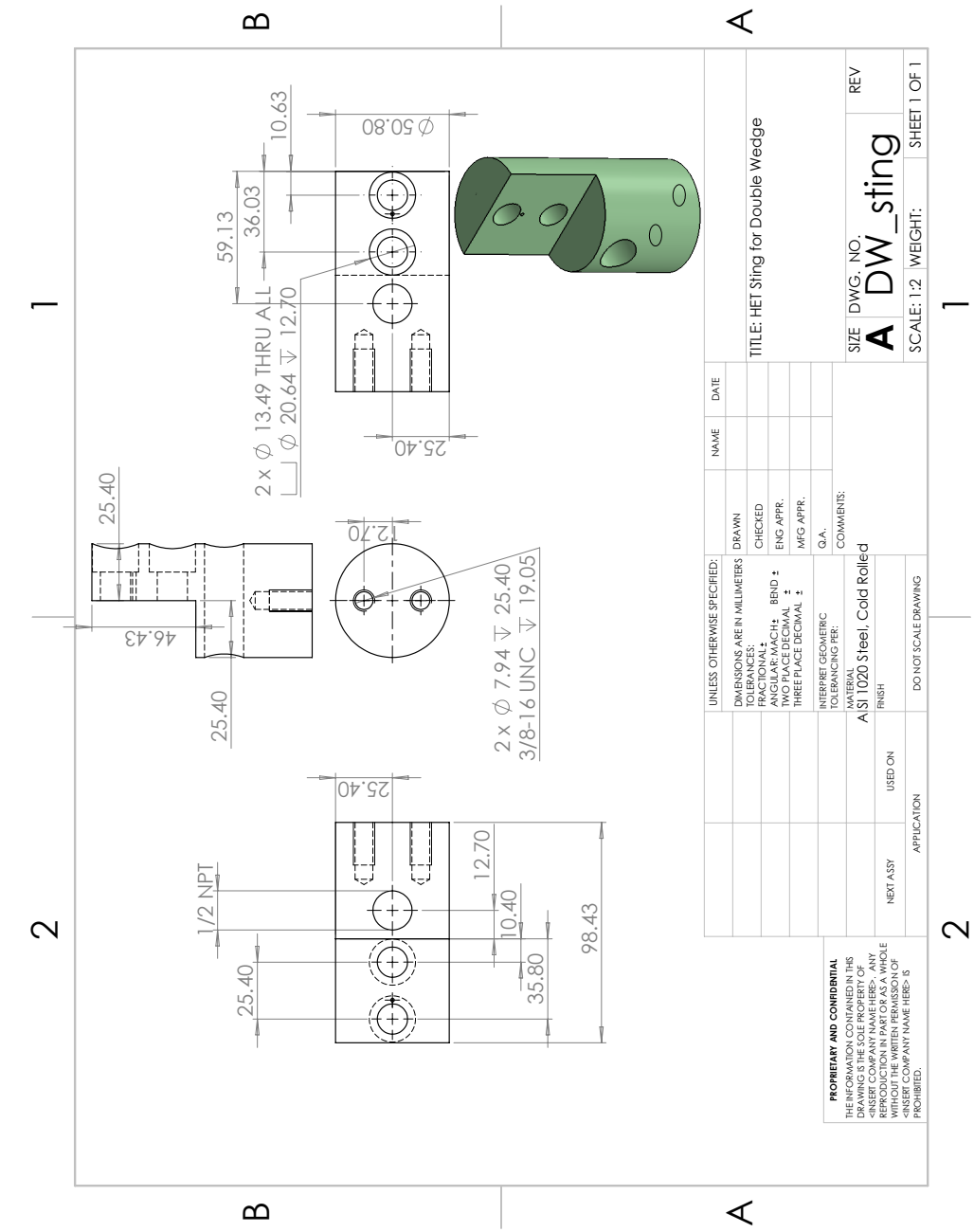
1/2 NPT
25.40
25.40
25.40
12.70
10.40
35.80
98.43
46.43
25.40
12.70
2 x ∅ 7.94 ↧ 25.40
3/8-16 UNC ↧ 19.05
2 x ∅ 13.49 THRU ALL
⌴ ∅ 20.64 ↧ 12.70
59.13
36.03
10.63
∅50.80
25.40
UNLESS OTHERWISE SPECIFIED:
DIMENSIONS ARE IN MILLIMETERS
TOLERANCES:
FRACTIONAL ±
ANGULAR: MACH ± BEND ±
TWO PLACE DECIMAL ±
THREE PLACE DECIMAL ±
INTERPRET GEOMETRIC TOLERANCING PER:
MATERIAL
ASI 1020 Steel, Cold Rolled
FINISH
DO NOT SCALE DRAWING
NEXT ASSY
USED ON
APPLICATION
DRAWN
CHECKED
ENG APPR.
MFG APPR.
Q.A.
COMMENTS:
NAME
DATE
TITLE: HET Sting for Double Wedge
SIZE
A
DWG. NO.
DW_sting
REV
SCALE: 1:2
WEIGHT:
SHEET 1 OF 1
PROPRIETARY AND CONFIDENTIAL
THE INFORMATION CONTAINED IN THIS DRAWING IS THE SOLE PROPERTY OF <INSERT COMPANY NAME HERE>. ANY REPRODUCTION IN PART OR AS A WHOLE WITHOUT THE WRITTEN PERMISSION OF <INSERT COMPANY NAME HERE> IS PROHIBITED.
A
B
1
2

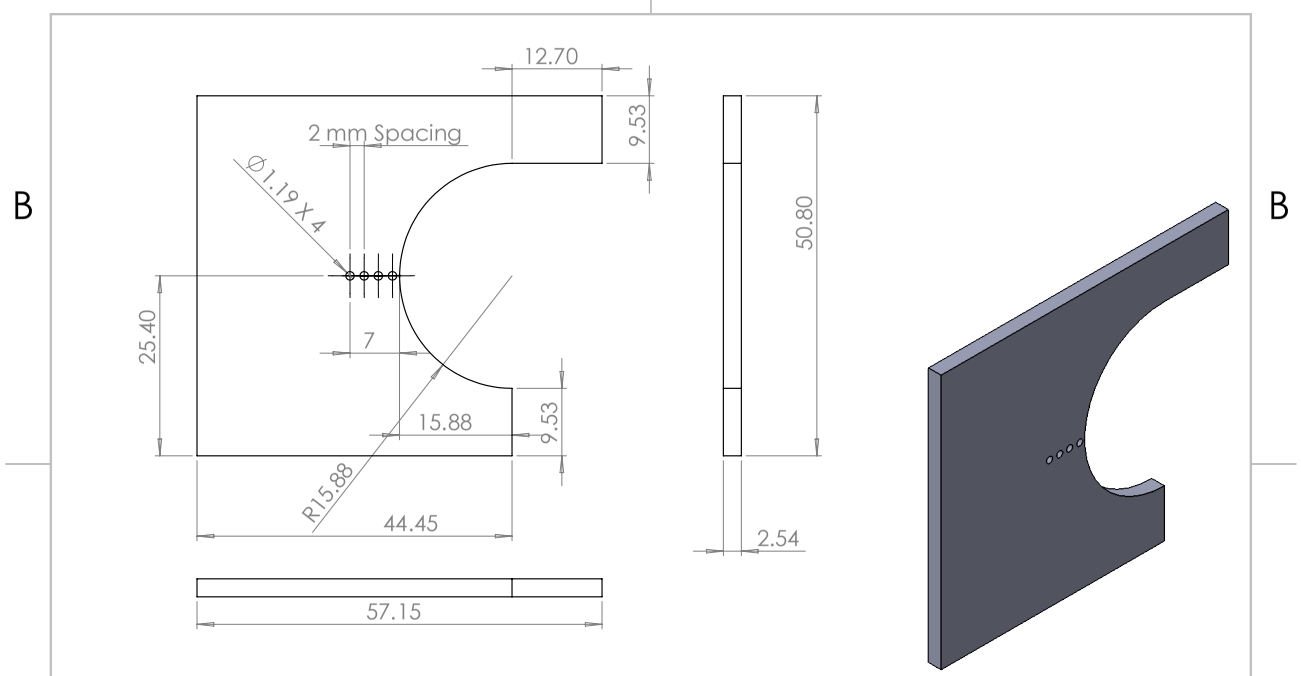

		UNLESS OTHERWISE SPECIFIED:		NAME	DATE
		DIMENSIONS ARE IN MILLIMETERS TOLERANCES: FRACTIONAL ± ANGULAR: MACH ± BEND ± TWO PLACE DECIMAL ± THREE PLACE DECIMAL ±	DRAWN		
			CHECKED		
			ENG APPR.		
			MFG APPR.		
		INTERPRET GEOMETRIC TOLERANCING PER:	Q.A.		
		MATERIAL	COMMENTS:		
NEXT ASSY	USED ON	FINISH			
APPLICATION		DO NOT SCALE DRAWING			

TITLE: Alignment Plate for 1.25 in Cylinder

SIZE	DWG. NO.	REV
A	Calibration_plate_cyl	
SCALE: 2:1	WEIGHT:	SHEET 1 OF 1

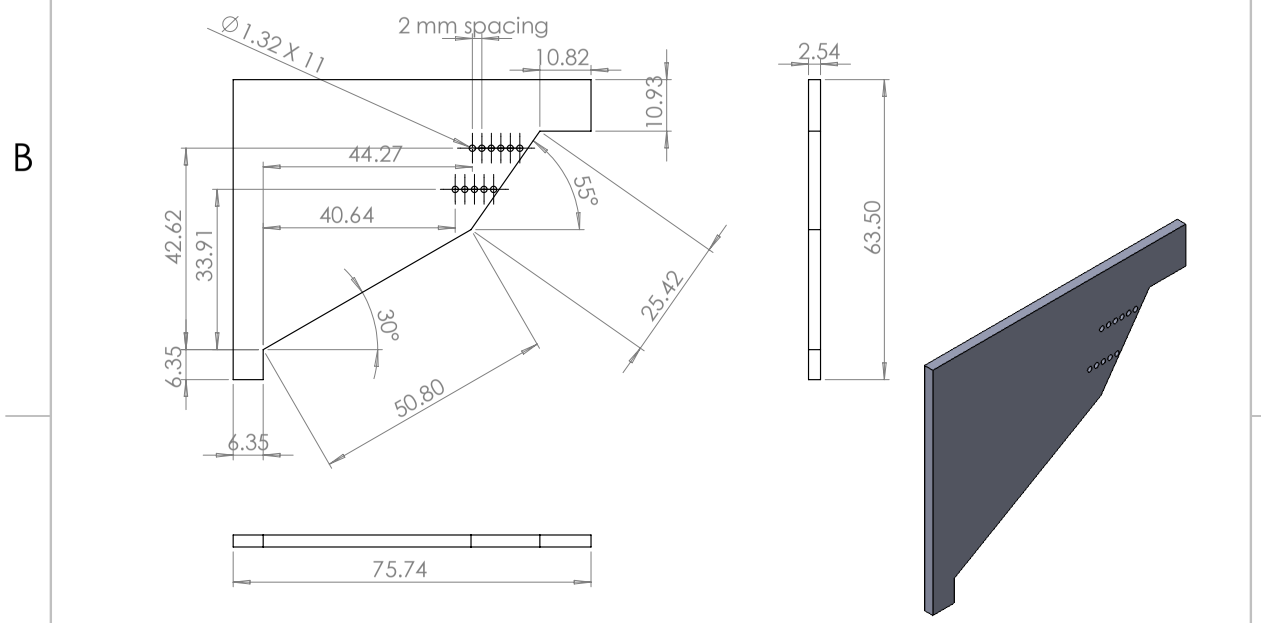

		UNLESS OTHERWISE SPECIFIED:		NAME	DATE
		DIMENSIONS ARE IN MILLIMETERS TOLERANCES: FRACTIONAL ± ANGULAR: MACH ± BEND ± TWO PLACE DECIMAL ± THREE PLACE DECIMAL ±	DRAWN		
			CHECKED		
			ENG APPR.		
			MFG APPR.		
		INTERPRET GEOMETRIC TOLERANCING PER:	Q.A.		
		MATERIAL: Aluminum	COMMENTS:		
NEXT ASSY	USED ON	FINISH			
APPLICATION		DO NOT SCALE DRAWING			

TITLE: Alignment Plate for double wedge

SIZE	DWG. NO.	REV
A	Calibration_Plate_DW	
SCALE: 1:1	WEIGHT:	SHEET 1 OF 1

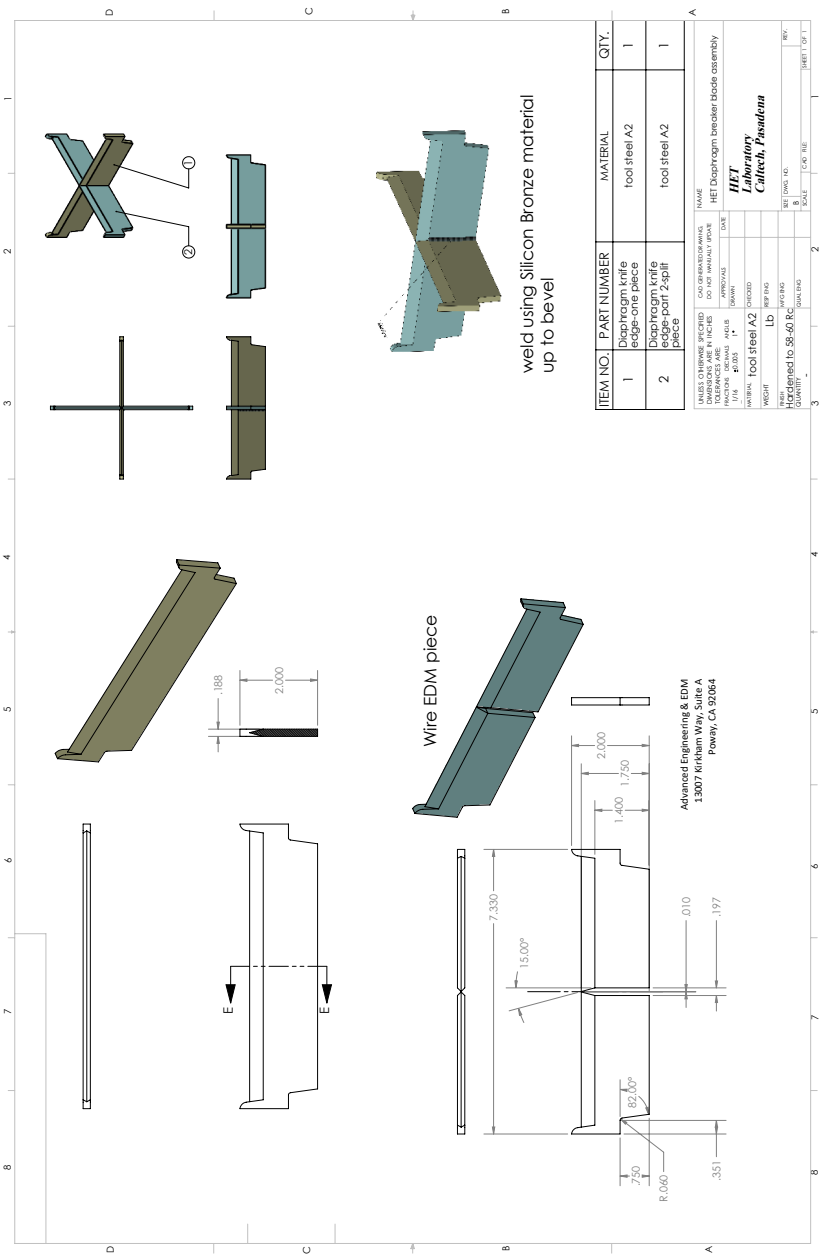
weld using Silicon Bronze material
up to bevel
Wire EDM piece
ITEM NO. | PART NUMBER | MATERIAL | QTY.
1 | Diaphragm knife edge-one piece | tool steel A2 | 1
2 | Diaphragm knife edge-pair 2-split piece | tool steel A2 | 1
Hardened to 58-60 Rc
Advanced Engineering & EDM
13007 Kirkham Way, Suite A
Poway, CA 92064
HET Diaphragm breaker blade assembly
HET
Laboratory
Caltech, Pasadena

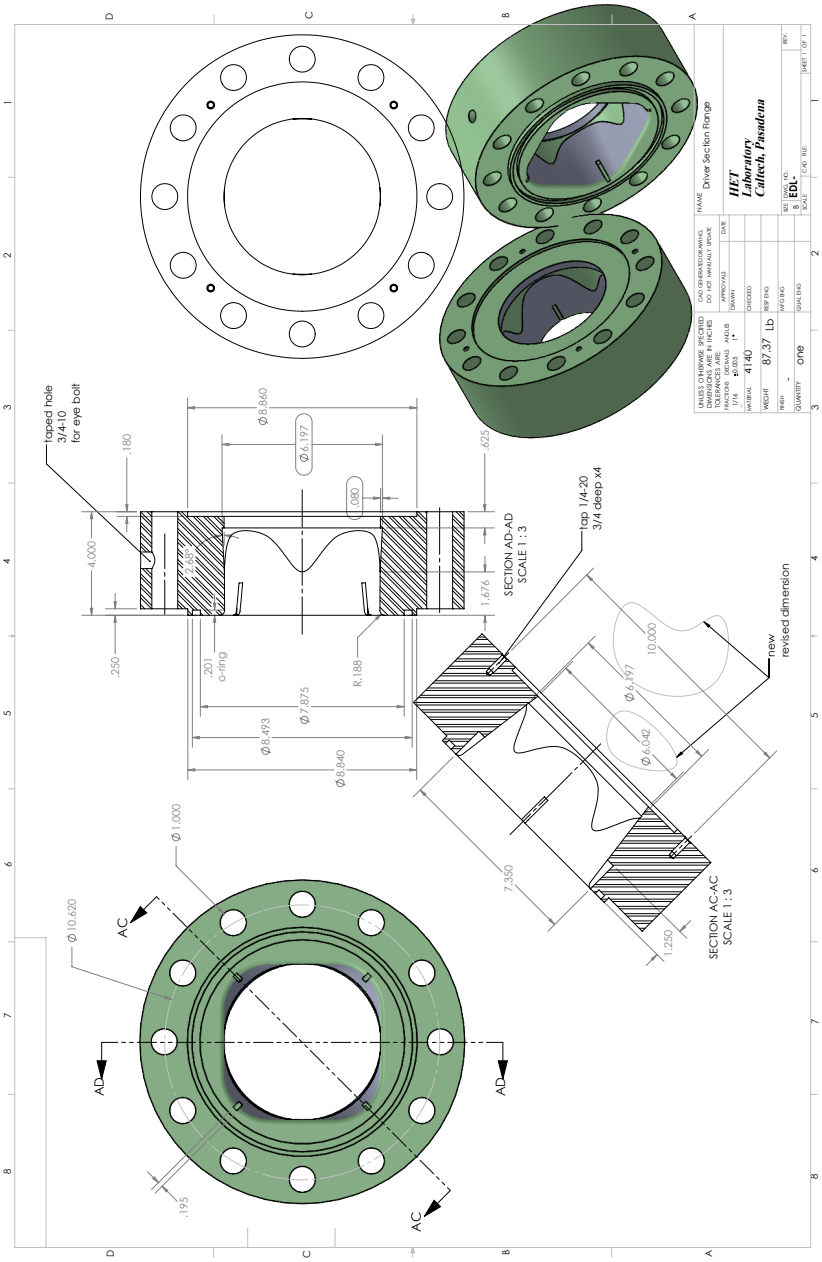
Drive Section Flange
HET
Laboratory
Caltech, Pasadena
taped hole
3/4-10
for eye bolt
.180
.625
Ø8.860
Ø6.197
.080
4.000
1.676
.250
.201
o-ring
R.188
Ø7.875
Ø8.493
Ø8.840
SECTION AD-AD
SCALE 1 : 3
tap 1/4-20
3/4 deep x4
10.000
Ø6.197
Ø6.042
new
revised dimension
7.350
1.250
SECTION AC-AC
SCALE 1 : 3
Ø1.000
Ø10.620
AC
AD
.195
WEIGHT 87.37 Lb
MATERIAL 4140
QUANTITY one
SIZE B
DWG. NO. EDL-